University of Kentucky
UKnowledge

University of Kentucky Doctoral Dissertations | Graduate School

2007

CAPACITANCE METROLOGY OF CURVED SURFACES: STUDY AND CHARACTERIZATION OF A NOVEL PROBE DESIGN

Philip T. Smith Jr.
University of Kentucky, psmith@engr.uky.edu

Click here to let us know how access to this document benefits you.

Recommended Citation
Smith Jr., Philip T., "CAPACITANCE METROLOGY OF CURVED SURFACES: STUDY AND CHARACTERIZATION OF A NOVEL PROBE DESIGN" (2007). *University of Kentucky Doctoral Dissertations*. 570.
https://uknowledge.uky.edu/gradschool_diss/570

This Dissertation is brought to you for free and open access by the Graduate School at UKnowledge. It has been accepted for inclusion in University of Kentucky Doctoral Dissertations by an authorized administrator of UKnowledge. For more information, please contact UKnowledge@lsv.uky.edu.

ABSTRACT OF DISSERTATION

Philip T. Smith Jr.

The Graduate School

University of Kentucky

2007

CAPACITANCE METROLOGY OF CURVED SURFACES: STUDY AND CHARACTERIZATION OF A NOVEL PROBE DESIGN

ABSTRACT OF DISSERTATION

A dissertation submitted in partial fulfillment of the requirements for the degree of Doctor of Philosophy in the College of Engineering at the University of Kentucky

By
Philip T. Smith Jr.

Lexington, Kentucky

Director: Dr. R. R. Vallance, Assistant Professor of Mechanical Engineering

Lexington, Kentucky

2007

Copyright © Philip T. Smith Jr. 2007

ABSTRACT OF DISSERTATION

CAPACITANCE METROLOGY OF CURVED SURFACES:
STUDY AND CHARACTERIZATION OF A NOVEL PROBE DESIGN

Capacitive sensors are frequently applied to curved target surfaces for precision displacement measurements. In most cases, these sensors have not been recalibrated to take the curvature of the target into consideration. This recalibration becomes more critical as the target surface becomes smaller in comparison to the sensor. Calibration data are presented for a variety of capacitance probe sizes with widely varying geometries.

One target surface particularly difficult to characterize is the inner surface of small holes, less than one millimeter in diameter. Although contact probes can successfully measure the inner surface of a hole, these probes are often fragile and require additional sensors to determine when contact occurs. Probes may adhere to the wall of the hole, and only a small number of data points are collected.

Direct capacitance measurement of small holes requires a completely new capacitance probe geometry and method of operation. A curved, elongated surface minimizes the gap between the sensor surface and the inner surface of the hole. Reduction in the size of the sensing area is weighed against electronics limitations. The performance of a particular probe geometry is studied using computer simulations to determine the optimal probe design. Multiple, overlapping passes are deconvolved to reveal finer features on the surface of the hole.

A prototype sub-millimeter capacitance probe is machined from tungsten carbide, with four additional material layers added using ebeam deposition. Several techniques are studied to remove these layers and create a sensing area along one side of the probe. Both mechanical processes and photolithography are employed.

KEYWORDS: capacitance gage, electric field, small hole metrology, non-contact probe, micro-EDM machining

CAPACITANCE METROLOGY OF CURVED SURFACES: STUDY AND CHARACTERIZATION OF A NOVEL PROBE DESIGN

By

Philip T. Smith Jr.

Dr. R. Ryan Vallance
Director of Dissertation

Dr. Scott Stephens
Director of Graduate Studies

October 16, 2007

RULES FOR THE USE OF DISSERTATIONS

Unpublished dissertations submitted for the Doctor's degree and deposited in the University of Kentucky Library are as a rule open for inspection, but are to be used only with due regard to the rights of the authors. Bibliographical references may be noted, but quotations or summaries of parts may be published only with the permission of the author, and with the usual scholarly acknowledgments.

Extensive copying or publication of the dissertation in whole or in part also requires the consent of the Dean of the Graduate School of the University of Kentucky.

A library that borrows this dissertation for use by its patrons is expected to secure the signature of each user.

Name	Date

DISSERTATION

Philip T. Smith Jr.

The Graduate School

University of Kentucky

2007

CAPACITANCE METROLOGY OF CURVED SURFACES: STUDY AND CHARACTERIZATION OF A NOVEL PROBE DESIGN

DISSERTATION

A dissertation submitted in partial fulfillment of the requirements for the degree of Doctor of Philosophy in the College of Engineering at the University of Kentucky

By
Philip T. Smith Jr.

Lexington, Kentucky

Director: Dr. R. R. Vallance, Assistant Professor of Mechanical Engineering

Lexington, Kentucky

2007

Copyright © Philip T. Smith Jr. 2007

ACKNOWLEDGEMENTS

I would first of all like to thank my advisor, Prof. Ryan Vallance, as well as the other members of my committee; Prof. Keith Rouch, Prof. Suzanne Smith, Prof. William Smith, and Prof. Ingrid St. Omer. Many thanks to Prof. Bruce Walcott, my outside reader, as well as the students of Prof. St. Omer for their help in the coating process and use of the clean room. For ongoing help with everything from the µEDM machine to models in Pro/Engineer, my sincere thanks to Chris Morgan. My thanks to Prof. Scott Stephens and his students for use of the Zygo interferometer and other BSL equipment. To Prof. Eric Marsh at Penn State University, much appreciation for his helpful suggestions and for pointing out that, in the end, most graduate students "live happily ever after." Much time and effort was given over to explanations by Prof. Stuart Smith, Larry Rice, and George Spiggle. Thanks to them for their contributions to this effort.

Finally, I would like to thank my family, without whom I would never have started on this grand undertaking. To my parents, thanks for always encouraging me to build on my education. Thanks to my daughter Jerusha Riess-Smith, who looked forward to helping me collate the final copies. Finally and most importantly, thanks to my wife, Jana Riess. She has provided words of encouragement, hours of her time, and wisdom from her own experience. I owe my family a debt that perhaps can never be repaid.

Table of Contents

Table of Contents iv
List of Tables vii
List of Figures viii
List of Files xii

1 Introduction 1
1.1 Introduction to Capacitance Sensors 1
1.2 Fundamental Equations of Capacitance 2
1.3 Literature Review 4
1.3.1 Capacitance Sensors 4
1.3.2 Sensor Types and Computational Methods 7
1.3.3 Spindle Metrology Literature 10
1.3.4 Finite Probe Deconvolution Literature 11
1.3.5 Small Hole Metrology Literature 15
1.4 Electric Field Analysis Formulation 16
1.5 Finite Element Modeling 19
1.5.1 Generalizing Spherical Target Geometry 21
1.5.2 Cylindrical Target Surfaces 22
1.5.3 Novel Probe FEA Modeling 24
1.5.4 Probe Deconvolution Methods 25
1.6 Manufacture of a Novel Probe Design 25
1.7 Contributions of This Research 29

2 Generalized Calibration for Spherical Targets 31
2.1 Introduction 31
2.2 Closed-Form Capacitance Solutions 33
2.3 Strain Energy Calculation 37
2.4 Finite Element Electric Field Formulation 38
2.5 Variables for Parametric Study 39
2.6 ANSYS Code for Iterative Analysis 41
2.7 Capacitance Results 42
2.8 Analysis of Results 47
2.9 Parametric Study and Conclusions 51
2.9.1 Sensing area diameter 51
2.9.2 Guard ring spacing 54
2.9.3 Relative permittivity of epoxy 55
2.9.4 Gap distance and slopes 58
2.10 Conclusions 59

3 Analysis of Cylindrical Target Surfaces 63
3.1 Introduction 63
3.2 Base Calibration of Capacitance Sensor 64
3.3 Determination of Capacitance with Finite Element Analyses 65
3.3.1 The Finite Element Model 65
3.3.2 Capacitance as a Function of Gap and Target Diameter 67
3.4 Effects on Displacement Sensing 69

3.4.1 Reduction and Shift of the Sensing Range 70
3.4.2 Increases in Sensitivity and Nonlinearity 72
3.5 Validation of Corrected Sensitivities...76
3.6 Corrections in Roundness and Spindle Metrology 77
3.7 Conclusions..79

4 Optimal Geometry of a Hole Probe 80
4.1 Introduction..80
4.2 Rough Design of Probe Geometry..81
4.3 Solid Models and Finite Element Analysis..83
4.4 Influence of Target Surface on Probe Resolution..84
4.5 The Analog Nature of the Capacitance Probe Output 86
4.5.1 Analog frequency limits...86
4.5.2 Digital and quantum limits...88
4.6 Simplified Geometry and Deconvolution 89
4.6.1 Single-conductor probe 89
4.6.2 Sensing area with guard ring..97
4.7 Conclusions..100

5 Capacitive Deconvolution of Probe Designs 103
5.1 Introduction..103
5.2 Integral Model of Probe Overlap 103
5.3 Approaches to the $C_{\min}$ Limitation...107
5.3.1 Indexing method of deconvolution 108
5.3.2 Continuous slot probe 112
5.4 Deconvolution of Nonuniform Surfaces...117
5.4.1 Step function simulation and deconvolution 118
5.4.2 Sinusoidal nonuniform surface 127
5.5 Extension to 3D..131
5.5.1 Multiple areas of influence 132
5.5.2 Hole measurement trajectories...133
5.5.3 Probe design considerations...135
5.6 Noise Considerations 140
5.6.1 Rectangular probe error 140
5.6.2 Long probe error 143
5.6.3 Sidewall errors 144
5.6.4 Effects of probe error motion...144
5.6.5 Monte Carlo Simulation...146
5.7 Conclusions..146

6 Probe Manufacture and Analysis..148
6.1 Introduction..148
6.2 Wire Electro-Discharge Grinding of the Probe 150
6.2.1 Rounding the edges of the probe 158
6.2.2 Improvements to the μEDM machine...160
6.3 Coating the Probe...163
6.3.1 Cleaning the probe surfaces...164

6.3.2 Ebeam deposition of layers 165
6.3.3 Probe surface metrology 175
6.4 Conclusions 181

7 Probe Etching and Testing 183
7.1 Introduction 183
7.2 Manufacture of a Physical Mask by μEDM 184
7.2.1 Creating the mask-making tool 184
7.2.2 Machining the slot 186
7.3 Etching of the Probe using the Physical Mask 188
7.3.1 Capacitance of probe with alumina in place 189
7.3.2 Underetching of probe layers 192
7.3.3 Redeposition of material 192
7.4 Etching Processes 193
7.4.1 Wet etching process 195
7.4.2 Dry etching process 197
7.4.3 Surface grinding 199
7.5 Conclusions 202

8 Conclusions and Future Work 203
8.1 Calibration and Spherical Targets 203
8.2 Solutions for Cylindrical Targets 205
8.3 Probe Design 207
8.4 Method for Deconvolving Capacitance Measurements 207
8.5 Manufacturing Method for Prototype Probes 208
8.6 Future Work 208
8.7 Reducing the Scale 209

Appendix A: List of Variables 212

Appendix B: Data Transfer from Pro/Engineer To ANSYS 213
B.1 Exporting Geometry Using IGES 213
B.2 Exporting Elements Using Pro/Engineering Mechanica 218

Appendix C: ANSYS Code for FEA 224
C.1 Capacitance Probe and Spherical Target 224
C.2 Capacitance Probe and Cylindrical Target 228
C.3 Importing IGES Format Code 235

Appendix D: Matlab Code for Machining and Analysis 240
D.1 Machining Routines 240
D.1.1 Machining a hemisphere 240
D.1.2 Grinding process for slot creation 241
D.2 Code for Analysis 242

References 244

Vita 252

List of Tables

Table 2-1. Variables and their values applied to the parametric study. 40
Table 2-2. Selected capacitance values for the spherical study. Capacitance values in pF. 45
Table 3-1: Nominal gaps, sensitivities, and nonlinearities for low and high sensitivities of the representative capacitive sensor 65
Table 3-2. Predicted changes in the gap and sensing range for low sensitivity (–0.394 V/μm) 72
Table 3-3. Predicted changes in the gap and sensing range for high sensitivity (–1.969 V/μm) 72
Table 3-4: Comparison of corrected sensitivities determined by finite element analyses and experimentally 75
Table 4-1. FEA capacitance values compared with parallel plate approximation. 93
Table 6-1. Initial probe shaping routine. 154
Table 6-2. Capacitance values and associated *Z* feed rates. 154
Table 6-3. Further shaping of probe. 156
Table 6-4. Final probe shaping routine. 157
Table 6-5. Materials applied to the tungsten carbide probe, in order of application. 175
Table 6-6. Values before and after incomplete alumina coating. 180
Table 6-7. Values before and after application of gold coating. 180
Table 7-1. Routine for creating the mask-making tool. 185
Table 7-2. Material removal rates for various materials and processes. 194

List of Figures

Figure 1-1. Lion Precision capacitance gage with key components labeled. 3
Figure 1-2. Spindle measurement using the Donaldson Reversal technique....................10
Figure 1-3. A conic AFM probe tip measuring a vertical step on a target surface. 11
Figure 1-4. Geometric deconvolution method proposed by Markiewicz and Goh from [61]. 14
Figure 1-5. Four-sided toroid element and its two-dimensional representation. 19
Figure 1-6. Ten-node tetrahedral element, one DOF at each node. 20
Figure 1-7. Sketch of cylindrical probe and cylindrical target surface, showing axis of symmetry for each. 23
Figure 1-8. An electron micrograph of a 50 μm diameter tungsten carbide probe. Image courtesy of Chris Morgan, Precision Systems Lab. 26
Figure 1-9. Light microscope images of the (a) top and (b) bottom surfaces where holes were machined using a tungsten carbide probe and micro EDM. Images courtesy of Chris Morgan. 27
Figure 1-10. Tungsten carbide probe coating procedure to provide localized position sensing...28
Figure 2-1. Cross section of the Lion Precision C1-C capacitance sensor. All dimensions are in mm. 32
Figure 2-2. Gaussian integral to calculate electric field. 34
Figure 2-3. Electric field analogy between identical spheres and sphere and infinite plate. 36
Figure 2-4. ANSYS Element 121, used to model cylindrical symmetry in an electrostatic analysis. 38
Figure 2-5. Model parameters varied for study. 39
Figure 2-6. Mutual-lumped capacitance numbering for FEA model...............................43
Figure 2-7. Comparison of capacitance plot to parallel-plate solution. 50
Figure 2-8. Comparison of capacitance plot to two-sphere solution. 50
Figure 2-9. Plot of normalized capacitance as a function of dimensionless target radius for the three sensing areas and the smallest gap distance *d*. 53
Figure 2-10. Plot of normalized capacitance as a function of dimensionless target radius for the three sensing areas and the largest gap distance *d*. 53
Figure 2-11. Plot of variation in capacitance as a function of guard ring spacing and small gap distance *d*. 54
Figure 2-12. Plot of capacitance vs. guard ring spacing and large gap distance *d*. 55
Figure 2-13. Plot of variation in capacitance as a function of both the width of the dielectric material and its permittivity for the smallest gap distance *d*...56
Figure 2-14. Plot of variation in capacitance as a function of both the width of the dielectric material and its permittivity for the largest gap distance *d*. 57
Figure 2-15. Plot of inverse capacitance as a function of gap distance *d* as a function of several different target diameters. 59
Figure 3-1: Geometry for the finite element analyses, consisting of one-quarter of the complete 3D geometry. 66

Figure 3-2: Electric potential in the non-conductive regions between the capacitive sensor and the cylindrical target. 68
Figure 3-3: Quiver plot showing magnitude and direction of electric field between sensor and the cylindrical target 68
Figure 3-4: Lumped capacitances between conductive electrodes as viewed in cross section of symmetry plane one. 69
Figure 3-5: Finite element analysis procedure. 70
Figure 3-6. Inverse capacitance for low sensitivity (–0.394 V/µm) as functions of the gap and target diameters. 71
Figure 3-7. Inverse capacitance for high sensitivity (–1.969 V/µm) as functions of the gap and target diameters 71
Figure 3-8. Output voltage for low sensitivity (–0.395 V/µm) as functions of the change in gap and target diameters (predicted by FEA) 74
Figure 3-9. Output voltage for high sensitivity (–1.969 V/µm) as functions of the change in gap and target diameters (predicted by FEA) 74
Figure 3-10. Residual voltages for low sensitivity (–0.394 V/µm) as functions of the change in gap and target diameters 75
Figure 3-11. Residual voltages for high sensitivity (–1.969 V/µm) as functions of the change in gap and target diameters 75
Figure 3-12. Sketch of experimental setup. 76
Figure 3-13. A common arrangement of spindle stator, rotor, and two capacitive displacement sensors used to measure the radial error motion of the spindle. 78
Figure 3-14. Simulated metrology of workpiece roundness and spindle radial error motion with a cylindrical Ø25 mm artifact on high sensitivity. 78
Figure 4-1. Target surface compared with stairstep approximation. 85
Figure 4-2. Primary and secondary contributors to capacitance. 85
Figure 4-3. A capacitance probe sweeping past a target surface with velocity v. 87
Figure 4-4. Two-dimensional model of rotating probe in a half hole. 90
Figure 4-5. Two-dimensional model of air gap to be meshed. 90
Figure 4-6. Polar plot of hole surface at three different probe diameters. 92
Figure 4-7. Images showing the magnitude of the electric field, in V/mm, as a function of position within a sinusoidal half-hole. 95
Figure 4-8. Geometric deconvolution, as applied to the probe data. 96
Figure 4-9. Deconvolved "probe shape" data for different gap distances. 97
Figure 4-10. Two-dimensional capacitance probe with guard ring structures. 98
Figure 4-11. Pro/Engineer model of air gap, including guard structures. 99
Figure 4-12. Comparison of distance measurements with and without guard structure. 100
Figure 5-1. Integrating over two probe areas. 104
Figure 5-2. Plot of capacitance as a function of entrance angle. 105
Figure 5-3. Capacitance probe reaching sensible level (a), passing through additional range (b), and after trailing edge has entered target surface (c). 107
Figure 5-4. Half-hole (a) and complete hole (b), each divided into 8 zones. 108
Figure 5-5. Two different three-dimensional probe designs. 114

Figure 5-6. Cross section of two probe designs midway through hole. 114
Figure 5-7. Pro/Engineer model of long probe geometry. 115
Figure 5-8. Long probe capacitance results. 117
Figure 5-9. Finite element model of half-hole including step. 119
Figure 5-10. Polar plot of surface for step test as a function of centerline position of probe. 119
Figure 5-11. Plot of capacitance as a function of centerline position. 120
Figure 5-12. Deconvolved distance from rectangular probe and width of probe. 121
Figure 5-13. Long probe raw results for step function. 122
Figure 5-14. Slope of long probe FEA results showing change in gap distance *d*. 123
Figure 5-15. Electric field at transition zone, in V/mm. Vector length as well as color indicates strength of electric field. 125
Figure 5-16. Pro/Engineer model of half-hole sinusoidal target surface and rectangular probe. 128
Figure 5-17. Raw data from scan of half-hole sinusoidal target. 128
Figure 5-18. Plot of deconvolved surface. 130
Figure 5-19. Raw data output from long probe and sinusoidal target. 131
Figure 5-20. Long probe targeting a sinusoidal surface, deconvolution results. 131
Figure 5-21. Areas of influence on the target surface for three-dimensional probe. 133
Figure 5-22. Two schemes for scanning target holes. 134
Figure 5-23. FEA simulations of the electric field in V/mm of a sharp corner (left) vs. a rounded corner (right). 136
Figure 5-24. Three-dimensional probe targeting cylindrical surface. 137
Figure 5-25. Plot of capacitance for rounded sensing area. 139
Figure 5-26. Deconvolved 3D surface using modified [D] matrix. 139
Figure 5-27. Spindle alignment and other causes of probe error. 145
Figure 6-1. Capacitance Probe Design. 149
Figure 6-2. Panasonic model MG-82 μEDM Machine. 150
Figure 6-3. Probe machining area. 151
Figure 6-4. Detail of μEDM spindle. 151
Figure 6-5. Probe Shaping on the Panasonic Model MG-82. 152
Figure 6-6. Possible geometries from provided Qbasic code. 153
Figure 6-7. Machining steps in probe manufacture. 155
Figure 6-8. Diameter measurements using the Image-Pro Express software. 156
Figure 6-9. Electron micrographs of tungsten carbide probe (a) rounded step (b) rounded tip. 160
Figure 6-10. Schematic of pump configuration. 162
Figure 6-11. Improved pump design. 163
Figure 6-12. Torr International Ebeam Evaporator. 165
Figure 6-13. Two aluminum bracket designs for mounting cylindrical probes in the ebeam evaporator (a) bar design (b) wafer design. 166
Figure 6-14. Assembly of sample support arm, probe holder, capacitance probe, and crucible showing relative positions of each within the vacuum chamber. 167
Figure 6-15. Photograph of ebeam evaporation chamber during coating process. 168
Figure 6-16. Diagram of asymmetric coating when two probes are present. 169

Figure 6-17. Probe coating peeling from tungsten carbide surface. 170
Figure 6-18. Uncoated tungsten carbide probe. 171
Figure 6-19. Tungsten carbide probe with nickel coating. 171
Figure 6-20. Probe with nickel and alumina coatings..172
Figure 6-21. X-ray spectrum from nickel coated probe...173
Figure 6-22. X-ray spectrum from nickel and alumina coated probe. 173
Figure 6-23. Model of coated probe, showing larger area for alumina coating than gold layer. Thicknesses of coatings are exaggerated for illustrative purposes. 174
Figure 6-24. The 'micro.app' profilometry application..176
Figure 6-25. Interference patterns or "fringes" from the Zygo NewView. 177
Figure 6-26. Oblique plot of incomplete alumina coating..179
Figure 6-27. Oblique plot of complete gold coating...181
Figure 7-1. Dimensions of the slot to be machined in the nickel mask. 185
Figure 7-2. Machining the nickel mask. 187
Figure 7-3. SEM image of completed nickel mask...188
Figure 7-4. Parallel plate capacitor with two different dielectric materials.....................189
Figure 7-5. Problem reduced to parallel plate capacitors in series. 190
Figure 7-6. Underetching of alumina through gold coating. 193
Figure 7-7. Assembly of probe and mask. 196
Figure 7-8. Blank and finished grinding tool. SEM image courtesy of Chris Morgan. 199
Figure 7-9. Debris left behind by grinding process. 201
Figure 7-10. Atomic spectrum of ground surface. 201
Figure 7-11. Ground surface of the probe...202
Figure 8-1. Mask with mechanical step to avoid probe fracture.....................................211

List of Files

pts_data.txt .... 446 kBytes

1 Introduction

1.1 Introduction to Capacitance Sensors

Precision capacitance devices have been used as a measurement tool for the last hundred years [1, 2], with each application demanding an optimal geometry. For the simplest systems, closed-form approximations are available, but for the most widely applied geometries these are only rough estimates. While several techniques for determining the capacitance of a system are available, for the quasi-static systems addressed in this work a finite-element solution has been adopted. This method allows readily-available engineering software to be applied to various systems with only minor modifications. Although the fundamental equations and the boundary conditions are straightforward, the generation of hundreds of nodes and assembly of large matrices is achieved only via computer analysis.

A common capacitance gage configuration is that of a circular sensing area closely surrounded by a second conductor, the “guard ring”. One commercial capacitance gage of this design is modeled, with capacitance determined as a function of the distance to a grounded target surface. A prior study examined how target curvature affected the output capacitance of the system. The new study addresses how each variable in the geometry affects the capacitance of the probe. By establishing a hierarchy of design features, as new methodologies are developed for manufacturing, the most important features can be incorporated first.

A second study examines a capacitance probe targeting a cylindrical surface. Although both items contain axial symmetry, the axes are perpendicular and so the geometry of capacitance probe and target surface must be built in three dimensions. By showing how the capacitance of a commercial probe can be recalibrated with *a priori* knowledge of the radius of the target surface, linearity of the system can be restored. This calibration is necessary for proper correction to axis-of-rotation alignment, and it is also useful in testing other designs. The calibration is also applicable to Donaldson Reversal, a method to separate out spindle error motion from surface errors. This technique always targets a spherical or cylindrical surface, and depends on the linearity of the capacitance gage. This linearity is called into question when the target surface is anything other than flat and parallel to the probe.

Once the design features of a capacitance probe have been studied, two wholly new probe geometries are presented. These probes are designed to capacitively measure the surface features inside small holes. As with commercially available capacitance probes, a sensing area is surrounded by a guard ring structure. The shape is optimized using the commercial probe study as a guide. Unlike the commercial probe, however, the surface of the new probe design is curved to closely follow the inside diameter of the target hole.

Because of the changes introduced with the new probe design, a series of finite element surface studies are executed. These studies determine the size of features that can be measured for a given probe sensing area. They also present a new method of deconvolving the resulting data to extract a resolution that is significantly better than the size of the probe sensing area. Each probe design requires a unique matrix solution to provide corrective terms for the target surface.

The manufacture of a small capacitance probe presents its own share of difficulties, as the methods of material deposition developed for wafer technologies must be applied to a cylindrical surface. This surface is formed using µEDM machining, then coatings are applied using ebeam deposition. Both of these techniques can be scaled down from the initial, sub-millimeter diameter probe, to the target diameter of less than 100 µm. The resulting surfaces of these coating operations are studied both qualitatively and quantitatively.

1.2 Fundamental Equations of Capacitance

Capacitance is the property of a conductor or a system of conductors to store and release charge. The fundamental relationship between charge Q, capacitance C, and voltage potential V, is given by Eq. (1-1). The energy stored in a capacitor is given by Eq. (1-2). From these equations, for a fixed voltage, both charge and energy storage ability goes up linearly as capacitance increases.

$$Q = C \cdot V \tag{1-1}$$

$$W = \tfrac{1}{2} C V^2 \tag{1-2}$$

Because negatively-charged electrons are naturally repelled by each other and are drawn to positive charges (i.e., a material with a dearth of electrons), the most common and efficient capacitor arrangements have two conductors in close proximity separated by a thin layer of insulator. When one plate is charged negatively and the other charged positively, many more electrons can be stored, as the electrons on the negative plate are drawn to the holes on the positively charged plate. Since the attraction of electrons to holes is larger as the gap between the two conductors decreases, a smaller gap between the plates results in a higher capacitance. Likewise, a larger surface area causes the capacitance to increase. If the gap distance or the surface area is variable, the capacitance between the two plates will vary as well. This configuration of flat conductors separated by a constant gap is termed a parallel-plate capacitor.

The property of capacitance to vary with either the gap distance d between the plates or the surface area A of the plates is the basis for the design of many commercial capacitance displacement sensors. These sensors are used in applications requiring high sensitivity, non-contact displacement measurement. In nearly all commercial capacitance gage applications, the gage is placed in close proximity to a conductive target surface that is electrically grounded. Figure 1-1 shows one commercially available capacitance displacement sensor manufactured and sold by Lion Precision, Inc.

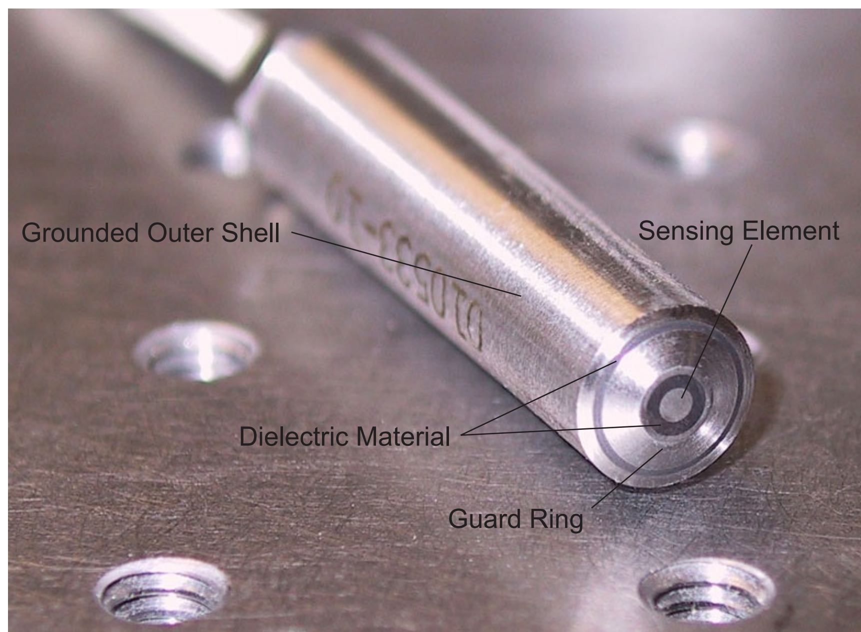

Figure 1-1. Lion Precision capacitance gage with key components labeled.

On this sensor the central conductor or "sensing element" is ground flat and perpendicular to the housing. This conductor is separated from the "guard ring" by an insulating epoxy. The guard ring is kept at approximately the same potential voltage as the sensing element, but is not part of the sensing circuit. This guard ring geometry minimizes the spreading or "fringe effects" of the electric field near the edges of the sensing element. By minimizing the fringing, the linearity is improved and the gage is also somewhat protected from spurious external electric fields. The sensor is operated with a driving frequency of a few hundred kHz so the effect of impedence on the system is negligible.

1.3 Literature Review

1.3.1 Capacitance Sensors

Capacitive displacement sensors are typically constructed from conductive electrodes separated by a solid dielectric material. The sensing electrodes are often flat surfaces [3, 4, 5, 6, 7], but cylindrical, spherical, and other electrode geometries have also been utilized for specific applications [8, 9, 10]. Equation (1-3) shows the simplest equation for capacitance between two parallel plates. This equation is the starting point for calculating many capacitance arrangements.

The capacitance C from Eq. (1-3) is exact for infinite parallel surfaces, where a uniform electric field spans the gap. The capacitance is proportional to the permittivity of free space ε_o, the relative permittivity of the dielectric material separating the sensor and target ε_r, and the area of the sensing electrode A. The capacitance C is inversely proportional to the distance d that separates the sensor and target, since the electric field strength decreases as the gap is increased. The permittivity of free space (vacuum) is a constant equal to 8.854×10^{-3} pF/m, and the relative permittivity, a dimensionless parameter, is the ratio of the dielectric's permittivity to the permittivity of a vacuum. Because any material present in the gap between plates will cause the capacitance to increase, the relative permittivity is always greater than one.

$$C = \frac{\varepsilon_o \varepsilon_r A}{d} \tag{1-3}$$

Capacitive displacement sensors such as Figure 1-1, which use only finite sized electrodes, have fringing of the electric field around the perimeter of the electrodes. This non-uniform electric field causes deviations from the ideal capacitance C given in Eq. (1-3). However, the homogeneity of this electric field is greatly improved by incorporating a guard ring into the sensor, first suggested by Lord Kelvin. A guard ring is an annular electrode that encloses the sensing electrode; the two electrodes are separated by an insulator but operated at the same electric potential. Maxwell [11] found that the increase in capacitance due to the field fringing into the annulus between the guard ring and sensing area is as small as a few parts per million, when the radial separation g between the sensing electrode and guard ring is very small compared to the gap distance. In such cases, the capacitance between the sensing electrode and target is reasonably predicted with Eq. (1-3).

Capacitance sensors use three approaches to detect displacements with changes in capacitance. In the first approach, the capacitance varies linearly when the overlapping area A of the electrodes is changed. Sensors using this approach are most suitable for measuring larger displacement ranges with lower sensitivity [12, 13, 14]. The second approach is more common in precision metrology and used by the sensor in Figure 1-1, since it is suited for higher sensitivity but smaller sensing ranges [4, 5, 15]. In this approach the area remains unchanged, perpendicular displacements produce changes in the gap distance d between the electrodes. A linear (rather than hyperbolic) dependence on the gap distance d is obtained by considering the inverse of the capacitance C^{-1} as shown in Eq. (1-4).

$$C^{-1} = \frac{d}{\varepsilon_o \varepsilon_r A} \tag{1-4}$$

A third application of capacitance gages is to measure the thickness or another property of a non-conductive material, by keeping the geometry constant but changing the relative permittivity ε_r within the gap [16, 8]. This is a more indirect method for specialized applications. For example, the moisture content of certain grains has been determined nondestructively using variations in permittivity and phase angle as a function of excitation frequency [17].

Electronics that detect small changes in capacitance often utilize AC bridges [18] such as the transformer ratio bridge [3, 4, 6, 19, 20] or other circuits [21, 22, 23, 24]. Most of these circuits compare the capacitance of the sensing electrode relative to ground with a fixed, internal reference capacitance C_{ref}. The inverses of the two capacitances are equal when the gap d equals the nominal gap distance d_{nom}. The electronics then produce an output voltage V with gain G that is proportional to the difference between the inverse capacitances so that V is zero when d equals d_{nom}. This result leads to the linear sensing relation in Eq. (1-6), where output V is proportional to changes in the gap Δd (measured from the nominal gap d_{nom} as shown in Eq. (1-7), and the proportionality constant is the sensor's sensitivity S. The methods used in this analysis are not dependent on the particular circuit, as long as they produce an output signal of this type.

$$V = G\left(C^{-1} - C_{\mathrm{ref}}^{-1}\right) \tag{1-5}$$

$$V = S\,\Delta d \tag{1-6}$$

$$\Delta d = d - d_{nom} \tag{1-7}$$

In practice, the capacitance C usually differs from analytical predictions such as the one given in Eq. (1-3) or those presented for other simple electrode geometries by Heerens and Vermeulen [25] or Heerens [26, 27]. This discrepancy can result from complex electrode geometries, physical factors, or electrical factors. Electrical factors can include stray capacitance [23], temperature drift [7] and dynamic hysteresis [28]. Hicks and Atherton [29] and others have considered physical factors that can cause variations in the capacitance values. Several of these effects are due to the probe itself, including the width of the guard ring [3, 1], changes in geometry due to thermal expansion of the electrode [4], fringing of the electric field between conductors in the capacitance gage [5, 11, 1, 30], finite thickness of the electrodes [31], nonflatness of the electrodes [29, 1], and elastic deformation due to the attractive electrostatic forces [32]. Factors related to the target surface and external conditions include variations in the relative permittivity of air [7], relative tilt of the target surface [1, 31, 33, 34, 35], and roughness of the target surface [31].

Because of the number of factors that can affect the sensing law given in Eq. (1-6), commercial sensors are usually calibrated experimentally to verify their sensitivity S and determine their nonlinearity. In most cases, the calibration is conducted by recording the voltage output V of the sensor's electronics while the sensor targets a flat surface in air. Displacements of the sensor from the nominal gap can be measured with precision sensors such as a displacement measuring interferometer [30], a traceable linear scale, or a Fabry-Perot etalon with a He-Ne laser [36].

1.3.2 Sensor Types and Computational Methods

Computation techniques such as finite element analyses (FEA), enable the capacitance to be determined for complex electrode geometries or deviations due to other factors. Several researchers have used FEA to determine the capacitance as a function of the gap distance [37, 38, 39, 40], and Lányi [41] used two-dimensional FEA analyses to study the effects of surface irregularities and machining variations on parallel plate capacitance gages.

Electrical engineering literature often references capacitance in combination with inductance when frequencies are high enough that the effects are non-negligible. One such study by Yu and Holmes [42] calculates the stray capacitance of a ferrite-core inductor by using FEA. Two different approaches are used, a 2D model with an axis of symmetry and a 3D model, with air and ferrite cores. Both capacitance from individual coils to ground, capacitances between two coils, and capacitances between coils and a conductive core are solved using matrix methods.

Other mathematical methods can be applied if the geometry is related to one of the simple shapes where a closed-form solution is available. Liang, Li, and Zhai [43] begin with a closed form solution for a circular conducting plate and derive closed-form solutions to elliptical plates, plates with two lines of symmetry, and finally arbitrarily shaped plates through the use of multiple triangles. Although the mathematics of this approach differs significantly from that of FEA, the geometric approach of breaking the model into triangular segments and summing the contribution over the segments closely parallels the FEA method. The capacitance resulting from this technique is for a single plate in isolation, a solution more applicable to antenna design or RF propagation than for capacitive position sensors.

Another significant research area that requires capacitance studies is in cable design. One common design for carrying power or high frequency signals uses concentric cylindrical conductors surrounded by dielectric materials. Du and Zhou [44] apply the method of moments [45] to determine the capacitance of a finite-length cable, a critical property for cables designed to carry lightning strikes to earth. This method was developed to solve boundary integral equations, which are arrived at from the boundary conditions of the finite length problem. These boundaries include the same conditions applied in the FEA case, namely, boundaries of dielectric and conductor and boundaries of dielectric and empty space. The method of moments produces capacitances of the conductors with respect to each other as well as with respect to ground. Once this capacitance matrix is produced, the solution for the capacitance of the cable follow the same methods as those found in the ANSYS software. Results from Du and Zhou show that the edge effect (at the ends of the cable) cannot be ignored when the cable is "short", in this case defined as a ratio of length to radius of less than 14.

Designs of capacitance sensors for tactile measurements utilize variations in gap distance d to achieve changes in capacitance [46]. Although in some cases an air gap is used, to provide the widest range of operating pressures (up to 6 orders of magnitude) an elastic, dielectric material is placed in the gap. While the primary change in capacitance with pressure is due to changes in gap distance d, there are smaller effects due to changes in the relative permittivity and the area of the electrodes. The theoretical modeling of such a system primarily addresses the full dielectric tensor ε_{ik} and modeling the polarizability of the atoms as a function of lattice spacing under deformation.

Differential capacitance sensors also benefit from numerical analysis in the design process. Rain-sensing applications require a differential device due to variations in thermal conditions that would otherwise skew the results. Bord *et al.* [47] present a design study where rectangular and interdigital electrodes [48] are compared to determine the optimal geometry for rain sensing. In this configuration, a protective glass substrate separates the sensor from the water, so electrode spacing must take this into consideration. The simulations in this study are all carried out using FEA analysis with the ANSYS software package.

An array of capacitance sensors can be used as an imaging device in applications where the cross section of an object cannot be directly observed. Electrical capacitance tomography is one such application, where the cross section of a gas or fluid is obtained. He *et al.* [49] describe one such system, used for imaging the cross-section of a flame in an internal combustion engine. Six capacitance plates surround the combustion chamber, offering a total of 15 independent capacitances from pairs of plates. The computational component of this work is in taking the capacitance data and reconstructing a two-dimensional image from it. The image is a combination of the measured capacitance and a predetermined field sensitivity distribution. This sensitivity is calculated using finite element methods. The most sensitive regions in this type of sensor occur near the edges of the volume, while the center of the chamber is the region of least sensitivity. The number of electrodes is limited by computation and speed requirements, as well as by the smallest capacitance that can be measured.

Another application that utilizes capacitance as a cross-sectional imaging tool is in “down-hole measurements” of pipeline flows. This application is a fixed geometry with variable permittivity, since the material pumped from an oil well varies in composition. Holler *et al.* [50] were able to distinguish water from hydrocarbons, due to the significantly higher permittivity of the former. Fifteen rectangular electrodes surround a cylindrical pipe, and a 2D finite element mesh is generated. The simulations were solved using the Matlab Partial Differential Equation Toolbox. The solution to such a complex system of conductors is simplified somewhat by assumptions made regarding flow in the horizontal pipeline. Still, the system required multiple voltages and sensing circuits to make measurements, and short circuiting of the electrodes is possible.

To simplify this approach for pipeline applications, Al-Mously and Ahmed [51] proposed a sensor composed of two concentric cylinders, with either a solid or a hollow core. The capacitance of infinitely long concentric cylinders is used for the first approximation, and experimental results are obtained. Schüller *et al.* [52] simplified their system even further by proposing a single electrode capacitance probe, exposed to the oil/water flow through a glass or ceramic window. This capacitor is part of a simple LC circuit whose frequency varies with the dielectric properties of the medium, from approximately 22 pF for air to 27 pF for 100% water.

1.3.3 Spindle Metrology Literature

One common application for capacitance gages in the field of precision engineering is the measurement and separation of spindle error and cylindrical surface error. The Donaldson Reversal technique separates out these two error motions from two different measurements of the target surface. It was first proposed by R. R. Donaldson [53], and has been applied with variations to many metrology applications. It has been incorporated into numerous standards [54, 55]. An overhead view of a Donaldson Reversal application is illustrated in Figure 1-2, reproduced from [54]. Two measurements are made of a rotating surface, a "normal" and a "reversed" measurement, with both angular and displacement values recorded. Because the reverse placement is 180 degrees out of phase from the normal measurement, the sum of these two measurements represents twice the surface profile, and the difference is the spindle radial error motion. In equation form this becomes Eqs. (1-8) to (1-11) from [56],where I_1 and I_2 are the forward and reverse measurements, respectively, R is the spindle radial error motion, and B is the surface profile.

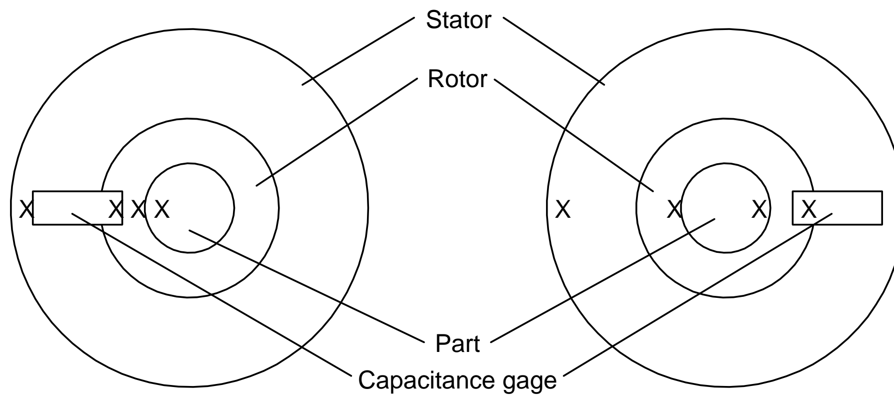

Figure 1-2. Spindle measurement using the Donaldson Reversal technique.

$$I_1(\theta) = R(\theta) + B(\theta) \tag{1-8}$$

$$I_2(\theta) = -R(\theta) + B(\theta) \tag{1-9}$$

$$R(\theta) = \frac{I_1(\theta) - I_2(\theta)}{2} \tag{1-10}$$

$$B(\theta) = \frac{I_1(\theta) + I_2(\theta)}{2} \tag{1-11}$$

These combinations assume that the measurements I_1 and I_2 utilize identical, linear gains in converting output voltage to displacement. The prior work with spherical target models [82] shows that the gain is not constant, but varies over the range of output voltages and gap distances between gage and target surface. Since the target surfaces in this application are by necessity cylindrical, the linearization of the resulting data must be considered before Eqs. (1-10) and (1-11) are applied.

1.3.4 Finite Probe Deconvolution Literature

Of particular interest in the design of a new capacitance probe is an understanding of its resolution capabilities. "Resolution" refers to both the ability of the probe to determine the height of a feature as well as the width and length. These last two dimensions are defined as being in the plane of the sensing element, or lateral resolution, while the height is defined as being perpendicular to the plane. It is known that a capacitance probe will have some "spreading" of the electric field beyond the size of the sensing area [82]. It will be shown that this spreading can be removed.

The problem of limited lateral resolution is also encountered in atomic force microscopy (AFM). In scanning probe microscopy, including AFM, a sharp probe is moved across the target surface. The probe interacts with the surface, and the resulting minute forces are recorded to create an image. Because the probe tip is of a finite size, it is unable to image all possible surface features. Tips with a conic shape encountering a vertical wall record a slope that reflects the angle of the probe tip, rather than the angle of the target surface. This interaction is shown in Figure 1-3.

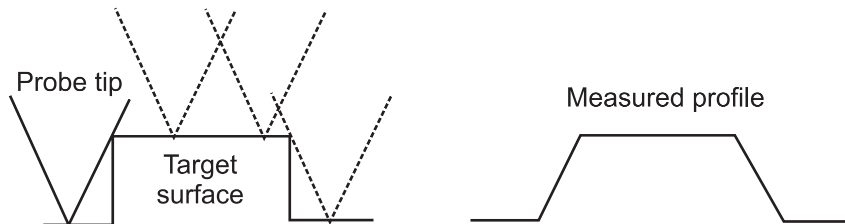

Figure 1-3. A conic AFM probe tip measuring a vertical step on a target surface.

The amount of tip that interacts with the surface varies with the amount of surface roughness present on the sample. If the surface is smooth to within 1 nm, then the few atoms that make up the tip are all that interact with the target. If the roughness of the target surface is on the order of 50 nm, then a larger section of the probe tip must be

considered to be convolved with the target. If a sample is known to have vertical or near-vertical step features, an approximation of the angle of the tip can be gleaned from the steepest angles found in the raw data from the scanning probe [57]. If the actual surface profile consists of objects that extend outward from the surface (e.g., a wafer containing manufactured probe tips), these objects have been shown to appear to have a larger radius of curvature and a larger base [58]. Holes or pits in a surface, on the other hand, appear narrower or less deep than their true dimensions.

The lateral resolution of the scan data from the probe is also limited by the geometry of the probe tip. In some models, the probe tip is approximated by a hemisphere of radius r. Surface roughness features smaller than this value generally cannot be resolved. The calculation of average roughness therefore contains errors introduced by this roundness. Tilt of the probe tip from perpendicular introduces a second type of artifact that affects the roughness calculation. Since there are several ways to determine roughness at different length scales, the relative merits of the mathematics of each method have been considered with regard to the surfaces to be measured [59].

Because probe tips are often damaged in scanning samples, it is imperative in atomic force microscopy to check the integrity of the tip on a regular basis. This testing uses a mechanical sample with a known, repeatable profile. Such test structures can be holes, pillars, or steps of a known height. For such patterns consistency is key, since only one or a few of the features will be imaged during a test. Patterns that can be cheaply and consistently manufactured are discussed in the literature [60]. A quick, qualitative test reveals whether the probe tip is still intact, and can resolve the fine features of the test structure. A quantitative test will use the output of the test structure to determine the shape of the probe tip.

These quantitative methods can be termed “geometric deconvolution.” With standard deconvolution methods two functions that have been combined are subsequently separable mathematically if one of the functions is known. For geometric deconvolution, the interaction of two surface geometries is mathematically separable if one geometry is known.

Another geometric deconvolution approach described by Markiewicz and Goh [61, 62] was first tested in this capacitance probe application. A two-dimensional

example of their methodology from [61] is shown in Figure 1-4. In this figure a probe tip with two peaks is shown measuring a rectangular trough (a). The AFM result shows a gradual slope and two flat regions (b). In this case the shape of the target surface is known, so in (c) an inverted form of this is applied to a solid surface. As the center of the inverted target traces the path of the raw data from (b), material above the inverted target is removed (d, e). The resulting profile is the best possible approximation of the probe tip (f). Mathematically, this procedure is applied to raw data by overlapping the inverted target shape with the raw output file at the same spatial resolution. A third set of data points represents the minimum value of the target curve throughout its swept path. Once the profile of the probe has been determined, this technique is applied equally well to the probe shape and raw data to determine the true shape of the target. Note that the reconstructed tip in Figure 1-4 (f) is not identical to the original tip, since the concave region between the two peaks cannot be resolved by the test surface.

More sophisticated methods have been developed for AFM applications in cases where the geometry of the probe tip cannot be determined. If, for example, the probe tip is destroyed during image collection, no convolution test can be done on a known target surface to determine the profile. Methods that attempt to reproduce the target surface without specific knowledge of the tip geometry are termed “blind restorations”. A raw image is processed with combinations of dilation and erosion methods to determine one or more parameters in an assumed probe shape. For shapes that incorporate two or more parameters, many more variations are needed before an optimal set of parameters can be deduced [63].

Other side-effects of the scanning probe process have also been studied. Distortion of the probe tip has been shown to vary with the speed of scanning [64]. The direction of scanning must also be taken into account when applying this correction. The scanning force, determined from the bending of the cantilever holding the probe tip, will also cause the probe tip to distort dynamically. Fortunately, these particular issues occur due to mechanical contact forces and so are not applicable to a capacitance probe.

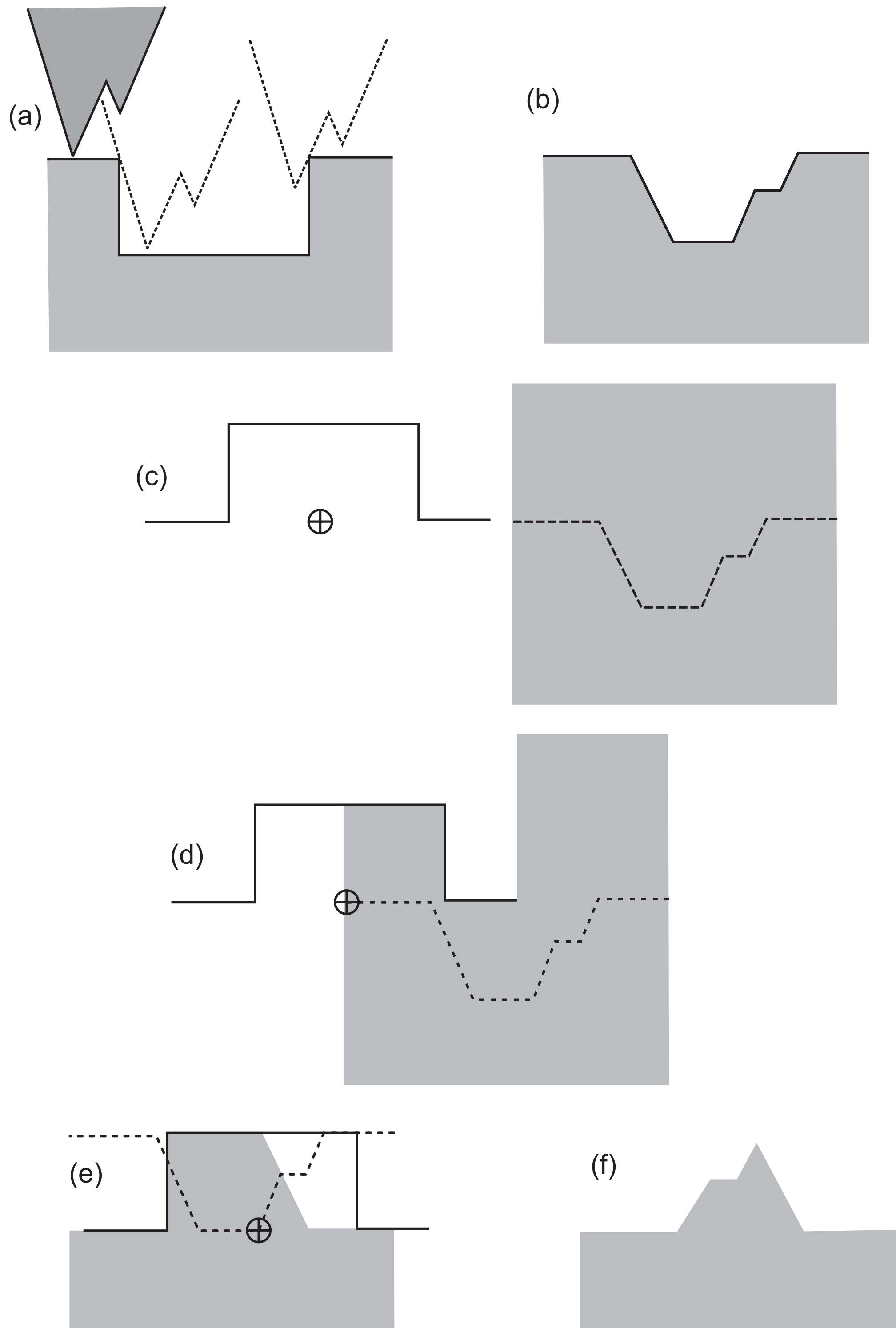

Figure 1-4. Geometric deconvolution method proposed by Markiewicz and Goh from [61].

With non-contact scanning probe microscopy, other techniques have been developed to record interactions between a probe tip and a surface. Electrostatic force

microscopy applies a potential voltage between tip and surface to determine properties such as charge density, dielectric permittivity, or dopant distribution. For the case of a sharp, unshielded tip, both the electric field and the electrostatic force must be taken into consideration. These calculations solve the Laplace equation for the probe tip geometry. Gomez-Monivas *et al.* show that changes in the dielectric properties of a thin material layer mimic the response due to changes in topology [65]. For new designs in capacitance probes, the presence of dielectric materials of varying permittivity must be carefully eliminated as a source of errors.

Other sources of errors in the literature include noise from the scanning probe output on the reconstruction of the probe tip. A method of geometric deconvolution is presented in matrix notation by Williams *et al.* [66], discussing the difference between the actual tip profile and the profile that can be recovered by geometric deconvolution. By adding noise to an image, the limitations of traditional deconvolution methods are shown. These are compared with mathematics that locate features in the image that cannot be generated by a physical probe. These non-physical artifacts are labeled “false” (the product of noise), and a more accurate reconstruction of the probe surface generated.

1.3.5 Small Hole Metrology Literature

Since a perfect hole can be defined as a true cylinder, deviations are defined as errors in cylindricity [67]. Measurement of cylindricity requires not only a roundness measurement of a single cross section of a hole, but also correlation from one roundness measurement to another. Destructive testing, where a hole is cut transversely and the cross section measured, only gives information about the roundness of the hole at that point. Similarly, a longitudinal cut through the centerline of a hole gives information in the linear direction, but no roundness details. Finally, there is the problem of reference. Surfaces are needed to define the linear direction of a hole, as well as the correct position on the part [68].

Measurement systems for small holes can be divided into systems that require contact with the hole surface, and systems that use optical or electrostatic methods of measurement. In the former category are systems that are considered “point” contact, even though at small enough scales the contact area is finite. The vibroscanning method [69, 70] which uses momentary contact between a probe edge and the hole surface to

establish electrical conduction, has a long and narrow contact surface. This geometry allows a much finer resolution of features along the length of the hole, as compared to the circular direction. Other contact systems utilize a spherical probe on the end of a narrow cantilever [71]. The sphere ensures that the point of contact is always on the surface of the sphere and not the cantilever arm. The diameter of such a sphere, however, dictates the size of small surface features to be measured. The diameter also dictates the maximum amount of declination and straightness errors that can be tolerated in a measurement.

A shape that better combines offset and sharpness is an inverted pyramid, similar to probe tips found in AFM applications [72]. Such a tip provides a tremendous increase in resolution along the length of the hole, at the cost of a probe that is easily damaged or destroyed. An AFM tip, unlike a spherical probe, also has a unique sensitive direction. To make measurements in the angular direction requires rotation of the probe system or the part, and any error of the rotational stage will contribute to the overall error of the measurement. Probe designs with similar limitations include twin silicon probes [73], where two parallel arms are inserted into a target hole.

Some methods have taken the above contact probes and applied improvements to the external sensing methods. If both the sphere and cantilever arm can be made of transparent material, then light can be used to sense proximity to the hole surface [74, 75, 76]. If the cantilever arm can be made long and flexible, then higher frequency resonances can be induced [77]. This eliminates the need for a spherical tip, since the cantilever tip at higher resonances has a greater displacement than other maxima along the arm.

1.4 Electric Field Analysis Formulation

Finite element analysis (FEA) software is most commonly used by mechanical engineers for stress/strain calculations or heat transfer modeling. The software package ANSYS can also solve electric and magnetic field problems. A complex electric field problem that cannot be calculated analytically can be solved using a sufficiently refined mesh [37].

As with heat transfer problems, the electric field solution takes the form of a scalar potential. The formulation for a conduction heat transfer problem is given in Eq.

(1-12), from [78], where q^B is the heat generation rate per unit volume, k_x, k_y, and k_z are thermal conductivities in orthogonal directions, and θ is the temperature.

$$\frac{\partial}{\partial x}\left(k_x \frac{\partial \theta}{\partial x}\right) + \frac{\partial}{\partial y}\left(k_y \frac{\partial \theta}{\partial y}\right) + \frac{\partial}{\partial z}\left(k_z \frac{\partial \theta}{\partial z}\right) = -q^B \quad (1\text{-}12)$$

Boundary conditions applied to heat transfer problems are either a known temperature on a surface, or a known heat flux. If there is no heat generation within the volume being studied, then the right hand side of Eq. (1-12) is zero.

Replacing the variables of Eq. (1-12) with those applied to electrostatic problems, the equivalent differential equation is shown in Eq. (1-13). Here q^B represents the presence of charges in the electric field or "charge density," the three ε values are the electric permittivity values of the material, and ϕ is the field potential in volts.

$$\frac{\partial}{\partial x}\left(\varepsilon_x \frac{\partial \phi}{\partial x}\right) + \frac{\partial}{\partial y}\left(\varepsilon_y \frac{\partial \phi}{\partial y}\right) + \frac{\partial}{\partial z}\left(\varepsilon_z \frac{\partial \phi}{\partial z}\right) = -q^B \quad (1\text{-}13)$$

The two possible boundary conditions in an electrostatic problem are either to prescribe the charge density on a boundary, analogous to a fixed heat flux; or to prescribe the voltage on a surface, analogous to surfaces of constant temperature. Because the simulations in this work all deal with conductors, the surfaces will have fixed voltages applied to boundaries.

To study the effect of isolated charges in an electric field problem (the q^B term) consider a particle that has been electrically charged by removing or adding electrons and then introduced into the volume being studied. When this particle is placed in close proximity to other conductors or insulators, electrons will "sense" the charges on the particle and be either drawn or repulsed by them, depending on their sign. The force felt by a single electron is the product of the field potential φ and the charge of a single electron, measured in Coulombs. The electric field lines represent the direction and magnitude of the total electrostatic force anywhere in the geometry of the problem. Returning to the conduction heat transfer analogy, surfaces of constant electric potential are analogous to lines of constant temperature, while electric field lines are analogous to the direction of heat flow.

Electric permittivity values (ε) represent a property of an insulator to allow charges to be rearranged within the insulator to counteract the presence of electric field. Because an insulator will develop a positive charge when placed in close proximity to a negatively charged conductor and vice-versa, the electric permittivity of an insulator is always greater than that of vacuum. For this reason electric permittivity is typically broken into the product of two values, the dimensioned constant value ε_0 representing vacuum, and a dimensionless multiplier denoted by ε_r, representing the relative increase in permittivity as a property of the material in the gap. For air the ε_r term is typically 1.0008, varying slightly with temperature and humidity. The electric permittivity is analogous to the conduction coefficient *k* in a heat transfer problem, since a larger *k* results in higher heat flux, just as an increase in ε results in higher capacitance for a given geometry.

For a material with an isotropic electric permittivity, the ε values can be moved to the right hand side of the equation. The differential equation now takes the form of Poisson's Equation, shown in Eq. (1-14).

$$\frac{\partial^2 \phi}{\partial x^2} + \frac{\partial^2 \phi}{\partial y^2} + \frac{\partial^2 \phi}{\partial z^2} = \frac{-q^B}{\varepsilon_0 \varepsilon_R} \tag{1-14}$$

In the case when no free charges are present within the volume of the capacitor, the q^B term on the right side of the equation goes to zero and the form of Eq. (1-15) is Laplace.

$$\frac{\partial^2 \phi}{\partial x^2} + \frac{\partial^2 \phi}{\partial y^2} + \frac{\partial^2 \phi}{\partial z^2} = 0 \tag{1-15}$$

A detailed analysis of possible solutions to this form of the Laplace Equation is given in [79], based on certain simplified boundary conditions. Closed-form solutions are also presented in Section 2.2. Unfortunately, the boundary conditions and the number of conductors in this document's capacitance problems are too complex for a closed-form solution. The commercial software package ANSYS was selected to provide finite element solutions.

1.5 Finite Element Modeling

To apply ANSYS to a capacitance problem, the geometry of the capacitance gage, target surface, and surrounding non-conductive volumes must be defined within the same software or imported from another package. When the geometry is defined from scratch, it is built by creating keypoints, lines, areas, and finally volumes. This is an example of bottoms-up modeling [80], which allows for the greatest control of the model. When the geometry is generated from an external software package, one approach is to import high-level entities from a common file format. If keypoints, lines, areas, and volumes are imported, then the meshing of the geometry is accomplished in ANSYS. When the meshing is achieved in a separate program, then the nodes comprising each element are imported into ANSYS for analysis, along with all boundary conditions.

When the geometry of a model is axisymmetric, a two-dimensional representation is sufficient to solve for the electric field. Although these elements appear rectangular in the 2D representation, in reality they represent a 4-sided toroid as shown in Figure 1-5. There are 4 nodes in such an element, each representing a scalar value of voltage potential, and corresponding to the 4 edges of the toroid. Since the model has been assumed to have axisymmetric properties, one node is sufficient to define the voltage potential for the entire circular edge. The solution of these axisymmetric models requires the fewest nodes and elements, and the smallest computation time.

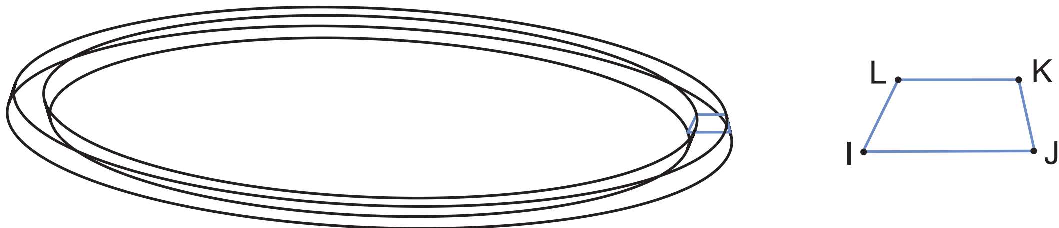

Figure 1-5. Four-sided toroid element and its two-dimensional representation.

When the geometry of a model is not axisymmetric, then a three-dimensional representation must be constructed. If planes of symmetry exist, only one-half or one-fourth of the volume is needed. By building only a fraction of the model, there is a reduction in the number of nodes and elements and a corresponding reduction in computational time. Because of the complicated geometry involved in these 3D models, a free mesh is typically applied using a ten-node tetrahedral element as shown in Figure 1-6

[81]. In this ten-node tetrahedral element there is a single, scalar degree of freedom representing voltage at each node. A quadratic element was selected because it best follows the complex, curved shapes of the 3D surfaces with a minimum number of elements.

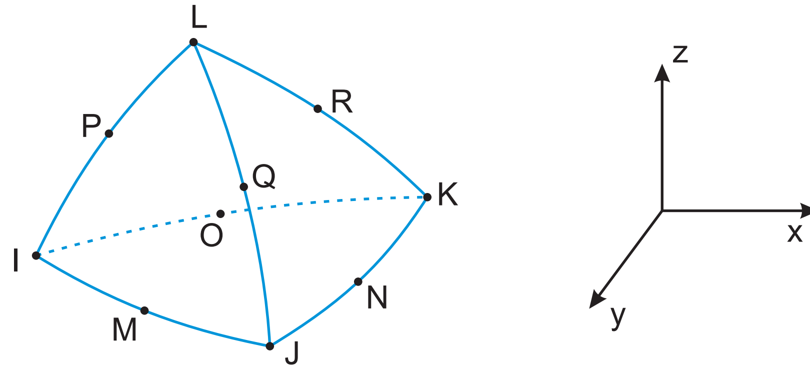

Figure 1-6. Ten-node tetrahedral element, one DOF at each node.

For any of the electrostatic FEA models, the only material properties needed are the electrostatic permittivity of the various materials involved. Most models in this document contain either an air gap, which has an ε_r of approximately 1, an epoxy between conductors, which has a varying ε_r, or a gap filled with a water as a dielectric, which has a permittivity of 80.

The first goal of this finite element modeling is to provide more general insight into the design parameters that affect the final capacitance of a probe. This is achieved by varying both geometric parameters and material properties. Such a study on a relatively simple model can show which parameters have the most significant effect and which parameters are largely negligible. These parameters can then be carried over from the relatively simplistic 2D models to the more processor-intensive 3D models involving cylindrical targets. Here the nonlinear effects are more subtle – but remain a significant source of error in some applications.

The ultimate goal of the finite element modeling is to test the geometry of a new and unique design for a capacitance gage probe. This probe is able to measure the surface profile inside a hole of 100 μm diameter or less in a conductive material without any contact required, a significant improvement over prior designs. The probe is modeled so that the sensing area is minimized, but the capacitance is still measurable with current electronics.

Because the area of the probe required for adequate capacitance will vary depending on the exact diameter of the hole being probed, mathematical techniques have been developed to deconvolve the large area of the probe with the raw data from the sensor. The end result of this deconvolution is a higher lateral resolution than what is possible based on the overall surface area of the probe. The deconvolution method involves baseline simulations of flat and step target surfaces, in combination with a matrix methodology that generates small subcapacitances from the raw probe data. FEA simulations of a more complex target prove that the resolution goal has been achieved.

1.5.1 Generalizing Spherical Target Geometry

In prior work by this author [82], one specific capacitance probe geometry and target surface, that of a commercial capacitance gage and a spherical target, was studied in great detail. Through this study a method was developed for comparing capacitance values between target spheres and target flat surfaces, the latter being the expected target surface specified by the capacitance gage manufacturer. The mathematics allowed for calculation of the actual gap distance, given the output voltage and known target geometry. These calculations removed the vast majority of the error associated with spherical target surfaces.

The previous work presented only data and correction factors for one specific capacitance gage and target surface geometry. While the theory was a close approximation to the experimental results, it was only applicable to this specific probe. Even from the same manufacturer, a variety of geometries are available, so a complete set of corrections as described in [82] would require a model of every probe.

When these results were produced, only the radius of the target surface and the distance to the capacitance gage were varied. The capacitance of the system is actually a function of several distances, including not only the radius and distance, but also the diameter of the sensing element and the spacing between sensing element and guard ring. Finally, the dielectric constant of the material present in the gap between sensing element and guard ring has some effect. With these different measurements, it is possible to perform a parametric study on each variable as it affects the overall capacitance of the system. This study is able to prioritize choices of geometry and materials from most

critical to least critical. Once this hierarchy is set, new probe designs can select manufacturing methods that produce the most precise critical values.

1.5.2 Cylindrical Target Surfaces

A second study of a commercial capacitance gage determines corrective linearization factors for cylindrical target surfaces. This linearization is critical for axial alignment of small diameter cylinders, and this alignment is needed when testing new probe designs.

Cylindrical surfaces appear as targets in several applications. Studies of spindle error motion use either a spherical target or a cylindrical target. In the previous work, a spherical target was selected for two reasons. First, a spherical target had shown larger errors in experiments, and therefore was deemed more suitable for developing corrections. Second, a spherical target in combination with a cylindrical capacitance gage had a common axis of symmetry, greatly simplifying the finite element model. In practice, however, cylindrical target surfaces are used for many types of measurements. Since a flat surface cannot be used in a spindle measurement, the most accurate data comes from a smooth cylindrical surface with as large a diameter as possible.

While the errors associated with cylindrical targets are smaller than spherical errors, they still exist and need to be quantified. Errors in offset distance and gain can be corrected if sufficient information is known about the effect of curvature on the capacitances in the system. A logical extension to the study of spheres is to extend this study to cylindrical surfaces.

Although the cylinder and the capacitance gage both contain an axis of symmetry, the axes are not aligned in the standard measurement case. A solid, three-dimensional model is required. If the capacitance gage is aligned with the target cylinder, two planes of symmetry exist through the center of the capacitance gage. Given these two symmetry planes, a model representing one-fourth of the complete three-dimensional geometry is needed. The complete solid model of capacitance probe and target cylinder is shown in Figure 1-7.

The initial study of the cylindrical geometry [83], as well as the data presented in Chapter 3, once again includes only the non-conductive volumes. The finite elements fill the gap between the capacitance gage and the target surface, as well as the epoxy volumes between the conductors in the capacitance gage itself. Because of the complex

shapes involved, a free mesh of tetrahedral elements is used. Just as with the spherical target, the guard ring has a powerful effect on the uniformity of the electric field within the gap.

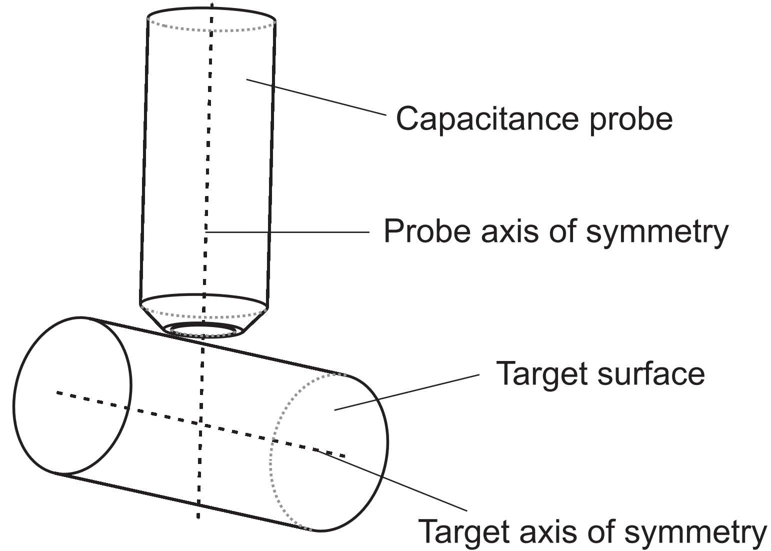

Figure 1-7. Sketch of cylindrical probe and cylindrical target surface, showing axis of symmetry for each.

In addition to providing linearity corrections for alignment of the new probe design, the cylindrical target results are also applied to a more traditional precision engineering technique, Donaldson Reversal. In this technique, the spindle error is separated from surface error by making two separate measurements. While this technique assumes that the position measurements are linear and correctly calibrated, the cylindrical FEA simulations show that neither is the case.

An improved method involves the linearization of the raw data from each capacitance measurement prior to combining the two, as shown in Eqs. (1-10) and (1-11). This linearization involves the conversion of data from the raw or “measured” displacements to actual or “true” displacements using a graph or lookup table.

The complete steps to apply this reversal are presented in Chapter 3. Since the general trend of the capacitance gages is that their actual gain in V/µm becomes larger as the radius of curvature decreases, without these corrections the data will show larger errors before correction. In other words, a part might fail a roundness test simply due to errors in the calibration of the capacitance gage.

1.5.3 Novel Probe FEA Modeling

In order to create a realistic model of a new probe design, more than one software package is employed. The ANSYS software, while capable of defining simpler geometries, does not allow for rapid modifications of dimensions on parts.

The Pro/Engineer software is most often used at the University of Kentucky for solid modeling. Parts created with this package can be dimensioned to reflect the intent of the designer, rather than merely the coordinates of corners and surfaces. Once the three-dimensional geometry of a part has been defined, it is not trivial to transfer the data from Pro/Engineer to ANSYS. This transfer is necessary since Pro/Engineer is not capable of providing electrostatic solutions. This transfer needs to happen not once, but every time the dimensions of the model change, so the methodology must be robust enough to accept changes in the topology of the model. Chapter 4 describes the process developed for building models in Pro/Engineer and transferring that information to the ANSYS software. Two techniques were employed, with each requiring manual modification of the data.

In the first method, the geometric data from a model is exported from Pro/Engineer. This data includes points, lines, surfaces, and solids. ANSYS is able to import this information, assigning numerical values to these entities in the order that they are imported. To mesh this model, additional keypoints, lines, areas, and volumes must be added manually. The meshing is achieved within the ANSYS software, and a capacitance solution is generated. Problems with this method occur when the geometry of the model is altered, since this often produces a model with different numbers of keypoints, lines, areas, etc. When the numbering of these components changes the modifications to the model must also be changed, a time-intensive manual process of visual inspection.

The second method uses the Mechanica FEM component of Pro/Engineer to mesh the model. Although Mechanica has no provision for solving electrostatic problems, heat conduction elements and boundary conditions are available. Recalling the parallel nature of these two problems as outlined in Section 1.4, the model is temporarily defined as a heat transfer problem. In addition to the volume of the model being meshed within Mechanica, the boundary conditions of the conductors (here, fixed temperature

conditions) are also applied. This data, as exported to ANSYS, does not contain the geometry of the model. Instead, this file contains the location of thousands of nodes, as well as the definition of elements that connect those nodes together. As exported from Pro/Engineer, these are ready-to-run heat transfer scripts. In order to have ANSYS provide an electrostatic solution, the text file containing the node and element data is modified to reflect a different element type and new boundary conditions. Fortunately these modifications are independent of the exact number of nodes or elements, and so are easily scripted.

1.5.4 Probe Deconvolution Methods

The finite element modeling of different geometries allows for several different probe designs and methods of measurement to be tested. In particular, a method is presented and tested in Chapter 5 that allows features of the target surface to be resolved that are smaller than the area of the capacitance probe itself. This method is termed "capacitive deconvolution," and it starts with the parallel plate approximation of capacitance of Eq. (1-3). From this basis, the sensing area of the probe is divided into several subregions, and a matrix is produced relating the capacitance of these subregions with the overall measured capacitance. By applying a least-squares solver to the results of FEA analysis, several small target surfaces can be reconstructed from the capacitance data. The deconvolution examples include a sinusoidal target with a spatial frequency less than half the size of the capacitance sensing area.

The development and application of these deconvolution methods results in two different optimized designs for capacitance hole probes. In the first, the area of sensing is rectangular, and the dimensions of the hole are allowed to be much larger than the dimensions of the sensing area. In the second design, the length of the probe sensing area exceeds the depth of the hole. This design simplifies the mathematics of deconvolution but has less flexibility with target selection.

1.6 Manufacture of a Novel Probe Design

Once the design of a hole probe has been accurately modeled, methods must be developed for manufacturing. Manufacturing includes not only machining the inner core of the probe, but also techniques to apply the necessary coatings to the exterior of the part.

The centerpiece of the Precision Systems Lab at the University of Kentucky is a state-of-the-art Panasonic micro-Electro-Discharge Machine (µEDM). The machine has been improved upon by the Precision Systems Lab, and many novel devices have been manufactured using it. One such unique device is a tungsten carbide probe with a small radius and high aspect ratio, as shown in Figure 1-8. The non-contact nature of the µEDM machine allows small parts to be manufactured without breaking, and variations in the operating parameters allow for a variety of surface finishes.

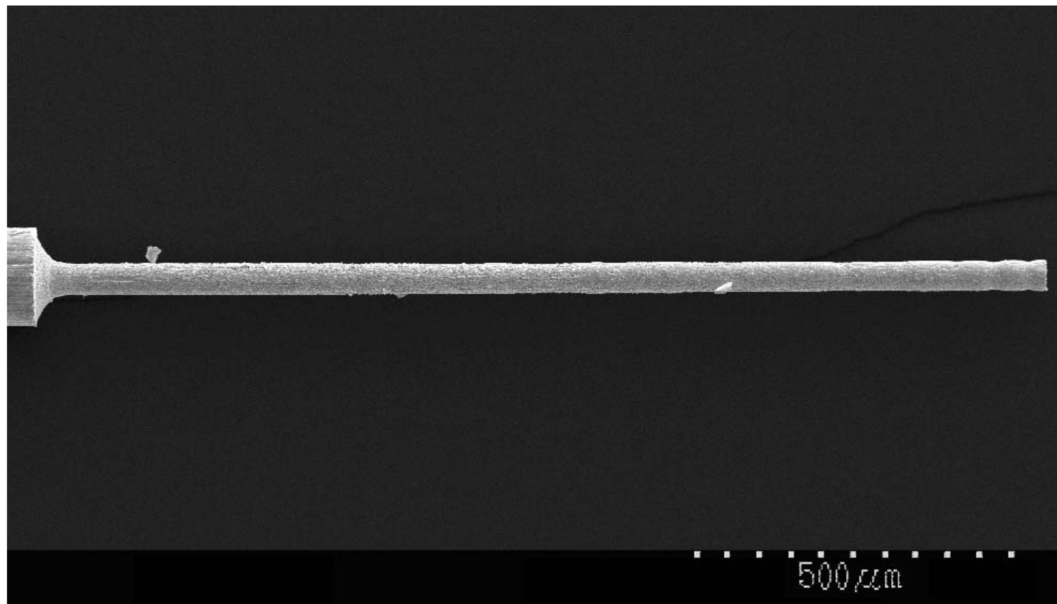

Figure 1-8. An electron micrograph of a 50 µm diameter tungsten carbide probe. Image courtesy of Chris Morgan, Precision Systems Lab.

The probe shown in Figure 1-8 was not in this case the end product, but rather a machine tool for a separate process. Once the tool is complete, the same machine can apply the tool to generate holes in a conductive substrate. Uniform, precisely-spaced holes are needed for solid-state low-light detection arrays. In many applications the exact dimensions of the holes are critical, and are measured and analyzed statistically.

With traditional large scale EDM it is expected that a hole would be of a uniform radius through the entire depth, since the wear of the tool is minimal (or in some cases, the wire is replaced before wear becomes appreciable). For the case of micro EDM, however, tool wear is a significant fraction of the diameter of the tool, and can never be completely discounted. As the tool passes through the material, the tip and sides of the tool experience wear through the discharge process. A cylindrical tool becomes tapered,

due to increasing wear along the sides as a function of contact time. The final hole is invariably tapered to some degree, depending on such machining variables as rotation speed, feed rate, material hardness, and discharge frequency.

Up to this point, the tapering of the hole has been estimated using imaging, as shown in Figure 1-9. The first problem with this method is that it is nearly impossible to determine depth measurements based on a direct viewing of the hole, and any other angle is not able to image more than a small distance down the hole. The top and bottom edges of the hole are also invariably tapered due to the EDM process, which has the effect of rounding the sharpest edges. Even if an estimate is made of the starting and ending diameter of the hole, little information is available about the cross-sectional profile of the hole, information that would improve the process.

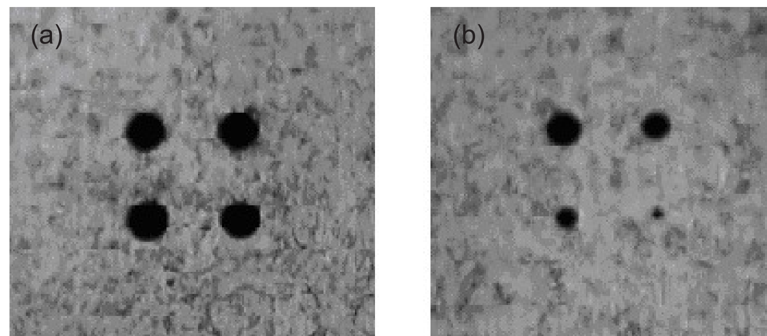

Figure 1-9. Light microscope images of the (a) top and (b) bottom surfaces where holes were machined using a tungsten carbide probe and micro EDM. Images courtesy of Chris Morgan.

The basis of the new probe design is the same tungsten carbide material shown in Figure 1-8. This material is provided in cylindrical “blanks” that are some 1.6 mm in diameter, which are shaped on the μEDM machine. The shaping process can be performed in several ways, depending on the complexity of the shape desired. Some simple probe shaping routines are provided by Panasonic as part of a library of Quick Basic functions. For steps not covered by this routine, an entire command structure exists that is unique to this device. These commands are passed to the μEDM through the serial port of an attached computer, allowing long scripts to be executed.

To prototype the tungsten carbide probe, a larger diameter is selected. This helps both with yield and also with determining the efficacy of the manufacturing steps. The prototype has a short cylindrical tip approximately 750 μm in diameter. An additional

length of probe surface is machined concentric with this section, to help align the probe. Custom routines are written to round the edges of the probe to ensure that coatings can adhere to the surface. If the entire surface of the probe were left as an exposed conductor, the capacitance gage would not be able to differentiate one section of a hole from another. To provide sufficient information about the profile of the hole through its depth, most of the tip of the probe is shielded from the surface of the hole. This shielding functions like the guard structure of a commercial capacitance probe.

The next step of the manufacturing process is to coat the tip with an insulating material on the order of a micron in depth. The material selected is alumina, and the coating is applied using ebeam deposition. On the outside of this layer an outer conductor is added, in this case gold. Again, this outer layer is analogous to the guard ring of the traditional capacitance gage of Figure 1-1. At this stage the inner conductor cannot "see" any other conductor outside of the gold layer. The final step in the manufacturing process is to remove a small portion of the guard layer, leaving an area of the sensing conductor exposed near the tip. These steps are diagrammed in Figure 1-10, with the layer thickness exaggerated for purposes of illustration. With such a probe and sufficiently sensitive electronics, an average distance to the inner surface of the hole can be determined from the capacitance of the system.

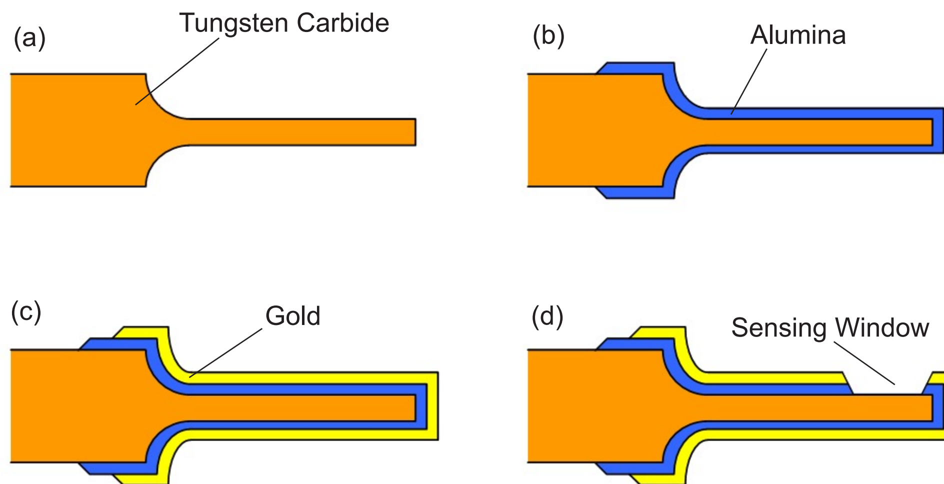

Figure 1-10. Tungsten carbide probe coating procedure to provide localized position sensing.

When the gap distance between the probe and the target surface becomes very small, it is important to remember that there is a limitation to what voltage can be applied

across a given air gap without arcing. The allowed voltage is determined by the electric field strength, which in turn is determined by the geometry of the system. Generally, small radii produce the largest electric field strength for a given voltage differential, so the design of the probe tip ideally avoids the sharpest edges. For this reason the area machined is convex, approximating the radius of the tungsten carbide wall, and the end of the tip is not exposed.

1.7 Contributions of This Research

The purpose of this research is to design a capacitance hole probe using FEA, and determine methods of manufacture. The first step is to consider an existing commercial probe in a relatively simple geometry, and study the effect that changes in geometry have on the performance of the system. With a relatively simple geometry, a large number of simulations can be carried out, and several system parameters can be varied. Once the effects of these geometric changes are ranked, a more complicated target configuration is studied. These steps add complexity to the finite element model, but experimental results are used to verify the validity of the finite element approximation.

After the FEA method is validated in three-dimensions, the geometry of the hole and the desirable features of a probe are presented. In prior work the area of the sensing element was taken *a priori* to be the minimum detectable feature size. In this work, a novel matrix method of deconvolution is demonstrated, one that can extract features smaller than half the size of the sensing area. This method is applied to two different probe geometries, and two different trajectories through the hole. Finally, this method is extended to three dimensional scans, and includes discussion of sources of noise and error in the measurement.

Once an optimal probe design is demonstrated using simulations, the remainder of this work is devoted to probe manufacturing techniques. This shows that probes of approximately 750 μm in diameter and 12 mm long can be machined from tungsten carbide. Once the first conductor is created, techniques for depositing layers of insulator and conductor are demonstrated. Two methods of producing the final step in the manufacturing process, creating a slot in the deposited layers, are also shown.

By combining studies of existing capacitance probe geometries, new mathematical techniques for determining capacitance, and new manufacturing techniques

for three-dimensional probes, this document provides a new tool for hole metrology. The resulting design is a robust, non-contact probe with multiple advantages over previous designs.

Copyright © Philip T. Smith Jr. 2007

2 Generalized Calibration for Spherical Targets

2.1 Introduction

The calibration of capacitance probes is described at some length in the author's master's thesis [82]. That study took a commercially-available capacitance probe and determined how this particular probe interacted with spherical targets of different diameters. By comparing the capacitance sensed by the probe with a spherical target to the capacitance sensed by the probe when targeting a flat surface, a plot of lookup values was generated. This plot of lookup values related the distance "sensed" by the probe electronics to the actual distance to the curved target. If the target diameter was known, then it was possible to recalibrate the output from the capacitance probe to account for the target curvature.

These functions work well for the specific case of the Lion Precision C1-C capacitance probe in combination with spheres of different diameters. The previous study, however, did not provide any generalized information for capacitance probes of other dimensions. This same commercial manufacturer offers several different sizes of the same capacitance probe, each with a guard ring and designed to target flat surfaces. For many capacitance gage applications the target surface cannot be flat, but is spherical or cylindrical in shape. In these cases, the user of the capacitance probe is forced to make a "best guess" as to whether the curvature of the target surface will significantly affect the gain, linearity, and operating range of the probe. If the precision of the probe is altered, then the user needs to know how the data are affected, and whether this effect can be reversed.

The previous study proved for the particular set of probe dimensions shown in Figure 2-1 that the nonlinearity of the probe increased as the target sphere diameter decreased. The nonlinearity also was significantly worse for higher gain settings, where the distance between the capacitance probe and the target sphere, the "working distance," was smaller. Finally, the actual distance to the target surface differed markedly from the distance indicated by the capacitance gage electronics.

The results of a more generalized analysis of capacitance probes and spherical targets will assist in designing a new probe geometry in several ways. With a new probe geometry the designer must set the relative dimensions of the sensing area, the gap between sensing area and guard ring, the width of the guard ring, and the optimal

distance to target. By varying each of these parameters separately and in combination, the output of a new design can be predicted. Since manufacturability constrains any design to some extent, knowledge of which dimensions are most critical to the operation of the probe will assist in selecting the best manufacturing technique.

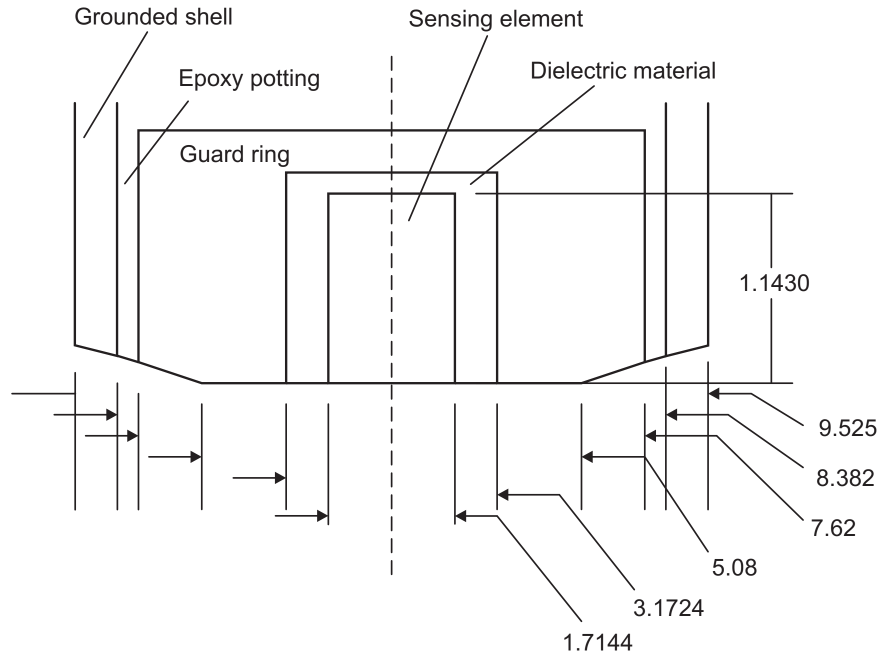

Figure 2-1. Cross section of the Lion Precision C1-C capacitance sensor. All dimensions are in mm.

The second way that a general study of commercial capacitance probes is applicable is in the calibration and alignment of a probe to a target surface. For initial alignment, a traditional capacitance probe can be utilized to give feedback on position and to calibrate the new sensor. For a curved target surface the calibration of the traditional capacitance probe must be understood precisely to ensure proper calibration of the new design. In other words, a complete calibration of the traditional capacitance probe will help “bridge the gap” between standard applications and an entirely new probe.

A third way that this data is applicable to a hole probe design is when a probe with a curved tip is outside a target hole. This synchronizes the moment when the probe begins to enter a hole with the moment that the capacitance meter first comes on scale, a distance measurement that is required for the deconvolution of the resulting probe data.

Finally, a generalized study of capacitance that includes dimensional analysis is helpful when determining how a capacitance probe will function at different scales. The capacitance of even the simplest geometries varies as each dimension is scaled up or down, sometimes in nonobvious ways. Cutting in half the gap distance between the plates of a parallel plate capacitor will of course double the capacitance (as per Eq. (1-3)), but cutting in half the gap distance between other conductors does not have the same effect. Finite element studies of these scale factors help predict the functioning of the final design.

2.2 Closed-Form Capacitance Solutions

As discussed in the previous work [82], Moon and Sparks [84] provide a closed-form approximation for the guard-ring geometry found in the commercial capacitance probe of Figure 2-1. Starting with the capacitance from Eq. (1-3), here called C_0, the effective radius of the sensing element is increased by half of the gap distance g, then an additional term is added to account for the fringing of the field. These results are shown in Eq. (2-1) through Eq. (2-4). Note that if the spacing to the guard ring g is reduced to zero, the capacitance becomes the idealized parallel plate condition.

$$r_e = r + \frac{g}{2} \tag{2-1}$$

$$C_0 = \frac{\pi \varepsilon_0 r_e^2}{d} \tag{2-2}$$

$$\chi = -\frac{g^2}{2\pi r_e d} \coth\left(\frac{\pi r_e}{d}\right) \tag{2-3}$$

$$C_g = C_0 [1 + \chi] \tag{2-4}$$

Equations (2-1) through (2-4) are also considered from a scaling perspective. In other words, if every dimension in this problem is doubled, what is the effect on capacitance? Equations (2-1) and (2-2) are exactly doubled in value, while Eq. (2-3) remains unchanged, since dimensions are found equally in the numerator and denominator of each term. If every dimension in the problem is doubled, the final

capacitance C_g is therefore exactly doubled. This occurs even though this solution is nonlinear in several of the variables.

Another geometry that can be approximated with a closed-form solution is that of long, concentric cylinders. This case is often given as either an example or a homework problem in introductory physics classes [85]. It is derived by applying Gauss' Law to a volume that includes the charged outer surface of the inner conductor and the oppositely charged inner surface of the outer conductor, as shown in Figure 2-2. The result of this integration is shown in Eq. (2-5), where q_0 is the charge on one of the conductors and L is the length of the system. The potential ϕ across the conductors is calculated by integrating the electric field from the smaller radius to the larger, as shown in Eq. (2-6). The resulting capacitance is shown in Eq. (2-7). Once again, if every dimension in the capacitor is doubled, the capacitance is exactly doubled.

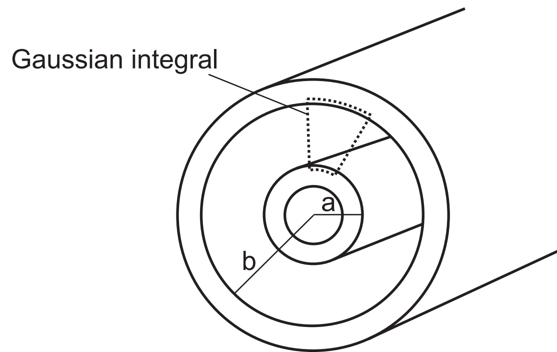

Figure 2-2. Gaussian integral to calculate electric field.

$$E = \frac{q_0}{2\pi\varepsilon_0 rL} \tag{2-5}$$

$$\phi = \frac{q_0}{2\pi\varepsilon_0 L}\int_a^b \frac{1}{r}dr = \frac{q_0}{2\pi\varepsilon_0 L}\ln\frac{b}{a} \tag{2-6}$$

$$C = \frac{2\pi\varepsilon_0 L}{\ln\frac{b}{a}} \tag{2-7}$$

A third closed-form solution considered before beginning this analysis is that of concentric spheres of radii a and b. Once again, a Gaussian surface is used to calculate

the electric field between the two surfaces, with the results as shown in Eqs. (2-8) through (2-10). Since there are no edges to this problem, there is no fringing, and therefore this solution is exact. Applying the same scaling test as before, if the dimensions in the problem are exactly doubled, the capacitance *C* is again doubled.

$$E = \frac{q_0}{4\pi\varepsilon_0 r^2} \tag{2-8}$$

$$\phi = \frac{q_0}{4\pi\varepsilon_0}\int_a^b \frac{1}{r^2}dr = \frac{q_0}{4\pi\varepsilon_0}\left[\frac{1}{a} - \frac{1}{b}\right] \tag{2-9}$$

$$C = \frac{4\pi\varepsilon_0}{\left[\frac{1}{a} - \frac{1}{b}\right]} \tag{2-10}$$

This scaling rule works irrespective of the geometry of the problem because of the way electric field is defined. The electrostatic constant ε_0 has the units of pF/mm, therefore it can be stated definitively that scaling any capacitive system uniformly will have the demonstrated effect. This is likewise true for finite element simulations of electric fields and capacitance. It is important to note, however, that this scaling must be applied to *every* dimension in the above problems, not just some of them. If only one dimension in each of the above problems is altered, the results vary widely.

The solution of the capacitance between two non-concentric spheres is not as straightforward as the previous problems. Closed-form solutions exist, but only in the form of infinite series [86]. The point where these series can be truncated depends on the spacing of the spheres. The first three terms of one series solution is shown in Eq. (2-11), where r_1 and r_2 are the radii of the two spheres and d is the distance separating them. If the radii are identical, Eq. (2-11) simplifies to Eq. (2-12), both from [86].

$$C_{ss} = 4\pi\varepsilon_0 r_1 r_2\left[\frac{1}{d} + \frac{r_1 r_2}{d^3 - d\left(r_1^2 + r_2^2\right)} + \frac{r_1^2 r_2^2}{d^5 - 2d^3\left(r_1^2 + r_2^2\right) + d\left(r_1^4 + r_1^2 r_2^2 + r_2^4\right)} + \ldots\right] \tag{2-11}$$

$$C_{ss} = 4\pi\varepsilon_0 r^2\left[\frac{1}{d} + \frac{r^2}{d^3 - 2dr^2} + \frac{r^4}{d^5 - 4d^3 r^2 + 3dr^4} + \ldots\right] \tag{2-12}$$

The solution to two equally-sized spheres approximated by Eq. (2-12) is also the solution to the problem of a sphere and an infinite plate. To see the analogy, consider the electric field diagrammed in Figure 2-3. From symmetry arguments, the plane containing all points equidistant from the centers of the spheres must have a voltage midway between the two potentials. Similarly, the electric field at this plane is normal to the surface. Both of these conditions mimic the boundary potential of an infinite plate, therefore the systems are analogous.

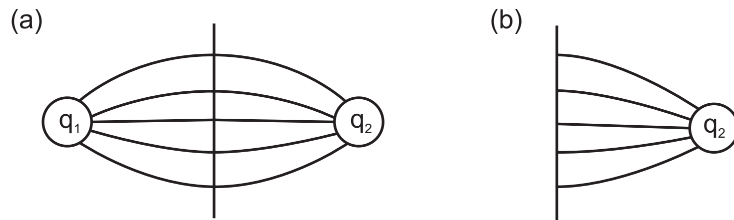

Figure 2-3. Electric field analogy between identical spheres and sphere and infinite plate.

Since there exists a series solution to the system shown in Figure 2-3 (a), the next step is to determine the capacitance in the system show in Figure 2-3 (b). One solution considers a line dividing the two halves of the system shown in Figure 2-3 (a) as shown. If a thin plate is placed at this location, the two halves of the system can be considered as two separate capacitors in series. From symmetry, the capacitances of the two halves are equal, and it is one of these values that represents the desired capacitance. The general formula for the capacitance of a system of two capacitors in series is shown in Eq. (2-13), and with two equal capacitors the capacitance between sphere and plate C_{sp} is determined to be double that of the capacitance between the spheres C_{ss}.

$$C_{eq} = \frac{C_1 C_2}{C_1 + C_2} \tag{2-13}$$

$$C_{ss} = \frac{1}{2} C_{sp} \tag{2-14}$$

Finally, consider again Eq. (2-12). As the distance d separating the centers of the two spheres becomes larger, the larger order terms with powers of d in the denominator drop out, and the resulting capacitance is as shown in Eq. (2-15). Substituting in the area

of a sphere, this equation reduces to the omnipresent Eq. (1-3). For a large distance, the two sphere approximation is the same as the parallel plate approximation.

$$C_{mutual} \approx \frac{4\pi\varepsilon_0 r^2}{d} \tag{2-15}$$

2.3 Strain Energy Calculation

There are several methods to calculate the energy stored in a capacitor, however most rely on simplified geometry such as the special cases discussed in the previous section. For the most general case, the strain energy in the system must be summed. Returning to the conduction heat analogy, the strain energy from [87] is written as shown in Eq. (2-16). Converting this to an electric field solution, the strain energy is written as shown in Eq. (2-17). Solving the simple case of a parallel plate capacitor with a constant electric field and a volume of *Ad*, the strain energy solves to the familiar solution of Eq. (2-18).

$$U = \frac{1}{2}\iiint_V \left[K_{xx}\left(\frac{dT}{dx}\right)^2 \right] dV \tag{2-16}$$

$$U = \frac{1}{2}\iiint_V \left[\varepsilon_0\varepsilon_r\left(\frac{d\phi}{dx}\right)^2 \right] dV \tag{2-17}$$

$$U = \frac{1}{2}\varepsilon_0\varepsilon_r \frac{V^2}{d^2} Ad = \frac{1}{2}CV^2 \tag{2-18}$$

The strain energy can also be used to solve the problem of the sphere and the infinite plane, one solution of which was discussed in Section 2.2. Starting with the general form of the energy stored in a capacitor as shown in Eq. (2-18), from symmetry arguments the energy stored in the volume of one-half of the system as shown in Figure 2-3 (b) is expected to be half of the total. Using E_{ss} and C_{ss} as the energy and the capacitance of the sphere-sphere system and E_{sp} and C_{sp} as the energy and capacitance of the sphere-plane system, two equations can be written as shown in (2-16). Because the voltage over half the system V_{sp} is half of the total voltage V_{ss}, these equations simplify to the same conclusion reached in Eq. (2-14); that the capacitance of the sphere-plane system is double that of the sphere-sphere system.

$$E_{ss} = \frac{1}{2} C_{ss} V_{ss}^2 , \quad E_{sp} = \frac{1}{2} C_{sp} V_{sp}^2 \tag{2-19}$$

2.4 Finite Element Electric Field Formulation

A brief review of the method of calculation of capacitance is in order, without repeating any more of the previous work than is absolutely necessary. The capacitance probe geometry shown in Figure 2-1 has cylindrical symmetry, as does the target sphere. Assuming that their axes are aligned, the entire system has cylindrical symmetry. Section 1.4 discussed the Laplace Equation, the basis of both heat transfer and electric field analysis. The Cartesian version of the Laplace Equation is given in Eq. (1-15), but in the case of a model with cylindrical symmetry, the electric field can be reduced to a system with two variables, *r* and *z*. This form is shown in Eq. (2-20).

$$\frac{\partial^2 \phi}{\partial r^2} + \frac{1}{r}\frac{\partial \phi}{\partial r} + \frac{\partial^2 \phi}{\partial z^2} = 0 \tag{2-20}$$

From the standpoint of finite element analysis, the fact that the system exhibits cylindrical symmetry allows the model to be accurately described by building it in only two dimensions. The cylindrical symmetry is included in the choice of element Plane121, where rectangular elements become toroidal when rotated through the axis of symmetry. This element both as displayed in the mode and in its three-dimensional toroidal form is shown in Figure 2-4.

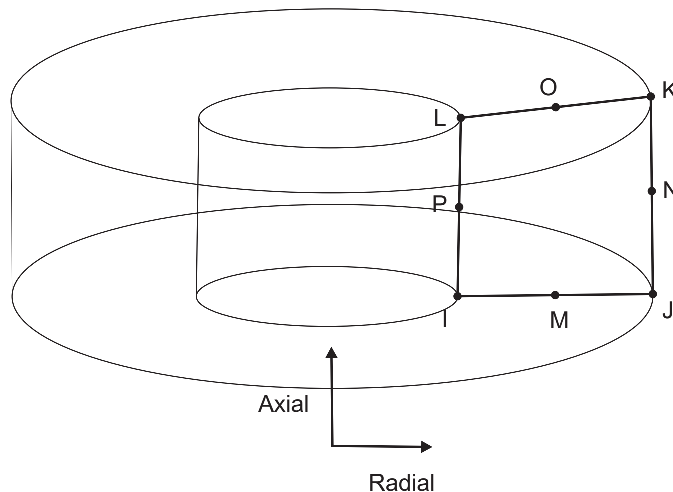

Figure 2-4. ANSYS Element 121, used to model cylindrical symmetry in an electrostatic analysis.

2.5 Variables for Parametric Study

Several variables are selected for this parametric study. Figure 2-5 shows these dimensions on the probe. The first, the inner brass diameter *b*, is the sensing area of the capacitance probe. The second dimension is the spacing distance *g* between the sensing element of the capacitance probe and the guard structure. The third dimension is the relative permittivity, ε_r, of the epoxy between the sensing element and the guard ring. The fourth dimension studied is the radius of the target sphere, r_s. Finally, the gap distance between sensing area and target surface is varied over a wide range of values. The complete table of values for these parameters is listed in Table 2-1. Several other geometric parameters were not chosen to be included in the study, both because each additional variable increased the time of computation, and because the prior work indicated little or no influence on capacitance. One such parameter is the outside diameter of the guard ring. Since the mutual capacitance of the guard ring and the target surface does not contribute to the mutual capacitance of the sensing area and the target, the position of the outer edge is inconsequential. The inner diameter, which restricts the electric field of the sensing element, is the critical parameter, and this has been varied for this study.

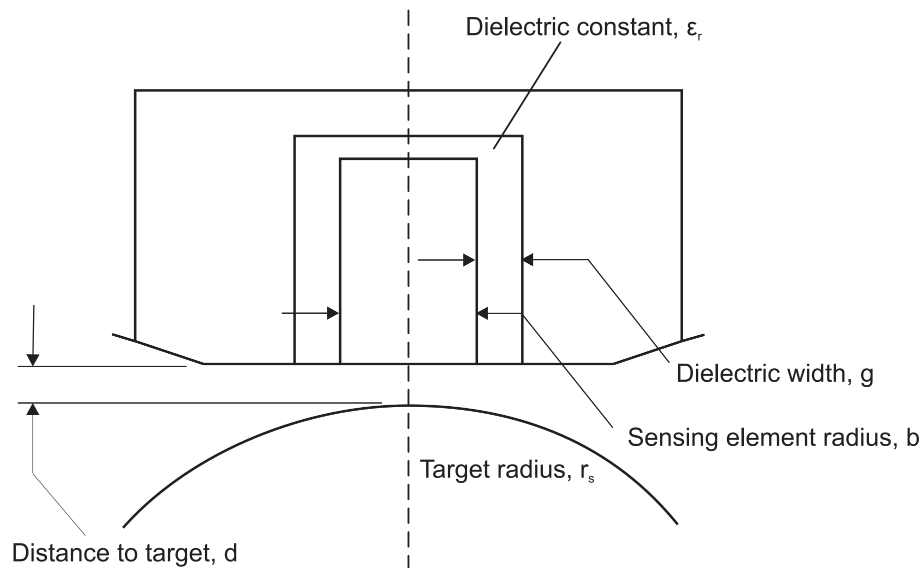

Figure 2-5. Model parameters varied for study.

Table 2-1. Variables and their values applied to the parametric study.

Parameter	Value (inches)	Value (mm)
b	0.0225	0.572
	0.0450	1.143
	0.0675	1.715
g	0.007175	0.1822
	0.014350	0.3645
	0.028700	0.7290
	0.043050	1.0935
d	0.0004	0.01016
	0.0008	0.02032
	0.0016	0.04064
	0.0064	0.16256
	0.0250	0.635
	0.1000	2.54
	0.5000	12.7
	2.0000	50.8
	4.0	101.6
	8.0	203.2
	16.0	406.4
	32.0	812.8
r_s	0.125	3.175
	0.1875	4.7625
	0.25	6.35
	0.375	9.525
	0.5	12.7
	1.0	25.4
	2.0	50.8
	4.0	101.6
	Flat	Flat
Parameter	**Value (dimensionless)**	
ε_r	1.0	
	1.9	
	3.8	
	5.7	

Other parameters not included in the study are the outer diameter of the housing of the capacitance probe and the angle ground into the edge of the gage. Since these portions lie outside the guard ring structure, they are also inconsequential to the mutual capacitance of the system. The dielectric constant of the material outside the guard ring is similarly irrelevant to the capacitance under investigation. Also, by eliminating the fourth

conductor in the model, the solution time for each set of capacitances is significantly reduced.

The dielectric constant of the material in the gap between the capacitance gage and the target surface matters enormously in the calculation of capacitance, yet this value is not included as a variable in the overall model. Instead, the effect caused by changes to its value are determined mathematically. A different dielectric material in the gap can be accounted for using the existing data. It is shown that the effects of certain dimension changes can be predicted as well.

The previous study has shown that the parallel plate approximation is most applicable when the gap distance d is at least an order of magnitude smaller than the radius of the sensing area. Closed-form approximations show that increasing the spacing g between the sensing area and the guard ring increases the capacitance slightly, as the sides of the sensing area are better able to interact with the target surface. Similarly, for a fixed g, increasing the electric field permittivity increases the capacitance of the sides of the sensing area with the target surface, slightly increasing the overall capacitance. Finally, as the radius of the target surface decreases, the nonlinearity of the probe increases, as the parallel plate approximation becomes less and less valid.

2.6 ANSYS Code for Iterative Analysis

The ANSYS code that generates these capacitance results is able to both define the geometry of the probe and generate a solution for multiple cases of different dimensions. Because this model is only two-dimensional, it is relatively straightforward to assemble the entire model within ANSYS. The model is built by first defining keypoints, then lines and areas. The keypoints are set at the intersection between different materials, with lines representing material boundaries. Since this is an axisymmetric model, points represent circles, lines represent surfaces, and areas represent volumes.

Since the goal of this electric field model is to determine the energy in the non-conductive volumes, the conductors become the boundaries of the model. The energy in the nonconductive regions where electric field exists is summed to determine the energy for a given set of applied potentials. The material properties of these volumes are simply the relative permittivities (ε_r) of the material. In the case of this capacitance model the

gap is assumed to be vacuum (relative permittivity of 1) and a second material has a relative permittivity between 1 and 6.

A single ANSYS program to cycle through every possible variation of the parameters listed in Table 2-1 would take weeks to run and be difficult to test and troubleshoot. In addition, any interruption of the ANSYS program would result in a substantial loss of data. Instead, a different script is created for each combination of the inner brass diameter b and the target surface radius r_s, with the remaining variables included within the script itself. For example, varying the permittivity ε_r is achieved with the following lines of code.

```
E=4                    ! Number of permittivity values to use***************
*dim,Er,array,E
Er(1)=1.0              ! Electric permittivity of epoxy, multiple values
Er(2)=1.9
Er(3)=3.8
Er(4)=5.7
```

The array `Er` therefore represents the permittivity ε_r. Similarly the gap d between sensing area and target surface is termed `Gapvals`. Finally, the spacing g between the sensing area and the guard ring structure has the array name `Ggap`. Three nested loops cycle through these values to produce capacitances for every configuration. One complete ANSYS script is presented in Appendix C.

2.7 Capacitance Results

In any system of two or more conductors, more than one capacitance exists. A single conductor in empty space has the ability to store charge and therefore has a self-capacitance. Two conductors each have their own self-capacitance, as well as their capacitance when used as a system, their mutual-lumped capacitance. It is this mutual-lumped capacitance that can be measured by external electronics and it is this mutual-lumped capacitance that is determined from the finite element model.

In the case of multiple conductors, the energy stored in the system is a complex function of the voltages of each conductor. To determine the mutual-lumped capacitance values, different combinations of voltages must be applied to the model and the electric field solved for each one. The energy stored in the model for these iterations allow a matrix of ground capacitance values to be calculated, and from these ground capacitances the mutual-lumped capacitances can be determined. For a system of three conductors there are three mutual-lumped capacitances as shown in Figure 2-6. The capacitance C_{12}

is the mutual-lumped capacitance between the sensing element and the guard ring, C_{13} is the mutual-lumped capacitance between the sensing element and the target sphere, and C_{23} is the mutual-lumped capacitance between the guard ring and the target sphere. Of these, C_{13} is the value sensed by the probe electronics, and C_{12} is of interest to the capacitance probes manufacturers.

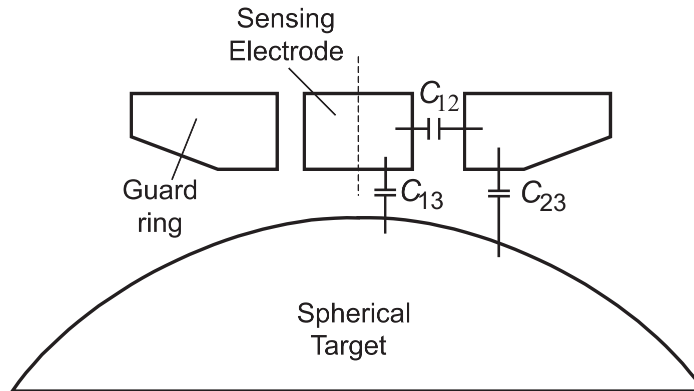

Figure 2-6. Mutual-lumped capacitance numbering for FEA model.

Fortunately, many of the calculations necessary to determine the mutual-lumped capacitances are automated in the ANSYS macro CMATRIX. This macro requires the user to first build a model in ANSYS and mesh the geometry. All of the nodes that define a single conductor must then be selected and grouped into a component. The component name includes an index number so that the CMATRIX macro can automatically cycle from one to the next. The sensing element, guard ring, and target conductors in this model are given the component names `cond1`, `cond2`, and `cond3` respectively. The commands to define these are shown below, followed by the single command that calls the CMATRIX macro.

```
lsel,s,,,12,14,,1          ! selecting center conductor
cm,cond1,node              ! Define 1st conductor for cmatrix analysis
lsel,s,,,15,18,,1          ! select ground ring
cm,cond2,node
lsel,s,,,3,6,,1            ! select lower sphere or plate
cm,cond3,node
cmatrix,1,'cond',3,1,'cmat'
```

The CMATRIX command, if called from the command line in an interactive ANSYS session, produces a text display of all the calculated capacitance values. The text of one such display appears below. This text is also temporarily stored in the file ‘cmatrix.out’, which is overwritten with each subsequent call of the command.

```
________________ CMATRIX SOLUTION SUMMARY ___________________
 *** Ground Capacitance Matrix ***
Self Capacitance of conductor  1. =     0.20735E+01
Self Capacitance of conductor  2. =     0.87852E+00
Self Capacitance of conductor  3. =     0.21534E+01
Mutual Capacitance between conductors  1. and  2. =    -0.39932E+00
Mutual Capacitance between conductors  1. and  3. =    -0.16742E+01
Mutual Capacitance between conductors  2. and  3. =    -0.47920E+00
Ground capacitance matrix is stored in 3d array parameter cmat  ( 3., 3.,1)
 *** Lumped Capacitance Matrix ***
Self Capacitance of conductor  1. =     0.46629E-14
Self Capacitance of conductor  2. =     0.58287E-14
Self Capacitance of conductor  3. =     0.13323E-14
Mutual Capacitance between conductors  1. and  2. =     0.39932E+00
Mutual Capacitance between conductors  1. and  3. =     0.16742E+01
Mutual Capacitance between conductors  2. and  3. =     0.47920E+00
Lumped capacitance matrix is stored in 3d array parameter cmat  ( 3., 3.,2)
```

Because each of the scripts created for this analysis generated hundreds of capacitance values, the values needed for analysis were copied from the CMATRIX results and stored in a separate array. ANSYS then writes these values, along with key geometric parameters, into a separate text file. Since this data set is too large to be included as a table or in the appendices of this document, it is included and linked here as the separate electronic ASCII file pts_data.txt. A small example of this text file is shown below, listing the inner conductor diameter *b*, the gap *g*, and the electric permittivity ε_r at the beginning of each data set, and the target diameter halfway through the set. In this example the target surface is flat, so the diameter is listed as 0 inches. The spacing *d* between probe and target is always given in millimeters, and the capacitance results are calculated in pF. Recall that the C_{13} values are of primary interest, appearing in the second half of each block of text.

```
Inner conductor diameter 0.067500 inches
Gaps between inner conductor and epoxy 0.043050 inches
electric permittivity of 5.7000
gap d:0.000445   C12: 0.5131260E+00
gap d:0.000889   C12: 0.5140833E+00
gap d:0.001715   C12: 0.5158430E+00
gap d:0.002540   C12: 0.5175793E+00
gap d:0.006350   C12: 0.5252908E+00
gap d:0.012700   C12: 0.5370709E+00
gap d:0.025400   C12: 0.5570155E+00
gap d:0.101600   C12: 0.6200413E+00
gap d:0.203200   C12: 0.6517898E+00
gap d:0.406400   C12: 0.6771187E+00
gap d:0.711200   C12: 0.6933444E+00
gap d:1.016000   C12: 0.7022912E+00
Target sphere diameter 0.0000 inches
gap d:0.000445   C13: 0.4715645E+02
gap d:0.000889   C13: 0.2402278E+02
gap d:0.001715   C13: 0.1283107E+02
gap d:0.002540   C13: 0.8886094E+01
gap d:0.006350   C13: 0.3895202E+01
gap d:0.012700   C13: 0.2162229E+01
gap d:0.025400   C13: 0.1233670E+01
gap d:0.101600   C13: 0.4043568E+00
```

```
gap d:0.203200   C13: 0.2224060E+00
gap d:0.406400   C13: 0.1181248E+00
gap d:0.711200   C13: 0.6948359E-01
gap d:1.016000   C13: 0.4927224E-01
```

A small subset of capacitance values appears in Table 2-2, approximately five percent of all the calculated values. The capacitance in the complete data set ranges from 0.004 pF to 462 pF, reflecting some 5 orders of magnitude in these results.

Table 2-2. Selected capacitance values for the spherical study. Capacitance values in pF.

	Probe props.				Gap *d*, micro-inches						
	Targ. dia.,in.	**Sense dia.,in**	**Ggap, in.**	**Er**	**0.0004**	**0.0008**	**0.0064**	**0.100**	**2.00**	**8.0**	**32.0**
1	0.25	0.0675	0.043050	1.0	1.719246	1.597861	1.230924	0.7485551	0.2711267	0.1242063	0.04442685
2	0.25	0.0225	0.007175	1.0	1.291722	1.169421	0.803971	0.3464517	0.05451938	0.01665905	0.004191695
3	0.375	0.0225	0.007175	1.0	1.820019	1.636675	1.089931	0.4230294	0.05694334	0.01703766	0.004324052
4	0.50	0.0225	0.007175	1.0	2.316968	2.072649	1.345559	0.4801911	0.05825153	0.01723414	0.004393075
5	0.75	0.0225	0.007175	1.0	3.246676	2.880613	1.795629	0.5615161	0.05963145	0.01743574	0.004464069
6	1.0	0.0225	0.007175	1.0	4.115301	3.627770	2.188561	0.6174500	0.06035032	0.01753853	0.004500327
7	2.0	0.0225	0.007175	1.0	7.217884	6.247220	3.426336	0.7361821	0.06146730	0.01769532	0.004555695
8	4.0	0.0225	0.007175	1.0	12.44963	10.52565	5.096979	0.8227240	0.06204407	0.01777492	0.004583833
9	8.0	0.0225	0.007175	1.0	20.99978	17.21930	7.102665	0.8774144	0.06233722	0.01781503	0.004598017
10	0.25	0.0450	0.007175	1.0	1.536913	1.414615	1.047767	0.5695152	0.1432996	0.04900442	0.01305034
11	0.375	0.0450	0.007175	1.0	2.191307	2.007744	1.457830	0.7460557	0.1598615	0.05150147	0.01356466
12	0.50	0.0450	0.007175	1.0	2.813415	2.568673	1.835938	0.8943064	0.1700325	0.05286584	0.01383690
13	0.75	0.0450	0.007175	1.0	3.991697	3.624693	2.527038	1.136164	0.1819266	0.05431929	0.01411987
14	1.0	0.0450	0.007175	1.0	5.107475	4.618286	3.156671	1.329723	0.1886786	0.05508271	0.01426558
15	2.0	0.0450	0.007175	1.0	9.191572	8.214325	5.306384	1.851049	0.2000573	0.05627788	0.01448965
16	4.0	0.0450	0.007175	1.0	16.36868	14.41862	8.662667	2.389234	0.2064141	0.05689951	0.01460427
17	8.0	0.0450	0.007175	1.0	28.76282	24.88030	13.59865	2.856317	0.2097854	0.05721666	0.01466224
18	0.25	0.0675	0.007175	1.0	1.674196	1.552812	1.185884	0.7036630	0.2291778	0.09008886	0.02599976
19	0.375	0.0675	0.007175	1.0	2.402204	2.219197	1.668739	0.9478659	0.2697406	0.09782416	0.02731563
20	0.50	0.0675	0.007175	1.0	3.097956	2.853471	2.119690	1.161884	0.2974624	0.1023252	0.02802769
21	0.75	0.0675	0.007175	1.0	4.422872	4.055774	2.955738	1.529135	0.3332817	0.1073635	0.02877967
22	1.0	0.0675	0.007175	1.0	5.684486	5.194986	3.729139	1.840324	0.3555727	0.1101202	0.02917172
23	2.0	0.0675	0.007175	1.0	10.34757	9.369068	6.444262	2.768334	0.3970867	0.1146029	0.02978128
24	4.0	0.0675	0.007175	1.0	18.67388	16.71891	10.89656	3.907306	0.4228768	0.1170208	0.03009625
25	8.0	0.0675	0.007175	1.0	33.35165	29.44961	17.91195	5.118157	0.4374504	0.1182786	0.03025640
26	1.0	0.0450	0.007175	1.0	5.107475	4.618286	3.156671	1.329723	0.1886786	0.05508271	0.01426558
27	1.0	0.0450	0.007175	1.9	5.131471	4.642270	3.180486	1.350990	0.1935888	0.05572988	0.01433516
28	1.0	0.0450	0.007175	3.8	5.161394	4.672173	3.210116	1.376586	0.1980075	0.05625402	0.01439090
29	1.0	0.0450	0.007175	5.7	5.178527	4.689292	3.227045	1.390772	0.1999538	0.05646928	0.01441361
30	1.0	0.0450	0.014350	1.0	5.123011	4.633822	3.172206	1.345225	0.2030340	0.06466841	0.01768529
31	1.0	0.0450	0.014350	1.9	5.159259	4.670057	3.208258	1.378501	0.2150071	0.06697865	0.01793264
32	1.0	0.0450	0.014350	3.8	5.209890	4.720664	3.258534	1.423796	0.2273242	0.06892478	0.01813028
33	1.0	0.0450	0.014350	5.7	5.242275	4.753030	3.290639	1.452013	0.2333072	0.06974470	0.01821072

Table 2-2 (continued).

	Probe props.				Gap *d*, micro-inches						
	Targ. dia.,in.	**Sense dia.,in**	**Ggap, in.**	**Er**	**0.0004**	**0.0008**	**0.0064**	**0.100**	**2.00**	**8.0**	**32.0**
34	1.0	0.0450	0.028700	1.0	5.140313	4.651123	3.189505	1.362501	0.2199049	0.07894583	0.02448962
35	1.0	0.0450	0.028700	1.9	5.190500	4.701297	3.239492	1.409631	0.2430894	0.08602000	0.02539142
36	1.0	0.0450	0.028700	3.8	5.266197	4.776969	3.314806	1.479489	0.2707741	0.09256320	0.02611942
37	1.0	0.0450	0.028700	5.7	5.318631	4.829381	3.366912	1.526972	0.2859815	0.09550067	0.02641780
38	1.0	0.0450	0.043050	1.0	5.151219	4.662030	3.200411	1.373391	0.2307287	0.08919126	0.03093833
39	1.0	0.0450	0.043050	1.9	5.210143	4.720941	3.259134	1.429247	0.2619769	0.1012936	0.03283816
40	1.0	0.0450	0.043050	3.8	5.301805	4.812576	3.350404	1.514941	0.3021927	0.1134073	0.03440144
41	1.0	0.0450	0.043050	5.7	5.367390	4.878138	3.415646	1.575324	0.3258343	0.1191665	0.03505013
42	0.25	0.0450	0.007175	1.0	1.536913	1.414615	1.047767	0.5695152	0.1432996	0.04900442	0.01305034
43	0.25	0.0450	0.014350	1.0	1.549966	1.427668	1.060816	0.5825006	0.1548816	0.05689668	0.01605823
44	0.25	0.0450	0.028700	1.0	1.564743	1.442445	1.075591	0.5972510	0.1690283	0.06865449	0.02189082
45	0.25	0.0450	0.043050	1.0	1.573937	1.451639	1.084786	0.6064405	0.1780927	0.07704333	0.02725414
46	0.375	0.0450	0.007175	1.0	2.191307	2.007744	1.457830	0.7460557	0.1598615	0.05150147	0.01356466
47	0.375	0.0450	0.014350	1.0	2.205484	2.021921	1.472003	0.7601749	0.1725958	0.06007438	0.01674273
48	0.375	0.0450	0.028700	1.0	2.221325	2.037762	1.487843	0.7759951	0.1878836	0.07285108	0.02296941
49	0.375	0.0450	0.043050	1.0	2.231209	2.047646	1.497727	0.7858749	0.1976713	0.08198696	0.02876181
50	0.50	0.0450	0.007175	1.0	2.813415	2.568673	1.835938	0.8943064	0.1700325	0.05286584	0.01383690
51	0.50	0.0450	0.014350	1.0	2.828146	2.583405	1.850666	0.9089887	0.1833922	0.06181956	0.01710748
52	0.50	0.0450	0.028700	1.0	2.844545	2.599803	1.867064	0.9253690	0.1992902	0.07516234	0.02355278
53	0.50	0.0450	0.043050	1.0	2.854805	2.610063	1.877324	0.9356248	0.2094711	0.08471490	0.02958972
54	0.75	0.0450	0.007175	1.0	3.991697	3.624693	2.527038	1.136164	0.1819266	0.05431929	0.01411987
55	0.75	0.0450	0.014350	1.0	4.006968	3.639964	2.542307	1.151396	0.1959429	0.06368553	0.01748841
56	0.75	0.0450	0.028700	1.0	4.023954	3.656950	2.559292	1.168362	0.2124811	0.07763893	0.02416863
57	0.75	0.0450	0.043050	1.0	4.034627	3.667623	2.569964	1.179027	0.2230823	0.08764323	0.03047355
58	1.0	0.0450	0.007175	1.0	5.107475	4.618286	3.156671	1.329723	0.1886786	0.05508271	0.01426558
59	1.0	0.0450	0.014350	1.0	5.123011	4.633822	3.172206	1.345225	0.2030340	0.06466841	0.01768529
60	1.0	0.0450	0.028700	1.0	5.140313	4.651123	3.189505	1.362501	0.2199049	0.07894583	0.02448962
61	1.0	0.0450	0.043050	1.0	5.151219	4.662030	3.200411	1.373391	0.2307287	0.08919126	0.03093833
62	2.0	0.0450	0.007175	1.0	9.191572	8.214325	5.306384	1.851049	0.2000573	0.05627788	0.01448965
63	2.0	0.0450	0.014350	1.0	9.207530	8.230282	5.322338	1.866958	0.2149333	0.06621099	0.01798904
64	2.0	0.0450	0.028700	1.0	9.225410	8.248162	5.340211	1.884755	0.2323217	0.08100055	0.02498859
65	2.0	0.0450	0.043050	1.0	9.236788	8.259539	5.351582	1.896049	0.2434989	0.09162999	0.03166657
66	4.0	0.0450	0.007175	1.0	16.36868	14.41862	8.662667	2.389234	0.2064141	0.05689951	0.01460427
67	4.0	0.0450	0.014350	1.0	16.38496	14.43490	8.678938	2.405373	0.2215554	0.06701513	0.01814488
68	4.0	0.0450	0.028700	1.0	16.40345	14.45339	8.697388	2.423521	0.2392121	0.08207357	0.02524638
69	4.0	0.0450	0.043050	1.0	16.41543	14.46536	8.709316	2.435118	0.2505765	0.09290640	0.03204560
70	8.0	0.0450	0.007175	1.0	28.76282	24.88030	13.59865	2.856317	0.2097854	0.05721666	0.01466224
71	8.0	0.0450	0.014350	1.0	28.77965	24.89712	13.61538	2.872609	0.2250605	0.06742588	0.01822383
72	8.0	0.0450	0.028700	1.0	28.79934	24.91680	13.63486	2.891031	0.2428540	0.08262219	0.02537744
73	8.0	0.0450	0.043050	1.0	28.81261	24.93006	13.64790	2.902891	0.2543152	0.09355992	0.03223907

2.8 Analysis of Results

The results from the capacitance studies could be plotted simply as capacitance *C* as a function of gap distance *d* on dozens of graphs without giving any insight into the nature of the capacitance probe design problem. Instead, the data need to be compared in a way that will allow for prediction of the behavior of new probe designs.

The first comparison to note is how the scaling discussed in Section 2.2 is apparent in some of the results shown in Table 2-2. Taking the data in row 4, the capacitance for this geometry with a gap distance of 0.0004 microinches (0.01016 mm) is 2.316968 pF. The data in row 30 represents a probe with twice the sensing area diameter, twice the spacing between sensing area and guard ring, and twice the target sphere diameter. The results from the analysis for a gap distance of 0.0008 microinches (0.02032 mm) is 4.633822 pF, approximately twice the capacitance of the first case (4.633936 pF).

The discussion in Section 2.2 predicted that this value of capacitance would be exactly double, which is true to four significant figures here. There are two factors that make these numbers less precise than the theory they are built on. First, the finite element method is only an approximation of the true capacitance of the system. For a correct formulation it has been shown to mimic experimental results quite well, nevertheless variations in the mesh and other aspects of the element formulation affect the final result. Another reason the capacitance values do not exactly match to more significant figures is because not every dimension in the model has been doubled from line 4 to line 30. In particular, the depth of the sensing area remains unchanged, and this thickness has a measurable effect on the capacitance of the system. For the system where other dimensions have been doubled the thickness is proportionally less. This means its contribution to capacitance is not as great as it would be if every dimension were doubled, hence a slightly lower than expected capacitance.

Because the capacitance of the system scales in this way, it is not necessary to vary the relative permittivity of the material in gap between sensing area and target surface. Instead a “scaling factor” can be applied to adjust for this relative permittivity of the material in the gap. The data in Table 2-2 and in the attached text file are calculated based on a vacuum between these two surfaces. Since the permittivity constant ε_0 is defined as the permittivity of a vacuum, the relative permittivity ε_r has a value of 1. The

presence of any non-conductor in the gap is known to lower the electric field strength, therefore the permittivity of any nonconducting material is always greater than 1. Air at room temperature, for example, has a value of approximately 1.0008 depending on density, humidity, and other factors. Distilled water has a permittivity of approximately 80.

The way this adjustment for relative permittivity is applied is to consider again Eqs. (1-3), (2-7), and (2-10) for the parallel plate capacitor, the concentric cylinders, and the concentric spheres. It has already been noted that, in each case, increasing all of the geometric dimensions by a multiple k results in a value of capacitance that is kC. Now this notion is revisited, considering instead that the relative permittivity has increased by this factor k. The relative permittivity ε_r and the absolute permittivity ε_0 are always a product, so whether the factor k is included with one or the other is irrelevant. Doubling the permittivity of all of the nonconductive material is mathematically equivalent to building a system that is twice as big: in either case the resulting capacitance is twice the original.

There is one caveat to consider with this model. With a simple system that contains only one dielectric material, there is a linear relationship between the capacitance of this system and the relative permittivity of that material. The capacitance gage modeled in this chapter, however, contains two different materials with separate permittivity values. If the desired effect is to double one value and keep the results linear, it is necessary to double the other as well. Specifically, if the permittivity of the dielectric material in the gap between sensing area and target surface increases by a factor of k, then the relative permittivity of the epoxy between the sensing element and the guard ring structure must also be increased by the same factor k. Solving this model will result in a capacitance of precisely kC.

Consider the data in line 36 of Table 2-2 for a gap distance d of 0.0008 microinches (0.02032 mm). The capacitance is 4.777 pF. Next assume a material is introduced between the sensing area and target surface with a relative permittivity of 2. Doubling this capacitance to 9.554 pF is incorrect because that result assumes that every relative permittivity has doubled. This result would be accurate if the permittivity of the epoxy had also increased by a factor of 2, from 3.8 to 7.6. The capacitance value from

line 35 is used instead, the same model with a relative permittivity of 1.9 for the epoxy. The capacitance calculated is 4.701 pF, and it is this capacitance that needs to be doubled. The capacitance of the system with the new dielectric medium is therefore predicted to be 9.402 pF.

The next test observes how close the slope of capacitance approaches one of the closed-form models from Section 2.2. The results are plotted from the flat target surface and these are compared to the simple parallel plate capacitor and the parallel plate capacitor with fringing. For a large sensing area and the smallest gaps, it is expected that the parallel plate approximation (which is, after all, based on infinitely large plates) is a good fit. Indeed, on the left side of Figure 2-7 the two approximations and the finite element results are merged. As the gap distance d becomes the same order of magnitude as the diameter of the sensing area, the two approximations diverge from each other, with the FEA results falling somewhere in between. Indeed, to a gap distance d that is 68 times smaller than the radius of the sensing area, the simple parallel plate approximation (red line) is accurate to within 6%. Although the error increases from this point onward, the lines appear to converge again because the magnitude of the difference becomes smaller as the capacitance decreases.

As a second measure of the relationship between the capacitance gage finite element model and closed-form solutions, consider a small diameter target surface and large gap distances. Taking data from a probe with a sensing diameter of 0.0675 inches (1.71 mm), a target sphere with a diameter of 0.25 inches (6.35 mm), the plot of capacitance as a function of gap distance d is shown in Figure 2-8. Also shown is the approximate closed-form solution for two non-concentric spheres of different radii separated by the same distance from Eq. (2-11).

The two-sphere approximation is applied by first converting the area of the capacitance plate in the finite element model to an equivalent radius. By using this radius and the radius of the target sphere, it can be seen how the capacitance compares to this idealized model. The plot of this data in Figure 2-8 shows a large discrepancy between these two plots when the gap distance is small.

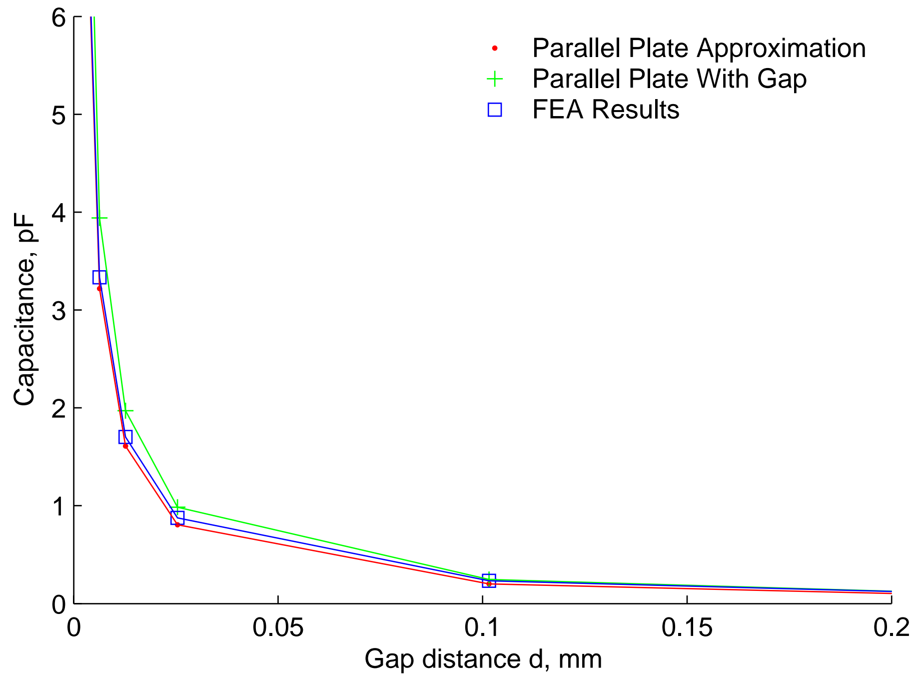

Figure 2-7. Comparison of capacitance plot to parallel-plate solution.

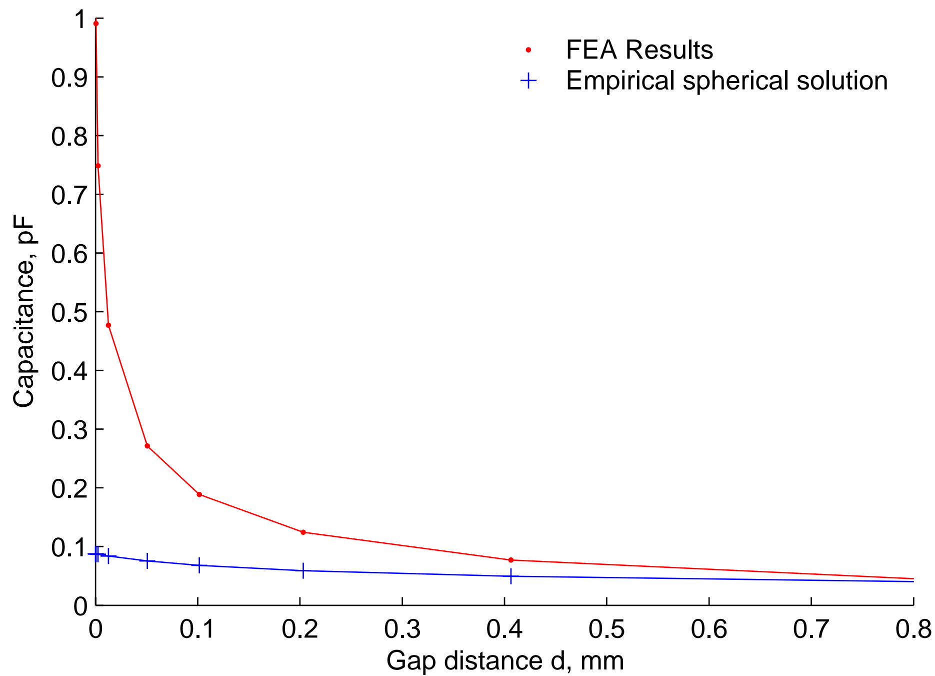

Figure 2-8. Comparison of capacitance plot to two-sphere solution.

There are several reasons for this discrepancy, starting with the geometric differences between the ideal model of two spheres separated in space and the actual geometry of the capacitance probe and target sphere. For large gap distances d, the

geometry of the two objects is less significant than their overall area, but for small distances the geometry has a greater effect. The gap distance is also less representative of the distance between the objects when this distance is small. Another cause of discrepancies is the series solution, of which Figure 2-8 represents the first five terms. This result is only an approximation and converges less rapidly as the gap distance d becomes smaller. This error is as large as 10% on the left side of the figure, compared with less than 0.1% at the right side.

The electric field that exists between the capacitance probe and the target sphere differs from the ideal case in a couple of key ways that affect this approximation. First, the sides of the sensing area are not included in this approximation, although they contribute to the overall capacitance of the system. Their influence is reduced by the presence of the guard ring structure, nevertheless they add a positive contribution to overall capacitance. Second, field lines from the idealized case of nonconcentric spheres extend to infinity at progressively lower field strength. These long field lines are captured in the series approximation, but the ANSYS model does not include large surrounding areas due to computational limitations. The ANSYS model also does not include a complete target sphere since the guard ring structure limits these field lines.

After the finite element results have been compared to other available solutions, it is time to compare one set of finite element results to another. This analysis determines which parameters are of primary importance in creating new probe designs.

2.9 Parametric Study and Conclusions

The large set of data generated by these ANSYS scripts includes variation in the five different parameters listed in Table 2-1, and is therefore impossible to visualize collectively. The analysis of data from such a broad parametric study instead takes the form of individual studies of one or two variables. This not only illustrates how these variables affect the results for the current geometry, but also reveals trends that can be rationalized and qualified for application to new capacitance probes. Each study, then, must indicate the relative importance of a parameter in the overall design.

2.9.1 Sensing area diameter

Since the sensing area of the capacitance probe is much smaller than the target surface, it is this area that is used in the simplest approximations of capacitance. From the parallel

plate approximation of Eq. (1-3), the capacitance is expected to increase as the area increases. To normalize capacitance it is necessary to apply a function of the variable *b*, the exact function to be determined by trial and error.

To reduce the effect of other variables, a minimum spacing *g* is selected between the sensing area and the guard ring structure of 0.007175 inches (0.1822 mm), and the lowest possible relative permittivity of the epoxy ε_r of 1.0 is also chosen. The target sphere radius is normalized by dividing that value by the radius of the sensing area. The normalized capacitance as a function of the normalized radius of the sphere is plotted for several different sensing areas. These results are shown in Figure 2-9 for the smallest gap spacing and Figure 2-10 for a larger gap spacing.

The capacitance is normalized using the sensing radius, but to different degrees for the small versus the large gap. This is so the first order discrepancies between the capacitance results can be eliminated, and the smaller differences due to variations in gap distance *d* and sphere radius r_s can be examined. For the small gap Figure 2-9, three lines are plotted for *b* values of 0.0225, 0.0450, and 0.0675 inches (0.572, 1.143, and 1.715 mm) and a gap distance *d* of 0.00001 mm. It is found in this case that the lines most closely converge when the capacitance is divided by the radius *b*. As can be seen in the figure, the lines begin to diverge as the target radius in increased (again, with a fixed gap distance *d*). For the lines to converge completely the power of *b* would need to be somewhat larger than 1.

Three lines are plotted in Figure 2-10 for the same *b* values and a gap distance *d* of 0.01016 mm. In this case, however, it is found that dividing by b^2 results in the lines more closely converging. These lines show far more nonlinearity than Figure 2-9, and in this case the curve related to the larger sensing diameter is below the smaller values. This is inverted from the order appearing in Figure 2-9, and it indicates that the capacitance value has been somewhat overcorrected. To get the lines to completely converge, the order of *b* must be somewhat less than 2. From these plots it is possible to determine that these operating ranges and curved targets cannot be perfectly represented by a dimensionless model, but rather the gap distance *d* as compared to the sensing area dictates which model is the best predictor of behavior.

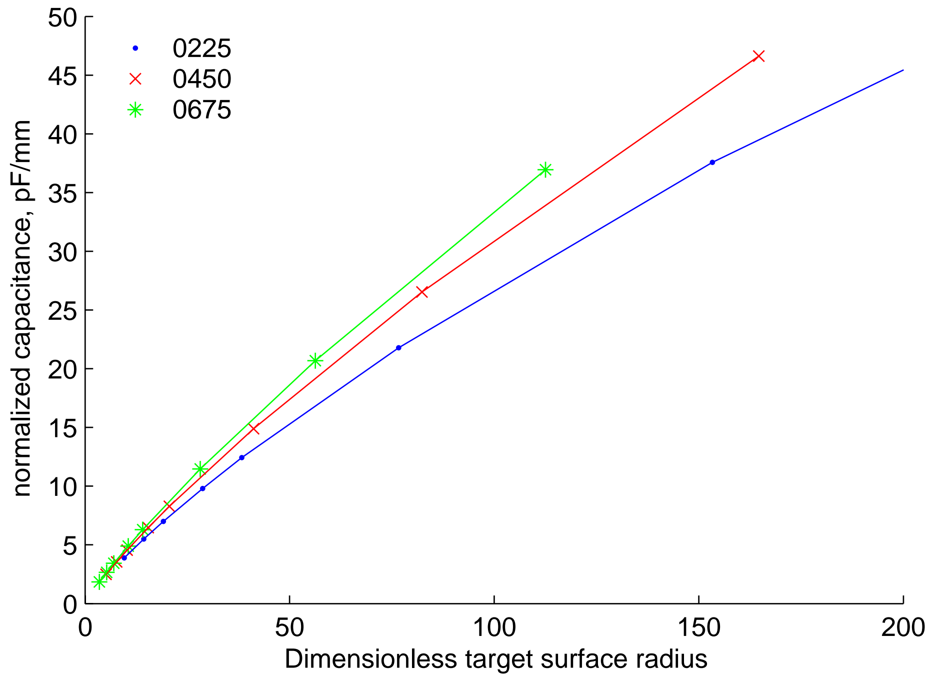

Figure 2-9. Plot of normalized capacitance as a function of dimensionless target radius for the three sensing areas and the smallest gap distance *d*.

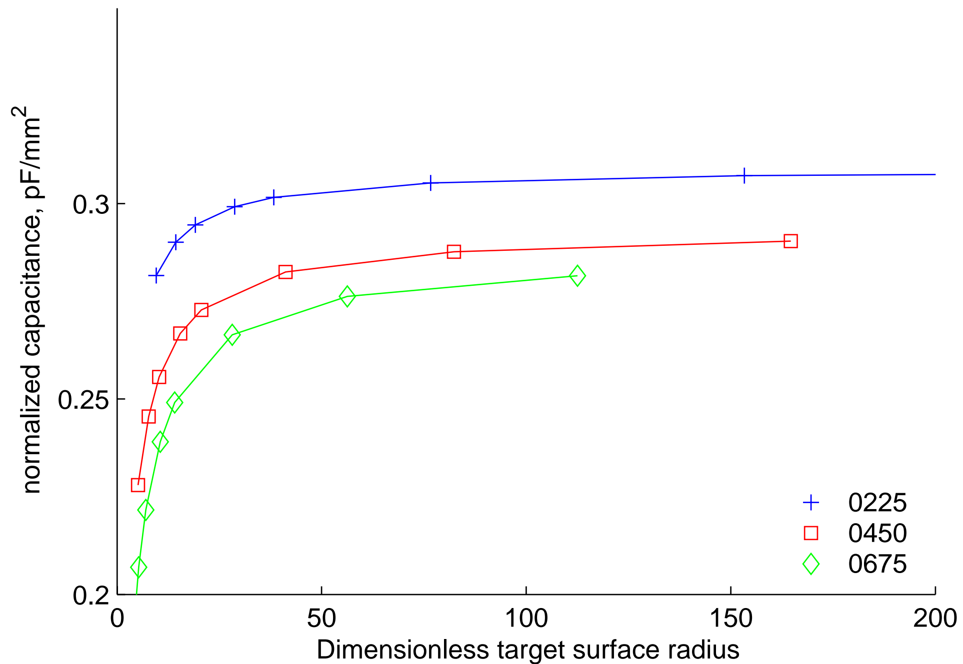

Figure 2-10. Plot of normalized capacitance as a function of dimensionless target radius for the three sensing areas and the largest gap distance *d*.

2.9.2 Guard ring spacing

The next variable to be examined separately is the guard ring spacing *g*. This is the distance from the outer edge of the sensing area to the inner edge of the guard ring. This space is filled with epoxy and provides a contribution to the overall capacitance of the model. This contribution was examined in some detail in the previous study [82]; to summarize, the side of the sensing area adds to the effective sensing area of the probe. The degree to which the sensing area contributes depends on the spacing *g*, the gap distance *d*, and the radius of curvature of the target surface r_s. For a given radius of sensing area *b*, the capacitance *C* increases as the spacing *g* is altered. Plots of capacitance probes with a constant sensing area radius *b* of 0.0450 inches (1.143 mm) are shown in Figure 2-11 and Figure 2-12. Each figure includes four curves. Figure 2-11, where the gap distance *d* is 0.00001 mm, shows almost no difference as the spacing between the sensing conductor and the guard ring is increased by a factor of 6. The maximum change in capacitance as the spacing varies is less than 0.2%. The conclusion from this graph is that the relative contribution of the sides with this gap spacing *d* is negligible.

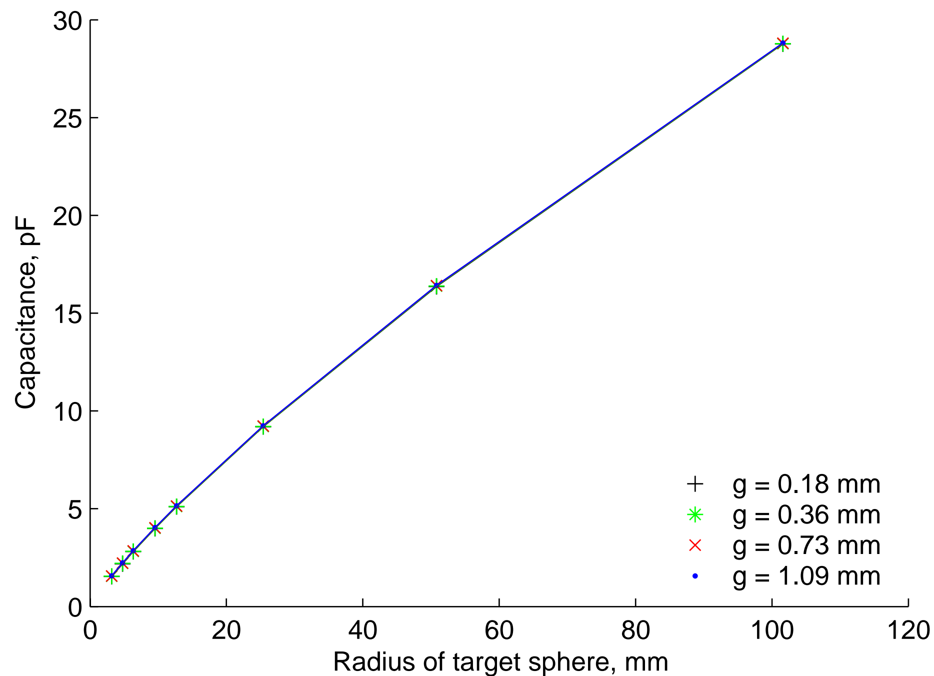

Figure 2-11. Plot of variation in capacitance as a function of guard ring spacing and small gap distance *d*.

Figure 2-12, where the gap distance *d* is 0.01016 mm, shows a different trend. Here there is a much greater deviation (as a percentage of capacitance) due to the change in guard ring spacing than in Figure 2-11. This is because the contribution of the sides of the sensing area is very little when the gap distance *d* is small, since the sides of the probe are far away relative to the front surface. With a larger gap distance *d*, the sides of the probe are now a comparable distance from the target surface, and therefore their contribution increases. Since their contribution is a function of the spacing *g*, increased spacing results in increased capacitance. From the smallest to the largest spacing *g* there is a 38% increase in capacitance.

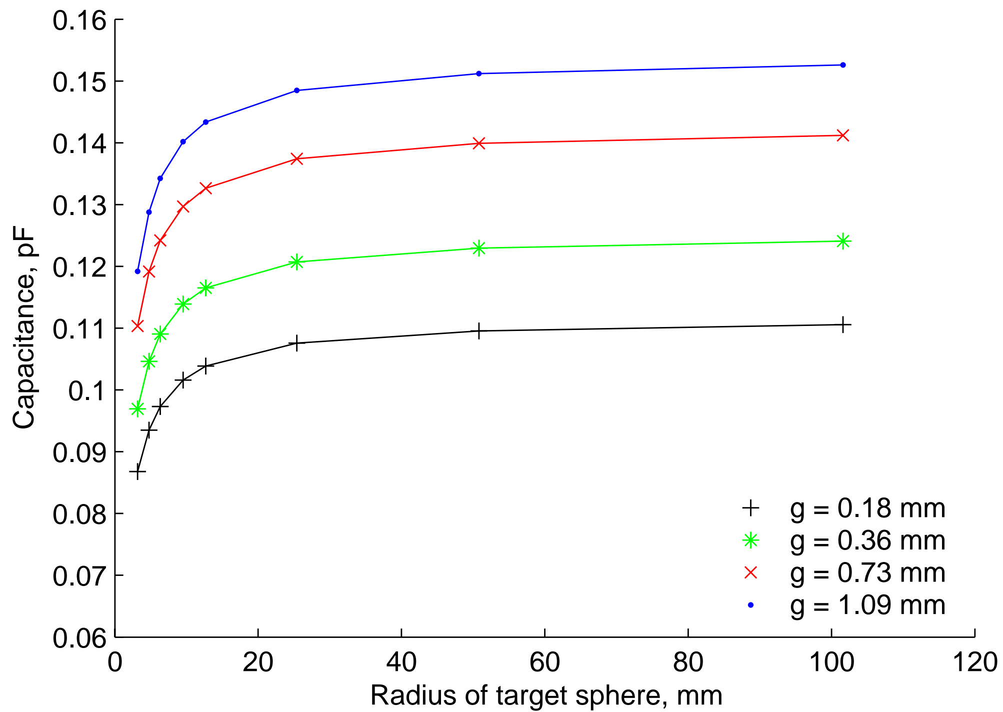

Figure 2-12. Plot of capacitance vs. guard ring spacing and large gap distance *d*.

2.9.3 Relative permittivity of epoxy

If the effect of the different variables of this study are listed in order of their influence on capacitance, the permittivity of the epoxy winds up at the bottom of the list of studied parameters. The permittivity does affect the strength of the electric field from the sides of the sensing area to the target surface. However, since the sides of the sensing area already

exert only a small influence on the overall capacitance, variation in the relative permittivity is a small change to a small effect. If changes in the gap distance *d* are a primary factor in determining the capacitance of the probe, and changes in the spacing between the sensing area and the guard ring *g* a secondary effect, then the relative permittivity can be considered tertiary.

To see the effect on capacitance caused by changes in the relative permittivity, data are selected with two different gap spacings *d* between a sensing element with a diameter of 0.0450 inches (1.143 mm) and a target surface with a diameter of 1.0 inches (25.4 mm). The spacing between the sensing area and the guard ring *g* is shown along the *x*-axis, while the four different values of electric permittivity ε_r are plotted as four different lines. The capacitance as a function of spacing is shown for a small gap distance *d* of 0.00001 mm in Figure 2-13, and for a large gap distance *d* of 0.01016 mm in Figure 2-14.

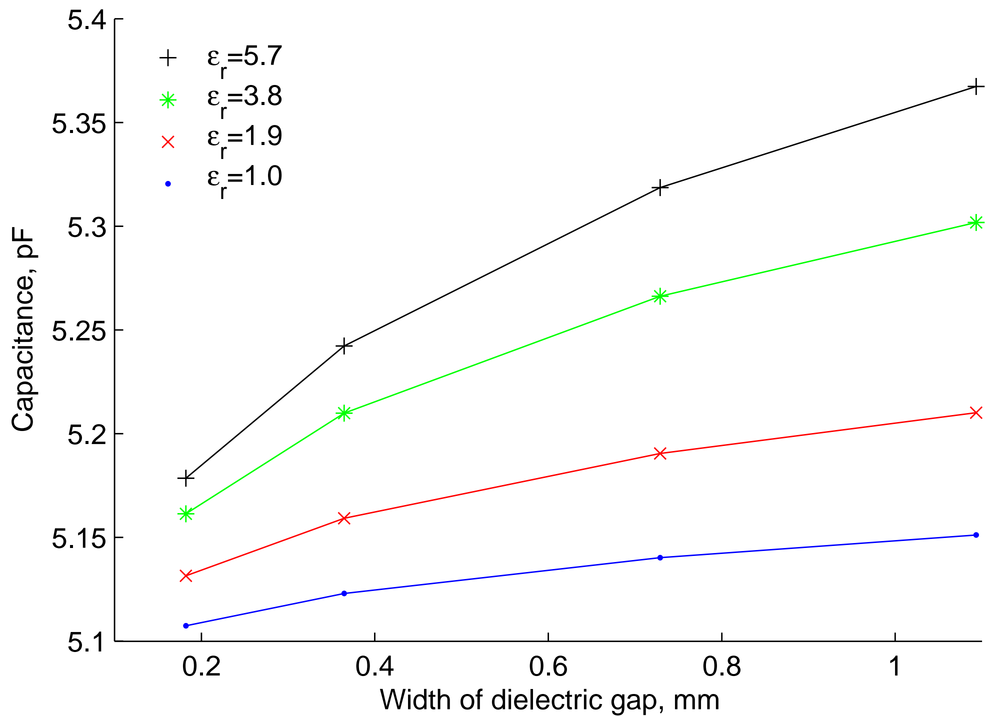

Figure 2-13. Plot of variation in capacitance as a function of both the width of the dielectric material and its permittivity for the smallest gap distance *d*.

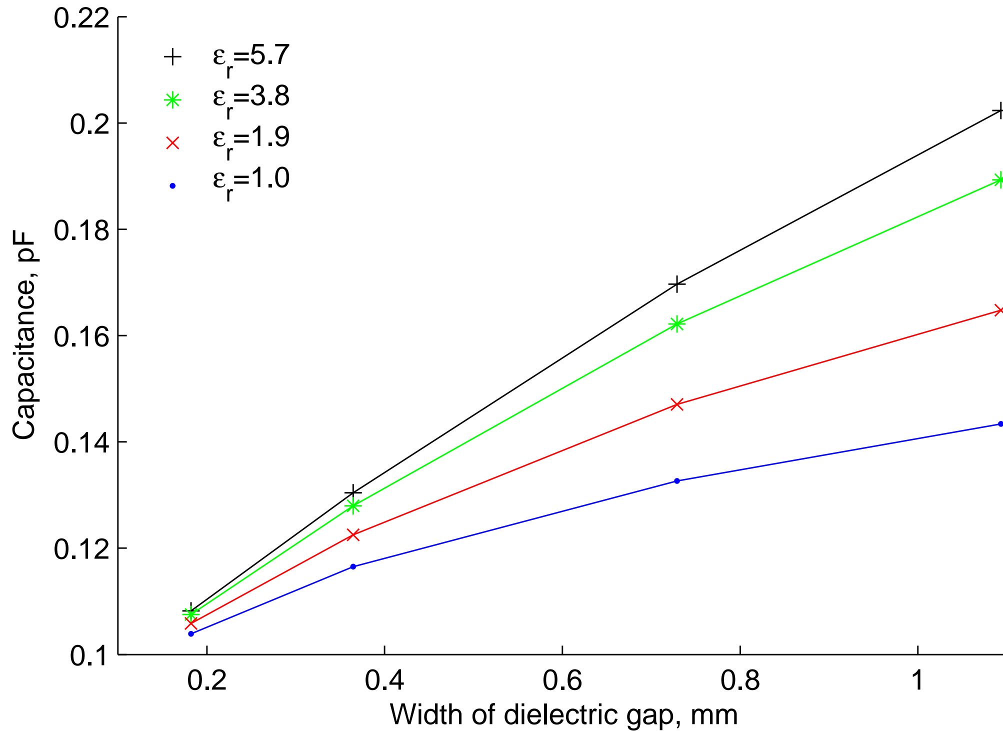

Figure 2-14. Plot of variation in capacitance as a function of both the width of the dielectric material and its permittivity for the largest gap distance *d*.

Figure 2-13 and Figure 2-14 show that the magnitude of this effect varies widely depending on the relative size of the other dimensions. For the smallest gap distance *d* represented by Figure 2-13, the increase in permittivity of a factor of 5.7 results in an increase in capacitance of 1.4% at the smallest spacing *g* and an increase in capacitance of 4.2% at the largest spacing. For the larger gap distance *d* represented by Figure 2-14, the capacitance increase ranges from 4.2% to 41.2%. As discussed in Section 2.9.2, at small gap distances *d* the sides of the probe have little relative contribution to the overall capacitance of the probe and target surface. At larger gap distances the contribution from the sides of the probe are a larger percentage of the overall capacitance, therefore changes in the electric field on the sides of the sensing area have a much more noticeable effect.

Changes in permittivity have a significant effect on the capacitance between the sensing conductor and the guard ring. The system of the sensing conductor and the guard ring can be approximated by concentric cylinders as described by Eq. (2-7). When relative permittivity is included, the result is as shown in Eq. (2-21). For this

approximation, the capacitance between the sensing conductor and the guard ring is linear as a function of permittivity.

$$C = \frac{2\pi\varepsilon_0\varepsilon_r L}{\ln\frac{b}{a}} \tag{2-21}$$

This can be seen by reviewing the capacitance C_{12} included in the attached data file. Since epoxy fills the entire gap between the sensing area and the guard ring, a doubling of the permittivity causes a near-doubling of the capacitance of these two conductors. Although this capacitance is not directly relevant to this study, the design of real-world capacitance sensing circuits requires knowledge of these values.

2.9.4 Gap distance and slopes

The final variable in the capacitance gage study is the gap distance d. Of course this variable is of primary importance: the gap distance appears in the simple parallel plate form of the capacitance equation. Where this study can show insight is regarding how closely the capacitance follows this simplified model.

To base expectations on a linear result, the first step is to convert the parallel plate capacitance Eq. (1-3) to a linear form. This is easily done by taking the inverse capacitance, as shown in Eq. (1-4) and again below in Eq. (2-22). By plotting inverse capacitance as a function of d, the slope is expected to be constant. Deviations from constant represent shortcomings in the approximation.

$$\frac{1}{C} = \frac{d}{\varepsilon_0\varepsilon_r A} \tag{2-22}$$

In reality, the smallest target sphere has one slope value, and the largest target sphere has another. Several different target surfaces have been plotted in Figure 2-15. Along with these graphs is plotted the slope calculated by applying Eq. (2-22) to the same distances. The area A is calculated using the effective radius of Eq. (2-1).

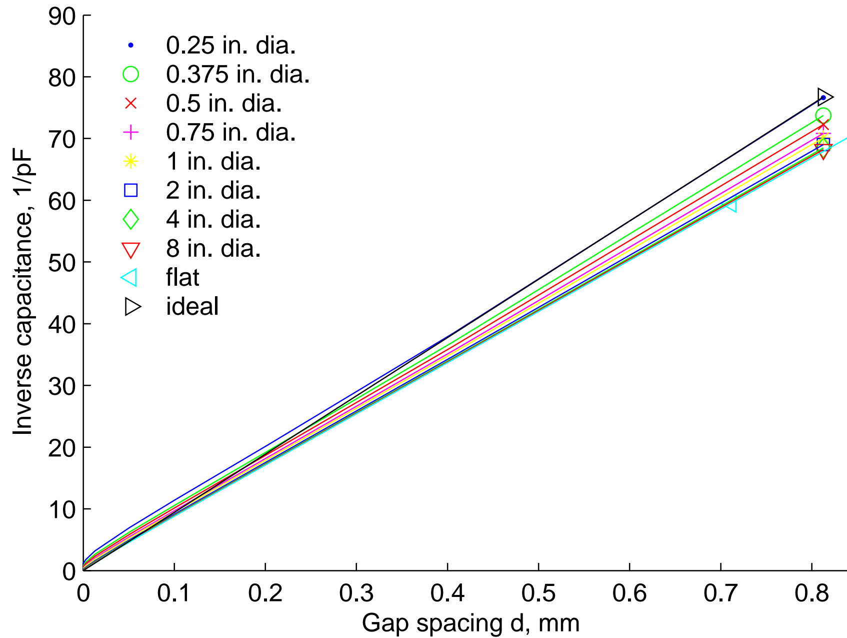

Figure 2-15. Plot of inverse capacitance as a function of gap distance *d* as a function of several different target diameters.

As can be seen in the lower left corner of Figure 2-15, the curves where the sphere diameter is large show the least deviation from linear at small gap distances. The flat target surface agrees best with the parallel plate approximation for the smallest gap distance, but the slope of the parallel plate approximation is steeper than any of the other curves. In the upper right corner of the figure, it appears as though the "ideal" parallel plate approximation is merging with the data from the smallest target sphere diameter, 0.250 inches (6.35 mm). Looking carefully once again at Eq. (2-22), a steeper slope indicates a smaller effective area *A*, therefore the effective area predicted by the FEA is larger for larger target diameters. The parallel plate approximation is not merging with the smallest target diameter result, but rather in the range plotted the two lines are momentarily crossing, indicating that the effective area is a good approximation at that particular gap distance *d*.

2.10 Conclusions

This chapter took a commercial capacitance gage and performed a parametric study of its dimensions, as applied to both curved and flat surfaces. The author's previous study [82] only showed how the distance to target surfaces were recalibrated, but not how the varying of different dimensions affected the capacitance of the system.

Closed-form solutions available for this geometry describe how the spacing between the sensing area and the guard ring structure influences the capacitance in a nonlinear way. Solutions for other geometries, including concentric cylinders and concentric spheres, were shown as closed-form solutions to emphasize how these capacitances are always linear to a characteristic dimension. Even a series solution for non-concentric spheres has a solution where each term is linear with a scale dimension. Double the dimensions of the geometry and the capacitance doubles. The solution for non-concentric spheres also plays an important role in determining the capacitance between a spherical surface and a flat target.

With an understanding of the closed-form solutions available, five parameters are selected for further study. They are the radius of the sensing element, the width of the dielectric material between the sensing area and the guard ring, the dielectric constant of that material, the radius of the target surface, and finally the distance from the sensing area to the target surface. Based on prior studies, other parameters such as the width of the guard ring were deemed inconsequential.

To perform this parametric study, several ANSYS scripts were created to generate the geometry and solve for the capacitances within the system. Of the calculated capacitances, only the mutual-lumped capacitance between the sensing area and the target surface is of interest here. Several thousand of these values were generated and written to a text file. It was shown that, although these results were calculated with a relative permittivity of 1 (vacuum) between the sensing area and the target surface, other permittivity results are derivable. Because permittivity and the dimensional scale of this system are tied together, clever selection of geometry from this large table can produce results that correlate with other permittivities.

The first metric applied to these FEA results is that of the closed form solutions, in particular the parallel plate approximations and the non-concentric spherical approximation. For the smallest gap distances, the FEA results fall between the simplest parallel plate approximation and the approximation including fringing. For larger gap distances, the non-concentric sphere solution is shown to approach the calculated capacitances from ANSYS. With these initial comparisons, the data can now be compared for the influence of each parameter.

The first parameter compared for its effect on the capacitance of the system was the sensing area. For this comparison, both the capacitance and the target surface were "normalized" by applying the sensing radius to these values before plotting. For both sets of results, a dimensionless target radius was produced by dividing the target radius by the radius of the sensing area. For a fixed, small gap distance, the capacitance was normalized by dividing by the radius of the sensing area. Although these "normalized" capacitance values were in the same range, larger sensing areas in this case resulted in capacitance values that were slightly higher. For a larger gap distance, dividing the capacitance by the square of the sensing radius brought the values much closer together. In fact, the correction was too great: the smaller sensing areas have a larger normalizing capacitance. No single parameter is able to correct entirely for all of these variations; the true "normalization" varies as a more complicated function of the gap distance d.

The dependence of capacitance on guard ring spacing is next considered. A wider guard ring spacing was shown to increase the capacitance of the probe for a fixed gap distance d, but the effect was much more pronounced at large gap distances as compared to small gap distances. For the smallest gap distance d, large changes in the guard ring spacing made almost no difference. As the gap distance d is widened, the four different curves representing the four different guard ring spacings begin to diverge. This was explained by considering the relative contribution to the overall capacitance of the sides of the sensing area. This contribution is relatively fixed, compared to the capacitance of the parallel surface. If this contribution can be approximated or calculated for an average gap spacing d, it can be estimated whether or not its contribution can be discounted.

The third parameter under study is the electric permittivity of the material between the sensing area and the guard ring structure. For a new capacitance probe a choice of dielectric material is available, so an understanding of how this selection will affect the overall capacitance is needed. The capacitance of a probe with fixed sensing area was shown as the width of the guard ring spacing was increased. For a large dielectric constant, the overall capacitance was larger. This is due to the fact that the lower electric field in that volume allows the sides of the probe to make a greater contribution to the overall capacitance. As the guard ring spacing is increased the volume is increased, increasing energy stored and therefore overall capacitance. The effect of

these changes are finite but small, and are sometimes outweighed by other material properties such as breakdown voltage.

Finally, it was shown how closely the capacitance of the system can be approximated by a closed-form solution. In the ideal case, inverting the capacitance produces a linear plot versus the gap spacing d. Due to variations in the factors described above, the resulting family of curves varies in both value and slope, depending on the curvature of the target surface. Even the case of the flat target varies considerably from the idealized case, indicating that the sensing area, the guard ring spacing, and the permittivity of the epoxy all cause noticeable changes to the resulting capacitance. The ideal probe would maximize the sensing area, minimize the gap distance d as well as the guard ring spacing, and minimize the permittivity of the material between sensing area and guard ring. As shown in both Chapter 6 and Chapter 7, the actual steps necessary to manufacture a new probe geometry often drive the limits of what geometry can be achieved.

Copyright © Philip T. Smith Jr. 2007

3 Analysis of Cylindrical Target Surfaces

3.1 Introduction

Many applications require the measurement of cylindrical artifacts. Errors from using a commercial capacitance sensor with a cylindrical target rather than a flat target (as calibrated by the factory) are typically neglected, but these errors cannot be ignored for nanometer-level accuracy. The capacitance between a sensor and a cylindrical target for a given gap distance is less than that of a sensor with a flat target, which causes four effects. As the diameter of the target shrinks, the sensitivity of the sensor increases, the sensing range decreases, the sensing range shifts towards the target, and the nonlinearity increases. This chapter quantifies and experimentally verifies these effects for a commonly used sensor. A simulation of a nanometer-level measurement of out-of-roundness and spindle error motion demonstrates that measurement accuracy is improved with corrected sensitivities.

Metrology applications frequently require non-contact measurements with nanoscale resolution, and capacitive displacement sensors are a common solution to this measurement problem. A typical commercial realization of the capacitive sensor is a sensing electrode and guard ring enclosed within a grounded sensor body. Figure 1-1 shows this configuration. The working distance and sensing range vary with the sensor size and electronic gain, but typical values for the working distance are from 100-1000 μm, with a typical sensing range of 50-2000 μm.

In many instruments and in fine motion control, the target is a flat surface with characteristic dimensions significantly larger than the sensing electrode. For other situations a flat target surface is not available. Examples of this include measuring the roundness of a cylindrical shaft [88, 89], measuring the accuracy of spindle rotation [90, 91], and measuring the accuracy of machine tools [92, 93]. Capacitive displacement sensors are typically calibrated targeting flat surfaces. Measurement error, often neglected, is introduced when such a calibrated sensitivity is used with a non-flat target or artifact. The magnitude of the error depends upon the geometry of the capacitive sensor, the diameter of the cylindrical target, the working distance, and possibly the sensor's electronics. In some cases the error is negligibly small, but it is found to be significant when measuring at the nanometer scale.

Chapter 2 and also prior work [94] considered the effects of using capacitive displacement sensors with spherical targets when calibration is done with flat targets. The effects were observed and quantified with 2D electrostatic finite element analyses, described by Smith [82], that determine the capacitance between the sensor and the spherical surface as a function of the sphere's diameter and the gap between the sensor and sphere. The work also described a simple procedure to determine corrected sensitivities and residuals. These studies demonstrated four effects for spherical targets. As the diameter of the target is reduced, the sensitivity increases, the sensing range decreases, the sensing range shifts towards the target, and the sensor becomes increasingly nonlinear.

This chapter considers the effects of using cylindrical targets with the representative sensor shown in Figure 1-1. Three-dimensional finite element analyses determine the capacitances and corrected sensitivities for various diameters of cylinders, and the results are verified experimentally. Since the inverse capacitance between the cylindrical target and the sensor decreases with decreasing target diameter, the same four effects observed for spherical targets are also observed for cylindrical targets. However, the effects are less severe. A simulation of a typical roundness measurement using Donaldson reversal [95] to separate spindle error motion demonstrates that using corrected sensitivities from this technique produces more accurate metrology measurements.

3.2 Base Calibration of Capacitance Sensor

Table 3-1 lists the calibrated sensitivities for the commercial sensor shown in Figure 1-1 when it targets a flat surface in air. This sensor operates in two alternative ranges. The first range yields a larger sensing range (50.8 μm) but lower sensitivity (–0.394 V/μm), and the second yields a higher sensitivity (–1.969 V/μm) but smaller sensing range (10.0 μm). Both ranges produce an analog voltage that ranges from –10 to +10 V. This sensor has excellent linearity when targeting a flat surface; calibration data indicates that the sensor is linear within 0.33% over the full measurement range for its high sensitivity setting.

Table 3-1: Nominal gaps, sensitivities, and nonlinearities for low and high sensitivities of the representative capacitive sensor

	Sensing Range	Nominal Gap, gnom	Sensitivity, S	Nonlinearity, %FS
Low Sensitivity	76.2 – 127.0 µm	101.6 µm	-0.394 V/µm	0.02%
High Sensitivity	20.3 – 30.5 µm	25.4 µm	-1.969 V/µm	0.33%

3.3 Determination of Capacitance with Finite Element Analyses

It is necessary to know how the capacitance varies with changes in the gap to quantitatively predict the effects of a cylindrical target. Unfortunately, closed-form analytical solutions, such as for the parallel plate Eq. (1-3) or the more complex relations described by Heerens and others [25, 26, 27, 29], can seldom account for the complexities of common sensors. For instance, at least four factors with the representative sensor will contribute to discrepancies from an ideal capacitance. First, analytical solutions generally assume that the target surface is flat. Second, the radial distance separating the sensing electrode and guard ring is not small compared to the nominal gap. Third, analytical solutions usually assume that air separates the guard ring and sensing electrode rather than an epoxy insulator ($\varepsilon_r = 3.8$), and, Kahn [30] previously found that this affected sensor output. Finally, the guard ring has a tapered geometry so that it is not entirely flat.

As with the spherical target case of Chapter 2, electrostatic finite element analyses are used to determine how the capacitance varies with changes in the gap. This electrostatic FEA determines the voltage drop across dielectric materials, the electric field, and the lumped capacitances between electrodes; and it readily accommodates different material properties for the dielectrics, multiple conductive electrodes, and complex geometries. In this work, as with the previous work on spherical targets [82, 94], the FEA results correlate well with experimental validations.

3.3.1 The Finite Element Model

As illustrated in Figure 3-1, the geometry of the sensor targeting a cylindrical artifact is reduced to one quarter of the complete 3D geometry, since two planes of symmetry exist that intersect at the centerline of the sensor. Only a portion of the cylinder's length is modeled, since the cylinder is significantly longer than the radius of the sensor. The model includes four conductors, two insulators, and the air gap. The four conductors are

the electrode, the guard ring, the outer body of the sensor, and the target surface. The two insulators are the epoxy between the sensing electrode and the guard ring and the epoxy between the guard ring and the sensor's body.

Only the non-conductive dielectric materials are meshed into finite elements, since these are the only regions where an electric field is present. The conductive electrodes cannot contain electric fields, so their surfaces are represented with electric potential boundary conditions. The non-conductive regions are meshed with tetrahedral elements that are assigned appropriate values of relative permittivity. The epoxy has a relative permittivity of 3.8, and the air between the sensor and target has a relative permittivity of approximately 1.0. Each tetrahedral element contains 10 nodes, and each node has a single degree of freedom, i.e., electric potential measured in volts. Some previous spherical models used infinite elements at the perimeter of the air gap to prevent electric field lines from being "drawn" to the edge of the model. However, results both with and without these infinite elements found identical capacitances to seven significant figures (due to concentration of field within the guard ring). Therefore, these infinite elements are not included in the present work.

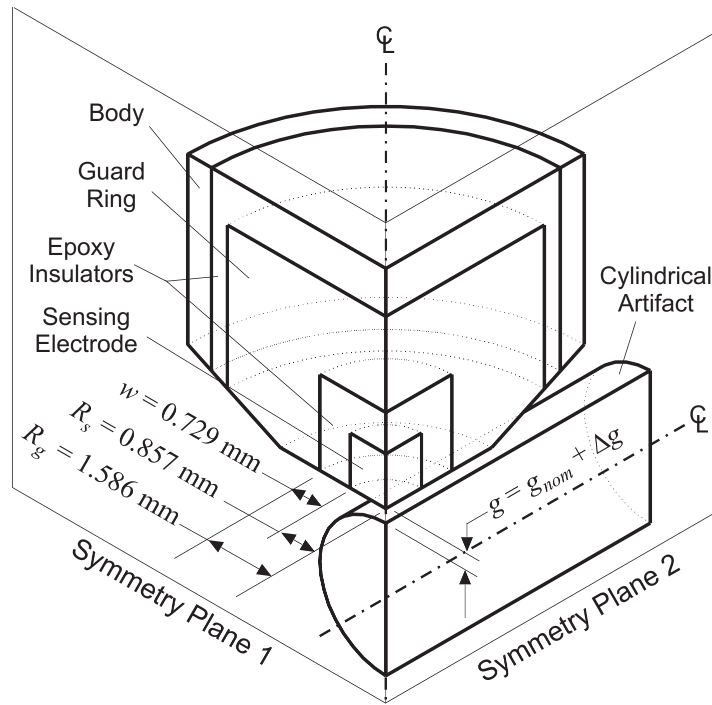

Figure 3-1: Geometry for the finite element analyses, consisting of one-quarter of the complete 3D geometry.

Figure 3-2 and Figure 3-3 illustrate typical results from an electrostatic FEA. Figure 3-2 shows a plot of the electric potential within the air and epoxy of symmetry plane 1. The sensing electrode and guard ring are both set at a 5 V, while the sensor's body and the cylindrical target are set to 0 V. It is observed from this plot that the guard ring concentrates the electric field within its confines, since the contours extend little beyond the guard ring. Most of the bending of the contours and fringing of the field occurs beyond the sensing electrode, where it has little effect on the detected capacitance between the sensing electrode and target surface.

The quiver plot in Figure 3-3 illustrates the direction and magnitude of the electric field within the dielectric materials for the potential distribution shown in Figure 3-2. The electric field vectors are calculated from the gradient of the electric potential, and point toward the surface of lowest potential. The electric field is strongest where the sensing electrode and the target are in closest proximity, and the strength decreases as the distance between the surfaces increases.

3.3.2 Capacitance as a Function of Gap and Target Diameter

Graphical plots such as those shown in Figure 3-2 and Figure 3-3 provide physical insight into the problem at hand, as well as a check of the accuracy of the computer code used to solve the model. These solutions do not provide a lumped capacitance, however, which is necessary for quantitatively predicting the effects of cylindrical targets. In cases that include more than two conductors, a matrix of lumped capacitances between each pair of conductors must be determined.

Figure 3-4 shows the four conductors and the six capacitances between each pair of conductors in this model. To determine these capacitance values the FEA must be solved multiple times, with different voltages applied to different electrodes. Fortunately, the ANSYS commercial software provides a convenient macro, CMATRIX, that solves a sequence of analysis cases with various boundary conditions and computes the matrix automatically. Although this macro yields all of the lumped capacitance values, it is only the capacitance C_{14} between conductors 1 and 4 (sensing electrode and target) that is detected by the sensor's electronics.

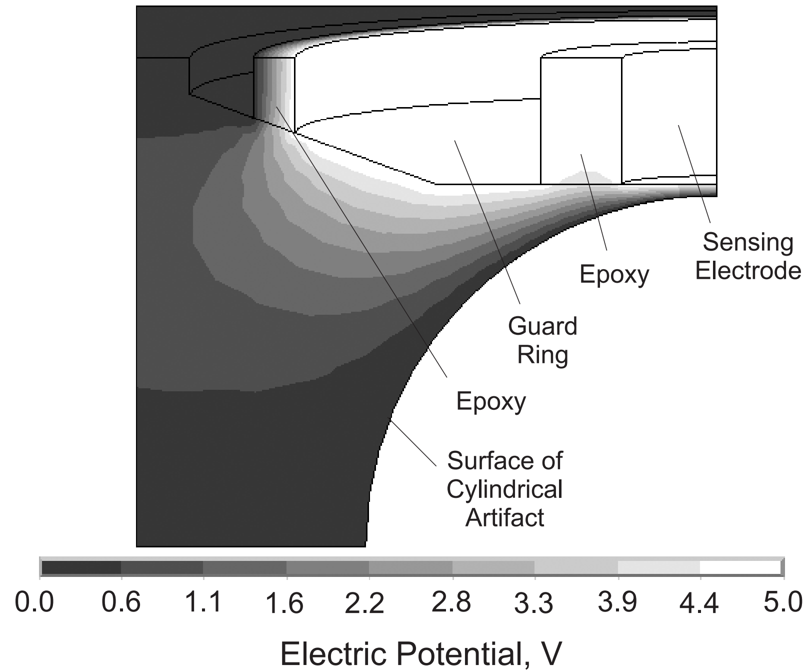

Figure 3-2: Electric potential in the non-conductive regions between the capacitive sensor and the cylindrical target.

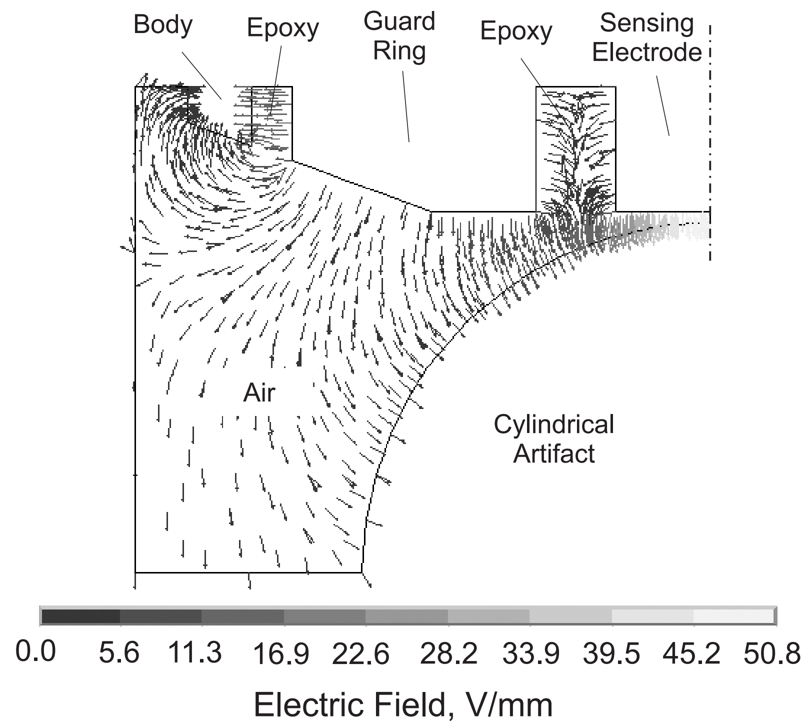

Figure 3-3: Quiver plot showing magnitude and direction of electric field between sensor and the cylindrical target

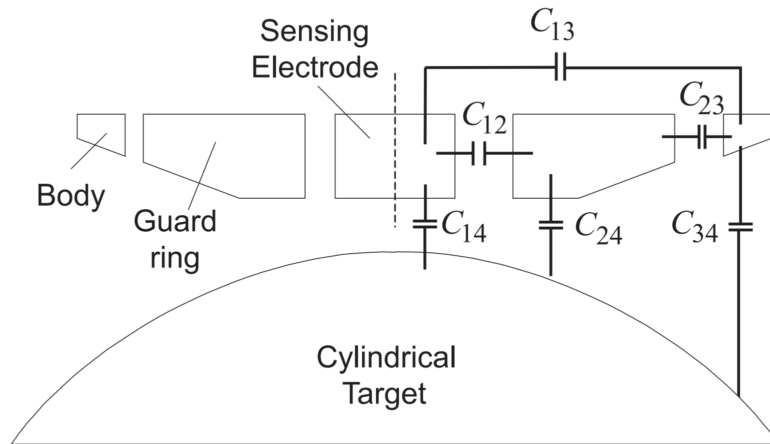

Figure 3-4: Lumped capacitances between conductive electrodes as viewed in cross section of symmetry plane one.

The complete FEA procedure based on the CMATRIX macro is illustrated in Figure 3-5. An outer loop generates the geometry and meshes the insulators for each gap distance, so that the end result is a list of capacitance values as a function of gap distance *d*. Between twelve and fifteen increments of the gap are analyzed for each cylindrical diameter; the increments are 5.10 μm for the low sensitivity and 1.02 μm for the high sensitivity. Capacitance values are calculated for cylindrical targets with diameters of 6.35 mm, 9.53 mm, 12.70 mm, 15.88 mm, 19.05 mm, 22.23 mm, and 25.40 mm. For comparison, the capacitances are also determined for a flat target. The values of capacitance for the low sensitivity setting are between 0.217 pF and 0.526 pF, while the capacitances for the high sensitivity setting are between 0.593 pF and 1.822 pF.

3.4 Effects on Displacement Sensing

Analysis of the lumped capacitances between the sensing electrode and target C_{14} reveal four effects from using cylindrical targets. As the diameter of the target is reduced, the sensing range decreases and the nominal gap moves toward the target. More significantly, both the sensitivity and nonlinearity increase, which is important since it degrades the accuracy of metrology as demonstrated in Section 3.6. All of these effects are more pronounced when sensors operate at their highest sensitivity and the diameter of the cylindrical target is small.

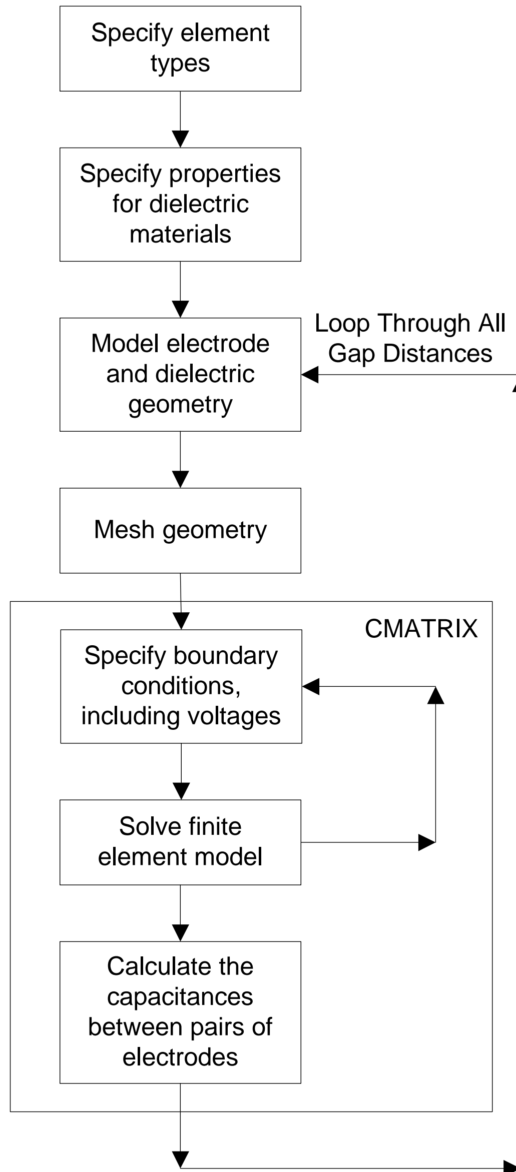

Figure 3-5: Finite element analysis procedure.

3.4.1 Reduction and Shift of the Sensing Range

Figure 3-6 and Figure 3-7 give the inverse of the capacitance between the sensing electrode and target ($1/C_{14}$) as a function of the gap distance d for both sensitivities and the seven target diameters. The parallel plate approximation in Eq. (1-3) suggests that the inverse capacitance is a straight line with positive slope, and this is very nearly the case for the representative sensor. Vertical lines in Figure 3-6 and Figure 3-7 indicate the minimum, nominal, and maximum gaps for a flat target as also listed in Table 3-1. Tracing these lines to the y-axis gives the inverse capacitances that correspond to the

minimum, nominal, and maximum gaps for the case of a flat target. The sensing range for each cylinder diameter is determined with the intersections of the horizontal lines (for minimum, nominal, and maximum capacitance values) with the cylindrical data curves.

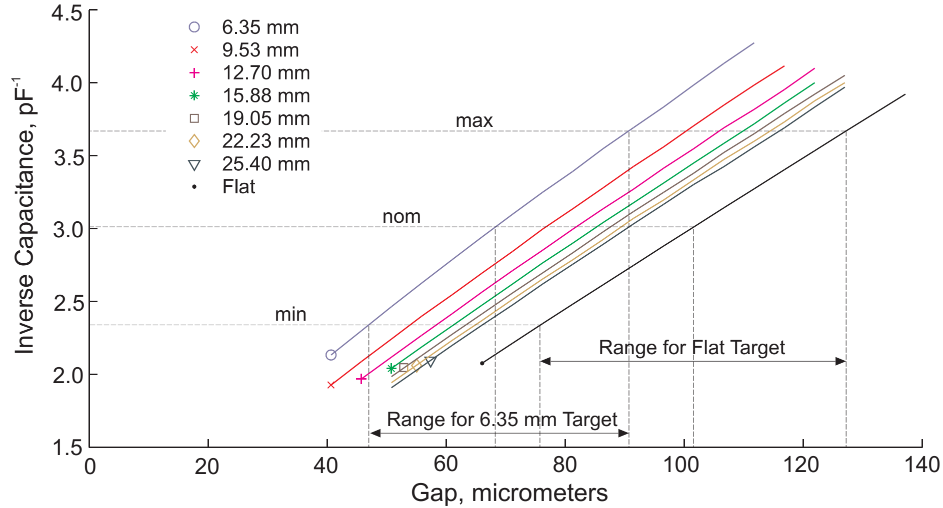

Figure 3-6. Inverse capacitance for low sensitivity (–0.394 V/µm) as functions of the gap and target diameters.

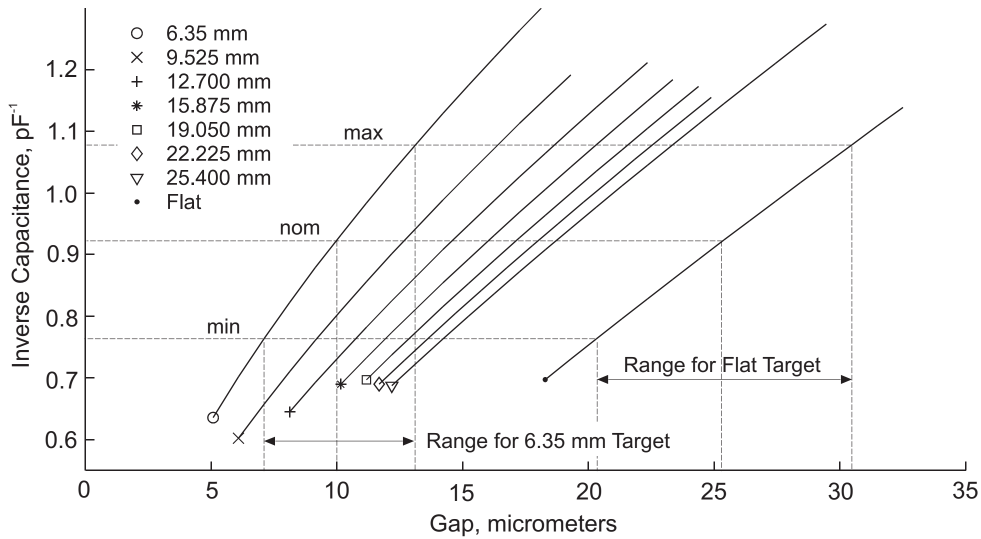

Figure 3-7. Inverse capacitance for high sensitivity (–1.969 V/µm) as functions of the gap and target diameters

The technique is illustrated for the Ø6.35 mm target at low sensitivity in Figure 3-6 and at high sensitivity in Figure 3-7. On the low sensitivity graph, the nominal gap shifts from around 102 µm for the flat surface to about 68 µm for the Ø6.35 mm target.

The sensing range reduces from about 51 μm to about 43 μm. On the high sensitivity graph, the nominal gap distance shifts from 25 μm for the flat target to around 10 μm for the Ø6.35 mm target. The sensing range for the high sensitivity decreases from around 10 μm for the flat surface to around 6 μm. Table 3-2 and Table 3-3 list the shift of the gap toward the target and the reduced sensing ranges for the remaining target diameters.

Table 3-2. Predicted changes in the gap and sensing range for low sensitivity (–0.394 V/μm)

Target Diameter (mm)	Gap			Change in Nominal Gap (%)	Sensing Range (μm)	Change in Range (%)
	Min Gap (μm)	Nom Gap (μm)	Max Gap (μm)			
6.35	47.2	68.3	90.5	-33 %	43.3	-15 %
9.53	54.2	76.8	100.2	-24 %	46.0	-9 %
12.70	58.6	81.9	105.7	-19 %	47.1	-7 %
15.88	61.5	85.3	109.7	-16 %	48.2	-5 %
19.05	63.6	87.6	112.3	-14 %	48.7	-4 %
22.23	65.2	89.4	114.3	-12 %	49.1	-3 %
25.40	66.4	90.7	115.8	-11 %	49.4	-3 %
Flat	76.2	101.6	127.0	--	50.8	--

Table 3-3. Predicted changes in the gap and sensing range for high sensitivity (–1.969 V/μm)

Target Diameter (mm)	Gap			Change in Nominal Gap	Sensing Range (μm)	Change in Range
	Min Gap (μm)	Nom Gap (μm)	Max Gap (μm)			
6.35	7.1	10.0	13.1	-61 %	6.0	-41 %
9.53	9.2	12.7	16.4	-50 %	7.2	-29 %
12.70	10.7	14.6	18.6	-42 %	7.9	-22 %
15.88	11.9	16.1	20.3	-37 %	8.4	-18 %
19.05	12.9	17.1	21.6	-32 %	8.7	-15 %
22.23	13.6	18.0	22.6	-29 %	9.0	-12 %
25.40	14.2	18.8	23.4	-26 %	9.2	-10 %
Flat	20.3	25.4	30.5	--	10.2	--

3.4.2 Increases in Sensitivity and Nonlinearity

To quantify increases in the sensitivity and nonlinearity due to cylindrical targets, the inverse capacitances plotted in Figure 3-6 and Figure 3-7 are converted to output voltages. The relationship presented in Eq. (1-6) indicates that the output voltage V is linearly

proportional to the change in gap Δd with respect to the nominal gaps that are listed in Table 3-2 and Table 3-3.

The gain G of the sensor's electronics is determined from the slope of the voltage-inverse capacitance line for the flat target, as shown in Eq. (3-1). The sensor electronics provide a ±10 V signal as the inverse capacitance varies between the minimum and maximum values for a flat target. The inverse capacitance for the low sensitivity setting ranges between 2.347 pF^{-1} and 3.663 pF^{-1}, and the high sensitivity setting ranges between 0.763 pF^{-1} and 1.078 pF^{-1}. Therefore, the gains are determined to be $G = -15.2$ V-pF and $G = -63.5$ V-pF for the low and high sensitivities, respectively.

Equation (3-2) gives the output voltage by multiplying the gain of the electronics with the difference between the inverse capacitance $1/C_{14}$ and nominal inverse capacitance $(1/C_{14})_{nom}$. The nominal inverse capacitances for the low and high sensitivities were 0.332 pF^{-1} and 1.083 pF^{-1}, respectively, as shown in Figure 3-6 and Figure 3-7.

$$G = -\frac{V_{max} - V_{min}}{\left(\frac{1}{C_{14}}\right)_{max} - \left(\frac{1}{C_{14}}\right)_{min}} \tag{3-1}$$

$$V = G\left(\frac{1}{C_{14}} - \left(\frac{1}{C_{14}}\right)_{nom}\right) \tag{3-2}$$

Figure 3-8 and Figure 3-9 show how the output voltage V varies as a function of Δd for the low and high sensitivities, respectively. The slope of these lines, which is the sensitivity S from Eq. (1-6), increases as the diameter of the target cylinder decreases. Corrected sensitivities for each diameter of the target are determined by finding the slope of the least-squares line through the data points in the ±10 V range for each target cylinder. These results are listed in Table 3-4. As the diameter of the cylindrical target increases, the sensitivities approach those for a flat target (–0.394 V/µm and –1.969 V/µm). For the Ø6.35 mm target and low sensitivity, the percent increase in sensitivity is about 17 %. For the same target and high sensitivity, the percent change in sensitivity is about 67 %. The sensitivity for the less severe case of a Ø25.4 mm target still differs

from the flat reference by about 3 % and 11 % for the low and high sensitivities, respectively.

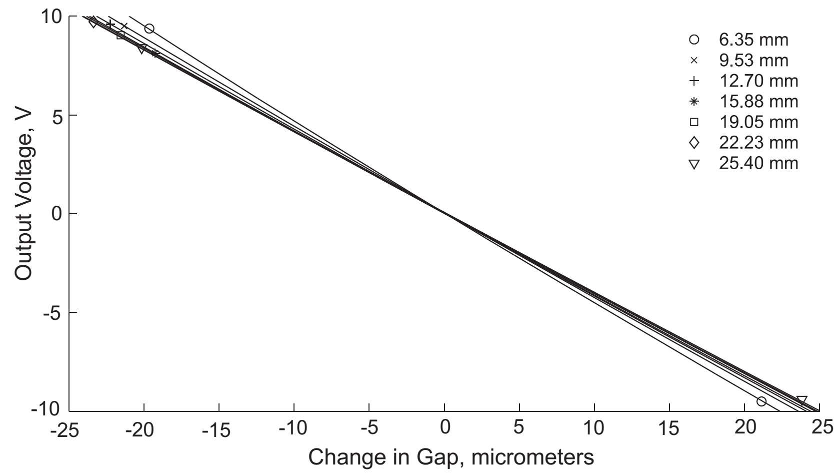

Figure 3-8. Output voltage for low sensitivity (–0.395 V/µm) as functions of the change in gap and target diameters (predicted by FEA)

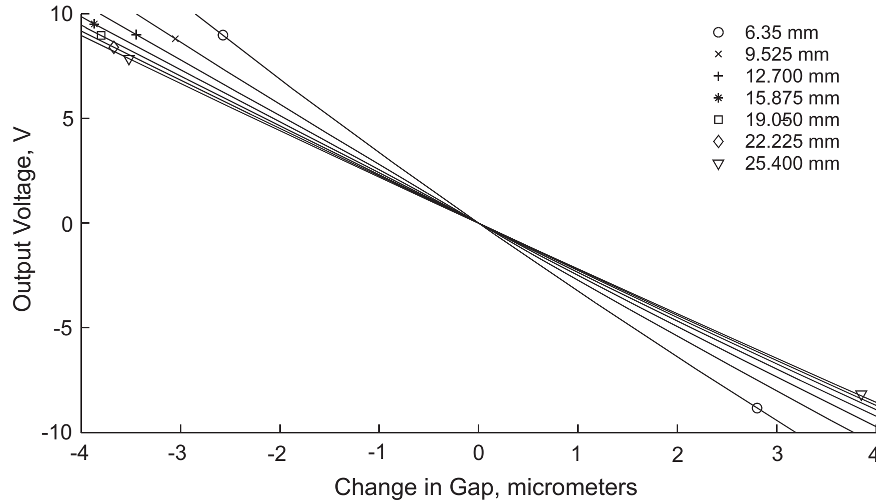

Figure 3-9. Output voltage for high sensitivity (–1.969 V/µm) as functions of the change in gap and target diameters (predicted by FEA)

Increases in the sensor's nonlinearity are observed by computing the residuals of the least-squares line. Figure 3-10 and Figure 3-11 show the residuals computed for the low and high sensitivities for each target diameter. The worst-case residual voltage of about 0.6 V or 3% is observed for the 6.35 mm target and high sensitivity, which is about an order or magnitude larger than the nonlinearity for a flat surface.

Table 3-4: Comparison of corrected sensitivities determined by finite element analyses and experimentally

Target (mm)	Nominal sensitivity: 0.394 V/μm			Nominal sensitivity: 1.969 V/μm		
	FEA (V/μm)	Exp. (V/μm)	Difference (%)	FEA (V/μm)	Exp. (V/μm)	Difference (%)
Flat	-0.394	-0.395	0.2 %	-1.969	-1.986	0.9 %
25.40	-0.406	-0.407	0.2 %	-2.190	-2.284	4.3 %
22.23	-0.409	-0.410	0.2 %	-2.224	-2.348	5.6 %
19.05	-0.411	-0.412	0.2 %	-2.289	2.404	5.0 %
15.88	-0.415	-0.419	0.9 %	-2.373	2.555	7.7 %
12.70	-0.421	-0.425	0.9 %	-2.517	--	--
9.53	-0.432	-0.437	1.2 %	-2.779	--	--
6.35	-0.460	-0.463	0.6 %	-3.296	--	--

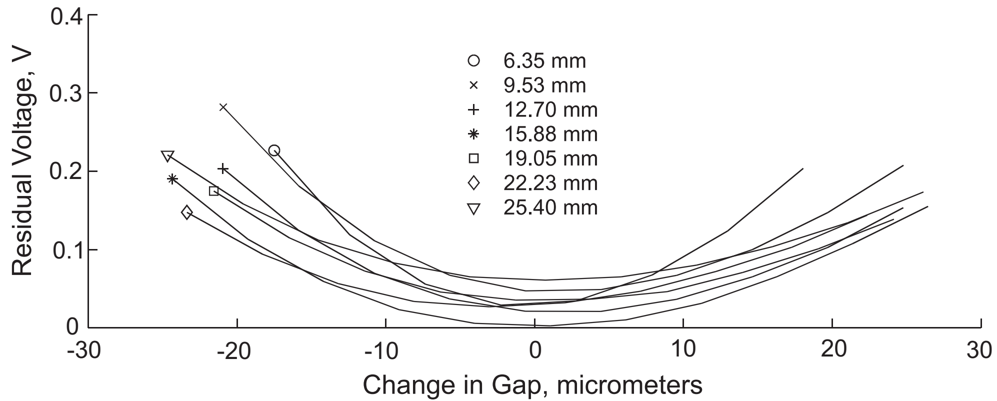

Figure 3-10. Residual voltages for low sensitivity (–0.394 V/μm) as functions of the change in gap and target diameters

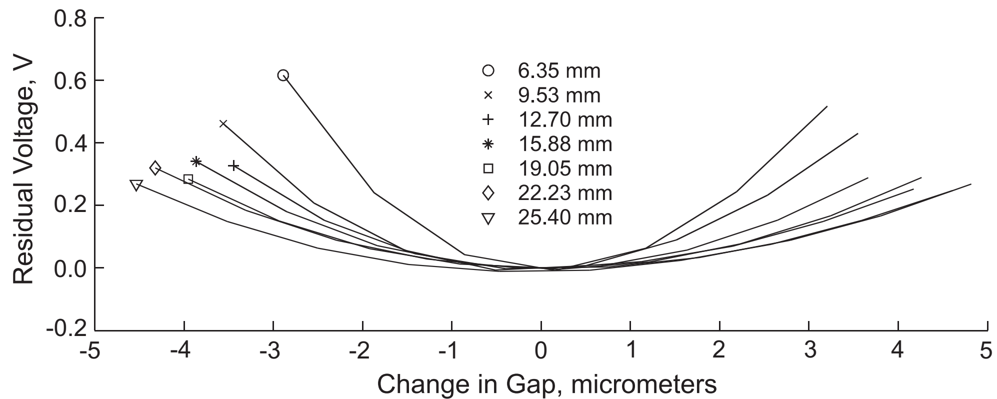

Figure 3-11. Residual voltages for high sensitivity (–1.969 V/μm) as functions of the change in gap and target diameters

3.5 Validation of Corrected Sensitivities

Experimental validation of the corrected sensitivities determined by FEA was conducted by Prof. Eric Marsh at Penn State University with the setup shown in Figure 3-12. One capacitive displacement sensor targets a flat surface, while a second sensor targets one of a set of cylindrical targets with various diameters. Both sensors are mounted collinearly in a common bracket in accordance with the Abbe Principle [96] to minimize the effects of off-axis motion. The flat and cylindrical targets are on opposing faces of the same block. The sensor bracket is mounted on the moveable base of a Moore No. 3 Universal Measuring Machine that translates in the direction along the sensors' axes. A translation produces equal changes in the gap distances, but opposite in sign. If both capacitive sensors had identical sensitivities, the sum of the measured outputs would be zero and independent of the position of the target stage. Because pairs of data points from each sensor are collected almost simultaneously, both sensors measure fluctuations in the stage velocity equally. The output from the sensor that targets the flat surface determines the position of the table, and the sensor that targets the cylindrical surface determines the nonlinearity and corrected sensitivity.

During calibration with two flat target surfaces, the sensor output repeats within 20 nm and matches the manufacturer's calibration data within 0.25%, which is small compared to the effects observed due to target diameter. This result confirms the accuracy of the sensor alignment, and the insensitivity of the experimental hardware to vibration, noise, and thermal drift.

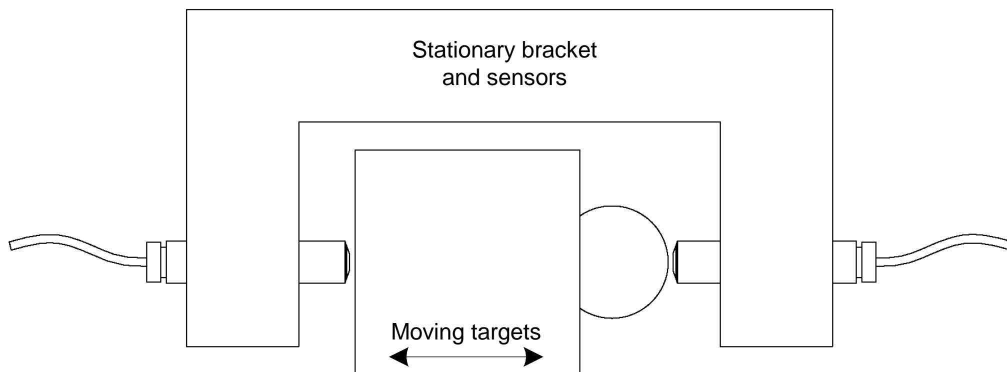

Figure 3-12. Sketch of experimental setup.

Prior to testing, the sensor is centered by finding the "high spot" on the cylinder target. By checking the repeatability of the comparative sensor output with different amounts of deliberate decentering, it was found that the effect is negligible for sensor centering within 50 μm of the high spot. It is straightforward to find the high spot to within 25 μm or better using the three axes of the Moore measuring machine, thereby satisfying this requirement. Once the highest point on each cylinder is found, both capacitive sensors are adjusted axially in the sensor bracket such that each sensor is within one micrometer of the middle of its sensing range.

As predicted by the finite element analysis, the sensor targeting the cylindrical surface had greater sensitivity than the "flat-sensing" sensor, and showed increased nonlinearity. The experimental results listed in Table 3-4 show excellent agreement with the finite element models. The maximum discrepancy between model and experiment was less than 1.2 % for the –0.394 V/μm sensitivity and less than about 7.7 % for the –1.969 V/μm sensitivity.

3.6 Corrections in Roundness and Spindle Metrology

One of the most common uses of capacitive sensors with cylindrical targets is found in precision spindle and roundness metrology. Figure 3-13 shows a typical measurement with a lapped cylindrical target such as a gage pin mounted on the rotor of a precision spindle. One or more sensors target the rotating cylinder and measure the runout of the cylindrical surface. In most high precision applications, the form error of the gage pin is significant with respect to the radial error motion of the spindle. The literature documents several methods of accurately separating the form error from the spindle's radial error motion [95, 56, 97, 98]. In fact, the best air bearing spindles actually have less radial error motion (less than ten nanometers) than most lapped cylindrical artifacts.

As previously shown, the radius of the cylindrical target affects capacitive sensor measurements, but using corrected sensitivities such as those listed in Table 3-4 for the representative sensor minimizes this effect. However, additional errors result since the cylindrical artifact is inevitably not perfectly centered on the axis of rotation, and this eccentricity causes the rotating target to explore the nonlinear response of the capacitive sensor. Simply employing corrected sensitivities does not eliminate error due to the nonlinear residuals.

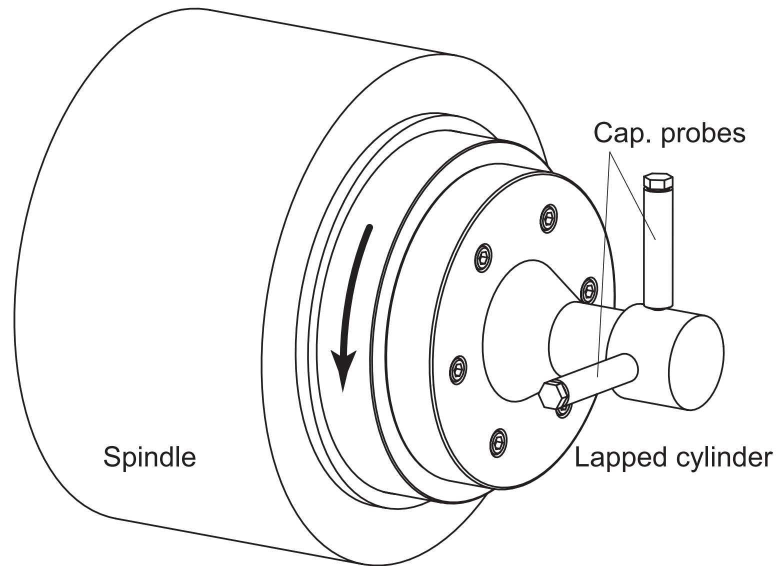

Figure 3-13. A common arrangement of spindle stator, rotor, and two capacitive displacement sensors used to measure the radial error motion of the spindle.

Figure 3-14 shows simulated results that compare the measurement results obtained using: 1) the nominal capacitive sensor calibration, 2) the corrected sensitivity for a Ø25 mm cylindrical target at high sensitivity, and 3) the actual solution. The rotating cylindrical target is eccentric with respect to the axis of rotation by 0.5 µm.

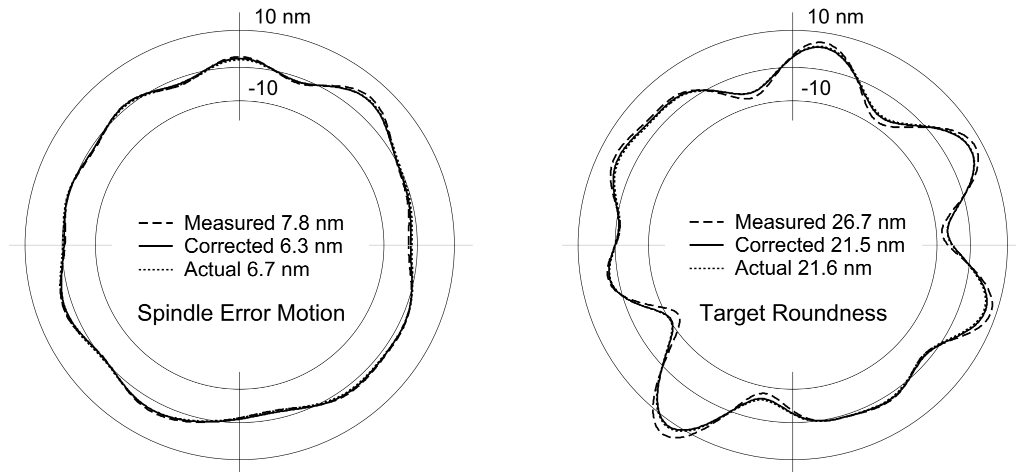

Figure 3-14. Simulated metrology of workpiece roundness and spindle radial error motion with a cylindrical Ø25 mm artifact on high sensitivity.

The simulation results demonstrate the importance of using the corrected sensitivities, which adjusted the measured values of the spindle error and roundness to within 0.4 nm and 0.1 nm of the actual values. However, errors still exist at the

extremities of the polar plot, where the nonlinearities are most significant. This accounts for the remaining discrepancy between the corrected and actual values. The effect of the nonlinear response is small compared with the improvement obtained by using the correct calibration factor, but the corrected measurements underestimated both the spindle error and roundness.

3.7 Conclusions

Commercial capacitive displacement sensors are often calibrated with flat surfaces, even though some precision manufacturing and metrology applications require displacement measurements of cylindrical targets. This common occurrence leads to four detrimental effects that become more severe as the diameter of the target reduces. First, the sensitivity of the sensing system becomes larger than the calibrated sensitivity, resulting in overstatement of measured displacements. Second, the sensing range decreases, and third, the sensing range shifts towards the target surface. Lastly, the relationship between the output voltage and the actual displacement, though highly linear for flat targets, becomes increasingly nonlinear. The nonlinearity can become important when a cylindrical artifact is eccentric with respect to an axis of rotation.

Electrostatic finite element analyses or experimental techniques like that used for verification successfully predict corrected sensitivities and nonlinear residuals. Higher gain settings, by virtue of their shorter working distances, are prone to the largest errors in gain and linearity. For the representative sensor, the FEA and experiments indicate that the error in sensitivity can be as much as 67 % and that the nonlinearity increases by an order of magnitude.

These concerns are addressable in demanding metrology applications, or in applications where alignment and calibration are critical. The calibration occurs either when a cylindrical target at known distances is used or when corrected sensitivities are applied to the post-processing of data. For all diameter cylinders, a corrected sensitivity compensates for most of the measurement error. However, for the smallest cylinders and the higher sensitivities, nonlinear terms might also be included in the correction to achieve even more accurate displacement measurements.

Copyright © Philip T. Smith Jr. 2007

4 Optimal Geometry of a Hole Probe

4.1 Introduction

A capacitance probe for measuring holes less than 1 mm in diameter tests several engineering limits. First, it requires precision engineering for the manufacturing and alignment of the completed probe. Second, as the size of the sensing area is reduced, the probe design requires sensitive electronics to measure small differences in capacitance as the probe is moved throughout the hole. Finally, the geometry of the probe and sensing area must maximize this signal for a given target surface.

This last design constraint, that of determining the size and geometry of the sensing area, lends itself to the computer modeling process. Not only can computer modeling predict the capacitance value for a given geometry, as has been shown in Chapter 2 and Chapter 3, but also the model can show how sensitive a probe design is to geometric features of the target surface. Although undulations in the target surface that are much larger than the probe area are easily measured using the output of the probe, features that are comparable in size or slightly smaller than the area of the probe are also resolvable.

The first step in designing a probe is to study the basic closed-form capacitance equations most applicable to a hole-probe. While the initial evaluation of the geometry might suggest cylindrical symmetry, in the limit as the gap d becomes small this equation can be simplified. With this simplified model, a working geometry is designed in Pro/Engineer. Because the 3D geometry of the probe is designed in one software package and the finite element solution developed in another, an efficient method of model transfer is needed. While Pro/Engineer excels at reflecting the intent of the designer, much of that information can be lost in the transfer to ANSYS. In particular it is critical to retain knowledge of the surfaces and boundary conditions, as well as the physical properties of each volume.

Two viable methods of data transfer are available between these two programs. In the first, the geometry of the model is stored in a file and recreated by ANSYS. This includes information on points, lines, areas, and volumes. Numbering for these entities is generated by ANSYS at the time of import. ANSYS is then used to mesh the file, but optimization of the mesh requires the manual addition of additional geometric

components. Because this import must occur for each change in the 3D model, it is impractical. In the second method the model is meshed using Pro/Engineer Mechanica, and only information on nodes, elements, and boundary conditions is transferred to ANSYS. Although Mechanica includes an FEA solver, electrostatic models are not supported.

Once a technique of solving the capacitance models is developed, a program is created to remove the probe geometry from the scan. When this method is applied to a single-conductor probe geometry and three different gap distances, three different surfaces result. The influence of surrounding conductors on this type of probe is significant, and varies nonlinearly with the gap distance between target and probe. Adding a guard structure produces a plot with a much steeper slope. As with previously studied geometries, the guard structure reduces the influence of nearby surface features to the point that new resolving techniques are possible.

4.2 Rough Design of Probe Geometry

The capacitance of two long cylinders has a closed-form solution from Gauss' Law, as described in Section 2.2. In Figure 2-2, two cylinders were shown to have a radial electric field between them (fringing at the end of the cylinders is ignored). For radii of a and b and a cylinder length of L, the capacitance was determined to be as shown in Eq. (2-7), rewritten in a more general form in Eq. (4-1).

$$C = \frac{\varepsilon_o \varepsilon_r 2\pi L}{\ln\left(\frac{b}{a}\right)} \tag{4-1}$$

This solution is commonly used to determine the capacitance of coaxial wires or cables. The solution is valid for any a and b, providing that the length L is sufficiently long so that fringe effects at either end of the model can be ignored.

Now consider the case where the gap distance d between the cylinder walls is small compared with the radii a and b. Rewriting the denominator of the right hand side of Eq. (4-1) by substituting the new variable d, the result is shown in Eq. (4-2).

$$\ln\left(\frac{a}{b}\right) = \ln\left(\frac{a+d}{a}\right) = \ln\left(1+\frac{d}{a}\right) \tag{4-2}$$

For the case where $d<<a$, a Taylor expansion for the natural log function is applied, shown in Eq. (4-3).

$$\ln\left(1+\frac{d}{a}\right) \approx \frac{d}{a} - \frac{1}{2}\left(\frac{d}{a}\right)^2 + \frac{1}{3}\left(\frac{d}{a}\right)^3 - \ldots \tag{4-3}$$

Substituting the first term of this expansion into Eq. (4-1), the result is as shown in Eq. (4-4).

$$C = \frac{\varepsilon_o \varepsilon_r 2\pi aL}{d} \tag{4-4}$$

From this result and the fact that the area A for the cylinder is given by $2\pi aL$, Eq. (4-4) is identical to the parallel plate approximation in Eq. (1-3). Once it is determined that Eq. (4-4) can also be used to approximate the capacitance of concentric cylindrical surfaces, each of the variables in the equation must be closely evaluated. With ε_0 fixed, a hole probe design must consider ε_r, A, and d.

To minimize the gap distance d, the optimal capacitance probe design for a small hole must be one that fits closely within the hole with only minimal clearance. As with the commercial capacitance probes such as shown in Figure 1-1, the sensing area is ideally in the same plane as the guard structure. Sharp corners are avoided as these have been shown to concentrate the electric field, not allowing for the capacitance probe output to be a true average of the target surface.

The first modification to the geometry of a commercial capacitance probe is to make the sensing area parallel or nearly parallel to the target surface. It has been shown in Chapter 2 and Chapter 3 that when the target surface differs in curvature from the sensing area that there are nontrivial changes in linearity, gain, and calibration. Since the target surface is a cylindrical wall, the sensing area will be given approximately the same curvature. This will produce an electric field that is nearly uniform across the gap.

The second modification to a commercial probe is to allow the probe to measure the walls of deep holes. This requires a mechanically stable probe base that is smaller in

diameter than the hole to be probed, and can provide electrical connection between the probe sensing area and the capacitance electronics. The most mechanically stiff configuration to fit within the confines of a cylindrical hole is a solid cylinder. Such a probe machined from a conductive material can probe a length many times longer than the diameter of the target hole.

4.3 Solid Models and Finite Element Analysis

Computer-aided studies of complex geometry often involve multiple software programs, each optimized for a particular application. This is the case for the geometry of a three-dimensional capacitance probe. For the modeling of the solid surfaces, a package such as Pro/Engineer is most suitable. Both the probe geometry and the target surface geometry can be modeled, and the resulting solids included in an assembly. The final step using Pro/Engineer is to build the geometry of the space between the solid surfaces, the "air" gap (which may also be filled with a dielectric material).

Once a solid model is defined, there are several choices of software for finite element modeling. Although Pro/Engineer contains its own finite element solution routines, an electrostatic model is not available. Since this model must be brought into a program with electrostatic finite element analysis capabilities, ANSYS is used to generate solutions. This software is capable of performing detailed capacitance calculations based on multiple solutions to an electric field problem.

The difficulty in working between two different software packages is in determining what format to use to transfer data. The two types of data export/import available between these applications are the export of geometric entities, or the export of a completed mesh. Both methods have advantages and disadvantages to the particular problem at hand, particularly when multiple models must be transferred. The export of geometric entities allows for the meshing of the model to be accomplished within the ANSYS software, which allows for control of minute details of the placement of the mesh. Unfortunately, it is necessary to know the keypoint, line, and area numbers of the different regions of the model to specify how these connect topologically. As this numbering can change if the dimensions of the model change, this method is not efficient when many sets of geometry are to be imported.

The second method of import, that of applying the mesh within the Pro/Engineer software and then exporting the nodes and elements, loses the identities of lines and areas in the process. Only the coordinates of the nodes and the list of elements are transferred to ANSYS. Furthermore, electrostatic models are not available in the current version of Pro/Engineer, and so a different element must be used. Boundary conditions must be applied in Pro/Engineer as well, as this information cannot be easily applied in ANSYS without surfaces to reference. On the positive side, the changeover from one element type to another, as well as one type of boundary condition to another, can be automated and does not depend on the exact geometry or topology of the model.

4.4 Influence of Target Surface on Probe Resolution

Once the finite element modeling method has been determined, the next step is to consider the limitations of sensing area geometries on the probe resolution. The geometry for a practical probe must satisfy both electronic and manufacturing constraints.

Standard capacitance gages of the configuration shown in Figure 1-1 have proven their ability to measure changes in the gap distance d with accuracy down to a few nanometers. What has not been determined for these devices is what surface periodicity can be resolved with such a device. A conservative estimate states that any features smaller than the area of the probe cannot be resolved, which is certainly true for a single, isolated measurement. A series of these measurements results in a 2D profile consisting of discretized measurements along the target surface, as shown in Figure 4-1. Since the capacitance gage itself can provide a continuous output as the probe passes over the surface, a great deal of information is available representing overlapping areas of the surface.

It can be shown that a capacitance gage has a spreading function when measuring a peak, analogous to the spreading function that occurs when an AFM tip scans a vertical edge, as described in Section 1.3.4. To apply this methodology, it must be determined if the capacitance gage has a fixed spreading function, or a spreading function that varies with the terrain of the surface.

To predict the output of a capacitance probe for a given hole geometry, a two-dimensional model is developed of a probe entering a half-hole. It is important to simulate the entering and exiting of the probe because the capacitance gage signal

integrates over the entire surface of the hole. By initially positioning the probe far from the hole and making measurements throughout the process of the probe entering it, it is possible to determine more details of surface features.

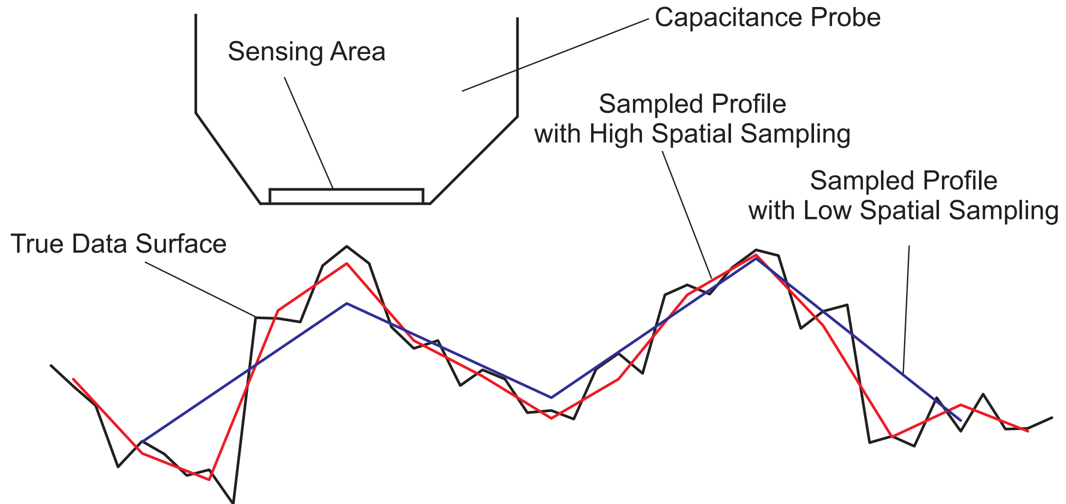

Figure 4-1. Target surface compared with stairstep approximation.

The first probe model includes only a sensing area, with no guard structure in place. This model shows the most influence from parts of the hole that are not yet directly opposite the sensing area of the probe as shown in Figure 4-2. These regions can be considered "secondary influence" areas, because they lie outside the area directly opposite the sensing area of the probe. Although they increase the capacitance sensed by the probe, because the distance is much greater the electric field is significantly reduced.

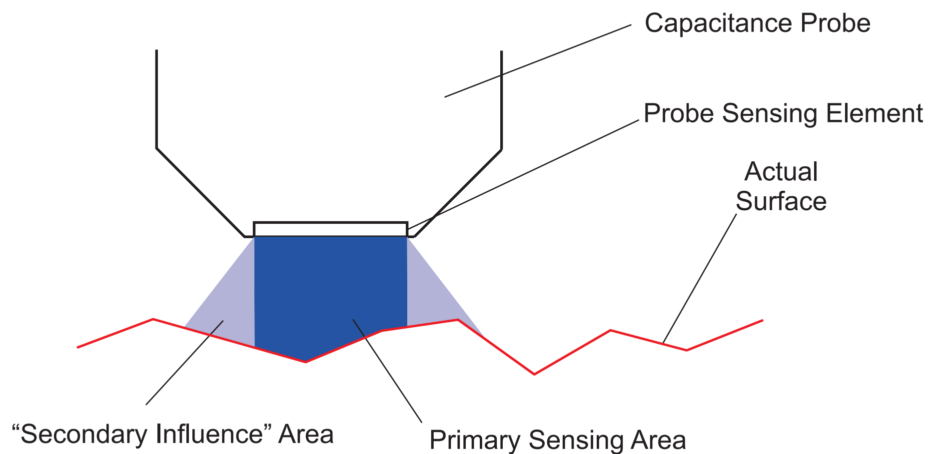

Figure 4-2. Primary and secondary contributors to capacitance.

The second two-dimensional model studied in detail includes a guard ring structure that is standard on all commercial capacitance gages. The ability of this guard structure to reduce the influence of areas outside the parallel plate approximation is shown. This model is also used to determine if various target surfaces can be numerically deconvolved after acquiring data.

Once the lateral resolution of the two-dimensional capacitance probe has been determined, the analysis needs to be extended to a full, three dimensional probe. While the half-hole target surface is useful for initial models, the full hole represents a different integration and therefore may impose a different set of limitations on the matrix deconvolution. These mathematical restrictions, in turn, affect the optimal final geometry of the probe.

Although the mathematics of the capacitance probe problem yield a resolution limit for an idealized system, the real-world performance of such a system includes other factors, such as noise, that must also be modeled. This noise limits not only the precision of an individual measurement, but it has a cumulative effect due to the integrating nature of the capacitance probe.

4.5 The Analog Nature of the Capacitance Probe Output

As with many electronic sensors, two fundamental categories exist: analog and digital. If a capacitance probe is an analog device, then certain criteria can be applied to its signal, while if a capacitance probe is inherently digital, other limitations must be considered. Capacitance probes are by themselves analog devices, but the instrumentation recording the analog signal digitally samples the probe output.

4.5.1 Analog frequency limits

The bridge circuitry described by Dratler [20] uses a lock-in amplifier to charge and discharge the plates of the sensing capacitor at a fixed frequency. The output from any bridge circuit is an analog voltage that varies continuously over a range. There are no digital artifacts present in such a signal, but there are certainly limits to the frequency performance of this analog device. Assume that a capacitance probe is swept by a surface at velocity v as shown in Figure 4-3.

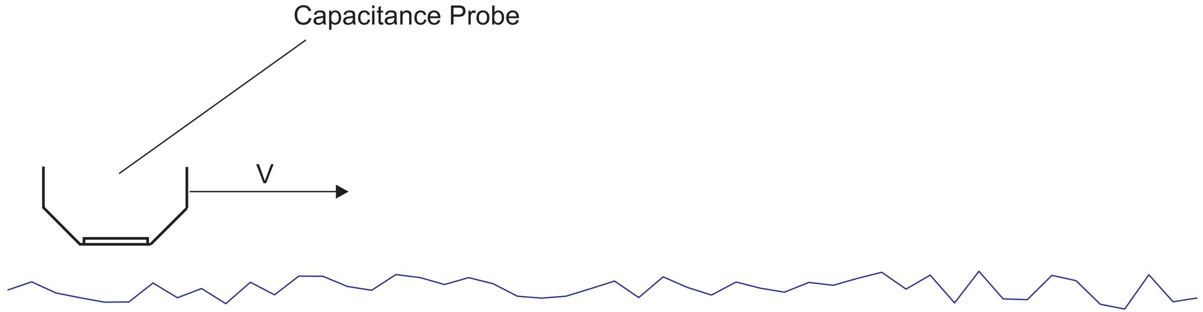

Figure 4-3. A capacitance probe sweeping past a target surface with velocity v.

If the probe is driven by frequency *f*, then there will be a Nyquist limit to the frequencies contained in the output. This Nyquist limit of *0.5f* translates to a lateral resolution shown in Eq. (4-5).

$$a = \frac{2v}{f} \tag{4-5}$$

The issue of lateral resolution of the probe itself is a separate question addressed in Section 4.6. The limit a is based solely on the scanning speed v of the probe as it passes the target surface, so to make this limit much smaller than the size of the probe itself, either the velocity v must be reduced or the frequency f must be increased.

It is important to point out that raising the frequency driving the capacitance has its own drawbacks. All of the electric field analysis in this dissertation assumes quasi-static potentials applied to surfaces. This assumption breaks down if there are strong magnetic fields present in the system, as is the case when the frequency driving the system is high. From Maxwell's Equations [99] Eq. (4-6) (Faraday's Law) is derived.

$$\nabla \times \vec{E} = -\frac{\partial \vec{B}}{\partial t} \tag{4-6}$$

This law defines how a changing magnetic field affects the electric field, and thus would adversely influence a capacitance probe. Assuming that the magnetic field is fluctuating sinusoidally with a frequency of ω, as shown in Eq. (4-7), then the frequency comes out in the partial derivative, shown in Eq. (4-8). As the frequency drops, the right hand side of Eq. (4-6) becomes vanishingly small.

$$\vec{B} = \vec{A}\cos(\omega t) \tag{4-7}$$

$$\frac{\partial \vec{B}}{\partial t} = -\vec{A}\omega\sin(\omega t) \tag{4-8}$$

Another, more qualitative way of looking at the quasi-static assumption is to consider the wavelength of the frequencies involved. For electromagnetic radiation in a vacuum, the wavelength λ is governed by Eq. (4-9), where c is the speed of light.

$$\lambda = \frac{c}{f} \tag{4-9}$$

For a frequency of 1 kHz the wavelength of radiation is 300 km, many orders of magnitude larger than the apparatus. A frequency of 1 GHz, on the other hand, has a wavelength of 30 cm, on the same scale as many experiments. As the frequency increases into the GHz range everything becomes an antenna, and the impedance of wires and other components of the system becomes critical. For this reason, the upper limit set for commercial capacitance gages is typically 20 kHz, where quasi-static assumptions are still valid.

4.5.2 Digital and quantum limits

Although the capacitance gage is itself an analog device, it is realistic to assume that the voltage output will be sampled and recorded using digital acquisition hardware. Fortunately if the sampling limits are sufficiently high, there will be no detrimental effect on the capacitance measurements due to digitization.

Digital acquisition hardware can collect data at speeds of 100 kHz or higher with a resolution of 16 bits (65,000:1). For a 10 volt signal, this translates into 153 μV per bit. For a signal that is changing rapidly, the A/D may fail to keep up, and the signal will change by many A/D counts between sampling points.

For these capacitance experiments, however, it was shown above that the analog signal has a frequency bandwidth of approximately 500 Hz (if a 1 kHz frequency is applied). Any data above that frequency is not meaningful (noise). So, for the case of the 100 kHz sampling rate, the digital Nyquist limit is some 100 times greater than the analog limit. Finally, it should be pointed out that, unlike many experiments, the capacitance

probe is not measuring a transient event. The speed *v* at which the probe is moved past the sample is set by the user. If at any time the speed of the probe begins to limit its resolution, the speed can be lowered as necessary.

Finally, for the purpose of completeness, the continuous models of small capacitances in this work are compared with the magnitude of the charge of the individual electron. In other words, the assumption that charge and therefore voltage are "continuous" is a good assumption for these cases.

Capacitances around 1 pF have been observed in many of these studies. To charge such a capacitor to 1 volt requires a charge of 10^{-12} Coulombs. The charge of an individual electron is 1.6×10^{-19} C, and so this charge represents approximately 6 million electrons. For a 16-bit A/D converter, each bit represents around 100 electrons.

4.6 Simplified Geometry and Deconvolution

The simplest model for a cylindrical capacitance probe is to model a section of cylindrical surface as it passes a target surface. Because this probe is effectively integrating over a surface area, this model will both enter and exit the target hole. Rather than rotating in a complete hole, this model will use a half hole as the target surface. By beginning the rotation far from the position of the hole, the capacitance will be several orders of magnitude smaller than what is sensed when the probe fully engages the target surface.

4.6.1 Single-conductor probe

For the initial model, a single conductor is the sensing area of the probe, as shown in Figure 4-4. In this model there are only two conductors, the half-hole target and the sensing area. From the previous examples, the finite element model is a model of the non-conductive volumes (or, for a two-dimensional model, areas) of the geometry. Boundary conditions are set for the conductive areas (lines in a two-dimensional model). For this model, the non-conductive areas are mapped using additional lines that will change as the model is changed. The area to be meshed is shown in Figure 4-5.

In Figure 4-5, the sensing area is expected to start well outside the half-hole, where there is no target surface opposite the sensing area of the probe. The simplest model would assume that the capacitance at this position is zero. On the other hand, objects of a finite size and distance always have some mutual lumped capacitance, which

are not negligible. To include the influence of the half-hole, its side wall is also part of the model. Because the electric field between these conductors must extend through the space in between (but primarily along the shortest distance), some additional geometry is added to the left side of the model so that the electric field in this area can be included in capacitance calculations.

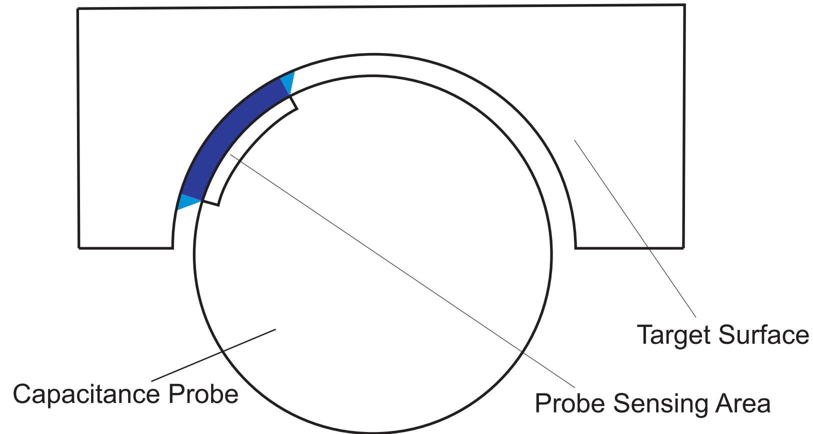

Figure 4-4. Two-dimensional model of rotating probe in a half hole.

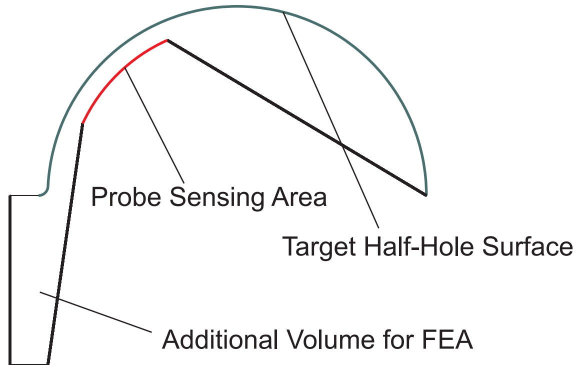

Figure 4-5. Two-dimensional model of air gap to be meshed.

As with the models described in Chapter 4, this model was generated in Pro/Engineer. The first feature created was a curve that represents the hole, with a surface that is described by Eqs. (4-10) and (4-11).

$$r = \frac{D}{2} + E_{OR} \cdot \cos(\kappa\theta) \tag{4-10}$$

$$\theta = 360t \tag{4-11}$$

These equations are programmed into Pro/Engineer and allow the surface to have a different number of sinusoidal oscillations depending on the parameter κ. The variable D is the nominal diameter of the target hole, while t is a parametric variable that varies from 0 to 1. In order to have the angle vary from 0 to 360 degrees, the new variable θ must be created. The variable E_{OR} is the amplitude of the sine wave, or the out-of-roundness specification. For these initial tests D is set to 2 and E_{OR} is set to 0, so a perfect circle is generated.

Once the hole surface is created, the sensing area is defined. The width of the sensing area is set as an angle of 40 degrees, irrespective of the radius of the probe. The position of the probe is defined as the angular position of the center of the probe. The probe is centered on the z-axis of the model (perpendicular to the page), and rotates about that same axis.

The model area shown in Figure 4-5 is created by adding connecting lines from the edge of the sensing curve to the edge of the hole model. Once this loop is closed, Pro/Engineer can create a solid model of the space between the probe and target surfaces. This model is given depth in the z-direction, even though this is not necessary for the planar analysis. To prevent an unrealistically large electric field at the corners of either the target hole or the probe, these corners are rounded with a radius of 0.05 mm.

Next, fixed-temperature boundary conditions are applied to the conductive surfaces of the model, a characteristic element size is defined, and the model is meshed using Mechanica. The nodal information is exported from Mechanica as an ANSYS file, fully ready for a heat-transfer analysis. Microsoft Word is used to modify the ANSYS script to an electrostatic analysis with capacitance calculations, and ANSYS is run in batch mode to produce a solution. To move the probe within the hole, the angular position of the centerline of the probe is modified within Pro/Engineer. Since the closed loop of the solid model is tied to this surface, the model automatically regenerates with the new dimensions. Because the topology doesn't change with each angle, there is no need to redefine the boundary conditions. However, since the geometry has changed, the model must be remeshed for each new angle. A separate ANSYS file is generated for each angle in the series, with an angular spacing between 2 and 5 degrees.

With this first model, three different probe radii of 0.80 mm, 0.90 mm, and 0.98 mm, are applied to a hole of radius 1.0 mm. The capacitance of the probe and target surface are converted into a surface profile using the parallel plate capacitance approximation of Eq. (1-3) and solving for the gap distance *d*. These surfaces are plotted in Figure 4-6. The angle of each point plotted represents the center of the probe surface, so the probe extends 20 degrees to ether side. The target surface ranges from 180 degrees to 0 degrees.

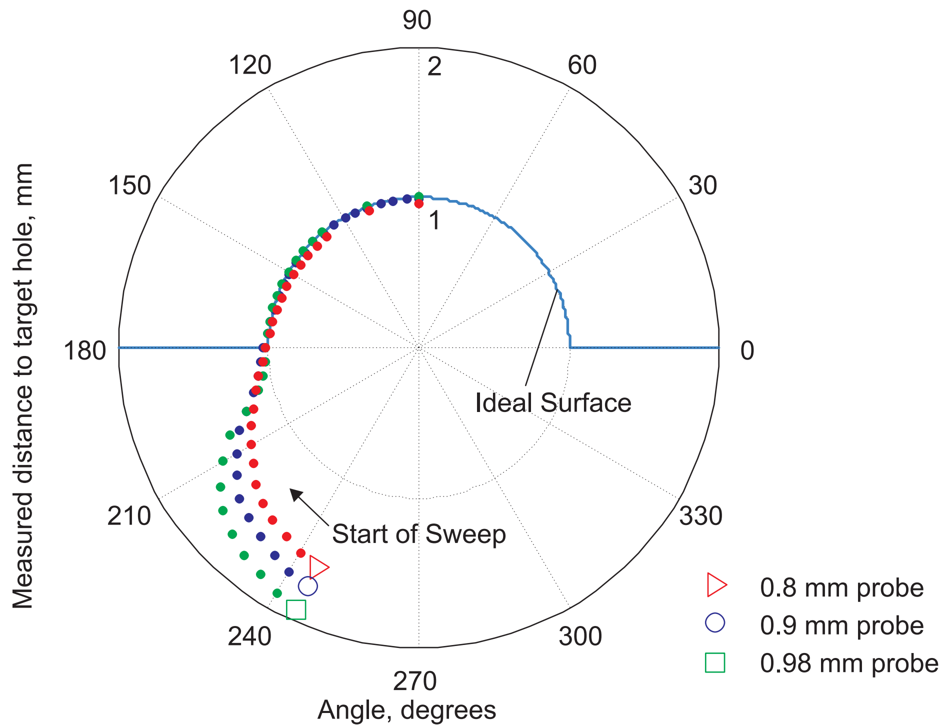

Figure 4-6. Polar plot of hole surface at three different probe diameters.

These results show that the side of the half-hole has a significant influence on the probe signal before the "shadow" of the probe intersects any of the hole surface, which begins at an angle of 200 degrees. Clearly, the parallel plate approximation is insufficient to model this part of the probe operation. In fact, it is illustrative to compare the capacitance values of the unshielded probe with the parallel plate approximation, to determine how much additional capacitance is caused by the electric field outside the "shadow" and in the "secondary influence" area. These values are shown in Table 4-1, where the FEA value is taken from the level reached when the probe has fully engaged the target surface.

The table shows that the accuracy of the parallel plate approximation improves as the probe is placed closer to the target surface. This is not to imply that the stray capacitance from outside the shadow zone has become smaller in the absolute sense. In fact, this capacitance grows as the probe is moved closer to the surface. However, the parallel plate capacitance becomes larger at a much higher rate, so that even though the stray capacitance is slightly larger, it is a much smaller percentage of the overall capacitance. This effect is also seen in the curves in Figure 4-6, where the curves rise more steeply when the target surface is closer. For this design of a capacitance probe, making the gap distance as small as possible is key to improving the linearity. It is also key to other designs and for other reasons as will be shown.

Table 4-1. FEA capacitance values compared with parallel plate approximation.

Radius of probe	*C* from FEA, pF	*C* from parallel plate, pF	Percent error
0.80 mm	0.311	0.252	23 %
0.90 mm	0.572	0.505	13 %
0.98 mm	2.61	2.524	3.2 %

A surprising feature of the data shown in Figure 4-6 is how the plots cross each other as the probe reaches a certain angle on entering or leaving the half-hole target. It at first seems that the influence of the side of the hole would always increase as the gap distance decreases. In fact this is where the curvatures of the probe and the target surface cause results that differ from a flat probe and target. This crossing of capacitance values occurs because, at a certain angle outside the half-hole, any position closer to the hole actually interferes with the electric field between the probe surface and the side of the hole.

In addition to the data in Table 4-1, the electric field between the conductors can be graphically represented in several ways. These illustrate how the field changes shape in response to the geometry of the conductors and their relative positions. One plot type supported in ANSYS is to color code the voltage potential at the different nodes, showing the shape of equipotential surfaces as the boundary between different color zones. One example of these equipotential surface is shown in Figure 3-2. For this case where the probe is rotated through the target surface, a different plot parameter is used, that of the

absolute value of the electric field strength. This field strength is the gradient of the voltage potential from the sensing area to the target surface. A series of images showing how this field strength varies with the position of the probe within a sinusoidal half-hole has been generated from ANSYS data. Several frames of this series are shown in Figure 4-7. Although the model itself is only two dimensions, the images have been given depth to assist in visualizing the strength of the electric field.

With the results for the unshielded probe complete, it is possible to apply the geometric deconvolution techniques developed for atomic force microscopy and described in Section 1.3.4. The AFM techniques assume that if a probe tip shape is well-defined, then the shape of an unknown target surface can be derived from a deconvolution of the tip shape and the raw output of the probe. Similarly, if the target surface is well-known (e.g., a test surface of known features) then the probe profile can be calculated by knowing both the raw data and the shape of the target surface.

In the case of the capacitance probe, the sensing area is not a physical surface with a definite, fixed shape, but instead the curves in Figure 4-6 are a representation of how the two surfaces interact at a distance. If a probe shape is calculated from each of these curves, the shape is different for each gap distance. Therefore, instead of a single curve representing the target surface, a family of curves is applied. If a relationship between the gap distance and the target surface is determined, only then is it possible to use a geometric deconvolution to recover the target surface (in this case, a half-hole) from the raw data.

A geometric deconvolution algorithm such as that proposed by Markiewicz and Goh [61], described in Section 1.3.4, and pictured in Figure 1-4 can be applied to this data using a Matlab script. The target surface is a known uniform height, and the output of the capacitance probe is converted to distance measurements. To generate a complete scan from the data plotted in Figure 4-6, the first half is duplicated and the order reversed. Next, the profile of the probe output is passed along the surface of the hole, and the minimum value of the two obtained. This code produces the effective profile of the probe tip.

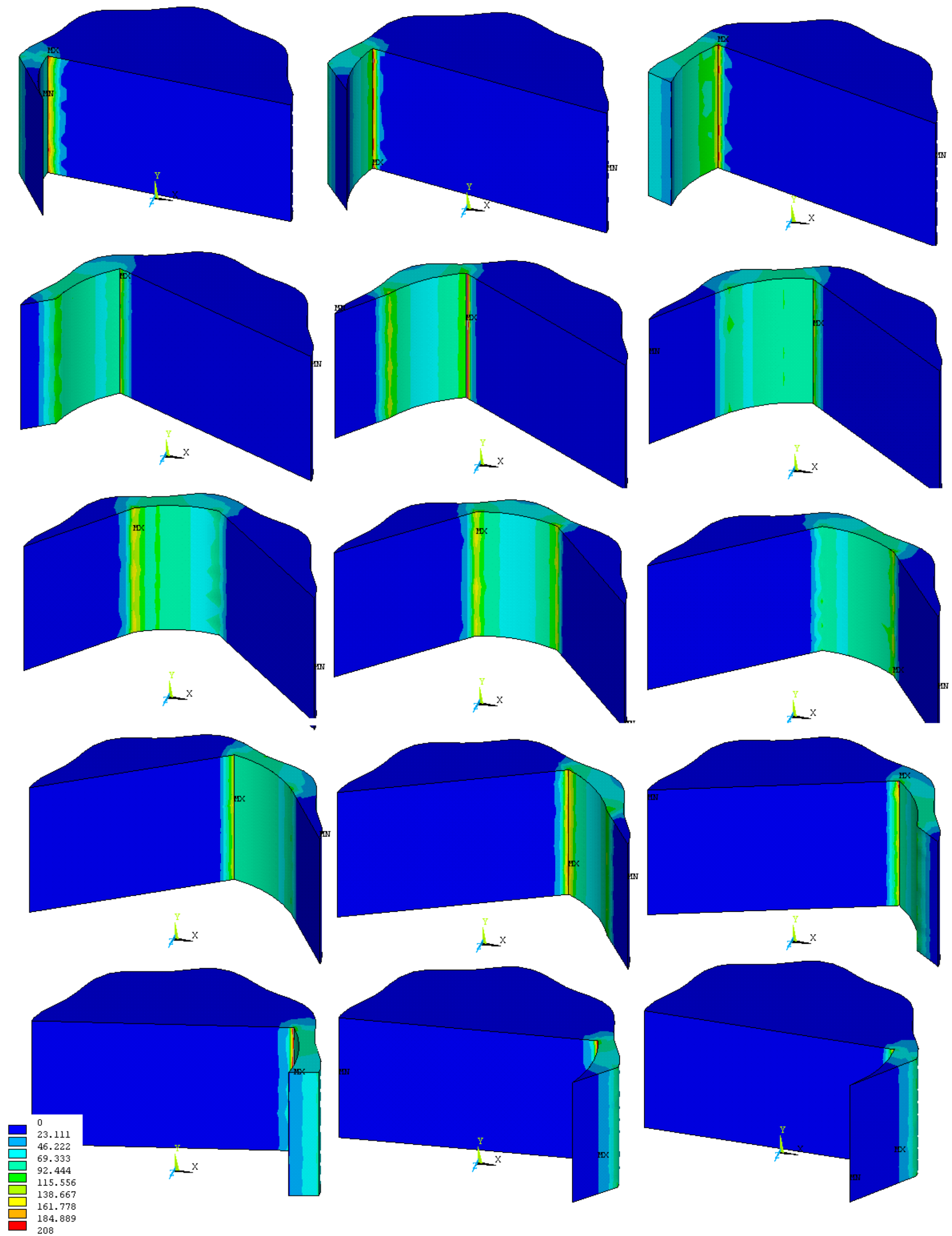

Figure 4-7. Images showing the magnitude of the electric field, in V/mm, as a function of position within a sinusoidal half-hole.

```
for n=1:length(d1)
   m=max([n-31 1]); % start point on tip1
   p=min([n+31 63]); % end point on tip1
   r=max([33-n 1]); % start point for Hole1
   s=min([95-n 63]); % end point for Hole1
   for q=m:p % range in terms of tip1
       Hole1temp=Hole1+d1pos(n);
       Hole2temp=Hole2+d2pos(n);
       Hole3temp=Hole3+d3pos(n);
       Tip1(q)=min([Tip1(q) Hole1temp(r)]);
       Tip2(q)=min([Tip2(q) Hole2temp(r)]);
       Tip3(q)=min([Tip3(q) Hole3temp(r)]);
       r=r+1;
   end
end
```

The full Matlab code is found in Appendix D, and a graphical representation is shown in Figure 4-8. The results of this processing are shown in Figure 4-9. The three different probe “shapes” are based on the 40 degree wide probe and gap distances *d* of 0.02, 0.1, and 0.2 mm. Although the height of each curve is related to the gap between probe and target surface, normalizing the curves in Figure 4-9 does not give a common shape to the probe tip. What is shown in the figure is that the probe shapes converge as the probe is moved further from the hole. In other words, the influence of the side of the half-hole is almost the same when the probe is far from entering the hole, but as the probe moves closer, the influence depends more and more on the precise spacing between probe and target surface.

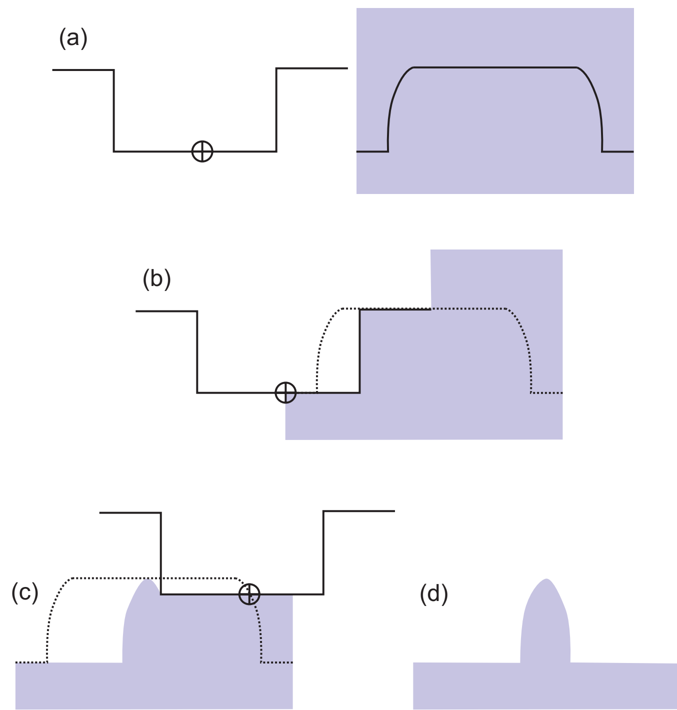

Figure 4-8. Geometric deconvolution, as applied to the probe data.

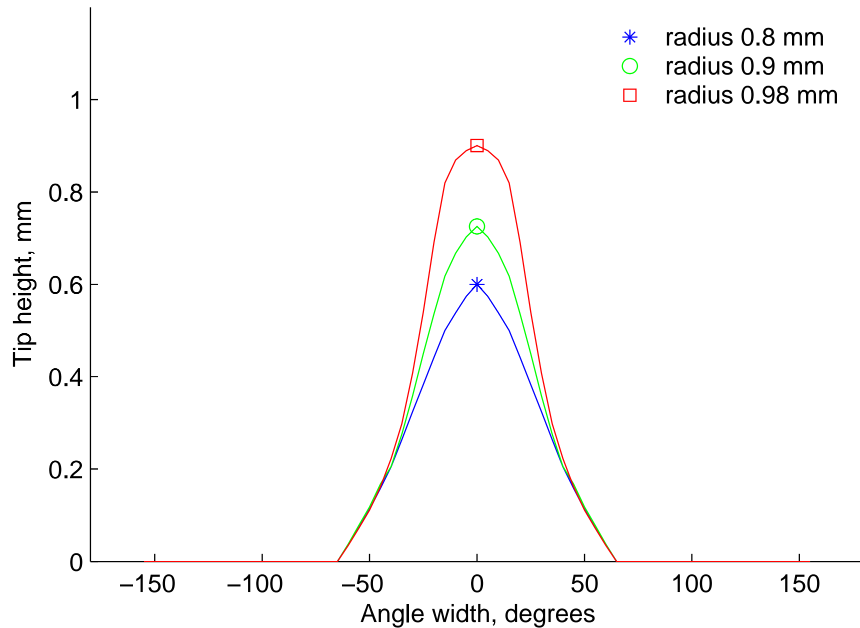

Figure 4-9. Deconvolved "probe shape" data for different gap distances.

Also, consider the shape at the center of the probe. For the smallest diameter of probe (0.8 mm), where the gap distance between probe and target is largest, the tip of the probe profile is sharpest. At the minimum gap distance of 0.98 mm, the probe profile is much more rounded. By interpolating between these curves it is possible to predict an approximate "shape" of a probe, and deconvolve the output from the probe to reconstruct the shape of the target surface. Based on prior AFM studies, these techniques are not able to resolve features smaller than the width of the probe. Instead, these techniques can be used to remove the influence of the side walls in the probe simulation, an important first step in determining the size of features that can be resolved.

4.6.2 Sensing area with guard ring

The commercial capacitance gages described in Chapter 2 and Chapter 3 incorporate a circular sensing area surrounded by a guard ring structure. This guard ring is typically set at the same voltage potential as the sensing area, but it is not itself part of the sensing circuitry. The goal of this guard ring is to reduce the size of the area of secondary influence (see Figure 4-2) as much as possible. In previous work [25], the presence of this zone in a traditional capacitance gage geometry has been shown to reduce the capacitance by restricting the electric field to an area only slightly larger than the conductive sensing area. In Chapter 2 it was shown that, for parallel surfaces, the

influence of the ring spacing *g* is more prominent for larger gap distances *d* than for smaller *d* values. In all cases, the electric field from the sensing area cannot extend beyond the inner diameter of the guard ring. For these reasons, this spacing will be minimized as much as possible.

A modified two-dimensional model of the capacitance probe is developed as shown in Figure 4-10. In this new model, two additional conductive surfaces are added to the central, sensing conductor, one leading and one trailing the sensing area. These are not two additional conductors, but rather a two-dimensional representation of a guard ring structure a distance of 0.05 mm from the sensing area. The target hole dimensions are unchanged, with the exception that the previous round radius at the entrance to the half hole has been reduced from 0.05 mm to 0.01 mm.

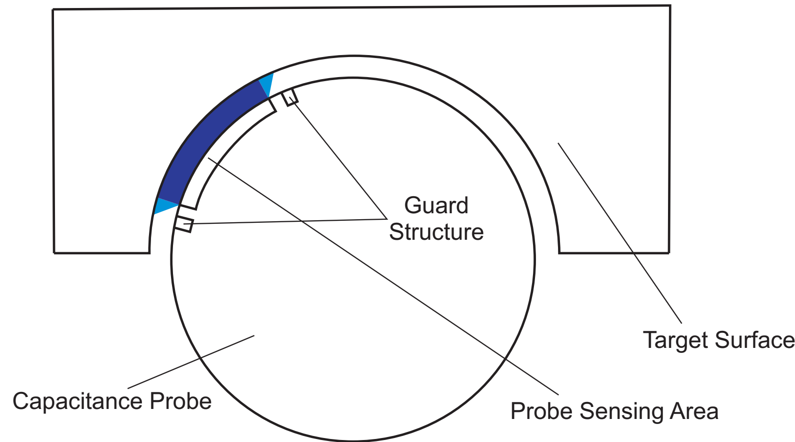

Figure 4-10. Two-dimensional capacitance probe with guard ring structures.

As with the previous model, this geometry is first built in Pro/Engineer, with the space between conductors being modeled as a solid volume. The edges of the sensing area are connected to the guard ring structures, which in turn are connected to the edges of the target surface as before. The entire area is given a depth of 0.10 mm and a volume is extruded, allowing a three-dimensional, 10-node tetrahedral element to be used. The top view of the gap volume is shown in Figure 4-11.

The steps to solve for this model are nearly identical to those for the simpler, two conductor system. Temperature boundary conditions are once again used as placeholders for the conductors, but in this case there are three different boundaries to be defined. The sensing area and target areas remain unchanged, but the guard surface areas are grouped

together as a single boundary condition and given a different temperature value from the sense or target areas. For each angular position of the probe the volume is meshed and an ANSYS file is generated. A new script in Microsoft Word replaces `TEMP` node parameters with `VOLT` conditions, and adds the commands necessary to calculate capacitance. These commands must now instruct the CMATRIX macro to calculate a three-by-three matrix of capacitance values, since this system now includes three conductors.

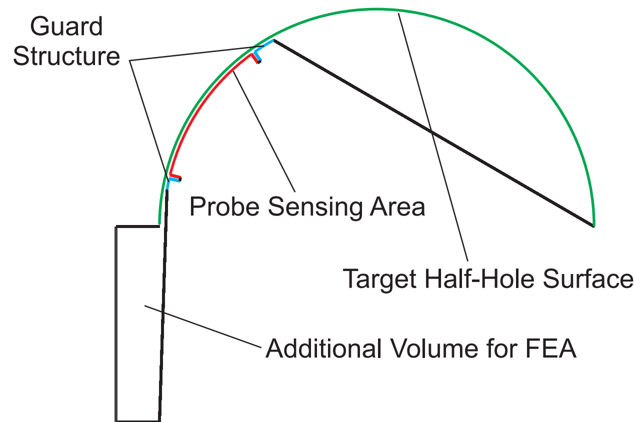

Figure 4-11. Pro/Engineer model of air gap, including guard structures.

Setting the temperature of the guard structure to a different value than the sensing area in no way changes the outcome of the capacitance calculations. While it is true that the temperature values are redefined as voltages by the Word macro, these values serve as nothing more than placeholders. Since the ANSYS file contains no information about surfaces or volumes, these fixed node values are the only way for the conductors to be differentiated from one another. In the completed ANSYS script the nodes with a common voltage are selected, then each group is named using the `cm` command. The following lines of code define the three conductors for the CMATRIX macro.

```
nsel,s,d,VOLT,5,5
cm,cond1,node
nsel,s,d,VOLT,10,10
cm,cond2,node
nsel,s,d,VOLT,15,15
cm,cond3,node
```

Once these groups of nodes are defined and named, the voltages assigned have no significance. The CMATRIX command, as described in Section 2.7, uses these group names to apply several different combinations of voltages to solve the capacitance matrix.

With the guard ring structure in place, a probe with a radius of 0.98 mm is rotated through the target surface and an ANSYS file is generated for every 5 degree increment. The capacitance values from this simulation differ markedly from the results for the same radius of 0.98 mm without a guard structure. These results are compared in the polar plot of Figure 4-12.

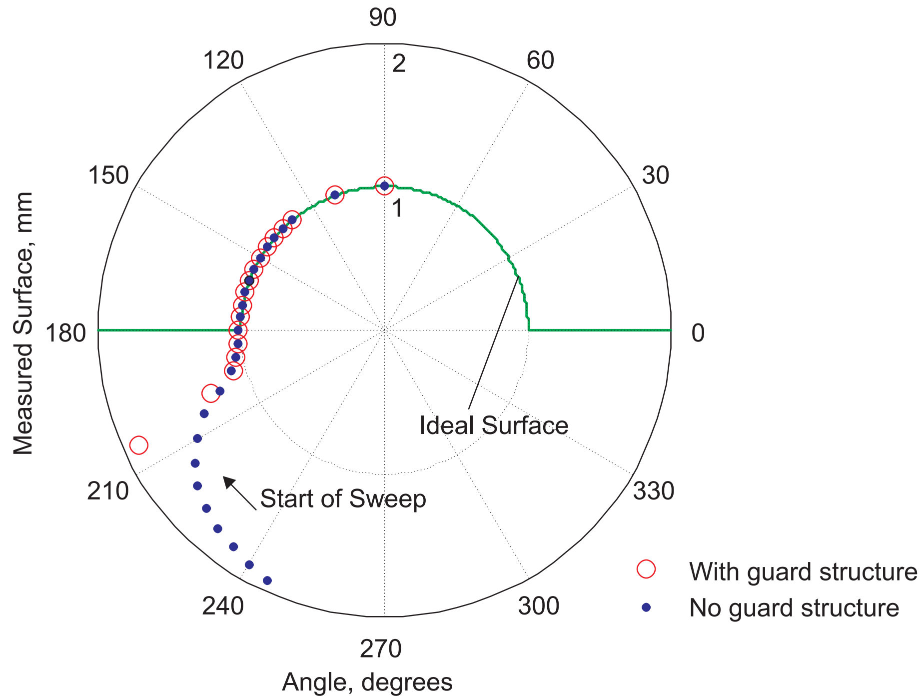

Figure 4-12. Comparison of distance measurements with and without guard structure.

From the two lines plotted in Figure 4-12 it can be seen that the capacitance gage with the guard structure has a much steeper change in sensed distance to the target surface than the probe without the guard structure. From 215 to 220 degrees, the probe with guard structure changes 0.12 mm/deg., while the probe without guard structure changes at a rate of 0.03 mm/deg over the same range. With the guard ring in place, the next step is to apply mathematical techniques to improve the resolution of the probe still further.

4.7 Conclusions

There are two methods of transferring a probe model from the Pro/Engineer software to the ANSYS software for electric field finite element analysis. The IGES format retains information about lines (edges), areas (surfaces) and volumes (solids). ANSYS scripts

based on these models must rely on the numbering of these elements, so the topology of the model must not change as different configurations are tested. Otherwise, the work of identifying the geometric elements that make up different components of the model must be redone for every import of data from Pro/Engineer. Since hundreds of different geometric configurations are to be tried, automation of the import steps is key. Unfortunately, in tests with the same Pro/Engineer model it has been determined that small changes to the relative geometry of the probe and the target surface result in changes to the topology. Because these changes prevent automation, the IGES type of data import is not practical.

The second type of data transfer is to export ANSYS code directly from Pro/Engineer. This code contains information about nodes, elements, and boundary conditions, but no information about the overall geometry of the model. Although this code is compatible with current versions of ANSYS, because Pro/Engineer cannot generate electrostatic problems directly the code must first be modified. These modifications are, fortunately, irrespective of the exact geometry of the components. The intermediate step of modifying the code is therefore automatic, and the completed ANSYS code can be executed in batch mode. With this model the data files are somewhat larger, and the burden of creating a suitable mesh is transferred from ANSYS to Pro/Engineer. Nevertheless, this type of import offers many practical advantages, and so it is this method that is applied as different probe geometries are studied.

To determine how the sensed area of the target compares with the sensing area of the probe, a simplified, two-dimensional model of the sensing area was modeled in Pro/Engineer. The first models consisted of only a sensing area and half-hole target surface. A half-hole is used so that the details of the probe entering and exiting the target surface can also be measured. These surfaces are assigned boundary conditions in Pro/Engineer, and many different geometric orientations are meshed and exported to ANSYS.

A study was done to determine if the probe can be considered a convolution of the width of the probe and the width of the target surface. A geometric deconvolution method was able to approximately recover the original surface, at the resolution of the probe itself. A second probe model included the guard ring structures that are commonly

applied in modern capacitance probes. The presence of these guard structures sharply limits the influence of surfaces outside the area directly opposite the sensing area of the probe. This further validates the use of the parallel plate approximation for analyzing these systems.

Copyright © Philip T. Smith Jr. 2007

5 Capacitive Deconvolution of Probe Designs

5.1 Introduction

It has been demonstrated that the capacitance sensed by a capacitance probe is primarily a function of the surface directly opposite the sensing area. Of secondary importance is the target surface in the immediate vicinity of this primary area. In the case of an unshielded sensor, this secondary influence is substantial. When a guard ring structure is added, there is a significant reduction in this influence.

To increase the resolving power of a capacitance probe still further, a method of “capacitive deconvolution” is derived to separate the probe area and the target surface. This method depends on the near-parallel nature of the electric field between the surfaces, and uses a matrix solution. The simplest two-dimensional case is presented of a smooth surface, followed by a smooth surface with a step in the center. The new deconvolution method is able to recreate this step. The final two-dimensional test case is of a sinusoidally varying target. This surface was also recreated, even though the sensor width was larger than the wavelength of the oscillation. A second probe geometry was also passed through these test cases, and finally the three-dimensional extension to this method is discussed. The three-dimensional sinusoidal test case was also successfully deconvolved.

5.2 Integral Model of Probe Overlap

To determine if a probe can resolve features smaller than its sensing area, a new approach is taken. First, a mathematical model is proposed, and capacitance solutions from FEA are compared to this idealized model. From the basic parallel plate capacitance formulation from Eq. (1-3), consider a fixed gap distance *d*, and changing area *A*. The capacitance is then considered an integration over all incremental areas *dA* to produce the capacitance shown in Eq. (5-1).

$$C = \int_{dA} \frac{\varepsilon_0 \varepsilon_R dA}{d} \tag{5-1}$$

This integration technique is first applied to the flat, two-dimensional case shown in Figure 5-1. The probe surface is opposite two different target areas at distances d_1 and d_2. If an integration is performed over the whole target area of the probe, and it is

assumed that the electric field is uniform and parallel in each of the two sections, then the integral in Eq. (5-1) becomes the two separate integrals shown in Eq. (5-2), which are easily integrated for constant values of *A* and *d*.

$$C = \int_{dA_1} \frac{\varepsilon_0 \varepsilon_R dA_1}{d_1} + \int_{dA_2} \frac{\varepsilon_0 \varepsilon_R dA_2}{d_2} = \varepsilon_0 \varepsilon_R \left(\frac{A_1}{d_1} + \frac{A_2}{d_2} \right) \tag{5-2}$$

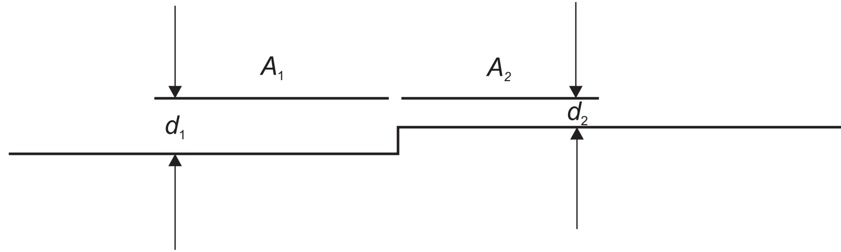

Figure 5-1. Integrating over two probe areas.

From this result, areas with a smaller gap *d* create a larger contribution to the capacitance value *C*. In fact, if the distance d_1 is made much larger than d_2, it is reasonable to begin to ignore the contribution of the first term of Eq. (5-2) and only consider the second. In this case, the only area that contributes to the capacitance is A_2, so the capacitance becomes linear as a function of the overlapping area. This is the basis for the design of certain capacitance gages, as described by Lion [100].

To consider the validity of these arguments, the data from the model shown in Figure 4-11 is unwrapped to a Cartesian form and the capacitance is plotted as a function of the rotation angle of the probe. This new curve is plotted in Figure 5-2. Also plotted in the same figure is a line that represents the integration of Eq. (5-1) over the intersection of sensing area and target surface. When the two areas are not overlapping, in the idealized curve the capacitance is zero.

The data from the capacitance simulation in Figure 5-2 agrees with the ideal case, indicating that this integral model is a good first approximation for calculating capacitance as a function of angle for the shielded probe. It is important to note that the approximation is better when the majority of the probe has entered the target hole, and worse when little or none of the probe is opposite the target. This can be explained by considering the first term in Eq. (5-2), which this approximation considers negligible. Although there is no surface parallel to the section of the probe that is outside the hole

itself, the half-hole has a side wall that is at the same potential as the target surface. In a real system, this "sidewall" interacts with the exposed area of the probe, contributing to the capacitance of the system of sensing area and target hole. When the *second* term of Eq. (5-2) is small, then this contribution of the first term is not negligible. As the probe enters the hole, the second term increases and at the same time the area outside the hole becomes smaller, so that the two curves in Figure 5-2 differ only by 0.5 percent once the probe has completely entered the hole. The error due to this "sidewall" interaction and why it can be subtracted from the system is discussed in Section 5.6.3.

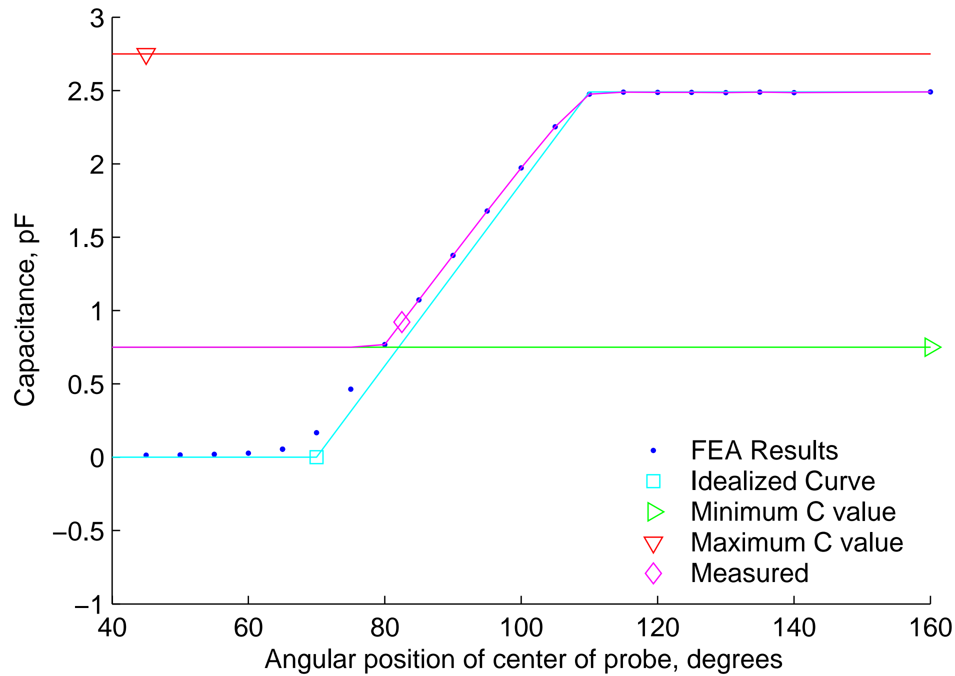

Figure 5-2. Plot of capacitance as a function of entrance angle.

As described previously, the signal from the capacitance probe is analog, but electronics downstream subsample the voltage output. One example of this averaging occurs when the limitations of the capacitance electronics are applied to the simulated data in Figure 5-2. Although the simulation can easily provide results that, in this case, range from 0.01 to 2.5 pF, the electronics will have a lower and upper bound of active and continuous sensing. Continuous sensing is important because the capacitance probe is integrating over the target surface. If part of the probe capacitance is unavailable due to saturation of the electronics, the data can no longer be deconvolved. This is true whether the system electronics are linear with capacitance, linear with gap distance *d*, or

logarithmic as a function of either parameter. In Figure 5-2, lower and upper sensing limits of 0.75 pF and 2.75 pF are also included. If the electronics are limited to this range, the capacitance signal must lie inside these limits, as shown by the 'Measured' curve.

It is vital that the maximum capacitance of the probe and target not exceed the measurable capacitance of the electronics. It is also important to note that this peak level is a function of the average gap distance *d* between probe sensing area and target surface. This upper electronic limit therefore indicates the smallest diameter of hole that can be measured with a probe of a given size.

Consider the minimum measurable capacitance (C_{min}). When the capacitance is below this level, the sensing electronics will read zero. The system is therefore not able to give any indication of the nature of the hole surface until the capacitance is above C_{min}. Call the initial point of entry of the leading edge of the probe into the hole s_0, and the position of the leading edge of the sensing area when the capacitance reaches the sensible level C_{min} as s_1. This position is diagrammed as part (a) in Figure 5-3. The integral equation for the capacitance C_{min} is shown in Eq. (5-3). The conclusion is that, due to the limitations of the probe electronics, no detailed information can be determined about the target surface from s_0 to s_1. Only an average distance *d* can be determined from the known area. After the leading edge of the sensing area passes position s_1, the signal from the probe is now continuous and on-scale, so some information on the target surface can be deduced.

$$C_{\min} = \int_{s_0}^{s_1} \frac{\varepsilon_0 \varepsilon_R dA}{d} \tag{5-3}$$

$$C = \int_{s_0}^{s_2} \frac{\varepsilon_0 \varepsilon_R dA}{d} = C_{\min} + \int_{s_1}^{s_2} \frac{\varepsilon_0 \varepsilon_R dA}{d} \tag{5-4}$$

At a later time, when the probe has reached a point s_2 as shown in part (b) of Figure 5-3, the capacitance is now approximated by Eq. (5-4). As indicated by the diagram, the trailing edge of the probe has not yet entered the hole.

At the moment where the trailing edge of the sensing area enters the hole, the integral in Eq. (5-4) is no longer a valid approximation. At the position shown in part (c) of Figure 5-3, the capacitance probe no longer covers the complete area from s_0 to s_1.

Since no detailed knowledge of this surface is possible, there is no way to calculate the contribution of new surface to the integral. Only after the trailing edge of the probe passes s_1 does the C_{min} term drops out of the equation.

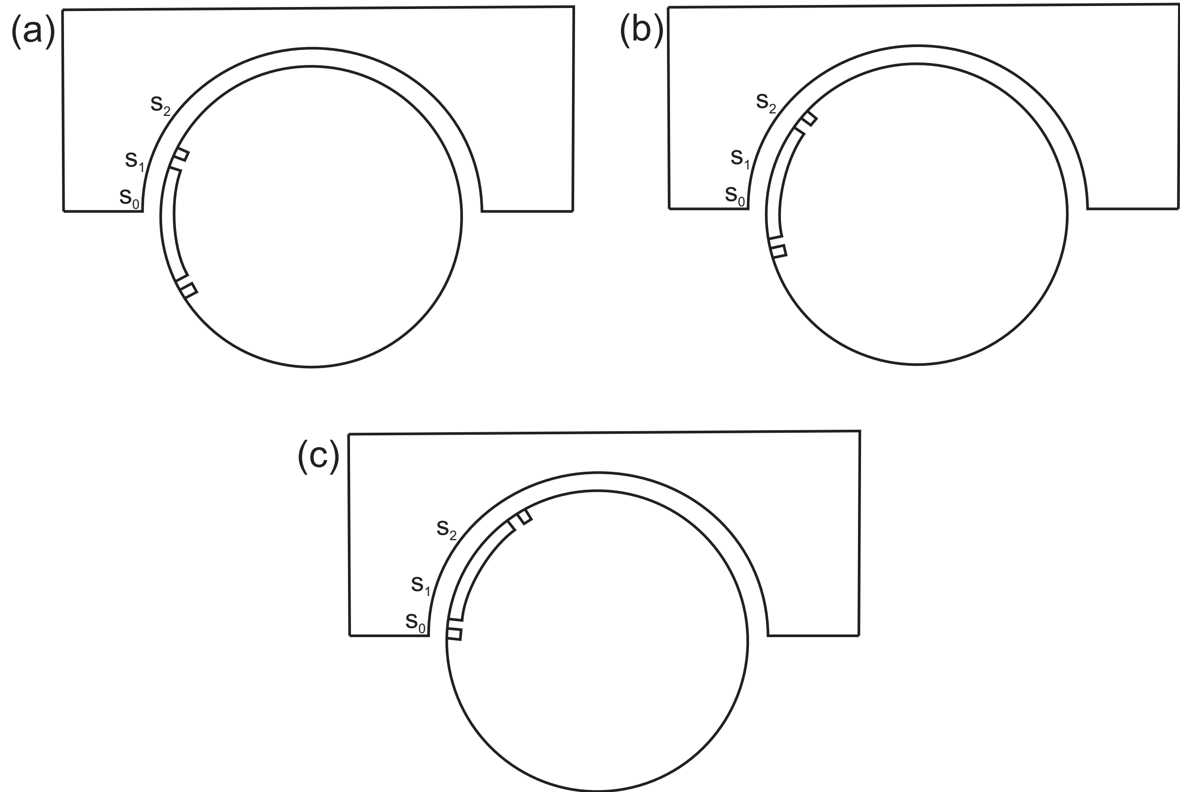

Figure 5-3. Capacitance probe reaching sensible level (a), passing through additional range (b), and after trailing edge has entered target surface (c).

5.3 Approaches to the C_{min} Limitation

There are various ways to increase the range of the capacitance sensing electronics, including the use of a logarithmic amplifier. While this approach increases the range, there still remains a fixed C_{min}. There are two possible integral approaches to this problem, depending on the range of the sensing electronics and the depth of the hole to be probed. In the first approach, the integral form is rewritten as a sum of finite surface areas, where the smallest detectable area becomes the basis of each measurement. In the second approach, a new probe geometry is introduced that increases resolving power, but requires a larger active electronic range.

5.3.1 Indexing method of deconvolution

This method of deconvolving the data is best described by use of an example. Consider the half-hole surface shown in Figure 5-4 (a). This half-hole is divided into 8 zones for the purposes of this example. The width of these zones is such that $C_{\min}$ is reached when the probe surface has overlapped the target surface by area A_0. The probe surface is equal to $3A_0$, again for the purposes of illustration.

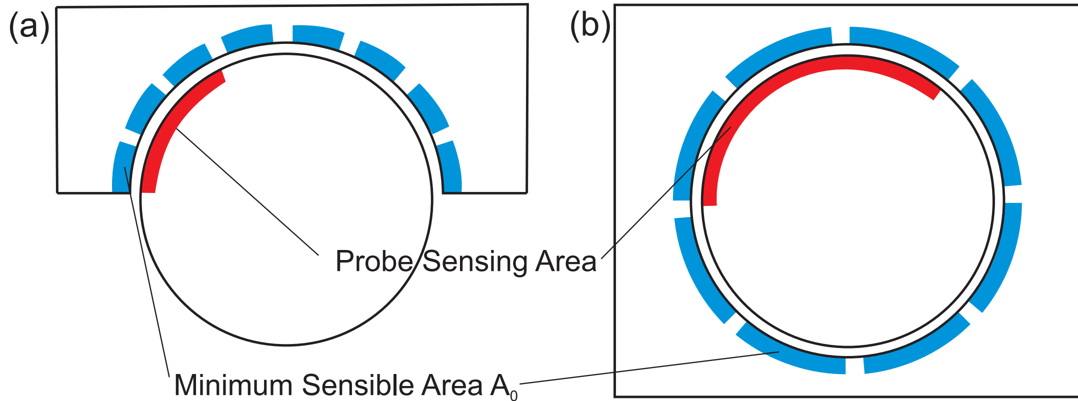

Figure 5-4. Half-hole (a) and complete hole (b), each divided into 8 zones.

Since it has been stated that a capacitance below the value $C_{\min}$ cannot be sensed, in this approach the target surface is divided into equal regions with approximately this capacitance value. The integral formulation of Eq. (5-1) thus becomes a finite sum of a series of small areas. If the capacitance gage is intersecting three areas, then the sum appears as shown in Eq. (5-5).

$$C = \int_{dA_1} \frac{\varepsilon_0 \varepsilon_R dA_1}{d_1} + \int_{dA_2} \frac{\varepsilon_0 \varepsilon_R dA_2}{d_2} + \int_{dA_3} \frac{\varepsilon_0 \varepsilon_R dA_3}{d_3} = C_1 + C_2 + C_3 \tag{5-5}$$

These small subcapacitances are named C_1, C_2, etc., over all the zones of the target surface, and the measured capacitances are named $C_{\text{meas}1}$, $C_{\text{meas}2}$, etc. The first four equations for these sums can now be written out, as shown in Eqs. (5-6) through (5-9).

$$C_{meas1} = C_1 \tag{5-6}$$

$$C_{meas2} = C_1 + C_2 \tag{5-7}$$

$$C_{meas3} = C_1 + C_2 + C_3 \tag{5-8}$$

$$C_{meas4} = C_2 + C_3 + C_4 \tag{5-9}$$

As can be seen from the pattern, each capacitance measurement in this example contains up to three subcapacitances, measured when the probe overlaps those zones precisely. The total number of equations over the half hole of Figure 5-4 (a) is 10 in this case, two shorter ones as shown in Eqs. (5-6) and (5-7), six that contain three terms, and two shorter equations at the end of the process.

The next step in this formulation is to write these equations in matrix form. Note that although these equations are solved for C_{meas1}, C_{meas2}, etc., the unknowns are of course the subcapacitances C_1, C_2, etc. There are ten equations and only eight unknowns, which can be written in matrix form as shown in Eq. (5-10). The matrix equation is rewritten in Eq. (5-11).

It is important to note that the width of the probe need not be an integer multiple of the area needed to achieve C_{min}. This approach can be generalized for any ratio that is a rational number larger than 1. If, for example, the probe area is 2.5 times the area needed for C_{min}, the ratio 5/2 is used to construct a new matrix. Because the denominator of this ratio is 2, the hole is divided into n segments, where the capacitance of each segment is $C_{min}/2$. To achieve the level C_{min}, the first equation in the matrix form now requires two terms. When the entire surface of the probe is completely enclosed by the half-hole, five terms will be added together to generate the measured capacitance. A portion of this matrix is shown in Eq. (5-12).

$$\begin{bmatrix} 1 & 0 & 0 & 0 & 0 & 0 & 0 & 0 \\ 1 & 1 & 0 & 0 & 0 & 0 & 0 & 0 \\ 1 & 1 & 1 & 0 & 0 & 0 & 0 & 0 \\ 0 & 1 & 1 & 1 & 0 & 0 & 0 & 0 \\ 0 & 0 & 1 & 1 & 1 & 0 & 0 & 0 \\ 0 & 0 & 0 & 1 & 1 & 1 & 0 & 0 \\ 0 & 0 & 0 & 0 & 1 & 1 & 1 & 0 \\ 0 & 0 & 0 & 0 & 0 & 1 & 1 & 1 \\ 0 & 0 & 0 & 0 & 0 & 0 & 1 & 1 \\ 0 & 0 & 0 & 0 & 0 & 0 & 0 & 1 \end{bmatrix} \begin{bmatrix} C_1 \\ C_2 \\ C_3 \\ C_4 \\ C_5 \\ C_6 \\ C_7 \\ C_8 \end{bmatrix} = \begin{bmatrix} C_{meas1} \\ C_{meas2} \\ C_{meas3} \\ C_{meas4} \\ C_{meas5} \\ C_{meas6} \\ C_{meas7} \\ C_{meas8} \\ C_{meas9} \\ C_{meas10} \end{bmatrix} \tag{5-10}$$

$$[\mathbf{D}][\mathbf{C_n}] = [\mathbf{C_{meas}}] \tag{5-11}$$

$$\begin{bmatrix} 1 & 1 & 0 & 0 & 0 & 0 & & \\ 1 & 1 & 1 & 0 & 0 & 0 & & \\ 1 & 1 & 1 & 1 & 0 & 0 & & \\ 1 & 1 & 1 & 1 & 1 & 0 & . & . \\ 0 & 1 & 1 & 1 & 1 & 1 & & \\ 0 & 0 & 1 & 1 & 1 & 1 & & \\ & & & . & & & & \\ & & & . & & & & \end{bmatrix} \begin{bmatrix} C_1 \\ C_2 \\ C_3 \\ . \\ . \\ . \\ C_n \end{bmatrix} = \begin{bmatrix} C_{meas1} \\ C_{meas2} \\ C_{meas3} \\ C_{meas4} \\ C_{meas5} \\ . \\ . \\ . \\ C_{meas(n+3)} \end{bmatrix} \tag{5-12}$$

The general case can be extrapolated from these examples. If the ratio of capacitance probe area to minimum sensible area is k/m and the target surface is broken into n segments where each segment has capacitance $C_{\min}/m$, the resulting matrix will have n columns and $n+k-2m+1$ rows. This can be checked for both the initial example above, where k=3, m=1, and n=8, as well as for the case where the ratio is 1/1, in which case the matrix is reduced to the identity matrix **[I]**.

The solution to a rectangular matrix, where the number of equations exceeds the number of variables, is possible through the use of a least-squares solver. Such a solver finds the best-fit solution for the variables in **[C$_n$]** given the equations in **[D]**. The linear solver built into Matlab is called by the command `Cn=lsqlin(D,Cmeas).`

This matrix method solves for the individual segments C_n from the larger capacitances C_{meas}. These segments are at the limit of the capacitance circuitry C_{min}, for the two-dimensional case of a half-hole. Now it is time to examine how this method holds up in the case of a complete hole, as shown in part (b) of Figure 5-4. Once again the hole is divided into 8 segments, and the probe overlaps three of these segments at a time. In this case it is not possible for the probe to intersect less than three segments, so the matrix for this system looks like Eq. (5-13). Since these equations are linearly independent, this particular square matrix can be inverted directly to solve for C_1, C_2, etc.

Some matrices for a closed hole, however, cannot be inverted. This is the case when the hole area is an integer multiple of the area of the probe. The matrix for a probe consisting of 2 segments is shown in Eq. (5-14). This square matrix has no inverse

because the rows are not linearly independent. For this probe additional information is needed to solve for the C_n values.

$$\begin{bmatrix} 1 & 1 & 0 & 0 & 0 & 0 & 0 & 1 \\ 1 & 1 & 1 & 0 & 0 & 0 & 0 & 0 \\ 0 & 1 & 1 & 1 & 0 & 0 & 0 & 0 \\ 0 & 0 & 1 & 1 & 1 & 0 & 0 & 0 \\ 0 & 0 & 0 & 1 & 1 & 1 & 0 & 0 \\ 0 & 0 & 0 & 0 & 1 & 1 & 1 & 0 \\ 0 & 0 & 0 & 0 & 0 & 1 & 1 & 1 \\ 1 & 0 & 0 & 0 & 0 & 0 & 1 & 1 \end{bmatrix} \begin{bmatrix} C_1 \\ C_2 \\ C_3 \\ C_4 \\ C_5 \\ C_6 \\ C_7 \\ C_8 \end{bmatrix} = \begin{bmatrix} C_{meas1} \\ C_{meas2} \\ C_{meas3} \\ C_{meas4} \\ C_{meas5} \\ C_{meas6} \\ C_{meas7} \\ C_{meas8} \end{bmatrix} \tag{5-13}$$

$$\begin{bmatrix} 1 & 0 & 0 & 0 & 0 & 0 & 0 & 1 \\ 1 & 1 & 0 & 0 & 0 & 0 & 0 & 0 \\ 0 & 1 & 1 & 0 & 0 & 0 & 0 & 0 \\ 0 & 0 & 1 & 1 & 0 & 0 & 0 & 0 \\ 0 & 0 & 0 & 1 & 1 & 0 & 0 & 0 \\ 0 & 0 & 0 & 0 & 1 & 1 & 0 & 0 \\ 0 & 0 & 0 & 0 & 0 & 1 & 1 & 0 \\ 0 & 0 & 0 & 0 & 0 & 0 & 1 & 1 \end{bmatrix} [\mathbf{C_n}] = [\mathbf{C_{meas}}] \tag{5-14}$$

While this methodology seems inadequate to take into account the variations in an actual target surface, it is straightforward to add factors to account for the secondary regions of influence. When different target surfaces are addressed, additional terms are added that reflect the subtle influence of capacitance areas beyond the primary zone.

The above method describes a numerical manipulation that allows a larger probe area to determine smaller surface features than the area of the probe itself. Theoretically, the area resolution that can be obtained is several times smaller than the area of the probe. This begs the question, why not simply make the probe with this smaller area and avoid the mathematics altogether? There are three key reasons why the application of this mathematics, while adding complexity, offers an improvement over a simple, small area probe with no deconvolution.

The first reason why the probe is not simply manufactured to a certain minimum area is because the area varies considerably. It depends on the gap distance d between the

probe sensing area and the target surface. Recalling the definition of C_{min} in Eq. (5-3), for a fixed C_{min} the minimum area A varies linearly with the gap distance d. Consider a hole with a nominal gap distance d, but that actually has a maximum gap distance $2d$. If the probe area is only large enough to provide a signal at a distance d, then an entirely new probe would have to be made; either with a larger area or a different diameter. For a probe whose area A and nominal distance d provide a capacitance several times larger than C_{min}, unexpected changes in the gap distance d can be resolved after the measurement is complete. In postprocessing the number of divisions in the hole surface is changed, and the corresponding matrix is applied.

The second reason why the above method is superior to a small probe lies in the manufacturability of the probe. At any time there exists a limit to the size of the sensing area that can be accurately and repeatably measured. This deconvolution method provides for a resolution limit that is not strictly dependent on the size that can be manufactured. As will be seen in Chapter 6, several factors in the manufacturing process affect the size of the final sensing area, so although the approximate size can be predicted, there is some variability in the final area. Finally, there is variability in the radius of the probe as well, where small changes can have a large effect on the capacitance. The margins allowed by the mathematical process provide a greater yield of useable probes.

The final reason why a probe is not simply manufactured to match a minimum electronic limit is because the electronic limits are subject to change. When new equipment or changes to existing systems lower the minimum detectible capacitance C_{min}, the mathematics can take immediate advantage of this improvement. Manufacturing a new probe to a new specification, on the other hand, is time-intensive and often requires several iterations to achieve success. The method proposed above is capable of optimizing the resolution output of a given probe to the limits of a given electronic system without having to match electronics and probe precisely.

5.3.2 Continuous slot probe

The matrix approach favors a probe design where the sensing area is a few times larger than the minimum area (for a given gap distance) that can be sensed by the electronics. The matrix mathematics then deconvolves this data to determine the distance d for each minimum area segment. The resulting data points are evenly spaced around the perimeter

of the target hole. The sensing area for such a probe can either be a square or rectangular area on the side of the cylindrical probe.

A second geometry offers a possible improvement to the matrix approach, but with two distinct drawbacks. Recall from Eq. (5-4) how the integral for capacitance was broken into a fixed value, C_{min}, and an additional integral representing an incremental increase in capacitance as the probe sensing area further overlaps the target surface. This incremental increase can be subdivided into very small units, but once the trailing edge of the probe begins to enter the hole, it will be impossible to maintain these subdivisions. One solution to this difficulty is to consider a probe with a sensing area that is larger, in one dimension, than the size of the hole. Under these conditions, the trailing edge of the probe never encounters the entrance to the hole, so the integral that comprises C_{min} need never be subdivided.

This probe design is best described by previewing the geometry for a three-dimensional scan of the target hole. Consider a cylindrical hole of a small diameter passing entirely through a plate of conductive material. The probe can scan the hole using several possible paths, but consider for the moment that the probe enters the hole moving in the z direction (i.e., along the axis of the hole) without rotating. If the sensing area is small and square or rectangular, the overlap of sensing area is very similar to the half-hole case described in Section 4.6. In this example, the area of overlap A is a steadily increasing ramp that eventually reaches a measurable capacitance C_{min}, from which point data can be collected continuously. This design is pictured in part (a) of Figure 5-5. Since the sensing area is shorter in the z-axis direction than the hole itself, the trailing edge of the probe will eventually enter the hole, with the same consequences as the two-dimensional case.

Now consider the long, narrow slot design of Figure 5-5 (b). Here the slot is longer than the hole itself. As the probe enters the hole there will be a period where the capacitance is below C_{min} and so the electronics will be offscale. Once sufficient surface is encountered, however, this area remains part of the integral throughout the measurement. Figure 5-6 shows the two probes at the same position midway through the hole. For the rectangular sensing area in part (a), the capacitance integral ranges from s_2 to s_3. Because s_2 falls in the range between s_0 and s_1 there is once again not enough data

to deconvolve this integral and solve for C_{rect}, as shown in Eq. (5-15). For the long probe shown in part (b), the integral will always begin at s_0, and so the C_{min} term can always be separated out, as shown in Eq. (5-16).

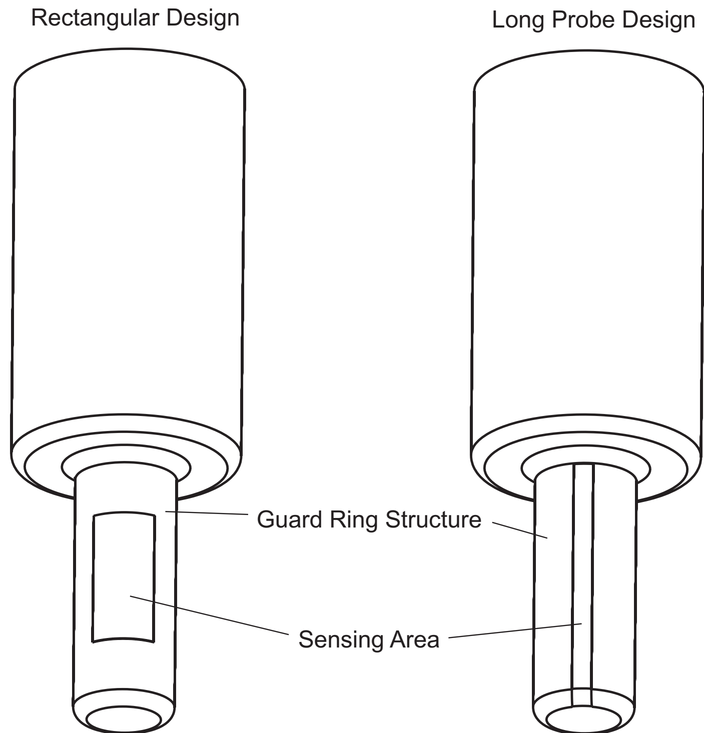

Figure 5-5. Two different three-dimensional probe designs.

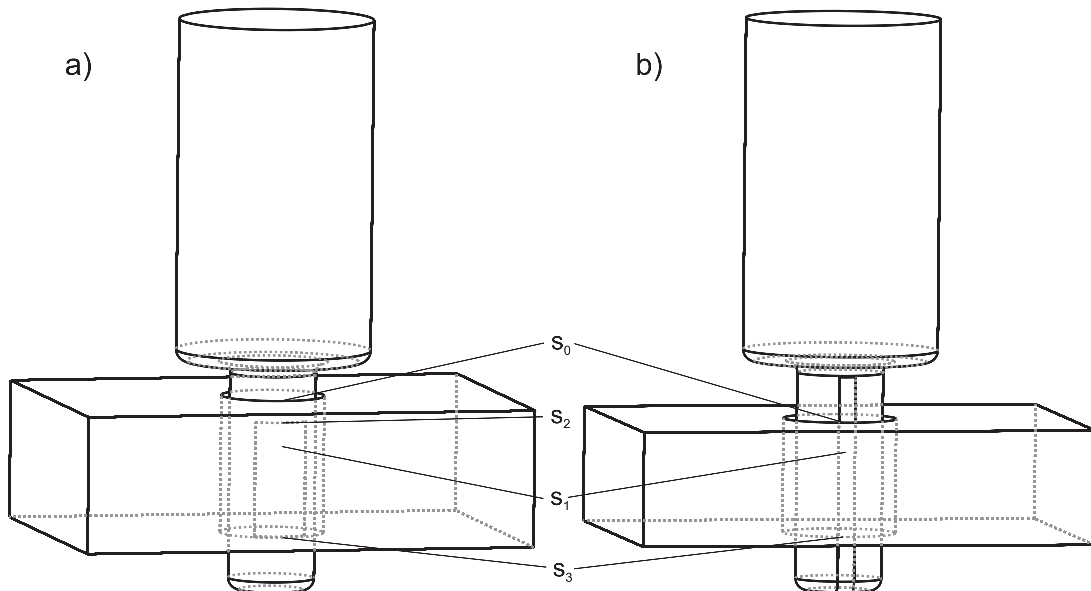

Figure 5-6. Cross section of two probe designs midway through hole.

$$C_{rect} = \int_{s_2}^{s_3} \frac{\varepsilon_0 \varepsilon_R dA}{d} = \int_{s_2}^{s_1} \frac{\varepsilon_0 \varepsilon_R dA}{d} + \int_{s_1}^{s_3} \frac{\varepsilon_0 \varepsilon_R dA}{d} \tag{5-15}$$

$$C_{long} = \int_{s_0}^{s_3} \frac{\varepsilon_0 \varepsilon_R dA}{d} = C_{\min} + \int_{s_1}^{s_3} \frac{\varepsilon_0 \varepsilon_R dA}{d} \tag{5-16}$$

This method thus allows a much smaller incremental area, once the threshold $C_{\min}$ has been reached. The first section of the hole (s_0 to s_1) is condensed to a single data point, but beyond this point the resolution can be much finer. The probe from Figure 5-6 (b) is reduced to the two-dimensional Pro/Engineer model in Figure 5-7, including the guard structure and additional lines necessary to enclose the model. As long as the electronics remain on-scale, the remainder of the hole can be measured to a high level of precision.

To contrast with the indexing method, the matrix representation of the long probe data is an ever-increasing sum, shown in Eq. (5-17). To prevent the minimum capacitance value $C_{\min}$ from becoming confused with C_1, the subsequent capacitances are numbered from C_2 onward. Since in this method the number of measurements beyond $C_{\min}$ is the same as the number of regions, the matrix will always be square and precisely of the form shown in Eq. (5-17). Only the number of rows will change. This square matrix can be inverted to determine how noise affects the result; noise considerations are discussed in Section 5.6.

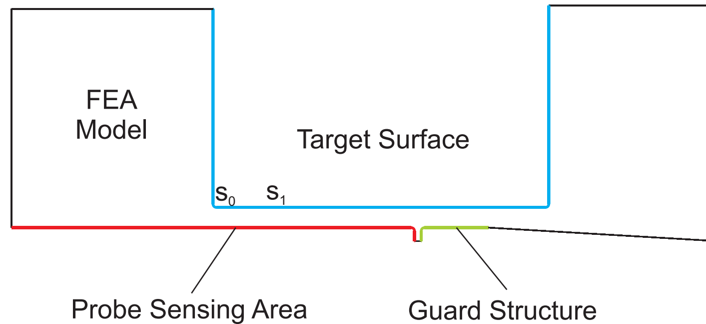

Figure 5-7. Pro/Engineer model of long probe geometry.

$$\begin{bmatrix} 1 & 0 & 0 & 0 & 0 & 0 & 0 & 0 \\ 1 & 1 & 0 & 0 & 0 & 0 & 0 & 0 \\ 1 & 1 & 1 & 0 & 0 & 0 & 0 & 0 \\ 1 & 1 & 1 & 1 & 0 & 0 & 0 & 0 \\ 1 & 1 & 1 & 1 & 1 & 0 & 0 & 0 \\ 1 & 1 & 1 & 1 & 1 & 1 & 0 & 0 \\ 1 & 1 & 1 & 1 & 1 & 1 & 1 & 0 \\ 1 & 1 & 1 & 1 & 1 & 1 & 1 & 1 \end{bmatrix} \begin{bmatrix} C_2 \\ C_3 \\ C_4 \\ C_5 \\ C_6 \\ C_7 \\ C_8 \\ C_9 \end{bmatrix} = \begin{bmatrix} C_{meas1} \\ C_{meas2} \\ C_{meas3} \\ C_{meas4} \\ C_{meas5} \\ C_{meas6} \\ C_{meas7} \\ C_{meas8} \end{bmatrix} - C_{\min} \begin{bmatrix} 1 \\ 1 \\ 1 \\ 1 \\ 1 \\ 1 \\ 1 \\ 1 \end{bmatrix} \qquad (5\text{-}17)$$

The model of a flat target surface from Figure 5-7 has been solved as the probe is moved past the target surface. As with the cylindrical model, the capacitance is shown to be approximately linear with the overlap distance. Unlike the cylindrical case, however, the data increases through the entire length of the hole. The results from this model are shown in Figure 5-8, along with the theoretical curve based on the parallel-plate capacitance equation. These curves have an almost identical slope, with an offset capacitance caused by the interaction of the probe surface and the perpendicular wall of the target hole. This discrepancy can be accounted for by adding a correction factor to the rightmost term of Eq. (5-17).

As mentioned before, there are limits to this method from an experimental standpoint. The first and most important limit is that most electronic systems have only a finite and somewhat limited range of capacitances between the minimum measurable value and the maximum measurable value. The long probe method assumes that the active range has no upper limit, a serious deficiency from an experimental standpoint.

A second limit is whether a long, narrow probe geometry can be manufactured. This ability depends on the nature of both the coating and etching process, including whether the coating is sufficiently uniform so that a long area can be removed, and whether the removal process can be applied to those area dimensions. Because the area of sensing must be longer than the hole itself, this probe geometry limits the depth of hole that can be probed. Since it proves simpler to etch a small hole on a long probe rather than etch a long slot on the same probe, the rectangular sensing area ultimately allows for a longer hole to be measured.

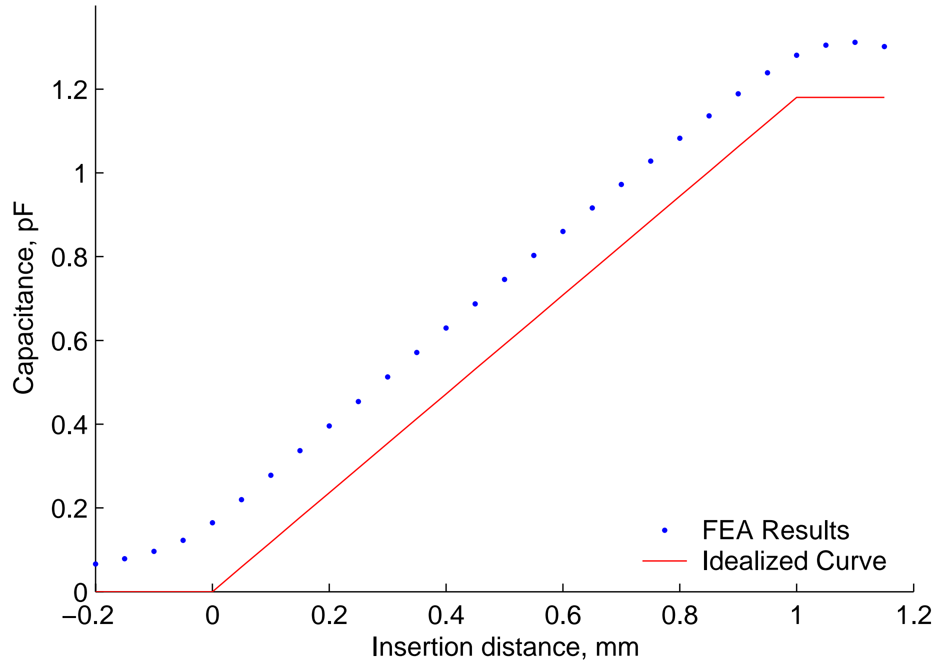

Figure 5-8. Long probe capacitance results.

From the standpoint of finite element simulations, the resolution of this method is likely to be limited to the element size and step size that are applied to the model. If a nonuniform surfaces cannot be reconstructed beyond a certain level, either the limits of finite element modeling have been reached, or the deconvolution method cannot resolve the features.

Finally, it is important to understand how errors might propagate through the mathematics of these matrix solutions. Some noise sources include the resolution of the sensing electronics, errors in probe positioning, and nonuniformities in the probe surface or geometry. Some of these errors are discussed in Section 5.6.

5.4 Deconvolution of Nonuniform Surfaces

Once the capacitive deconvolution method has been simulated for cases of uniform target surfaces, this method can be applied to other geometries to determine their limitations. These simulations can in turn be used to further refine the matrix methods used to solve for the profile of the target surface.

The assumptions made about the electric field between the sensing area of the probe and the target surface is that the field is uniform and perpendicular to the surface. This assumption is valid for cases where the target surface is uniform, but of course the

purpose of the capacitance probe is to determine nonuniformities. When a sharp edge is present, the electric field lines necessarily emanate from the side of this edge. In close proximity to an edge or step, a different approach must be used. To determine how these “leading” or “lagging” errors might be corrected, the first nonuniform target surface simulated is a step function. The height of the step function is set to the sensing range of the capacitance gage, so that the step ranges from the minimum gap distance to the maximum gap distance. In this way, changes on a smaller scale can be interpolated from the data.

Once the matrix methods have been refined somewhat, it is time to simulate a sinusoidal hole surface. Such a surface will indicate whether features of a given size can be measured with a capacitance gage. At the first stage of the analysis the features remain two-dimensional. The probe is swept past this surface, and the measurements before and after deconvolution are compared to the known original. The error is then compared with expected limitations of the finite element method.

5.4.1 Step function simulation and deconvolution

Up to this point, the target surfaces for these convolution studies have been uniformly curved or uniformly flat. This is a good starting point, but the ultimate goal of the capacitance probe is to accurately show the profile of a real, and therefore imperfect, surface. It is therefore necessary to model a test shape or shapes that will give insight into the functioning of the probe. The first such simple shape is a step.

A step function inserts a single discontinuity between otherwise smooth surfaces. It has been seen that the rectangular probe design reaches a very flat plateau (see Figure 5-2) once the entire probe has entered the half-hole target. By adding a step midway through the hole, the effect on the probe output can be isolated from the effects of entering and exiting the half-hole. In this test case, the radius of the hole is stepped from 1.00 mm down to 0.96 mm halfway through the hole. The probe diameter is 0.94 mm. This is a good approximation of the active range of many capacitance sensors. This new geometry is built into Pro/Engineer, and a volume is created of the gap between sensor and target surface. The resulting volume is shown in Figure 5-9.

With the step taking place halfway through the hole, the symmetry in the system that existed for earlier models is lost. This simulation requires a complete pass through

the target hole, where the position of the leading edge ranges from -30 degrees to 230 degrees. As before, the mesh is generated by the Mechanica module of Pro/Engineer, with three temperature boundary conditions applied to the three conductors. The mesh is exported to an ANSYS file, which is modified to an electrostatic model and then solved by ANSYS running in batch mode. As before, this data is plotted on a polar plot as calculated gap distance *d* in Figure 5-10. Unwrapping this plot to a Cartesian space and plotting the capacitance as a function of centerline position of the probe, the result is shown in Figure 5-11.

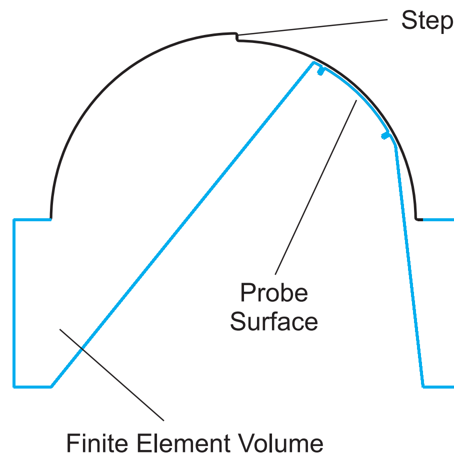

Figure 5-9. Finite element model of half-hole including step.

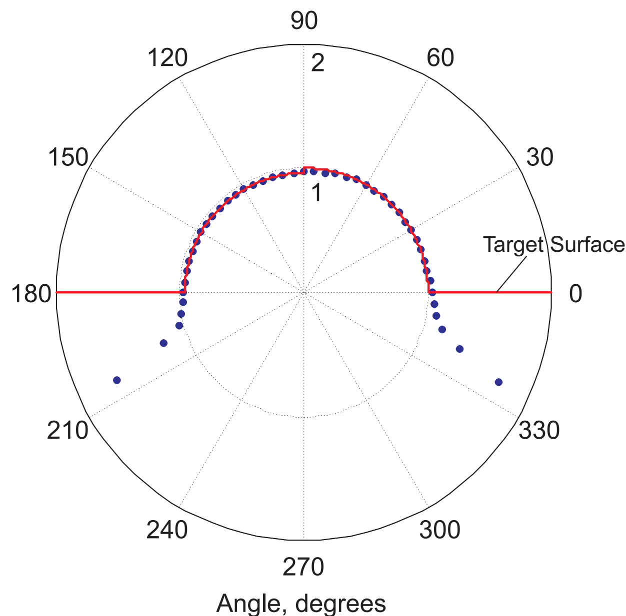

Figure 5-10. Polar plot of surface for step test as a function of centerline position of probe.

By unwrapping the plot and changing the plotted variable to capacitance, it can be seen that the slope of the initial entrance is again highly linear with only slight rounding at the endpoints. The Cartesian plot also shows more clearly the largely linear slope down from one radius value to the other. Recalling Eq. (5-2), where the capacitance is a function of two areas opposite targets that are at two different distances, the constraint of Eq. (5-19) is added. This states that the area of the probe is the sum of these areas, and rearranging the variables results in Eq. (5-20). The first term of this equation is constant, and the slope of the second term depends on the rate of change of A_2 as well as the relative values of d_1 and d_2. In the example, as the probe rotates clockwise in the hole the rate of A_2 is increasing. As the distance d_2 is smaller than d_1, the capacitance increases at a steady rate. Calculating the average slope from the finite element results produces a value of 0.0387 pF/degree, in excellent agreement with the theoretical value of 0.0387 pF/degree.

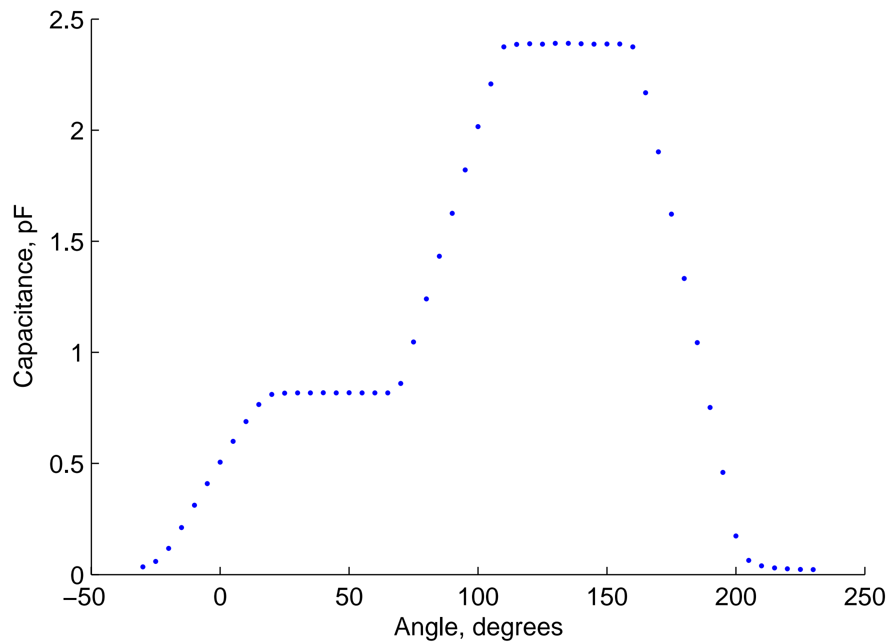

Figure 5-11. Plot of capacitance as a function of centerline position.

$$C = \varepsilon_0 \varepsilon_R \left(\frac{A_1}{d_1} + \frac{A_2}{d_2} \right) \tag{5-18}$$

$$A_{probe} = A_1 + A_2 \tag{5-19}$$

$$C = \frac{\varepsilon_0 \varepsilon_r}{d_1 d_2}\left[d_2 A_{probe} + (d_1 - d_2) A_2\right] \tag{5-20}$$

The deconvolved distance measurements from the rectangular probe are plotted, along with the physical width of the probe for comparison, in Figure 5-12. While the slope of the step function has been reproduced in the graph, there is some cost in the accuracy of the measurement at the longer distance. This is the roughness seen on the left of the figure.

As with the rectangular probe, the long probe design can be run through a similar step function to produce a plot of capacitance as a function of probe overlap. The results of this capacitance plot are shown in Figure 5-13. The change in distance, which occurs at a position of 0.5 mm along the surface, is reflected in a change in the overall slope of the plot. A better way to represent this data is by looking at the derivative of the data, in other words the slope of the line. It would be expected that, for this simple integral model of the capacitance of the probe, the overlapping area dA can be replaced with the width w times the incremental length dx. With these substitutions and the notation that d is a function of position x as well, the result is Eq. (5-21).

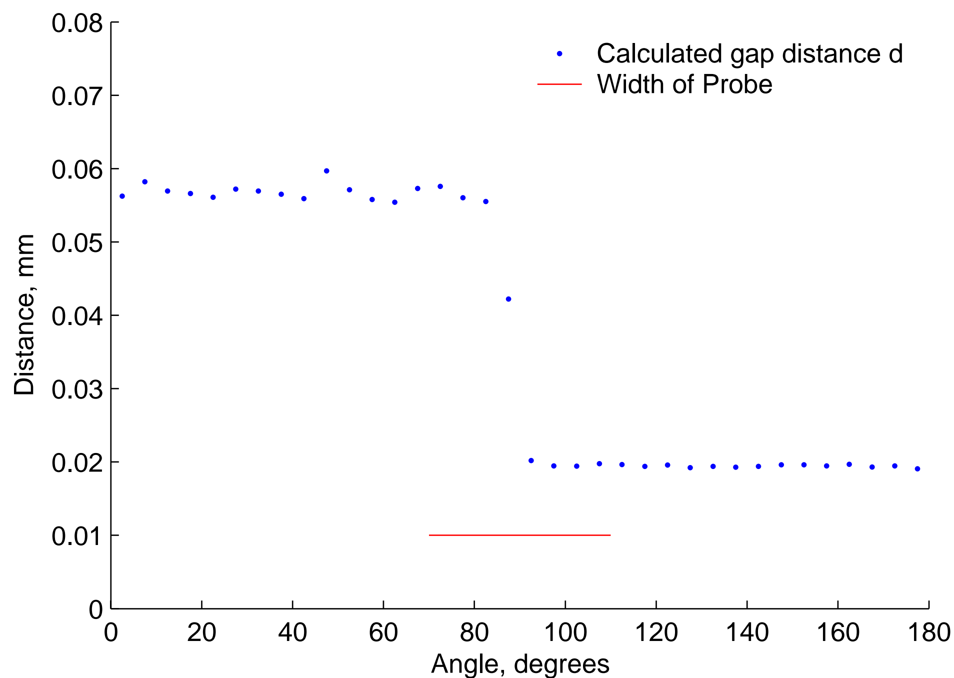

Figure 5-12. Deconvolved distance from rectangular probe and width of probe.

Because the data resulting from either finite element modeling (as in this case) or from experimental measurements are ultimately measured over a finite interval Δx, the finite change in capacitance ΔC from one measurement to the next can be rewritten in terms of the change in linear displacement Δx. The gap distance d is assumed to be constant over this short interval, with the result as shown in Eq. (5-22). Calculation of gap distance d from the data in Figure 5-13 results in the plot in Figure 5-14.

$$\frac{\partial C_{long}}{\partial x} = \frac{\partial}{\partial x}\int \frac{\varepsilon_0 \varepsilon_R dA}{d(x)} = \frac{\partial}{\partial x}\int_{x_0}^{x_1} \frac{\varepsilon_0 \varepsilon_R w dx}{d(x)} \tag{5-21}$$

$$\Delta C = \int_{x_0}^{x_0+\Delta x} \frac{\varepsilon_0 \varepsilon_R w dx}{d(x)} = \frac{\varepsilon_0 \varepsilon_R w \Delta x}{d(x_0)} \tag{5-22}$$

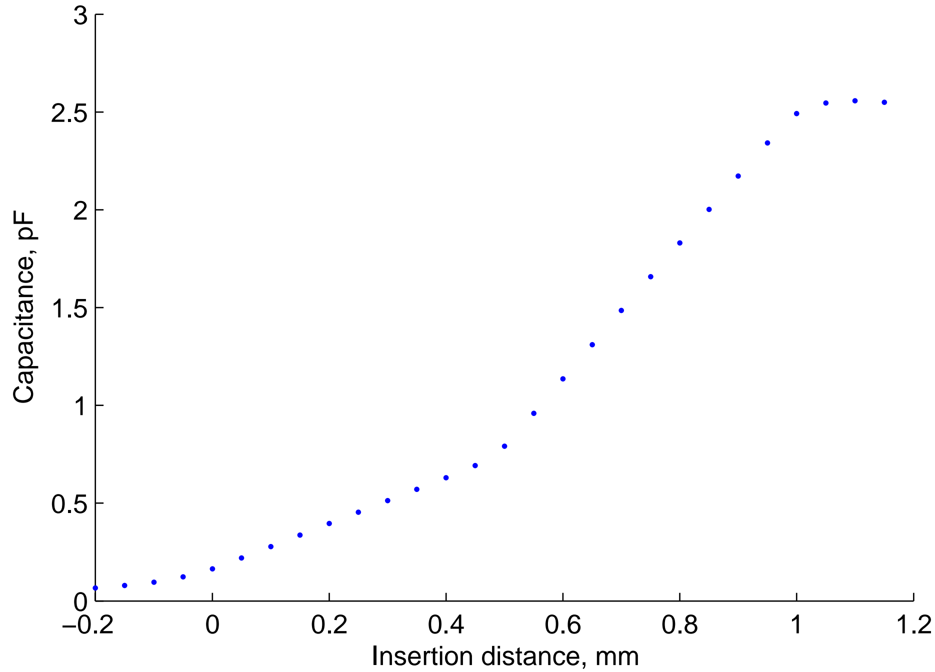

Figure 5-13. Long probe raw results for step function.

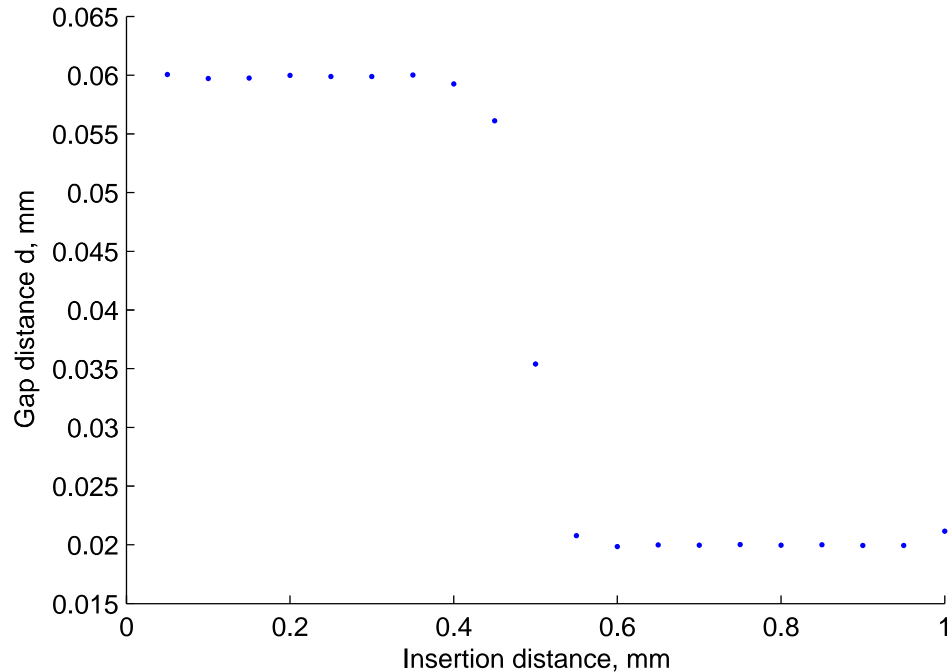

Figure 5-14. Slope of long probe FEA results showing change in gap distance *d*.

As can be seen from Figure 5-13, the slope of the probe changes quickly at the point where the step occurs in the target surface. Equation (5-22) predicts that this slope will change instantaneously as this transition is encountered. As described before, there exist at least two limitations to having a completely instantaneous step from one distance to the other.

The first limitation has to do with the resolution of the finite element approximation. The elements in this model span a length on the order of 0.040 mm, so these elements have difficulty measuring a sudden change in electric field strength. The second limitation is that the electric field is not truly parallel at the transition point between one level and the other. One electric field solution for this problem can be examined in detail by applying voltages to the probe sensing area and to the target surface and using the ANSYS `solve` command to produce a nodal solution. The resulting electric field lines in the area of interest are as shown in Figure 5-15.

This figure shows that electric field emanates from the side of the step to the section of the probe just to the left of where the transition occurs. This effect means that the probe can sense the transition before it is precisely opposite the step. This appeared before in Figure 4-7 on a larger scale, where the probe is able to sense the entrance to the

hole before the leading edge is opposite the entrance to the hole. Because this edge is smaller, the corresponding effect is smaller but still present, in both the rectangular probe design and the long sense area design.

The data plotted in Figure 5-14 and Figure 5-11 as well as the electric field plotted in Figure 5-15 show that the probe is able to sense the approaching step up before it is encountered. In the case of Figure 5-11 the mirror image of this plot can be considered, where the probe rotates counterclockwise through the same hole. This is possible because, although the hole is not symmetric, the leading and the trailing edge of the probe have the same shape. Since the electric field is considered static in all of these simulations, the direction of probe rotation is immaterial, only the position dictates the level of capacitance sensed. In the case of counterclockwise rotation, the probe is sensing the step up *after* it has passed out of that region. Not only is there a "leading" effect, but for the rectangular probe at least there is also a "lagging" effect to the presence of a step.

It is possible to quantify this effect and add this to the matrix solution methods, pushing the model beyond the parallel plate approximation to include the complexity due to surface features. In particular, terms need to be added that indicate influence by surfaces that have not yet been encountered. Returning to the matrix formulation in Eq. (5-13) for a rectangular probe, small δ factors are added to the matrix showing where the capacitance is influenced. This matrix is shown in Eq. (5-23). These factors indicate that, for example, if the probe surface is opposite C_3, C_4, and C_5, then the probe can also be influenced by the capacitance of C_2 or C_6.

$$\begin{bmatrix} 1 & 1 & \delta & 0 & 0 & 0 & \delta & 1 \\ 1 & 1 & 1 & \delta & 0 & 0 & 0 & 0 \\ \delta & 1 & 1 & 1 & \delta & 0 & 0 & 0 \\ 0 & \delta & 1 & 1 & 1 & \delta & 0 & 0 \\ 0 & 0 & \delta & 1 & 1 & 1 & \delta & 0 \\ 0 & 0 & 0 & \delta & 1 & 1 & 1 & \delta \\ 0 & 0 & 0 & 0 & \delta & 1 & 1 & 1 \\ 1 & \delta & 0 & 0 & 0 & \delta & 1 & 1 \end{bmatrix} \begin{bmatrix} C_1 \\ C_2 \\ C_3 \\ C_4 \\ C_5 \\ C_6 \\ C_7 \\ C_8 \end{bmatrix} = \begin{bmatrix} C_{meas1} \\ C_{meas2} \\ C_{meas3} \\ C_{meas4} \\ C_{meas5} \\ C_{meas6} \\ C_{meas7} \\ C_{meas8} \end{bmatrix} \tag{5-23}$$

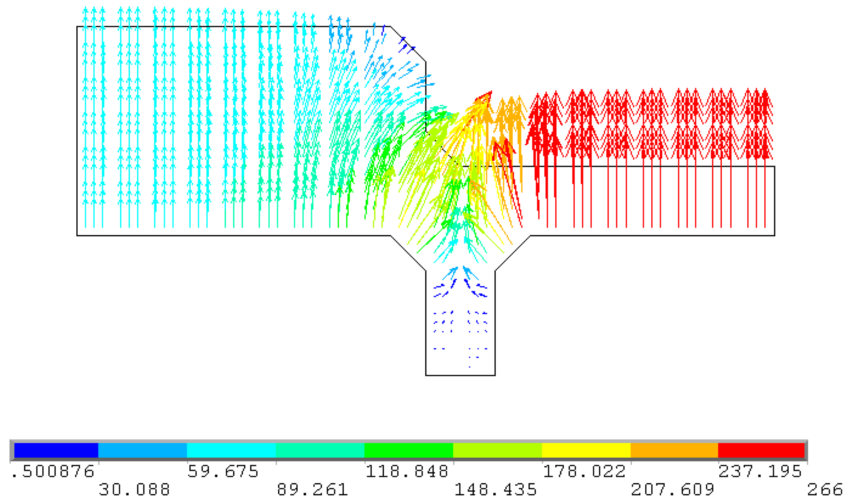

Figure 5-15. Electric field at transition zone, in V/mm. Vector length as well as color indicates strength of electric field.

The formulation presented in Eq. (5-23) still does not capture the subtlety of the interaction of probe and target surface. Assume for example that C_6 is a smaller capacitance (i.e., further away) then it would be reasonable to assume that this would have a negative influence or no influence. This "influence" matrix will therefore depend on the surface features and will be unique to a particular target surface. In fact it must be created from an approximation of the target surface itself, so the process of determining the target surface goes through at least two iterations before a surface is determined.

To determine a better version of the "influence" matrix, first consider that it needs to have the following properties.

- If applied to a flat surface, the resulting sum of capacitances is the same.
- An approaching step up (decrease in gap d), will have a positive influence.
- An approaching step down (increase in gap d), will have a negative effect.
- A rectangular probe will be symmetrical with respect to the leading and trailing edge.
- The effect is proportional to the difference between capacitances or distances.

Possibly the most straightforward approach to this method is to write out equations that show this effect and then convert these into a matrix. Back to the example of Eq. (5-13), the fourth row of the matrix can be written out as Eq. (5-24). To add the

influence of C_6 and C_2, consider the difference between these values and their nearest neighbor. This produces the terms (C_6-C_5) and (C_2-C_3). Taking care with the signs to indicate positive influence, the end result is Eq. (5-25). This passes all of the five tests listed above, with the size of the effect being proportional to the increase in capacitance. The improved **[D]** matrix appears in Eq. (5-26). In this approximation all δ terms are equal, although the terms can be further customized for a known probe or target.

$$C_3 + C_4 + C_5 = C_{meas4} \tag{5-24}$$

$$\delta(C_2 - C_3) + C_3 + C_4 + C_5 + \delta(C_6 - C_5) = C_{meas4} \tag{5-25}$$

$$\begin{bmatrix} 1 & 1-\delta & \delta & 0 & 0 & 0 & \delta & 1-\delta \\ 1-\delta & 1 & 1-\delta & \delta & 0 & 0 & 0 & \delta \\ \delta & 1-\delta & 1 & 1-\delta & \delta & 0 & 0 & 0 \\ 0 & \delta & 1-\delta & 1 & 1-\delta & \delta & 0 & 0 \\ 0 & 0 & \delta & 1-\delta & 1 & 1-\delta & \delta & 0 \\ 0 & 0 & 0 & \delta & 1-\delta & 1 & 1-\delta & \delta \\ 0 & 0 & 0 & 0 & \delta & 1-\delta & 1 & 1-\delta \\ 0 & 0 & 0 & 0 & 0 & \delta & 1-\delta & 1 \end{bmatrix} = [\mathbf{D}] \tag{5-26}$$

This matrix assumes that a solution exists for the capacitances C_1, C_2, etc., even though the measured quantities are C_{meas1}, etc. One method of solving this system is to invert the matrix **[D]** symbolically, but the variable δ that appears in **[D]** must be calculated. First, approximations for the individual capacitances of the system, called C_1', C_2', or C_n', are determined. This matrix can be termed **C'**, and from this a solution for δ is derived, as shown in Eqs. (5-27) and (5-28).

$$[\mathbf{D'}]^{-1}[\mathbf{C_{meas}}] = [\mathbf{C'}] \tag{5-27}$$

$$[\mathbf{D}][\mathbf{C'}] = [\mathbf{C_{meas}}] \tag{5-28}$$

The system of equations in (5-28) actually represents multiple solutions for δ, once again giving us a measure of the error in δ and also a view into the validity of this

method. This variable δ will be dependent on the number of divisions of the target surface.

For the case of the long sensing area there is no trailing edge, only a leading edge and therefore only one set of terms to add to the existing equations. Following the same arguments above, the form of the matrix from Eq. (5-17) is expected to change into the form of Eq. (5-29).

$$\begin{bmatrix} 1-\eta & \eta & 0 & 0 & 0 & 0 & 0 & 0 \\ 1 & 1-\eta & \eta & 0 & 0 & 0 & 0 & 0 \\ 1 & 1 & 1-\eta & \eta & 0 & 0 & 0 & 0 \\ 1 & 1 & 1 & 1-\eta & \eta & 0 & 0 & 0 \\ 1 & 1 & 1 & 1 & 1-\eta & \eta & 0 & 0 \\ 1 & 1 & 1 & 1 & 1 & 1-\eta & \eta & 0 \\ 1 & 1 & 1 & 1 & 1 & 1 & 1-\eta & \eta \\ 1 & 1 & 1 & 1 & 1 & 1 & 1 & 1-\eta \end{bmatrix} \begin{bmatrix} C_2 \\ C_3 \\ C_4 \\ C_5 \\ C_6 \\ C_7 \\ C_8 \\ C_9 \end{bmatrix} = \begin{bmatrix} C_{meas1} \\ C_{meas2} \\ C_{meas3} \\ C_{meas4} \\ C_{meas5} \\ C_{meas6} \\ C_{meas7} \\ C_{meas8} \end{bmatrix} - C_{\min} \begin{bmatrix} 1 \\ 1 \\ 1 \\ 1 \\ 1 \\ 1 \\ 1 \\ 1 \end{bmatrix} \quad (5\text{-}29)$$

There are two notes to make regarding this form. First, there is no need for any “trailing” edge terms, since the assumption with this probe is that the probe sensing area is longer in the direction of motion than the area being probed. The second point to note is that the $C_{\min}$ term can incorporate a constant offset, so there is not a necessity for both terms to contain the same variable η.

5.4.2 Sinusoidal nonuniform surface

Now that a deconvolution method has been developed and its functionality has been proven in the simplest cases, it is time to apply this same theory to a more complicated set of data. A “sinusoidal” surface is modeled in Pro/Engineer, and the capacitive deconvolution method applied.

For the case of the rectangular area probe, the surface of the half-hole is shown in Figure 5-16. This form error is two-dimensional only: there is no variation in the surface in the z-direction. There are a total of 6 complete sine waves in the surface of the half-hole: recall that the probe is 40 degrees wide and so the probe itself fits fewer times than this in the span of 180 degrees.

As before, the probe is started well outside the half-hole and it is gradually passed through the hole. Because the surface is fluctuating relatively rapidly, measurements are made every 2 degrees of angle. The target surface varies in diameter from 0.96 to 1.00 mm, the same range that was modeled as a step height in Section 5.4.1. This raw data are plotted in Figure 5-17.

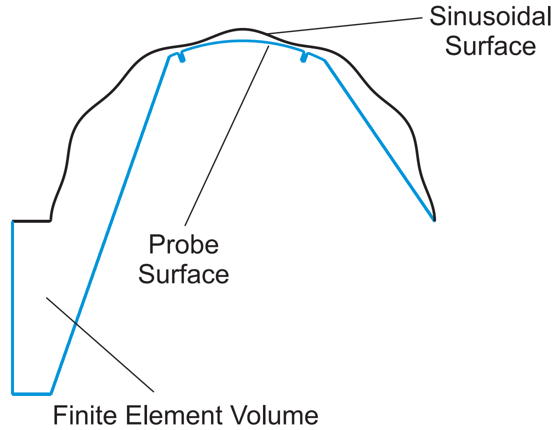

Figure 5-16. Pro/Engineer model of half-hole sinusoidal target surface and rectangular probe.

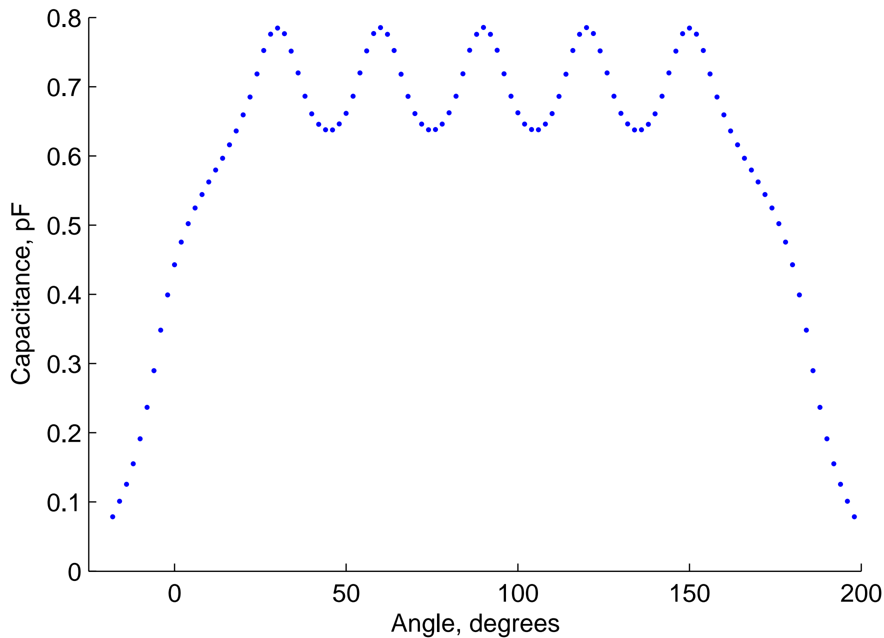

Figure 5-17. Raw data from scan of half-hole sinusoidal target.

The maximum surface resolution that can be expected from this simulation is on the same order as the step angle in the simulation, in this case 2 degrees. Because of symmetry, the total width of one-quarter of the hole (90 degrees) is broken into 45

segments. The data from one half of the FEA simulation is then duplicated to complete the profile. With this duplication and the probe overlapping a total of 20 of these segments, the total size of the matrix applied to this model is 111 rows and 90 columns. A portion of this matrix **[D]** is shown in Eq. (5-30).

This seems to dispute the general model that was discussed beginning on page 110 that predicted the number of equations that would be generated for a half hole model. Applying that math, where $k = 20$, $m = 1$, and $n = 90$, the matrix would be expected to have 109 rows and 90 columns. Recall, however, that it is assumed that the hole begins to influence the probe before it enters, this generates one additional equation at the beginning of the series. Similarly there exists influence as the probe exits the hole, this is an additional equation at the end of the series. So for a probe with a sensing area that is k/m times the minimum sensible area and where the hole is divided into n segments, in the corrected model the final array has $n+k-2m+3$ rows and n columns.

$$[\mathbf{D}] = \begin{bmatrix} \delta & 0 & 0 & 0 & 0 & 0 & 0 & 0 & 0 & 0 & 0 & \\ 1-\delta & \delta & 0 & 0 & 0 & 0 & 0 & 0 & 0 & 0 & 0 & \\ 1 & 1-\delta & \delta & 0 & 0 & 0 & 0 & 0 & 0 & 0 & 0 & \\ 1 & 1 & 1-\delta & \delta & 0 & 0 & 0 & 0 & 0 & 0 & 0 & \\ 1 & 1 & 1 & 1-\delta & \delta & 0 & 0 & 0 & 0 & 0 & 0 & \\ 1 & 1 & 1 & 1 & 1-\delta & \delta & 0 & 0 & 0 & 0 & 0 & \cdots \\ 1 & 1 & 1 & 1 & 1 & 1-\delta & \delta & 0 & 0 & 0 & 0 & \\ 1 & 1 & 1 & 1 & 1 & 1 & 1-\delta & \delta & 0 & 0 & 0 & \\ 1-\delta & 1 & 1 & 1 & 1 & 1 & 1 & 1-\delta & \delta & 0 & 0 & \\ \delta & 1-\delta & 1 & 1 & 1 & 1 & 1 & 1 & 1-\delta & \delta & 0 & \\ 0 & \delta & 1-\delta & 1 & 1 & 1 & 1 & 1 & 1 & 1-\delta & \delta & \\ & & & & & \cdots & & & & & & \end{bmatrix} \qquad (5\text{-}30)$$

This matrix, **[D]**, is used to deconvolve the raw capacitance data of Figure 5-17. A plot of the surface after deconvolution is shown in Figure 5-18, along with the actual hole surface as generated by Pro/Engineer and ANSYS. Since the width of the probe is wider than each individual sine wave, this probe should not be able to model such a process. In fact, if this probe is rotated in a complete hole there is not enough information to resolve

these wavelengths. Because the probe has a "beginning" and an "end," however, the actual shape of the surface can be largely recovered.

A second test set of data is applied to the linear model of the long probe. This data, also a sinusoidal pattern and one-dimensional, ranges from a gap distance *d* of 0.04 mm to a gap of 0.08 mm. The raw output of this measurement consists of the average slope of the capacitance curve overlaid with the sinusoidal variation, as shown in Figure 5-19. A plot of the results from **[D]** along with the original surface is shown in Figure 5-20.

These results are further from the ideal surface than the results from the rectangular probe. There are two possible reasons for this larger discrepancy. In the long probe case, the matrix **[D]** used to solve for the capacitances is a square matrix, and therefore the routine for solving such a system has no redundancy. In the case of the rectangular probe such redundancy exists, which helps reduce error due to one or two bad data points. The second reason for this discrepancy is that the long probe model inadvertently used larger gap distances (from 0.04 mm to 0.08 mm) rather than the same gap distances as the rectangular probe. This adds some error to the resulting capacitances and distance calculations.

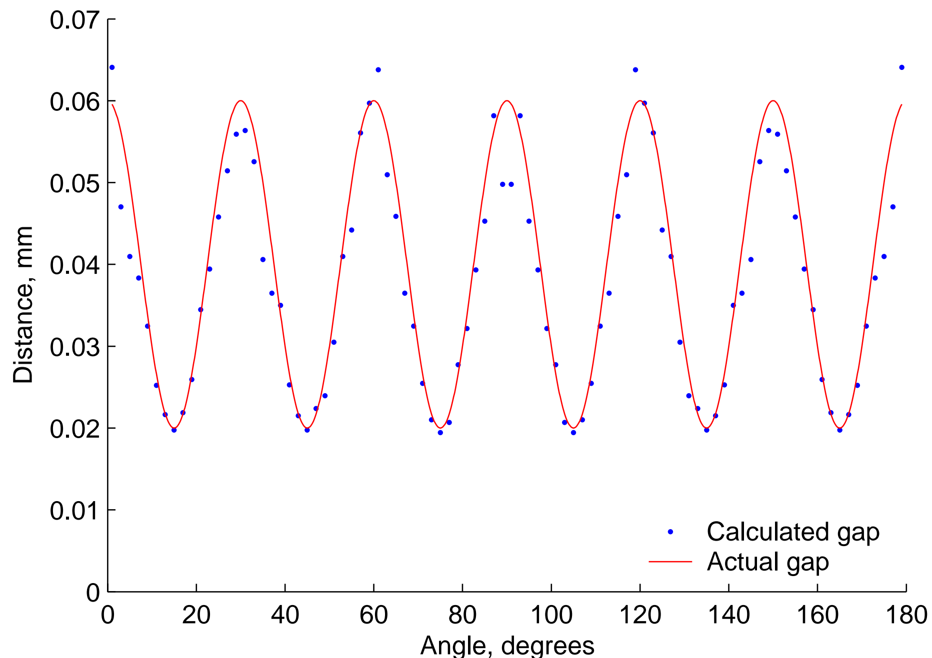

Figure 5-18. Plot of deconvolved surface.

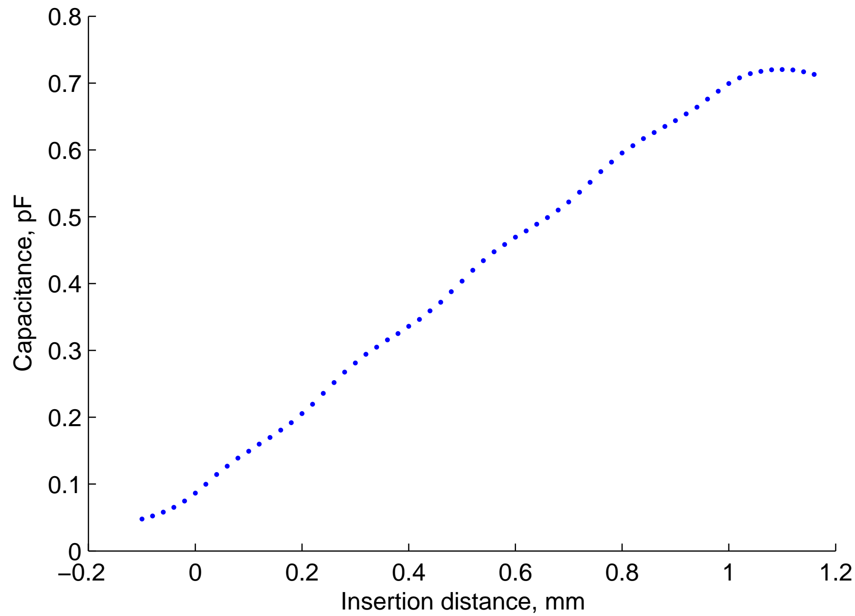

Figure 5-19. Raw data output from long probe and sinusoidal target.

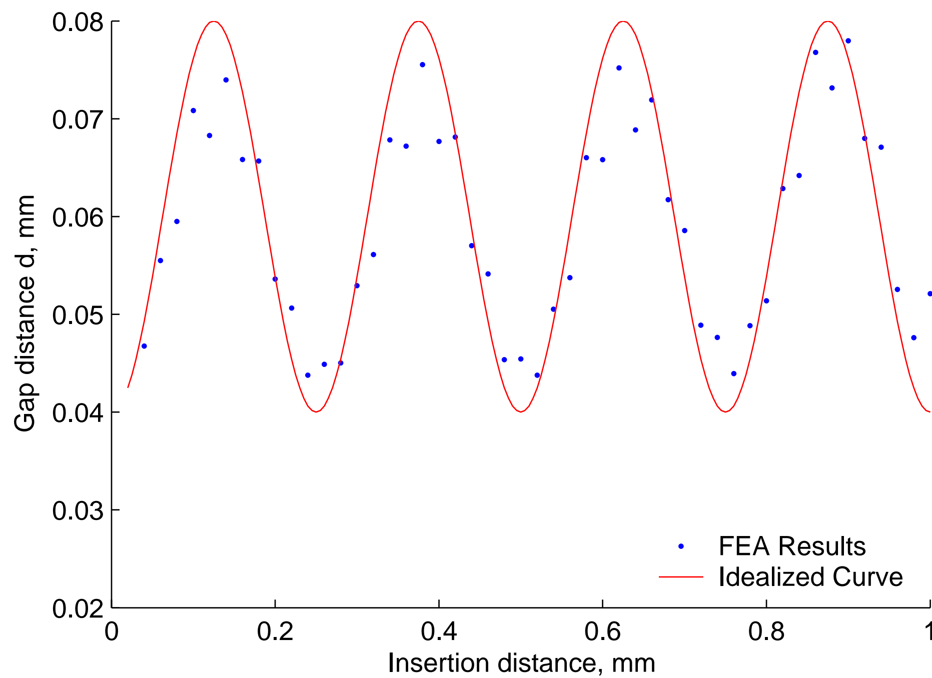

Figure 5-20. Long probe targeting a sinusoidal surface, deconvolution results.

5.5 Extension to 3D

To this point it has been proven that data from a capacitance probe can in theory be deconvolved to show surface details smaller than the surface of the probe. Sinusoidal surfaces with variation along a single direction have been generated and the probe passed

in a direction perpendicular to the target surface. The next question is to determine whether these methods can be extended to a three-dimensional probe and a cylindrical target surface that shows variation in two directions. Also, if these methods are applied to a three-dimensional hole, what is the trajectory of the probe through the hole? Finally, it is important to consider what will happen if the probe geometry differs from the ideal case, either due to manufacturing issues or other concerns.

5.5.1 Multiple areas of influence

The first consideration when analyzing a probe in three dimensions is to realize that the simplest form of the parallel plate approximation remains almost entirely unchanged. As before, an area must be integrated to determine capacitance, but instead of assuming a fixed width as in Eq. (5-21), the gap distance d is considered to vary over both x and y, as shown in Eq. (5-31). Breaking the surface of the hole into finite areas $\Delta x \Delta y$ results in a two-dimensional array of capacitances, with a corresponding series of **[D]** matrices.

$$C = \iint_{x,y} \frac{\varepsilon_0 \varepsilon_R dxdy}{d(x,y)} \tag{5-31}$$

To prevent the mathematics of the problem from becoming impossibly convoluted, it is suggested that the probe be moved in one of the integration directions only. Fixing the y position and moving the probe in x results in a measure of d as a function of x but only averaging this d over the finite width of the probe. Depending on the trajectory chosen, it is possible to ferret out additional information on $d(y)$ after the first step is complete. Possible trajectories are discussed in Section 5.5.2.

A second issue of concern is when the probe deconvolution method is extended to consider additional areas of influence. In the two-dimensional models there was only a single approaching area of the target surface that was considered to influence the capacitance. Now, the sensing area is surrounded on three or four sides by areas that will affect the capacitance reading. These are shown schematically in Figure 5-21. The model must take into consideration all of these areas when deconvolving the data.

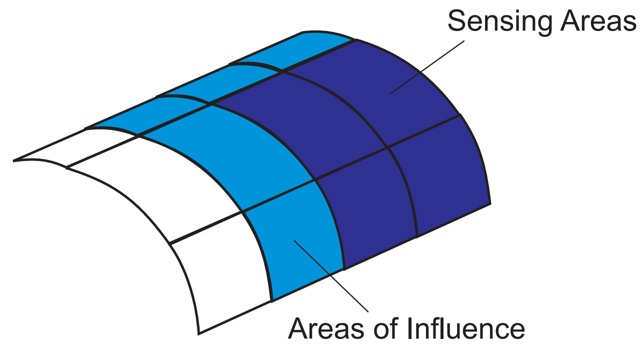

Figure 5-21. Areas of influence on the target surface for three-dimensional probe.

5.5.2 Hole measurement trajectories

There are many possible ways to move the probe in a hole so that every area of the hole is "seen" by the probe. One way initially considered was to spiral down the length of the hole, following a helical pathway. If the spot were several threads wide then this trajectory would provide overlap from section to section, and would in time trace the entire inner surface of the hole. Considering the probe design with a rectangular sensing area along the side of a cylinder, the best direction to move the probe would be into the hole (z-direction) or rotating at a fixed z (θ-direction). These two schemes are illustrated in Figure 5-22. In scheme (a), the probe is moved a short distance in the z-direction, followed by a full 360-degree rotation in the θ-direction. The probe is then moved a second incremental distance in the z-direction, and again the probe is rotated 360˚ in the θ-direction. This "step-spiral" path is continued until the probe exits the far end of the hole.

The second possible trajectory is illustrated in Figure 5-22 (b). In this diagram the probe moves a long distance in the z-direction, passing entirely through the hole and emerging on the other side. The probe is then rotated a small amount in the θ-direction and the probe is pulled back through the hole. The probe is rotated another small increment and the process is repeated until the entire hole is traversed. This is termed the "zigzag" trajectory.

Both of these proposed trajectories can be plotted so any desired amount of overlap can be accomplished. In the case of trajectory (b), it is preferable that the path close on itself, which will occur if 360 is an integer multiple of the step size. A step size of 5 degrees, for example, gives a closed loop trajectory after 72 passes.

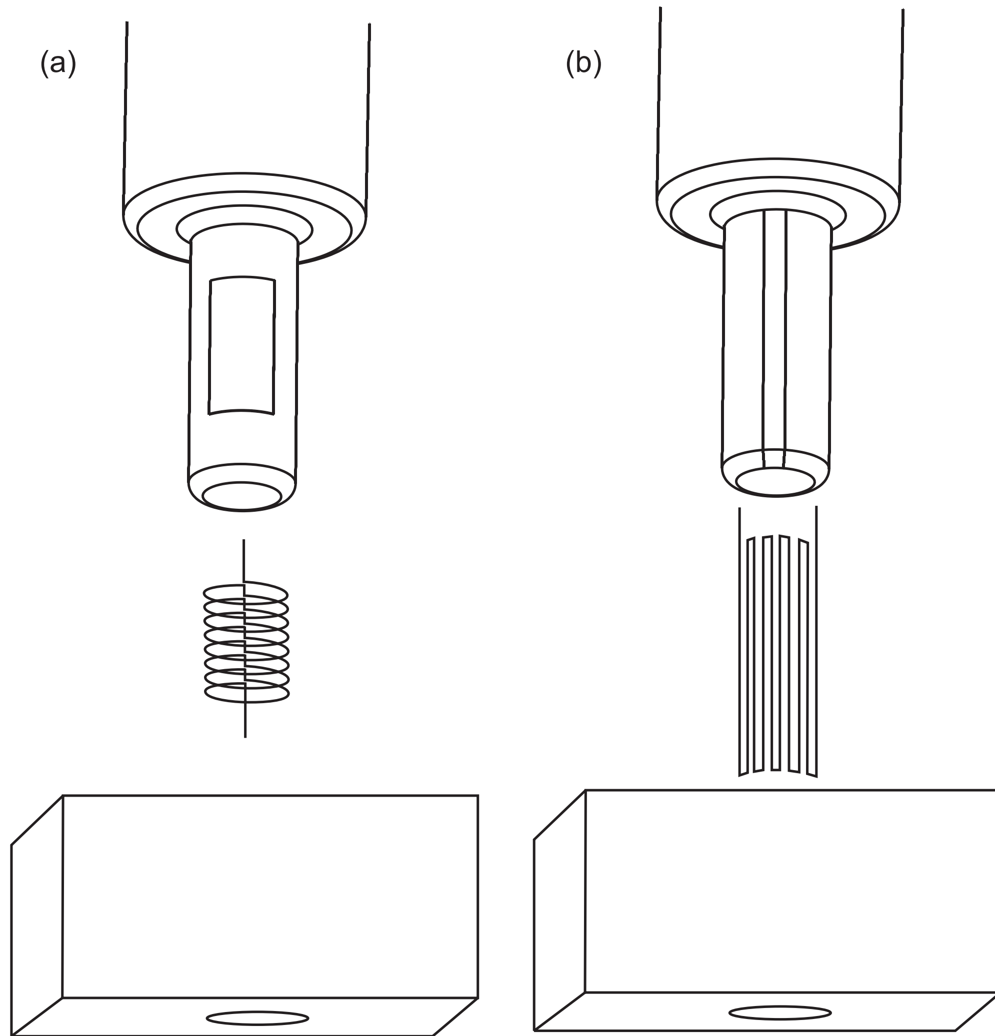

Figure 5-22. Two schemes for scanning target holes.

It is important to note a fundamental difference between these two trajectories that will play an important role in the evaluation of noise contributions. In trajectory (a) the probe enters the hole and covers the entire surface before exiting. As seen in one-dimensional passes through the hole, a data set consists of one pass into and out of the hole. Smaller data sets than this are problematic because there is no redundancy in the equations, so there is no opportunity to check the accuracy of the data through a least-squares method. If the hole is to be broken into 1000 small subareas with capacitance $C_{\min}$, then the final matrix will have dimensions of approximately 1000 × 1000. While this does not sound like a difficult task for a computer to solve, adding the noise component to the equations shows that there is a significant downside to having a large matrix.

Contrast this conclusion with trajectory (b). In this path the probe enters and exits the hole on each pass. Since the probe is providing data that starts and ends with $C_{\min}$, each of the individual passes can be solved using a separate matrix. Going back to the case of 1000 sub-areas, if there are 20 passes and each pass gathers 50 data points, the matrix that must be solved is approximately 50 × 50. Twenty of these matrices must eventually be solved, but this still results in a huge reduction in required computing power. More importantly, for each capacitance there will be at most 50 terms contributing to the noise of the system, as described in detail in Section 5.6.

5.5.3 Probe design considerations

As presented in Chapter 2, a traditional capacitance probe system utilizes a circular sensing area with a ring-shaped guard structure. This contrasts with the rectangular shape of probe described thus far in this chapter. While a rectangular sensing area would best mimic the properties shown in the 2D FEA probe studies of Section 5.4, in reality the nature of electric fields would prevent this from working properly due to the presence of corners.

Electric fields occur when electric charges accumulate on the surface of a conductor. Since like charges repel one-another, charges on the outside of a conductor will accumulate in places where there are fewer “neighbors”, in other words charges will try to move as far as possible from other charges. Consider the electric field strength at the surface of a sphere of radius r, as given by Eq. (5-32), and compare that with the capacitance of an isolated sphere as given by Eq. (5-33).

$$E = \frac{Q}{4\pi\varepsilon_0 r^2} \tag{5-32}$$

$$C = 4\pi\varepsilon_0 r \tag{5-33}$$

Reducing the radius of the sphere by a factor of two, for example, yields a twofold reduction in the capacitance (and thus its charge Q for a given voltage). At the same time, however, at the surface of the sphere the electric field has doubled. As the radius shrinks, then, the electric field increases. This effect can be seen in finite element

analyses of an object with a corner (i.e., a zero radius). An “infinitely sharp” corner would have a corresponding infinite electric field, at least at that point.

Another way to consider the problem of corners is to recall that the electric charge on the surface of a conductor orients itself so that the electric field lines are perpendicular at the surface. This can be proven by the definition of a conductor: if charges within the surface of the conductor felt forces parallel to the surface, they would reorient themselves to cancel out this component. At a sharp corner, however, the normal to the surface is discontinuous. The electric field is also similarly difficult to model. The electric field of such a sharp corner would require many additional finite elements, to the level of detail that the corner can be considered to have a finite radius. To illustrate this point, two diagrams of a 3-D electric field finite element simulation are given in Figure 5-23 that compare the direction of the electric field at the node points between a sharp corner and one that includes a slight round. In the case of the sharp corners, the direction of the field varies through the thickness of the model, even though all other parameters are equal. This is revealed by the multiple arrows at the corners within the model. For the rounded corners, the electric field strength is lower and the direction is much better defined.

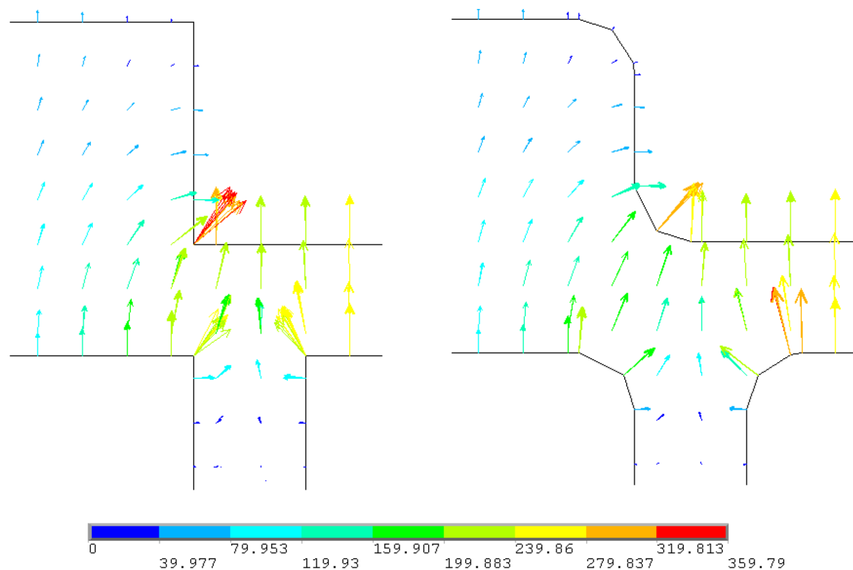

Figure 5-23. FEA simulations of the electric field in V/mm of a sharp corner (left) vs. a rounded corner (right).

Given that sharp corners should be rounded, how does this affect the rectangular probe design? Considering the three-dimensional surface of the probe, the most likely

problem area is with regard to the corners. Here, two edges come together, so the electric field would be unacceptably large at this point. Even given that the point cannot be atomically sharp, having an unknown curvature would nevertheless affect the outcome of measurements in unexpected ways.

It is proposed to round these corners in the actual probe, to make the electric field as uniform as possible. It remains to be seen, then, how a probe with a rounded sensing area fares when targeting a surface. Such a probe geometry as built in Pro/Engineer is shown in Figure 5-24. As before, the spacing between conductors is modeled as a solid for the purpose of meshing. This model is a full three-dimensional representation of the probe sensing area, with a width of 250 μm and a length of 800 μm. By modeling the two parts separately and creating an assembly to represent their relative positions, maximum flexibility is maintained in altering this model.

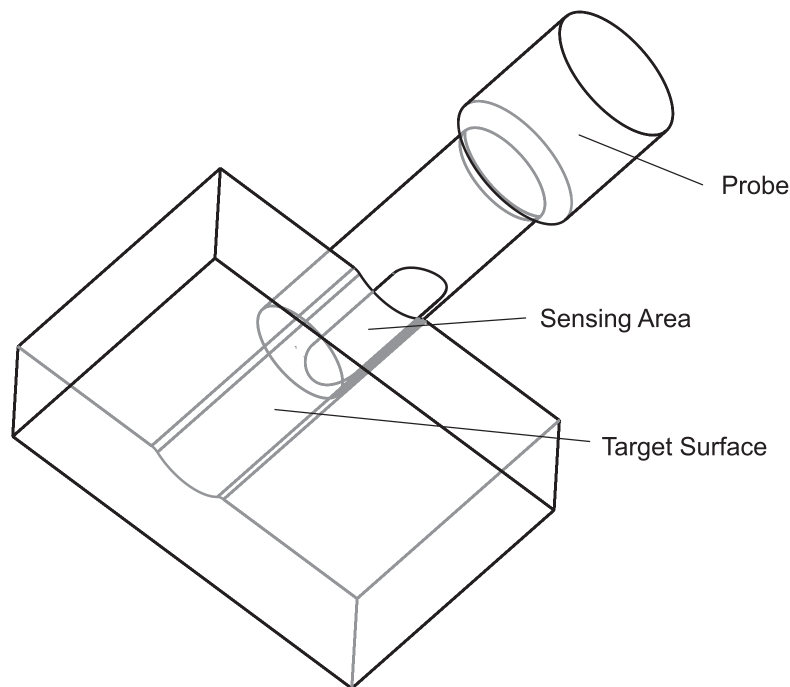

Figure 5-24. Three-dimensional probe targeting cylindrical surface.

When this probe is moved along the cylindrical target surface and FEA capacitance data are calculated, the plot of capacitance as a function of overlapping distance is no longer linear. This is not surprising, considering that this data is generated by a complex, three-dimensional model. In prior models the profile of the probe sensing area was constant, so that the overlapping area was a function of just the penetration

depth z. Now, the probe has a variable width as well, varying from the first moment of overlap until the semicircular area is completely engaged with the target surface. The integral represented in Eq. (5-31) can now be rewritten by substituting the value of y as calculated by Eq. (5-34) from the geometry of the semicircular region. The result for capacitance is as shown in Eq. (5-35). This equation is valid for $z < r$, when only the semicircular area is overlapping the target surface. Once z is larger than this, a second integral with constant y must be added. At the other end of the probe a third integral determines the capacitance.

$$y = 2\sqrt{r^2 - (r-z)^2} \tag{5-34}$$

$$C = \int_z 2\sqrt{r^2 - (r-z)^2}\,\frac{\varepsilon_0 \varepsilon_r dz}{d(z)} \tag{5-35}$$

In the case of a constant gap distance d these integrals can be solved in closed form. The solution of capacitance as a function of overlap distance can then be plotted against the data as determined by FEA. The integral solution and the FEA flat results are shown in Figure 5-25. As can be seen in the figure, given the expected behavior of this geometry of probe, the results are in good agreement with the theoretical values.

The final test of the deconvolution method examines a three-dimensional probe targeting a surface that is sinusoidal in the z-direction (along the depth of the hole). Results from this series are also plotted in Figure 5-25. The **[D]** matrix, partially shown in Eq. (5-30), does not contain ones or zeros, but must represent the varying area of the probe as it intersects the target surface.

$$[\mathbf{D}] = \begin{bmatrix} \delta & 0 & 0 & 0 & 0 & 0 & \\ 0.41-\delta & \delta & 0 & 0 & 0 & 0 & \\ 0.71 & 0.41-\delta & \delta & 0 & 0 & 0 & \\ 0.86 & 0.71 & 0.41-\delta & \delta & 0 & 0 & \cdots \\ 0.95 & 0.86 & 0.71 & 0.41-\delta & \delta & 0 & \\ 1 & 0.95 & 0.86 & 0.71 & 0.41-\delta & \delta & \\ & & & \cdots & & & \end{bmatrix} \tag{5-36}$$

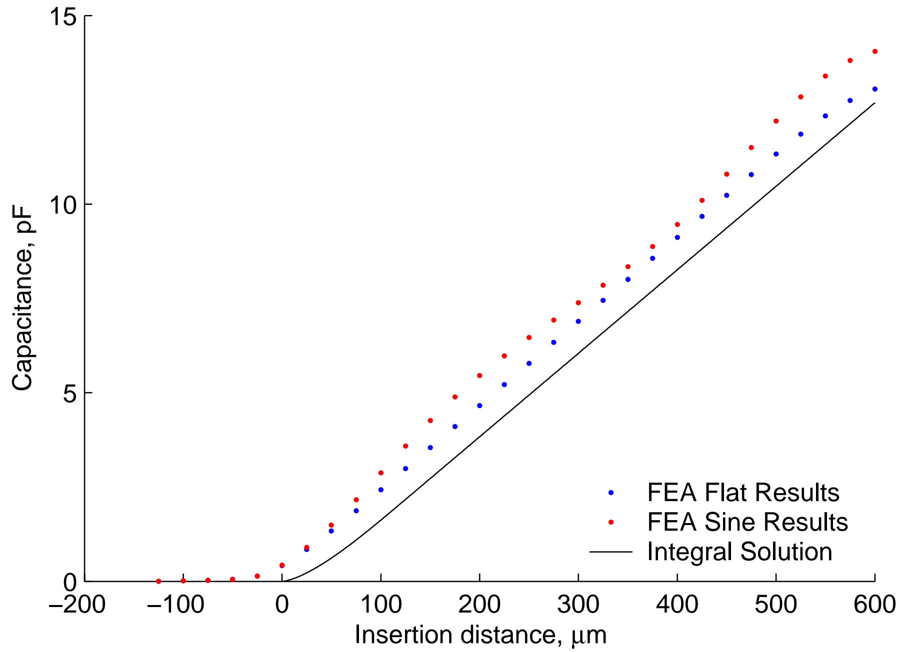

Figure 5-25. Plot of capacitance for rounded sensing area.

The first four values represent the integral of Eq. (5-35) as a fraction of the area $A_{\min}$, after which the terms of the matrix are ones. The full matrix contains 24 × 24 elements. The deconvolved surface of the sine data plotted in Figure 5-25 is shown in Figure 5-26.

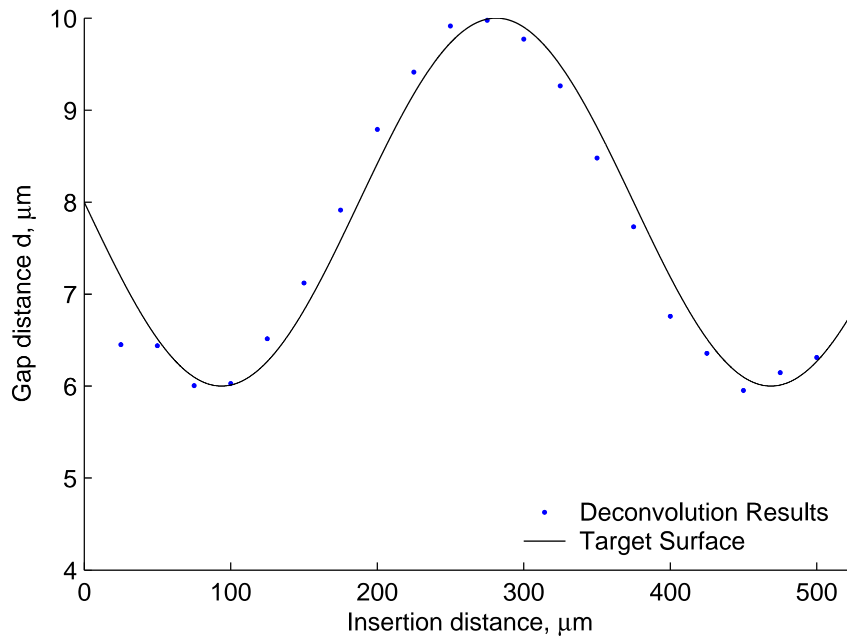

Figure 5-26. Deconvolved 3D surface using modified [D] matrix.

5.6 Noise Considerations

It was shown that FEA data from a capacitance probe can be deconvolved to reveal surface features smaller in scale than the surface area of the probe itself. The important question from an experimental standpoint then becomes, how does this method respond if noise is added to the system? Several sources of noise must be considered.

5.6.1 Rectangular probe error

This calculation starts with the rectangular sensing area and recalls the matrix relating the measured capacitances C_{meas} to the smaller capacitances C_n. Equation (5-13) on page 111 is the square matrix that results from a probe rotating in a full hole. This matrix has a condition number of 7.24, showing that the matrix is far from singular and its inversion should be well-behaved. The condition number is a function of the matrix only, and is therefore independent of the capacitance values applied to it. The result of inverting this matrix is shown in Eq. (5-37).

$$[\mathbf{D'}]^{-1} = \frac{1}{3}\begin{bmatrix} -1 & 2 & -1 & -1 & 2 & -1 & -1 & 2 \\ 2 & -1 & 2 & -1 & -1 & 2 & -1 & -1 \\ -1 & 2 & -1 & 2 & -1 & -1 & 2 & -1 \\ -1 & -1 & 2 & -1 & 2 & -1 & -1 & 2 \\ 2 & -1 & -1 & 2 & -1 & 2 & -1 & -1 \\ -1 & 2 & -1 & -1 & 2 & -1 & 2 & -1 \\ -1 & -1 & 2 & -1 & -1 & 2 & -1 & 2 \\ 2 & -1 & -1 & 2 & -1 & -1 & 2 & -1 \end{bmatrix} \tag{5-37}$$

This solution shows a worst-case-scenario: each capacitance value C_n is dependent on *all* of the measured values of capacitance. The higher the number of measured values, then, the higher the error is expected to be. Explicitly the function for a variable, in this case C, is the sum of several other variables with different coefficients k_i as shown in Eq. (5-38). In general, the error in the measurement of C, here called δC, is a function of the partial derivatives of the function C, as shown in Eq. (5-39), from Taylor [101]. Since the equation for C is a linear combination it is straightforward to take the partial derivatives with respect to each C_{meas} variable, as shown in Eq. (5-40). Finally, if the error in each capacitance measurement is assumed to be equal, those terms can be

pulled outside the sum over N. The result is Eq. (5-41). The sum, once calculated, is termed the error factor, or e_{erf}, as shown in Eq. (5-42).

$$C = \sum_N k_N C_{measN} \tag{5-38}$$

$$\delta C = \left(\sum_N \left(\frac{\partial C}{\partial C_{measN}} \delta C_{measN} \right)^2 \right)^{\frac{1}{2}} \tag{5-39}$$

$$\delta C = \left(\sum_N \left(k_N \delta C_{measN} \right)^2 \right)^{\frac{1}{2}} \tag{5-40}$$

$$\delta C = \delta C_{meas} \left(\sum_N k_N{}^2 \right)^{\frac{1}{2}} \tag{5-41}$$

$$\delta C = e_{erf} \delta C_{meas} \tag{5-42}$$

If the coefficients from Eq. (5-37) are applied and the same error margin δC_{meas} is assumed for all of the capacitance measurements, then the error in C is found to be 1.37 times larger than the error of each measurement, or an error factor e_{erf} of 1.37.

As mentioned above, this matrix is a worse-case scenario. Although it is not possible to invert the rectangular matrices such as Eq. (5-10) on page 109, a condition number can still be calculated, in this case 5.92. Because there are more equations than variables, this matrix is more robust than the previous example, and a linearly independent subset of these equations can be used to calculate an inverse. Taking the first 8 rows of this equation, the inverse is calculated to be as shown in Eq. (5-43). For this particular selection of rows, it can be seen that the number of variables that the capacitance C depends on varies from 1 to 6. The least-squares method will take into account all combinations of equations with equal weight, with the result that the data will not show such an obvious skew.

$$[\mathbf{D'}]^{-1} = \begin{bmatrix} 1 & 0 & 0 & 0 & 0 & 0 & 0 & 0 \\ -1 & 1 & 0 & 0 & 0 & 0 & 0 & 0 \\ 0 & -1 & 1 & 0 & 0 & 0 & 0 & 0 \\ 1 & 0 & -1 & 1 & 0 & 0 & 0 & 0 \\ -1 & 1 & 0 & -1 & 1 & 0 & 0 & 0 \\ 0 & -1 & 1 & 0 & -1 & 1 & 0 & 0 \\ 1 & 0 & -1 & 1 & 0 & -1 & 1 & 0 \\ -1 & 1 & 0 & -1 & 1 & 0 & -1 & 1 \end{bmatrix} \quad (5\text{-}43)$$

A second, important contribution from the least-squares method is an estimate of the error of the solution. Unless these coefficients are perfectly selected, no solution will give the exact result expected. In the nomenclature of this problem, Eq. (5-44) is being solved to determine the best fit values for **[C_n]**. Subtracting the expected solution **[C_meas]** from the result of the least-squares method gives an error vector **[E]**, as shown in Eq. (5-45). This matrix is of course the solution that is minimized during the least-squares routine, but the residual error is one measure of the validity of the combination of measured capacitance values and the matrix **[D']**. Matlab automatically calculates this value in its `lsqlin` command, if entered in the following format.

```
[Cn,Resnorm,E]=lsqlin(Dprime,Cmeas)
```

$$[\mathbf{D'}][\mathbf{C_n}] \approx [\mathbf{C_{meas}}] \quad (5\text{-}44)$$

$$[\mathbf{D'}][\mathbf{C_n}] - [\mathbf{C_{meas}}] = [\mathbf{E}] \quad (5\text{-}45)$$

Finally, for the case of the rectangular probe, the influence term δ must be added to the matrix **[D']** to produce **[D]** and to determine how many additional error terms are present in this case. Setting δ to 0.05, the matrix in Eq. (5-43) becomes the form of Eq. (5-46) below. Although this shows that now many additional C_{meas} terms are represented, the coefficients on many of the terms are small, resulting in an e_{erf} that varies from 1.12 for the uppermost row of Eq. (5-46) to an e_{erf} of 2.80 for the last row of this matrix.

$$[\mathbf{D}]^{-1} = \begin{bmatrix} 1.115 & -0.062 & 0.004 & 0 & 0 & 0 & 0 & 0 \\ -1.177 & 1.180 & -0.066 & 0.004 & 0 & 0 & 0 & 0 \\ 0.066 & -1.180 & 1.180 & -0.066 & 0.004 & 0 & 0 & 0 \\ 1.111 & 0.004 & -1.177 & 1.180 & -0.066 & 0.004 & 0 & 0 \\ -1.177 & 1.177 & 0 & -1.177 & 1.180 & -0.066 & 0.004 & 0 \\ 0.066 & -1.180 & 1.177 & 0 & -1.177 & 1.180 & -0.066 & 0.004 \\ 1.111 & 0.007 & -1.180 & 1.177 & 0.004 & -1.180 & 1.180 & -0.062 \\ -1.173 & 1.111 & 0.066 & -1.177 & 1.111 & 0.066 & -1.177 & 1.115 \end{bmatrix} \tag{5-46}$$

5.6.2 Long probe error

Recall that the matrix in Eq. (5-17) on page 116 for the long probe design is square in this case, and with a condition number of 10.65 it can be inverted. Starting with the basic **[D']** form of Eq. (5-17), the inverse is taken to produce the matrix shown in Eq. (5-47).

$$[\mathbf{D'}]^{-1} = \begin{bmatrix} 1 & 0 & 0 & 0 & 0 & 0 & 0 & 0 \\ -1 & 1 & 0 & 0 & 0 & 0 & 0 & 0 \\ 0 & -1 & 1 & 0 & 0 & 0 & 0 & 0 \\ 0 & 0 & -1 & 1 & 0 & 0 & 0 & 0 \\ 0 & 0 & 0 & -1 & 1 & 0 & 0 & 0 \\ 0 & 0 & 0 & 0 & -1 & 1 & 0 & 0 \\ 0 & 0 & 0 & 0 & 0 & -1 & 1 & 0 \\ 0 & 0 & 0 & 0 & 0 & 0 & -1 & 1 \end{bmatrix} \tag{5-47}$$

This solution at first appears simpler than expected, considering that the rectangular probe matrix resulted in a completely populated matrix. Closer examination reveals that this matrix is determining the derivative of the C_{meas} results, in effect calculating the slope of the capacitance probe output and equating each capacitance value C_{n} with the difference between subsequent measured values. For this result, almost every capacitance value is based on two measured values, so if the noise of each measured value is δC_{meas}, then the noise inherent in each calculated value is only 1.4 times this value (an error factor e_{erf} of 1.4).

As before, it is necessary to examine the case where the influence term η is added to the matrix. Again this value is set to 0.05 and the matrix is inverted numerically to

determine what the coefficients will be for this more complex case. The results are shown in Eq. (5-48). These results show that, for the case where the influence term is included, the overall error factor e_{erf} ranges from 1.12 to 1.67, as compared with as much as 2.80 for the rectangular probe geometry.

$$[\mathbf{D}]^{-1} = \begin{bmatrix} 1.115 & -0.062 & 0.004 & 0 & 0 & 0 & 0 & 0 \\ -1.177 & 1.180 & -0.066 & 0.004 & 0 & 0 & 0 & 0 \\ 0.066 & -1.180 & 1.180 & -0.066 & 0.004 & 0 & 0 & 0 \\ -0.004 & 0.066 & -1.180 & 1.180 & -0.066 & 0.004 & 0 & 0 \\ 0 & -0.004 & 0.066 & -1.180 & 1.180 & -0.066 & 0.004 & 0 \\ 0 & 0 & -0.004 & 0.066 & -1.180 & 1.180 & -0.066 & 0.004 \\ 0 & 0 & 0 & -0.004 & 0.066 & -1.180 & 1.180 & -0.062 \\ 0 & 0 & 0 & 0 & -0.004 & 0.066 & -1.177 & 1.115 \end{bmatrix} \quad (5\text{-}48)$$

5.6.3 Sidewall errors

Referring back to Figure 5-15, electric field lines can be seen to connect the probe surface and the side of the approaching half-hole. The errors that are due to the influence of perpendicular surfaces have been termed "sidewall errors," and must also be considered. Prior to any overlap of parallel surfaces, this is the dominant contributor to capacitance.

Although closed solutions are not available for the guard ring geometry, it is possible to both predict the influence of these sidewall errors and remove their contribution. The first step, predicting their influence, can be achieved using either finite element modeling or experimentally. Although the perpendicular surface is not as flat as a simple model, in practice the surface imperfections make little difference to the overall capacitance. This is because the curved distance from surface to surface is large compared to the gap distance d between the sensor and the target surface. In other words, the roughness of the surface that contains the hole is of little consequence.

5.6.4 Effects of probe error motion

There are other sources of error that must be considered when analyzing these probe geometries and determining what accuracy in capacitance and distance measurements can be expected. Some of these errors become more pronounced as the probe geometry is reduced in the future, and smaller holes with tighter tolerances are probed.

One such source of errors is with the alignment of the capacitance probe, the axis of rotation, and the *z*-axis motion of the probe. It has been assumed that a precision bearing is to be used in combination with the capacitance probe to rotate the probe within the hole, but all of the previous studies have assumed that the precision bearing will be in perfect alignment with the axis of the probe. Because the probe is manufactured on one type of spindle and must be removed to be mounted on another, there is a need to align this probe precisely. Improper alignment can result in several types of errors in the axis of rotation [55], which in turn cause anomalies in the capacitance data. A second source of error is from the geometry of the probe itself. If instead of a rectangular sensing area, the sensing area is skewed or keystone shaped, the resulting data will contain systematic (nonrandom) errors. A diagram showing these two sources of error appears in Figure 5-27.

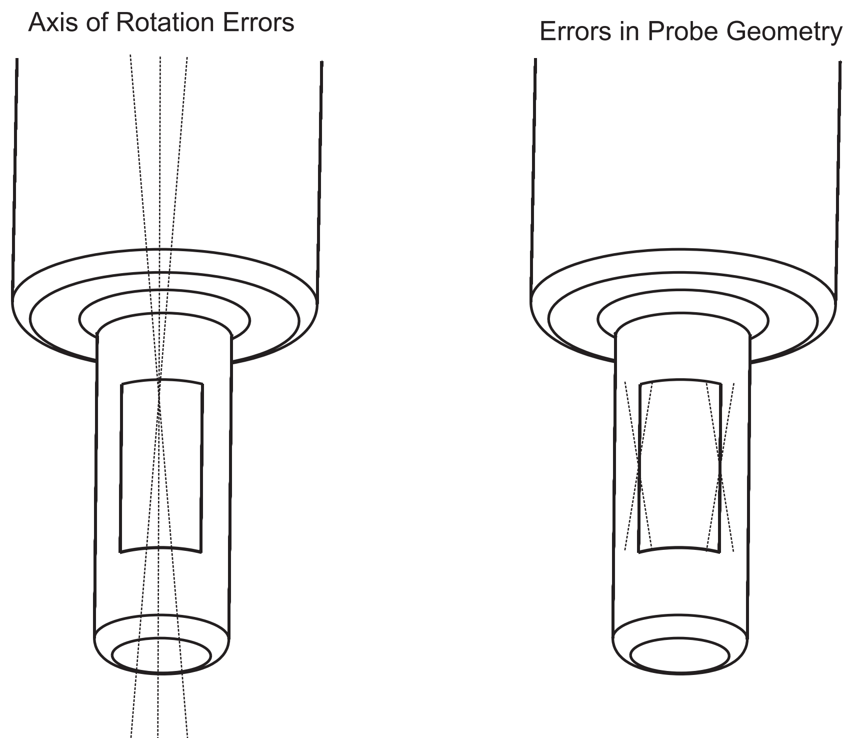

Figure 5-27. Spindle alignment and other causes of probe error.

In general, errors in the axis of rotation will limit the precision or accuracy of the measurement, and errors in the probe geometry will limit the accuracy. A simple, repeatable offset of the axis, however, can actually be beneficial to the experimental results. As described previously, these probe designs are limited in the range of holes that

can be measured for a given probe. Minimizing the distance between the probe sensing area and the target surface is critical to produce a measurable capacitance from a small probe area. If the target hole is too small for a given probe, there is no way to make a measurement. If, on the other hand, the gap is a few microns too large for measurement, it is possible to offset the axis of the probe from the axis of rotation of the spindle. This would bring the target area into range and allow measurement. Since most of the circumference of the probe is shielded and does not contribute to the measurement, if the gap on the back side of the probe increases there is no measurable effect.

5.6.5 Monte Carlo Simulation

The final test of the matrix solution method was to vary the measured capacitance values C_{meas} to determine how the resulting values C_1, C_2, etc., were affected. The noise of a commercial capacitance sensor is derived from the overall range and the error provided by the manufacturer. For the Lion Precision C1-C, the range on the fine setting is 2.0 minches (0.05 mm) and the RMS resolution is listed as 0.09 minches (0.0023 mm). The corresponds to a capacitance error of 0.0065 pF with a maximum capacitance value C_{max} of 0.4261 pF. The percentage error is therefore 1.5%.

The matrix in Eq. (5-36) was studied to determine how the error and the condition number were related. For this 24 × 24 element matrix, the condition number was higher at 142.3. This is in large part due to the rounding of the leading area of the probe; the 24 × 24 matrix for a probe with a square area has a condition number of 31.1.

Error values with a normal distribution and the σ value determined above were added to the C_{meas} values, then the C_n values were calculated. One-thousand of these calculations were made, and an error value for each of the C_n values was calculated. These errors were consistently between 5.2 and 5.3 times larger than the original error added to the measured capacitances. This example shows clearly that the extraction of additional spatial features comes at a cost in the ability to resolve the gap distance d.

5.7 Conclusions

This chapter studied two different probe geometries, each with its own advantages and limitations. The first geometry is a rectangular sensing area that is much smaller than the inner surface of the hole to be measured. The second geometry consists of a long, narrow sensing area that must be *longer* than the target hole.

Although a single measurement from a capacitance probe was capable of providing no more than the distance to the target surface averaged over the entire surface area, a capacitance probe was capable of providing data continuously as it was moved over a surface. When the area of the capacitance probe was broken into several smaller areas, these areas provided additional information about the target surface. The sensing limit of the probe was the minimum measurable capacitance $C_{\min}$ of the system, and not the limit of the sensing area of the probe. While this analysis added complexity to the solution, it allowed for improvements to the electronics to be instantly reflected in the output.

The capacitive deconvolution method for the capacitance data was written in matrix form. These matrices varied depending on the probe shape (rectangular or long) and the ratio of probe area to minimum sensing area. In cases where more equations are available than are strictly necessary, the additional equations helped to determine the error in the overall result. To show how the deconvolution method works, data files were generated for flat target surfaces and for steps halfway through the hole. The deconvolution of these results gave confidence in the ability of this method to solve for the general case. A sinusoidal surface was also analyzed and it was shown that the capacitance probe was able to determine details of the surface considerably smaller than the overall area of the probe.

With a two-dimensional proof of the method of deconvolution, the extension of this method to three dimensions was presented. Since there exist any number of trajectories to scan a target hole, the advantages of a zigzag pattern are discussed from the matrix solution standpoint. A zigzag solution to a three-dimensional sinusoidal surface was presented. The noise is also shown to be minimized for the zigzag configuration. Finally, other sources of noise and possible solutions to these problems were discussed.

Copyright © Philip T. Smith Jr. 2007

6 Probe Manufacture and Analysis

6.1 Introduction

As the precision requirements for machining mechanical features become more demanding and the size of features is reduced, new techniques of manufacturing must be developed. These techniques must of course borrow from existing technologies, combining them in new and novel ways to increase precision and decrease size.

Current probe technologies for small hole probes incorporate combinations of electronics or optical sensors and miniature contact probes, the former being used to sense contact by the latter [102, 103, 104]. A hole is measured at multiple points by approaching the surface from the normal direction multiple times. This limits the wavelengths of features that can be detected in the hole surface. Decreasing the sampling distance between measurements also greatly improves the ability to measure waviness and roughness within the hole surface. Nevertheless, a continuous measurement of the complete inner surface of the hole is not achieved with contact probes.

This chapter presents the manufacturing process for a prototype capacitance probe. This probe is capable of measuring the inner surface of holes that are approximately one millimeter in diameter, in any conductive material. The probe will sense the inner surface using non-contact capacitance micrometry. This allows for much smaller sampling distances and many overlapping data points to be collected quickly using a rotating probe.

The typical arrangement of conductors on a commercial capacitance sensor includes a flat, circular sensing area surrounded by a guard ring structure. This geometry yields a very sensitive sensor with high linearity when targeting flat, conductive surfaces that are parallel to the sensing area. However, linearity can decrease substantially when the target surface is not flat [105, 106]. A capacitive probe for small hole metrology as described in Chapter 5 will have a cylindrical target surface and can be designed with a cylindrical sensing area. This design will minimize the gap distance, and therefore maximize sensitivity.

The size of the sensing area, approximately 400 μm by 800 μm, is a balance between lateral resolution, depth resolution, and electronics sensitivity. The optimal probe is only a few micrometers smaller than the hole it is measuring, therefore this approach prefers a custom probe for each size of hole to be measured, rather than a

generic hole probe suitable for a wide variety of holes. For a rectangular sensing area in close proximity to the target surface, the parallel plate approximation of Eq. (1-3) is applied. A gap distance of 260 micrometers and a relative permittivity of 80 (that of water), produces a capacitance of approximately 1.3 pF.

Three-dimensional finite element modeling predicts the linearity and sensitivity of two cylindrical probe designs beyond that available by simple closed equations. These finite element models indicate that the geometry of the probe has both sufficient lateral resolution for sensing hole features, as well as sufficient capacitance for the available electronics. Both the sensing area and the material of the guard ring, now a guard layer enclosing most of the probe, must be connected to a sensitive bridge circuit. This circuit measures changes in the capacitance of the probe and target system as the inner surface of the hole is examined [107, 108]. A general schematic of the hole probe is shown in Figure 6-1. This chapter describes efforts to manufacture a prototype of the probe shown.

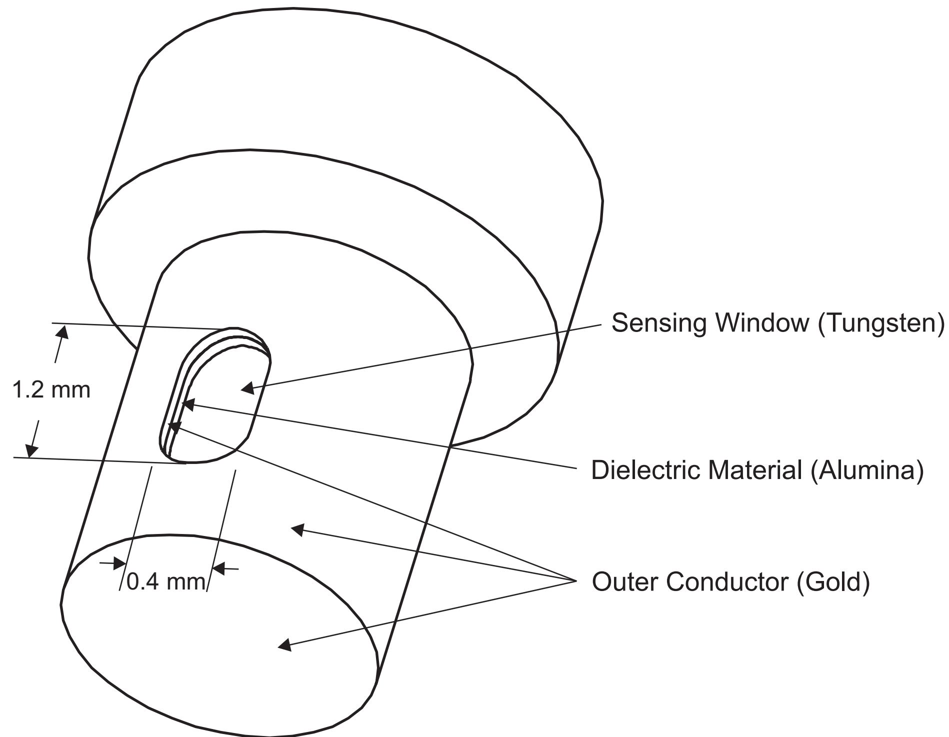

Figure 6-1. Capacitance Probe Design.

There were four manufacturing steps required:

- Excess material was removed from a blank cylinder using wire electro-discharge grinding (WEDG) μEDM [109]. This generated the correct probe shape.

- After the probe was machined, the surfaces were cleaned to remove debris and oil in preparation for coating.
- Ebeam deposition next applied a thick (on the order of 1 μm) layer of aluminum oxide (alumina), a non-conductive material.
- The probe was then repositioned and a layer of gold, a conductor, is applied. This layer was also on the order of 1 μm thick.

6.2 Wire Electro-Discharge Grinding of the Probe

The wire electro-discharge grinding (WEDG) μEDM process used the Panasonic Model MG-82 Micro Electro-Discharge machine, pictured in Figure 6-2. Details of the probe machining area are shown in Figure 6-3. It consists of a cast iron base with an *x-y* stage that moves a brass tub holding dielectric EDM fluid. The column supports a *z*-stage, on which is mounted a spindle. The spindle consists of a V-block and rotating mandrel, shown in Figure 6-4, which is driven by an elastic drive belt. The electrical connection to the mandrel is provided by a precision ball at the upper end of the mandrel. This ball contacts a stationary flat sheet of gold foil, which is wired to the discharge circuit.

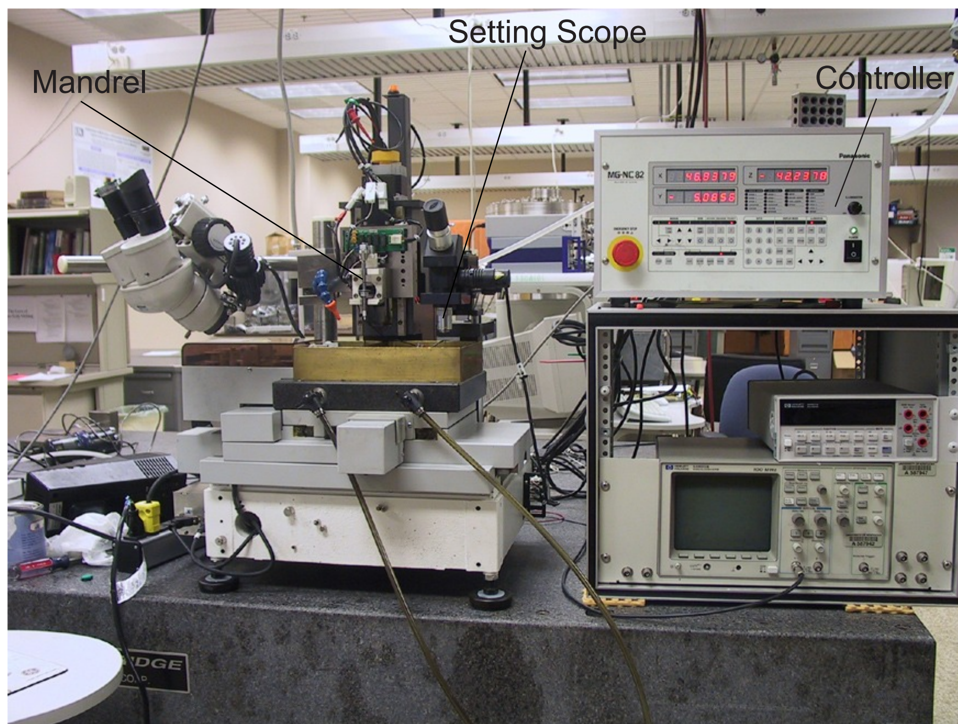

Figure 6-2. Panasonic model MG-82 μEDM Machine.

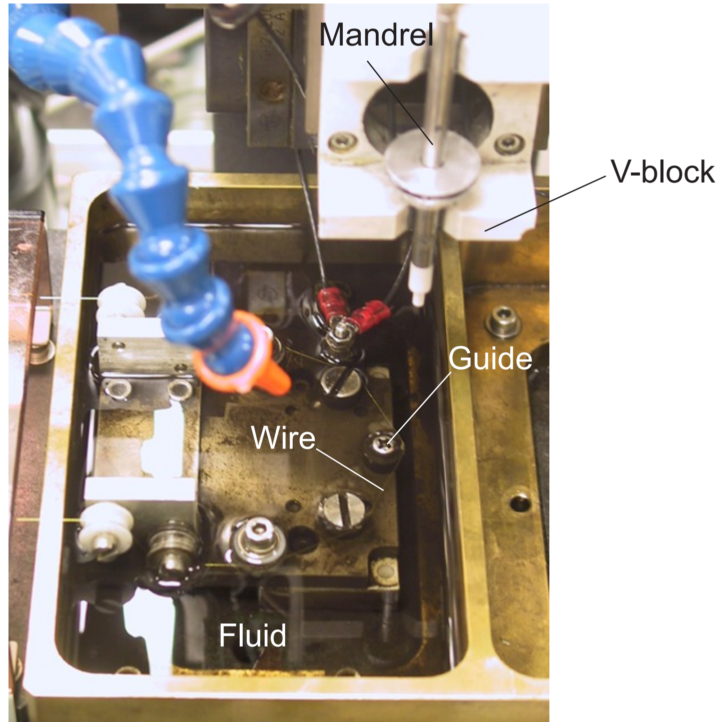

Figure 6-3. Probe machining area.

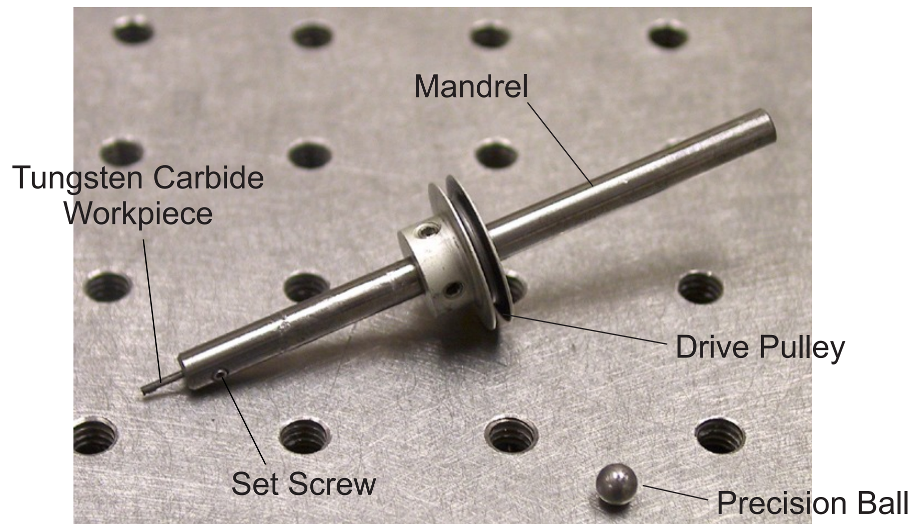

Figure 6-4. Detail of µEDM spindle.

The wire guide area, on the left side of the *x-y* stage and depicted in Figure 6-5, contains a series of spools that feed a brass wire with a nominal diameter of 100 µm. The non-rotating guide provides support and alignment of the wire at the point where the probe is to be machined.

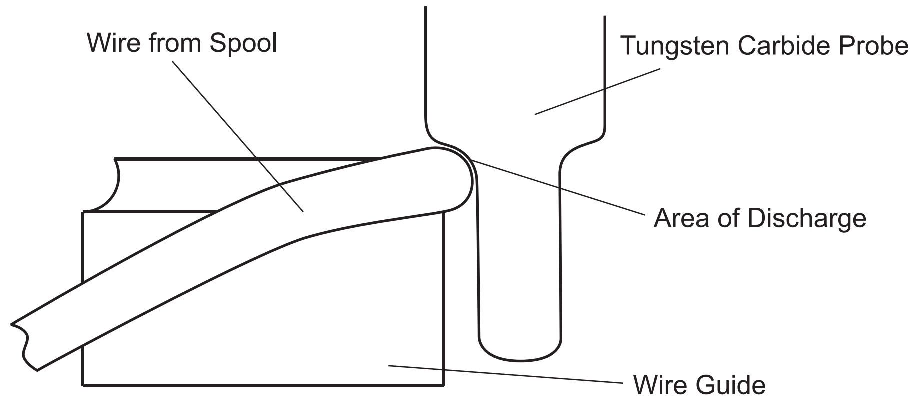

Figure 6-5. Probe Shaping on the Panasonic Model MG-82.

The mandrel used for holding the prototype probe during WEDG is shown in Figure 6-4. The tungsten carbide rod is held in the mandrel by an Allen key set screw in a hollow shaft. Because the inner diameter of this shaft is approximately 1.8 mm and the blank tungsten carbide probes are only 1.7 mm in diameter, there is some offset between the center of the blank tungsten carbide probe and the center of the mandrel. This offset is eliminated as a step in the machining process. Because the positioning of the probe shaft in the mandrel is not repeatable, all machining of the probe must be completed without removing the tungsten carbide probe from the mandrel. Once the tungsten carbide blank is mounted in the mandrel, the machine is operated by the controller shown in Figure 6-2. This controller displays the current coordinates of the *x, y* and *z*-stages (relative to a "home" position), and it allows individual μEDM steps to be entered directly.

In conventional WEDG processing, the spindle rotates the workpiece and the *x-y* stage brings the wire in close proximity to the probe blank. The electric circuit provides the voltage for a series of discharge sparks, and the copper wire is continuously spooled to refresh the working surface. The controller provides settings for the discharge voltage, the capacitance, the spindle rotation rate, the wire feed rate, the speed of the axes, and several closed-loop feedback options. For any but the most simple shapes, it is advantageous to use either preprogrammed software routines or to write code for a specific machining procedure. For this purpose, the controller is operated remotely by a PC.

Several Quick-Basic (Qbasic) routines are provided with the MG-82 machine for creating standard probe shapes including cylinders and cones. The existing routine

provided by Panasonic and applied to this probe is EDM72.BAS, which is run under the program QBASIC2.EXE. Some of the possible geometries available with this routine are shown in Figure 6-6, including (a) a cylinder, (b) a cylinder with rounded end, (c) a tapered cylinder, and (d) a two-step cylinder with a rounded end. Any other probe features require that custom routines be programmed.

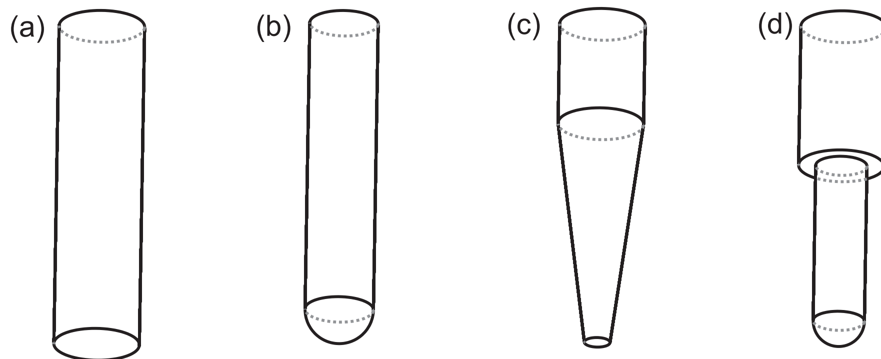

Figure 6-6. Possible geometries from provided Qbasic code.

This Qbasic routine prompts the user for up to eight processing steps at a time. Data values are entered as text, via a DOS prompt, and the entire table of values is then shown for review. The first eight steps in machining the capacitance probe are shown in Table 6-1. These values include two different radial values, 'X high' and 'X low', in micrometers, for cases where a tapered probe is needed. The 'Z length' is the length of probe to be machined in the step, also in micrometers. The 'Z offset' is not used. The radius value 'R' is for cases where a rounded end is desired. In Table 6-1, no rounds are applied to any surfaces. The capacitor and voltage are selected based on criteria determined by Morgan *et al.* [110]. The goal in the first passes is to maximize the material removal rate. Subsequent passes use a lower voltage and smaller capacitance, with the result that the surface has features typically smaller than a micrometer. The 'Z speed' values correlate with the voltage and capacitor selected. These values are shown in Table 6-2. The rotate value is simply a flag, setting this to 1 sends a command to the controller to activate the spindle motor.

Table 6-1. Initial probe shaping routine.

Step	1	2	3	4	5
X high	0	800	750	703	700
X low	0	800	750	703	700
Z length	100	12000	12000	12000	12000
Z offset	0	0	0	0	0
R	0	0	0	0	0
Capacitor	3	1	1	1	3
Voltage	80	110	110	110	80
Z speed min	1	3	3	3	1
Z speed max	30	50	50	50	30
Rotate	1	1	1	1	1

Table 6-2. Capacitance values and associated *Z* feed rates.

Capacitor number	Voltage	Capacitance, pF	Z speed min., µm/sec	Z speed max. , µm/sec
1	110	3300	3	50
2	100	220	3	50
3	80	100	1	30

The overall material removal routines steps are graphically depicted in Figure 6-7. They include (a) a step to shape the full length of the probe, (b) a step to initially shape the tip, (c) a step to round the tip end, and (d) a step to add a round partway up the probe. The machining parameters are applied eight steps at a time. The length of the probe (12 mm) is approximately the maximum travel available to the z-axis of the µEDM machine. This length allows not only for a larger diameter cylinder concentric with the smaller diameter sensing area of the shaft, but this surface also has the same roughness properties. Since coatings are required to extend up through this area, both for electrical connections and for alignment, the surface should be as similar as possible to the tip itself.

The WEDG steps listed in Table 6-1 perform an initial shaping routine on the probe, giving it a cylindrical form with a centerline that is nearly identical to the spindle's axis of rotation. Step 1 is simply an end facing process, where 100 µm of tungsten carbide are removed from the end of the blank shaft. Steps 2 through 4 remove 50 µm of tungsten carbide with each pass. Step 5 uses a smaller capacitor and discharge voltage to remove the last 3 µm of material, creating a smoother surface. This surface finish is important when applying thin coatings as described in Section 0.

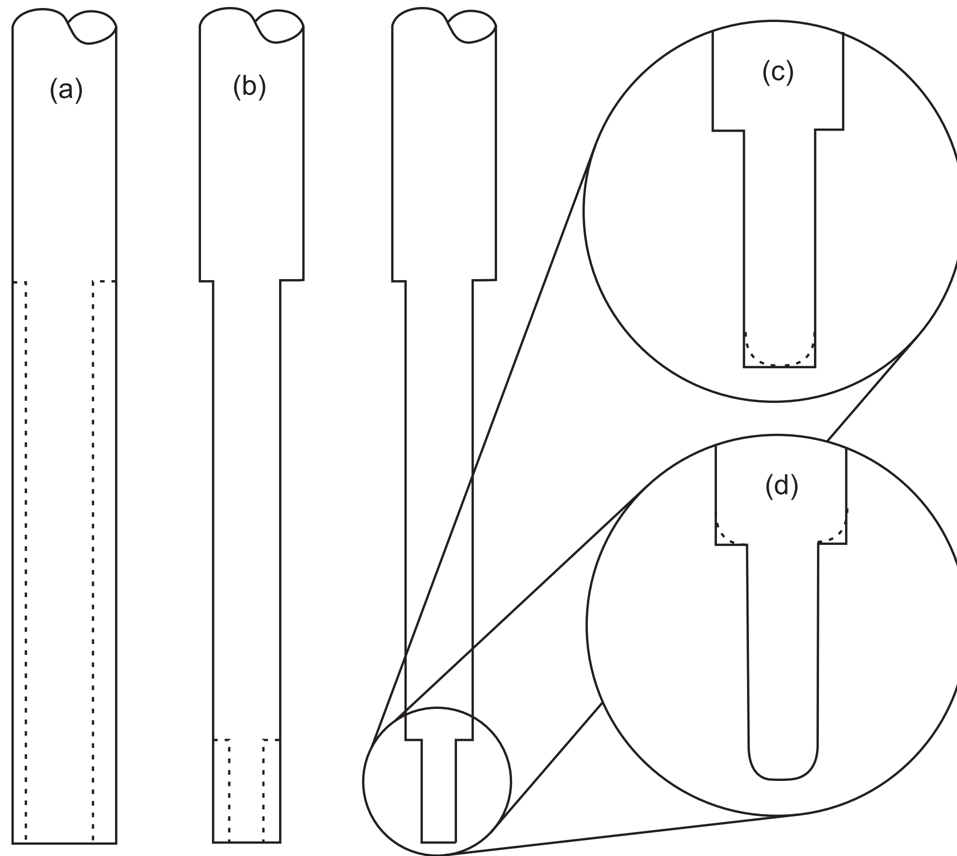

Figure 6-7. Machining steps in probe manufacture.

These parameters also assume that the spindle rotates at 3000 rpm. Although the rotation of the spindle can be turned on and off by software control, there is no closed-loop control of the spindle rotation rate. Since the spindle speed influences the ability of the µEDM machine to remove material, it is necessary to periodically check the spindle speed. A reduced speed usually indicates a lack of lubricant between the spindle's V-grooves and the mandrel.

Once the general outline of the probe is completed, the steps in Table 6-3 are applied. Step 6, which is another end finish, is common to each set of routines. A small value (5 µm) is set for this step. Steps 7 through 13 reduce the diameter of the end 2 mm of the probe from 1.4 mm to 0.8 mm. The last step in this series uses the lower capacitance value, lower voltage, and lower feed speed necessary for the proper surface finish.

The steps in Table 6-3 do not reduce the diameter of the probe to the target diameter of 750 µm, because the µEDM machine requires calibration of the home

position of the *x* stage. The calibration process uses a Nikon model MM40U microscope, a Diagnostic Instruments Spot Insight color CCD camera, and the Image-Pro Express software package. Images of the profile of the probe are collected using the software, and multiple measurements of the diameter are made using tools built into Image-Pro Express. Multiple measurements are made so that both an average and a standard deviation can be calculated. A screen shot of such a measurement appears in Figure 6-8.

Table 6-3. Further shaping of probe.

Step	6	7	8	9	10	11	12	13
X high	0	650	600	550	500	450	403	400
X low	0	650	600	550	500	450	403	400
Z length	5	2000	2000	2000	2000	2000	2000	2000
Z offset	0	0	0	0	0	0	0	0
R	0	0	0	0	0	0	0	0
Capacitor	3	1	1	1	1	1	1	3
Voltage	80	110	110	110	110	110	110	80
Z speed min	1	3	3	3	3	3	3	1
Z speed max	30	50	50	50	50	50	50	30
Rotate	1	1	1	1	1	1	1	1

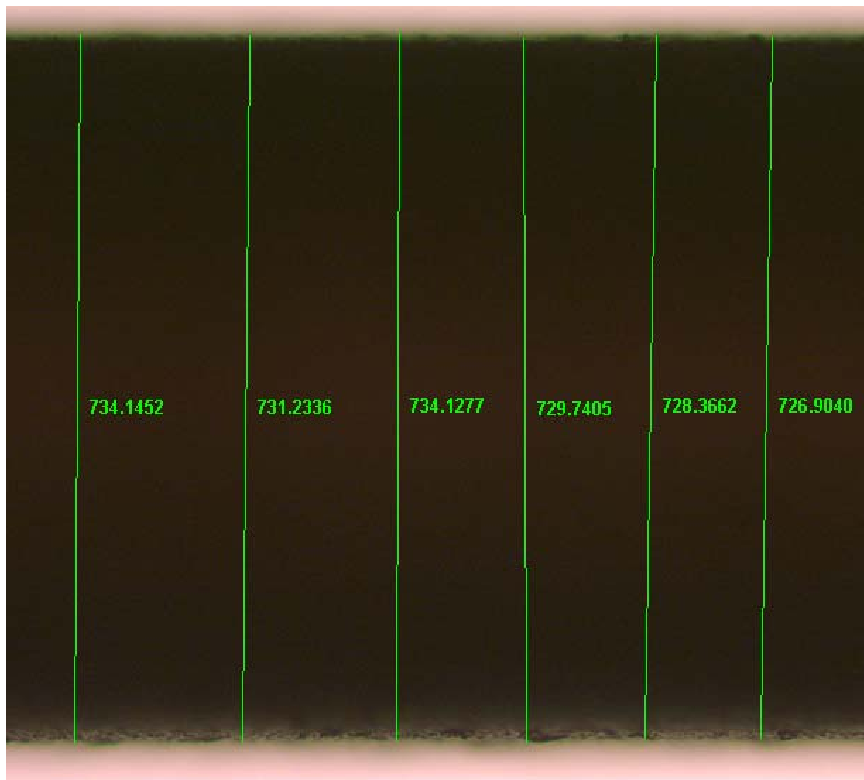

Figure 6-8. Diameter measurements using the Image-Pro Express software.

One set of five measurements resulted in a diameter of 794.255 ± 2.655 μm. Since the μEDM machine was programmed for a diameter of 800 μm, there is an error of 5.745 μm on the diameter, or 2.873 μm on the radius of the probe. Because the probe is too small, this difference in radius must be added to the current home position. If the probe was too large, on the other hand, the error would be subtracted from the home position. This home position is stored as the variable 'X.wedg.org' in the subroutine 'M.Param' within the 'EDM72.BAS' file. The units of this parameter are in tenths of a micrometer, so the home position of 469928 indicates an x home position of 46,992.8 μm or 46.9928 mm. The error of 2.873 μm is rounded to the nearest tenth of a micrometer and the integer 29 is added to the home position, producing a revised 'X.wedg.org' of 469957. This new parameter is entered manually into the Qbasic file.

After the home position of the μEDM machine is corrected, the final 25 μm of tungsten carbide can be removed from the probe. This is achieved using the steps shown in Table 6-4. Step 14 is the required end facing. Steps 15 and 16 follow the same pattern as previous routines, removing the bulk of the material using a high capacitance and voltage, and removing the final 3 μm using the lower capacitance and voltage. Step 17 represents a new feature, applying a round with a radius of 155 μm to the end of the probe. This end round was deemed necessary after early coating tests, described more fully in Section 6.3.3. The final diameter of the probe was once again measured optically as shown in Figure 6-8. The diameter was 750.65 μm, with a 2.1 μm standard deviation.

Table 6-4. Final probe shaping routine.

Step	**14**	**15**	**16**	**17**
X high	0	378	375	225
X low	0	378	375	225
Z length	3	2010	2020	300
Z offset	0	0	0	0
R	0	0	0	155
Capacitor	3	1	3	3
Voltage	80	110	80	80
Z speed min	1	3	1	1
Z speed max	30	50	30	30
Rotate	1	1	1	1

6.2.1 Rounding the edges of the probe

Initially, probes were produced without the rounded end, as the square end required fewer steps. Coating tests revealed the need to round not only the end of the probe, but also the "step" where the diameter changes from 1.4 mm to 0.75 mm. This type of feature is not available in any of the preprogrammed routines provided by Panasonic, so a custom program was written to achieve step (d) shown in Figure 6-7. Although customized code to pass commands to the μEDM controller can be created in Qbasic, these commands can also be passed using other programs. Since Matlab is a familiar interface, machining routines were created as Matlab scripts (.m files). The complete code to this program appears in Appendix D.

Beyond the standard Matlab commands to clear any predefined variables, the first information the Matlab code contains is the home position of the stage. This position is represented by integers that are tenths of micrometers.

```
HomeX=469928;
HomeY=-50872;
```

The *x*-coordinate of the home position of the stage changes with temperature as well as with adjustment and wear of the wire guide. Because this program is not linked to the Qbasic program, the current home position must also be entered into this Matlab script.

The machining of the round begins along the side of the probe where the diameter is larger. The starting position of the probe is determined by several variables found at the beginning of this program, including wire radius and radius of the edge (100 μm). Because there are no commands to automatically create a rounded edge, a series of steps in the *x* and *z*-directions are listed in the code that will closely follow a radial arc. These values are stored in the arrays `xmove` and `ymove`.

To communicate with the μEDM controller, the serial port must be configured and opened. Commands are passed to the port using the `query` command, as shown here.

```
EDM = serial('COM1','BaudRate',9600,'timeout',1000);
fopen(EDM);
query(EDM,['buz 2'])
```

The programming language for the Panasonic μEDM controller consists of three and four letter commands followed by additional specifying characters or numerical

values. All commands are passed to the controller as alphanumeric characters. The command shown above, `buz 2`, causes the controller alarm to sound momentarily. The commands below start the spindle motor, set the capacitor number, set the voltage, turn on the voltage, and turn on the wire winding motor, respectively.

```
query(EDM,['spn 0'])
query(EDM,['con 3'])
query(EDM,['vol 2 -80'])
query(EDM,['vol 0'])
query(EDM,['wire 1'])
```

The above controller initialization commands are necessary for almost any µEDM application. Curiously, some of the logic bits are the opposite of what would be expected, for example `spn 0` applies power to the spindle and `spn 1` causes the spindle to stop spinning.

To machine the round, the controller must first find the edge of the probe by sensing discharges between the probe and the wire. The `abs` commands shown below align the probe correctly in x and y-directions, then the `map` and `cui` commands are used to sense the edge. Once the edge is located the `res` command is used to reset the z-axis to zero. Note that numerical values must first be converted to alphanumeric strings using the Matlab `num2str` command before being passed to the controller.

```
query(EDM,['abs x ',num2str(HomeX+Rsafe)])
query(EDM,['abs y ',num2str(HomeY)])
query(EDM,['map 10'])
query(EDM,['cui z 10 x 0 0 250'])
query(EDM,['res z'])
```

Once the edge is located, the coordinates stored in the `xmove` and `ymove` variables must be applied sequentially. A loop passes these 42 pairs of coordinates to the µEDM controller.

```
for N=1:42
    query(EDM,['abs x ',num2str(HomeX+Rsafe+xmove(N))])
    query(EDM,['cua z ',num2str(zmove(N)),' x 0 0'])
end
```

The controller will not accept new commands until the previous command is complete. The timing of the machining actions is therefore dictated by the controller and the parameters that are programmed into it. Once the machining is complete, the closing commands of the script move the probe to a safe distance, power down the spindle, the

voltage, and the wire winding motor, and activate the beep once again. The completed rounds of the probe are shown in Figure 6-9.

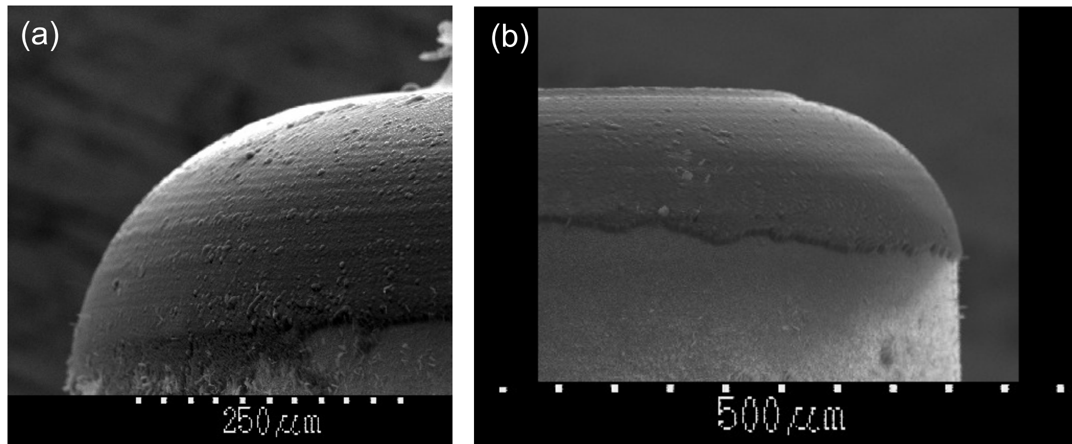

Figure 6-9. Electron micrographs of tungsten carbide probe (a) rounded step (b) rounded tip.

6.2.2 Improvements to the µEDM machine

Machining of a probe took as many as 10 hours in some cases, due to the relatively large amount of material that needed to be removed from the tungsten carbide workpiece. This machining time necessitates automation of the µEDM machine, in particular automation of the circulation of dielectric fluid. The dielectric fluid must always be present between the probe and the copper wire, as it carries away particles from the discharge gap.

Although the tank shown in Figure 6-3 can hold a small volume of dielectric fluid, experiments with this machine have shown a greater consistency in the machining process if the working area is continuously flushed with a laminar stream. The nozzle in the foreground of Figure 6-3 provides this flushing, and can be positioned relative to the workpiece as needed.

The original pump design consisted of a single plastic tank, an external rotary pump, a filter, and a manually-operated valve. The entire assembly sat on the floor below the granite table that supports the µEDM machine. The pump operated continuously, pushing fluid through the filter and valve and out the nozzle to the workpiece. The dielectric fluid washed down into the µEDM machine's own small tank and from there drained by gravity into the plastic tank on the floor below. A minimum fluid level was required to keep the pump primed, therefore the pump could not be located above the level of the fluid.

Two key problems plagued this system. The first was a rise in fluid temperature due to overworking of the pump. Since the pump is capable of pumping a much larger fluid volume than is needed by the μEDM machine, the valve must be almost completely closed to reduce the fluid volume to the desired, laminar flow. This results in a large backpressure on the pump, causing the pump to work harder and generate more heat. This heat in turn, raises the temperature of the dielectric fluid, which affects the accuracy and calibration of the μEDM machine.

The second problem caused by this backpressure was constant leakage of the dielectric fluid. Fittings between the pump and the valve, where pressure was high, were prone to leak; but the connection between the pump and the plastic reservoir also leaked due to vibrations of the pump itself. This connection could not be moved above the minimum fluid level as the pump needed priming. This constant loss of fluid limited the amount of time the EDM machine could operate without user intervention to a few hours. The processing time for machining a full probe required long periods of automated operation, so the pump system needed upgrading.

Recommendations from Panasonic engineers were considered for the new pump design, with the primary goals being the reduction of the pump cycle time, minimization of the temperature fluctuations, and elimination of the problematic leaks. The design consists of two plastic tanks, one "drain" tank consisting of used dielectric fluid placed on the floor below the machine, and one "reservoir" tank placed overhead. To keep the pump primed at all times, it is located at the same low level as before, but this time within the tank itself. An internal barrier separates the pump from the fluid filled drain tank. A schematic of the improved pump configuration is shown in Figure 6-10, and the assembled system is pictured in Figure 6-11.

Two float switches are located in the lower drain tank, one placed at the minimum fluid level and one placed at the maximum. When the drain tank is full, the upper float switch activates a locking relay, and power is supplied to the pump. The fluid is pumped through the filter, mounted just above the drain tank. Any small leaks from the filter simply run back into the drain tank. After the fluid is filtered it is pumped up to the top of the reservoir tank, mounted 2 m above the level of the μEDM machine. When the lower float switch (indicating minimum fluid level) is tripped the pump is deactivated. Fluid is

provided to the working area using a gravity feed the bottom of the reservoir tank. The fluid passes through the regulator valve, and then on to the nozzle shown in Figure 6-3. The typical cycling time of the pump during operation of the system is approximately 5 minutes for every hour of use. Since the pump is only energized when needed, the system can be powered on continuously. Once an experiment is complete, the valve is closed to prevent unnecessary cycling of the pump. An override switch allows a manual start of the pump system.

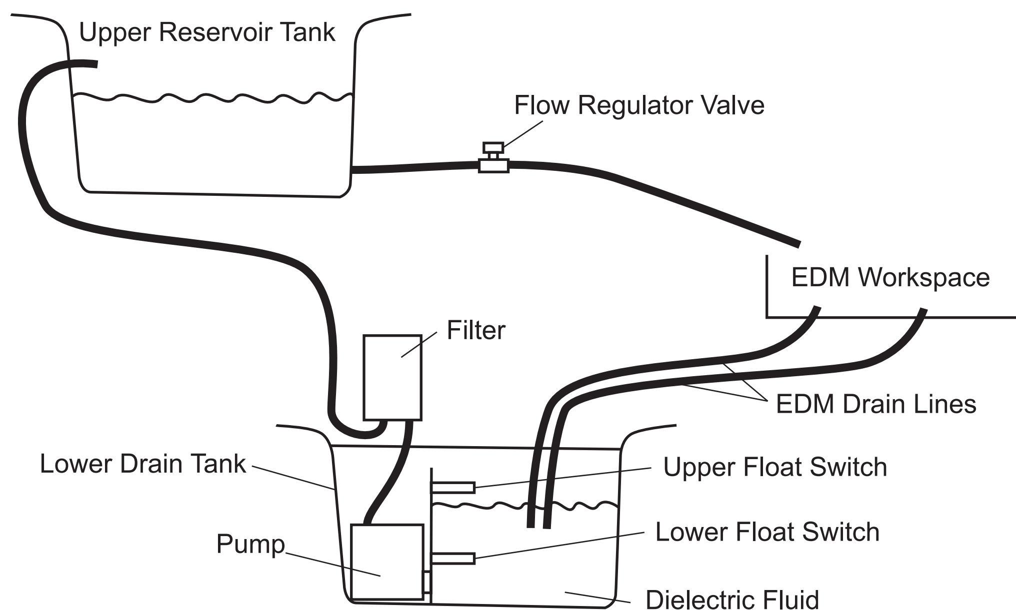

Figure 6-10. Schematic of pump configuration.

The temperature stability of the system is improved in two ways. First, the cycling of the pump has been reduced by approximately 90%, so the amount of heat introduced to the fluid is reduced by at least a corresponding amount. Secondly, the fluid is pumped to a large holding reservoir, which helps the fluid equilibrate to room temperature before being applied to the workpiece. Also, by reducing backpressure and cycle time, the pump life is extended.

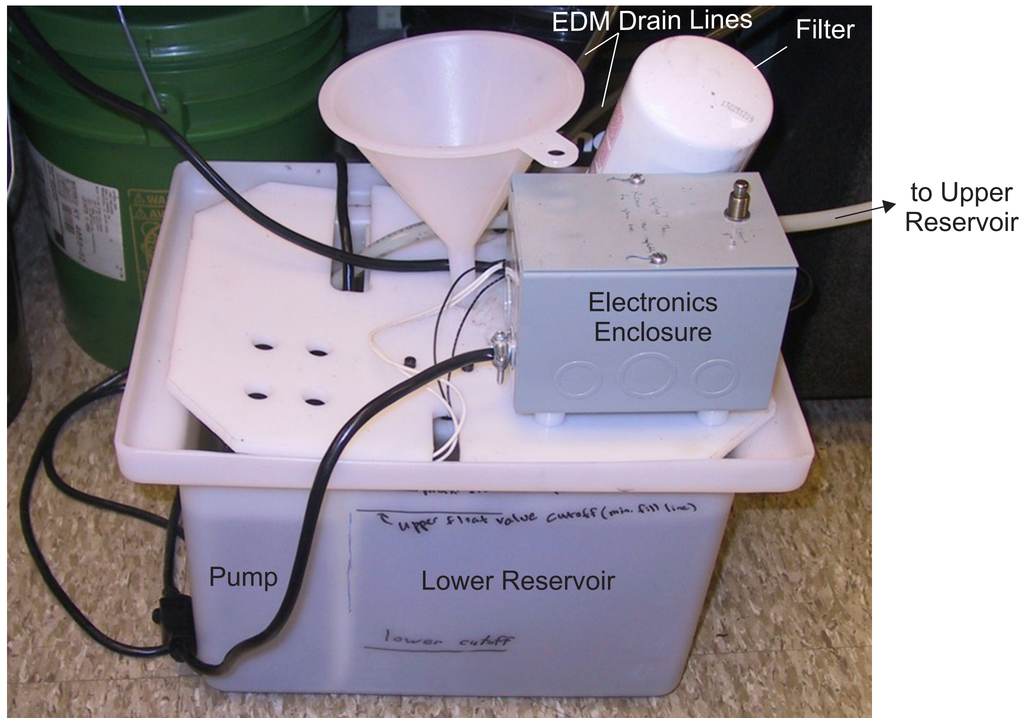

Figure 6-11. Improved pump design.

6.3 Coating the Probe

Once the tungsten carbide is shaped using WEDG, the probe is cleaned and coated with multiple layers of metals and oxides to create the electrical shielding necessary for a proper functioning capacitance probe. As with other capacitance probes, the sensing element, in this case the tungsten carbide, must be surrounded by an insulating material and an outer conductor. This outer conductor serves the same function as the guard ring, shielding the majority of the sensing conductor from the influence of nearby surfaces. Once the coatings are applied, a later step creates an opening back down to the tungsten carbide.

The material selected as the insulator is aluminum oxide (Al_2O_3 or alumina), and the outer conductor is gold (Au). These layers are added using ebeam deposition in a vacuum chamber, along with additional layers of material to enhance their adhesion. The coated probe is studied under the electron microscope and using a surface profilometer to determine the properties of the coatings.

6.3.1 Cleaning the probe surfaces

The µEDM process exposes the tungsten carbide probe surface to oils and other contaminants that would adversely affect the coating process and the vacuum level achievable in the coating equipment or in the scanning electron microscope (SEM). Before the probe can be coated, it must be thoroughly cleaned.

The cleaning process adopted for use with these capacitance probes is based on the RCA wafer clean process developed by Werner Kern at RCA Labs [111]. This process uses hydrofluoric acid (HF), hydrochloric acid (HCl), hydrogen peroxide (H_2O_2), and ammonium hydroxide (NH_4OH). Cleaning must be conducted in a clean room under a fume hood, and it requires extreme care and protective equipment. The prototype probes were cleaned in the Center for Nanoscale Science and Engineering (CeNSE) at the University of Kentucky.

The probe is first degreased with acetone, and then washed with isopropyl alcohol to remove the acetone. The probe is rinsed with deionized water to remove any remaining isopropyl alcohol. Next, the probe surface is exposed to a solution of deionized water and HF for 30 seconds. This finishes the preparation of the probe surface.

The first part of the RCA process, RCA-1, requires a solution of deionized water and NH_4OH to be heated to 70˚C. After the temperature is reached, H_2O_2 is added. Once the solution is bubbling continuously, the probe is added to the solution. After 10 minutes in the RCA solution, the probe is removed and rinsed with deionized water. This step is designed to eliminate organic contaminants from the surface of the probe, however, a thin oxide layer may be generated by this process. To remove this oxide layer the probe is soaked for 1 minute in a solution of deionized water and HF.

The second portion of the RCA process, RCA-2, removes any metals or ions adhering to the probe surface. This consists of a solution of deionized water and HCl heated to 70˚C. After temperature is reached, a volume of H_2O_2 is added, and the solution begins to bubble. The probe is immersed in the RCA-2 solution for 10 minutes and then rinsed several times with deionized water. Dry nitrogen is used to remove any remaining water from the probe.

Some other components destined to be used in vacuum can also be cleaned using the RCA method, including stainless steel mounts and screws. Aluminum parts and steel

screws coated with black oxide, on the other hand, reacted violently with the RCA process and were therefore cleaned ultrasonically in acetone instead. This proved sufficient to remove machining oils and to allow a good quality vacuum in the ebeam equipment.

6.3.2 Ebeam deposition of layers

Once the surfaces of the machined probe are clean, the probe is ready for coating. The two essential layers of material, a non-conductive oxide and an outer conductor, are applied using a Torr International Ebeam Evaporator system, available in the CeNSE Laboratory and pictured in Figure 6-12.

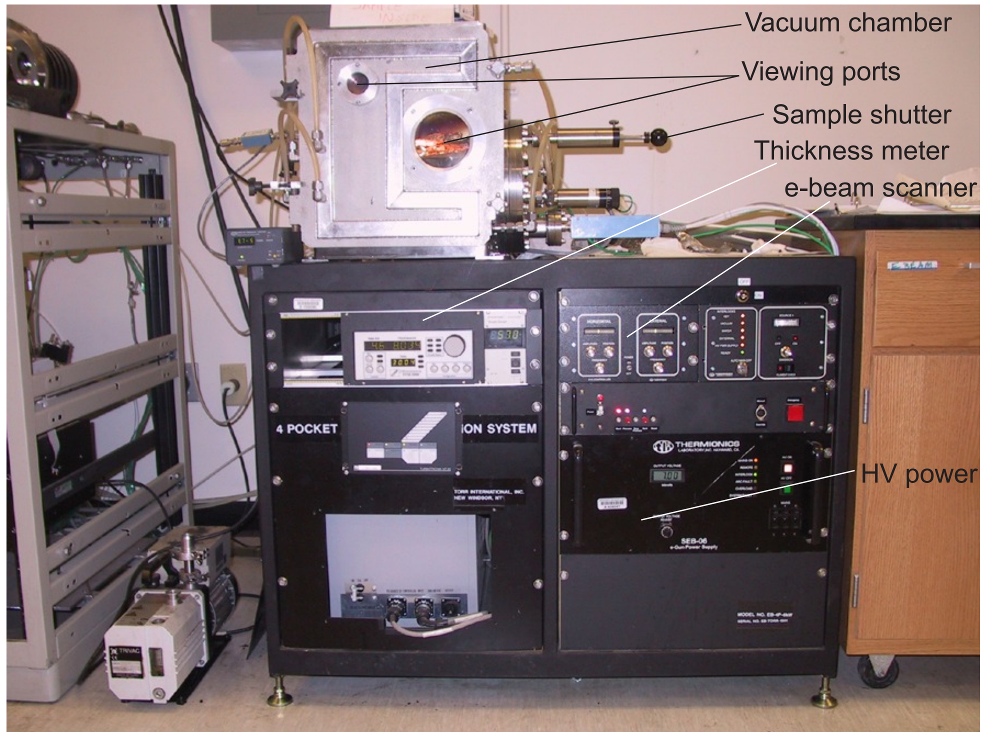

Figure 6-12. Torr International Ebeam Evaporator.

Ebeam evaporation offers several features that can be utilized in the probe manufacturing process. First and foremost, the system is able to monitor the thickness of coatings and provide constant feedback to the user as to what thickness has been deposited. The system is capable of relatively "thick" coatings, of 1 μm or greater, which are difficult to achieve with other technologies. Because the material is only evaporated locally, less material is used in the process, and unused material can be reused. This reduces the cost of coating with expensive materials such as gold. Finally, up to three

materials can be applied to the target surface without breaking the vacuum and requiring hours of additional vacuum pumping.

The deposition material is placed in a crucible within a vacuum chamber. The probe to be coated is suspended above the crucible, with the surface or surfaces to be coated facing downward. Once the system is pumped to a reasonable vacuum level, an electron beam is directed toward the target material in the crucible. This energy heats a small volume of the material to its melting point, where it evaporates into the chamber and coats the exposed surface of the probe. The melted material is contained by the non-melted portion of the material, or by the crucible itself.

As with many of the coating and etching steps, this machine is designed to process thin flat wafers such as those used in semiconductor manufacturing. As such, the available mounting system is designed to hold wafers, and an additional mount was added to accommodate the cylindrical probes. Two designs for probe holders are depicted in Figure 6-13. In (a), three possible mounting positions are offered. In (b), centering and alignment of the probe have been given the highest priority. The crucible, sample support structure, and one probe holder are shown in Figure 6-14.

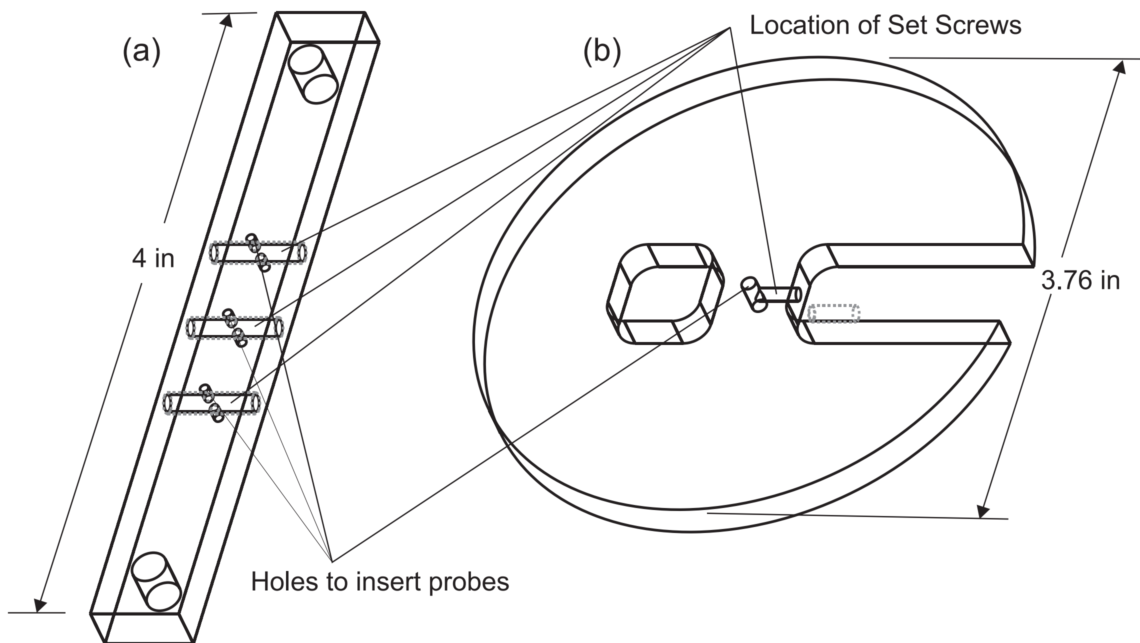

Figure 6-13. Two aluminum bracket designs for mounting cylindrical probes in the ebeam evaporator (a) bar design (b) wafer design.

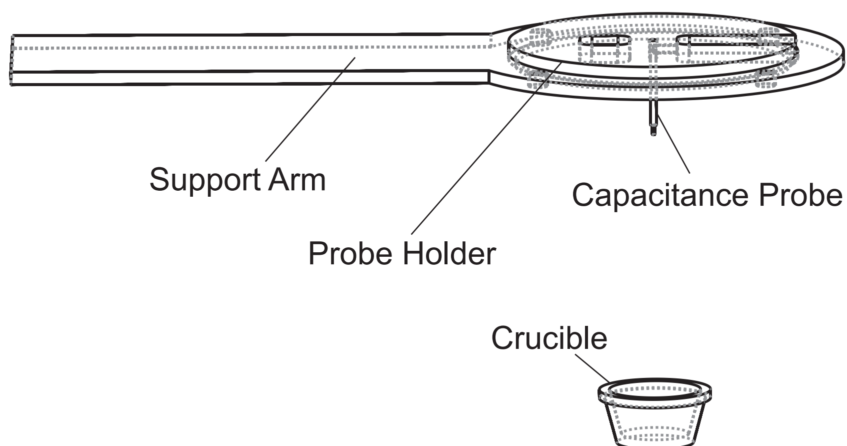

Figure 6-14. Assembly of sample support arm, probe holder, capacitance probe, and crucible showing relative positions of each within the vacuum chamber.

The ebeam evaporative coating process is directional, so two possible probe mounting positions are considered. In the first, the probe is mounted horizontally so that one side of the probe faces downward (i.e., toward the coating material). To achieve an even coating, the probe would have to be rotated, as if on a spit over an open fire. Unfortunately, although the ebeam chamber pictured in Figure 6-12 does offer mechanical feedthroughs, the design of the bellows prevents any rotation to be transferred to the interior of the chamber.

The second mounting orientation of the probe is with the probe pointing directly downward, shown in Figure 6-14. Although the material will preferentially coat the downward facing surfaces (in this case, the end of the probe and the edge where the diameter changes), this has no effect on the functioning or application of the probe. These areas are not directly adjacent to the sensing area that is etched in the side of the probe. The application of the probe is not affected, since additional buildup on the downward edges will not change the diameter of the completed probe. The range of holes that can be scanned with a given probe is affected only by the thickness of the material on the sides of the probe and not on the leading edges.

For the dielectric layer, alumina is placed in a graphite crucible. Once the probe and the crucible are placed in the chamber, the door is sealed and the system is pumped for 2-3 hours. After pumping but prior to coating, the vacuum level achieved by the system is approximately 10^{-6} Torr. Next, a voltage of 9 kV is applied to the electron gun, and a localized region of the alumina begins to be heated. This localized heating produces

an orange-yellow glow due to the temperature-dependent black body radiation of the material, as shown in the photograph in Figure 6-15. This photograph shows the holder from Figure 6-13 (a).

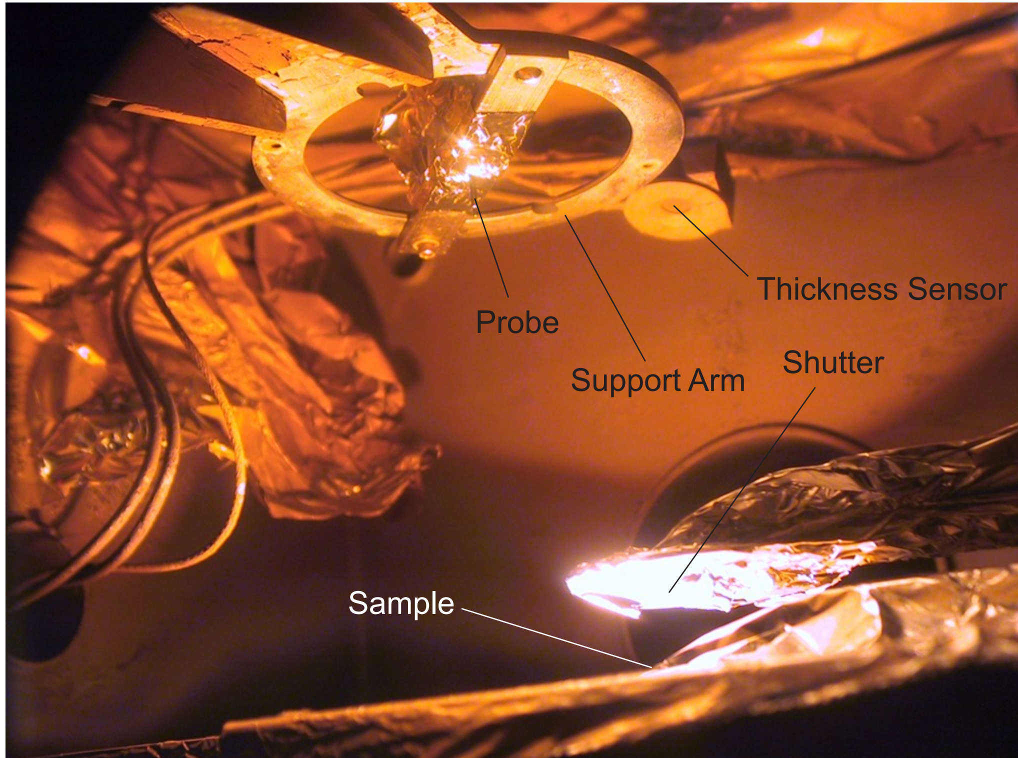

Figure 6-15. Photograph of ebeam evaporation chamber during coating process.

Once the material begins to melt and evaporate, the quality of the vacuum in the chamber decreases by an order of magnitude or more, depending on the rate of evaporation. To increase the quality of the coating, a shutter blocks the deposition of material during the initial melting process. Once a deposition rate of 3-6 Å/s (0.3-0.6 nm/s) is reached, the shutter is moved manually so that coating of the probe can begin. The coating sensor, also labeled in the photograph, is never blocked by the shutter, so both an overall coating thickness and a coating rate can be measured both before and during the actual coating of the probe.

This sensor measures the thickness of material deposited on it vibrationally. The probe oscillates and the frequency of oscillation is measured. As the mass on the probe increases due to deposition of material, the frequency slows by a measurable amount. With a known surface area, the thickness can be determined simply by knowing the density of the coating material. These densities are entered manually into the system, and

preprogrammed densities can be selected by a menu on the front panel of the ebeam system.

Two problems were revealed in early coating tests. The first difficulty stemmed from attempts to coat two probes simultaneously in the ebeam chamber. As shown in Figure 6-13, the initial probe holder can support as many as three probes at a time. Two probes were coated in this manner, and these probes both showed a distinct asymmetry. The close proximity of one probe caused a lopsided distribution of coating material on the other. A diagram showing how some areas of the probe receive extra material appears in Figure 6-16.

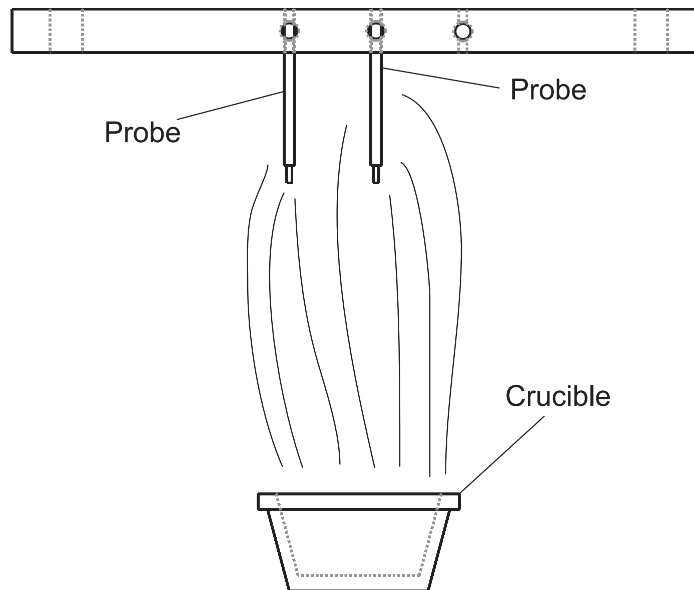

Figure 6-16. Diagram of asymmetric coating when two probes are present.

The second problem revealed in early coating tests was poor adhesion to the tungsten carbide. As shown in Figure 6-17, early coatings had a tendency to separate from the tungsten carbide, particularly at corners and edges of the probe. Since good shielding requires all of the layers to strongly adhere to the probe, two changes were instituted after this discovery. The first change was to the geometry of the probe. As described in section 6.2.1, the two convex edges of the probe are rounded using additional μEDM steps. These changes have no bearing on the electrical functionality of the probe, they are only for the purposes of eliminating the sharp angles.

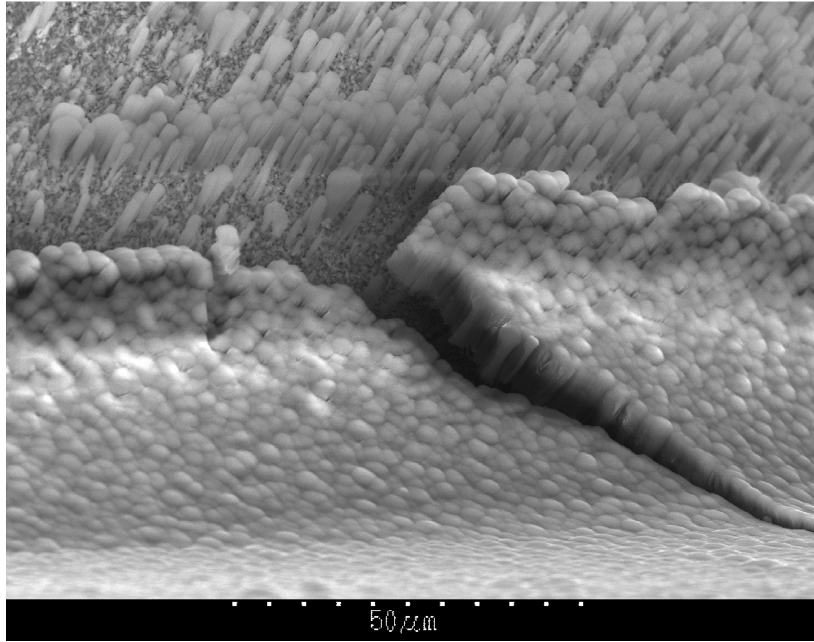

Figure 6-17. Probe coating peeling from tungsten carbide surface.

The second change begun as a result of this peeling was to add an interstitial coating between the tungsten carbide base and the alumina. A search of machine tool literature reveals that nickel is commonly applied to tools edges prior to tungsten carbide [112, 113]. Because the ebeam evaporation chamber can handle up to three coatings, it is relatively straightforward to add a second crucible of nickel to the chamber. For the nickel, a thin coating of only 30 nm is applied at a potential of 800 V. At a rate of 1-2 Å/s (0.1-0.2 nm/s) this extra step takes only a few minutes.

Once the probe is coated with nickel and alumina, it is important to verify that these coatings are present on the entire exposed surface of the probe. The light microscope is unable to show enough differentiation between tungsten carbide and alumina to allow for differentiation, and the nickel coating is too thin to make a visible difference. Instead, the scanning electron microscope (SEM) tests the surfaces at various points to verify the presence of the coatings.

Figure 6-18 is of an uncoated probe, showing details of the surface obtained from the μEDM machine. The second picture (Figure 6-19) shows the surface after a 30 nm coating of nickel, and the Figure 6-20 shows the alumina coating. Even at a magnification of 15,000, there appear to be no obvious visual differences between the three surfaces, at

least not any differences that can be exploited to determine the thickness of the coating. An elemental analysis was necessary.

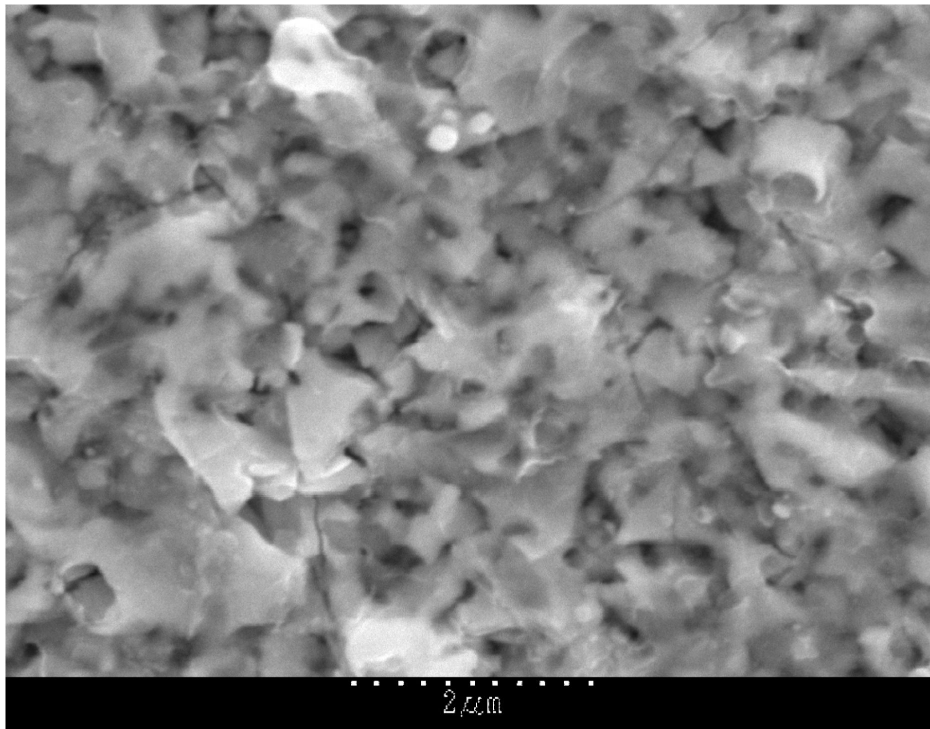

Figure 6-18. Uncoated tungsten carbide probe.

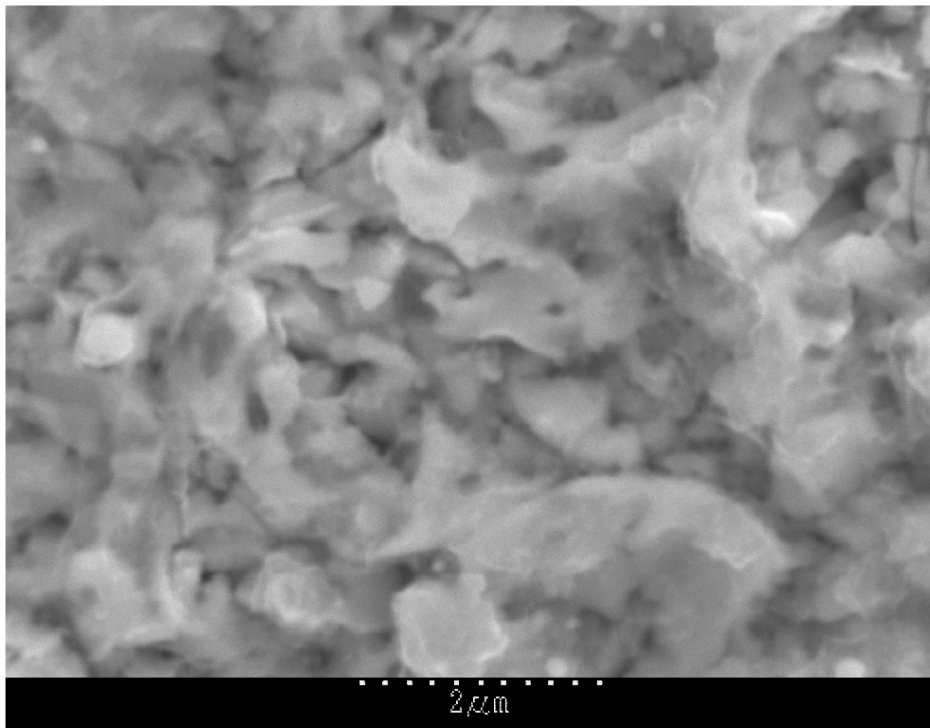

Figure 6-19. Tungsten carbide probe with nickel coating.

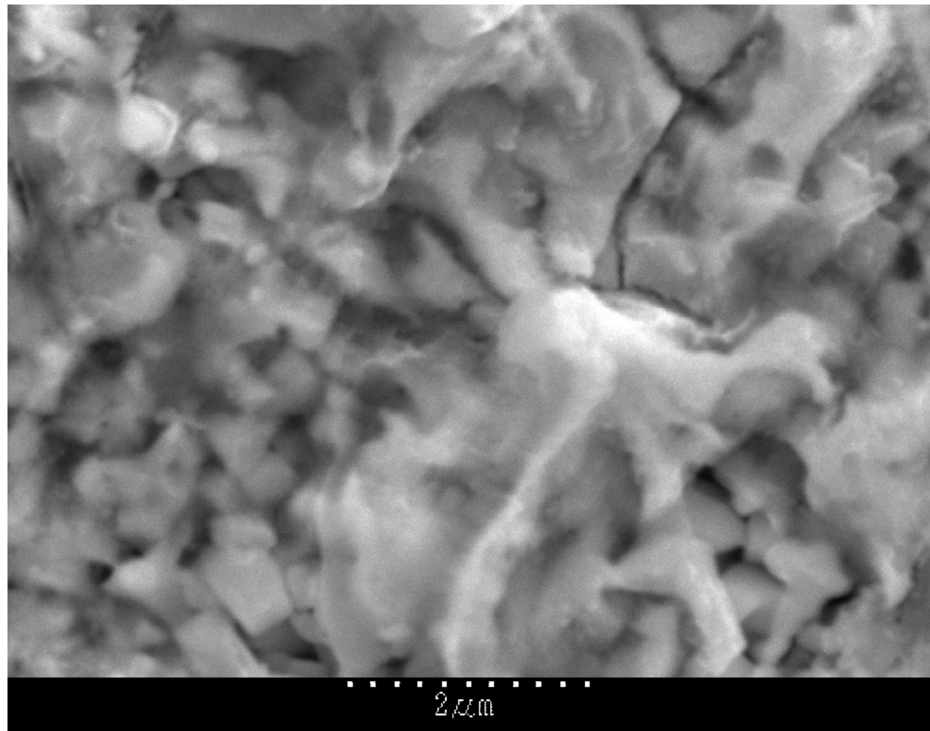

Figure 6-20. Probe with nickel and alumina coatings.

Fortunately, the Hitachi S-3200 SEM available in the Electron Microscopy Center at the University of Kentucky is capable of point or area X-ray elemental analyses. The point analysis samples a small three dimensional volume at the location selected on the display of the SEM and determines the likely elements present. The area analysis scans a larger surface and provides an X-ray spectrum that represents a thickness of approximately 3 μm. In either case, a Sun workstation provides automatic selection of possible elements given the X-ray peaks. Results from analysis of two coated probes are shown in Figure 6-21 and Figure 6-22. These spectra show the energy of detected photons (in keV) on the abscissa and the number of photons detected ("counts") on the ordinate.

The data as plotted by the X-ray software represent a 60-second exposure of the graphically selected point or area of interest. The peaks can be labeled automatically, although elements with similar spectral peaks can be mistakenly identified by the software. By correlating several peaks, the user can manually confirm the presence or absence of specific elements. Unfortunately, no method exists to export the numerical spectral data from the Sun workstation to another program.

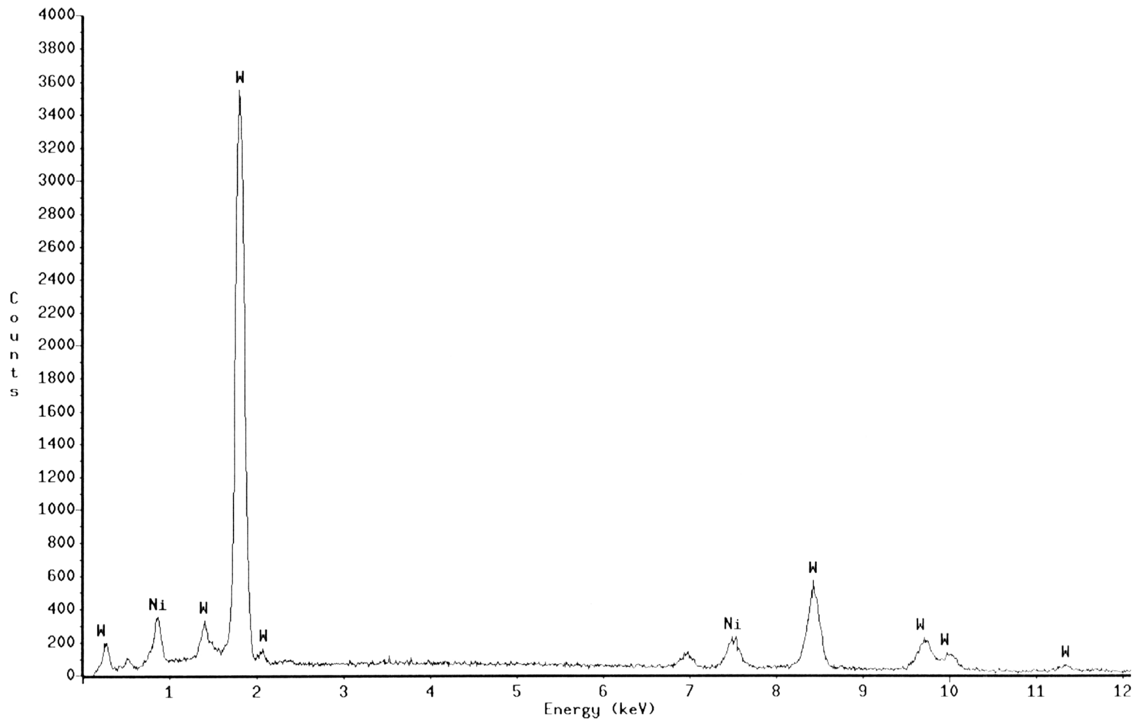

Figure 6-21. X-ray spectrum from nickel coated probe.

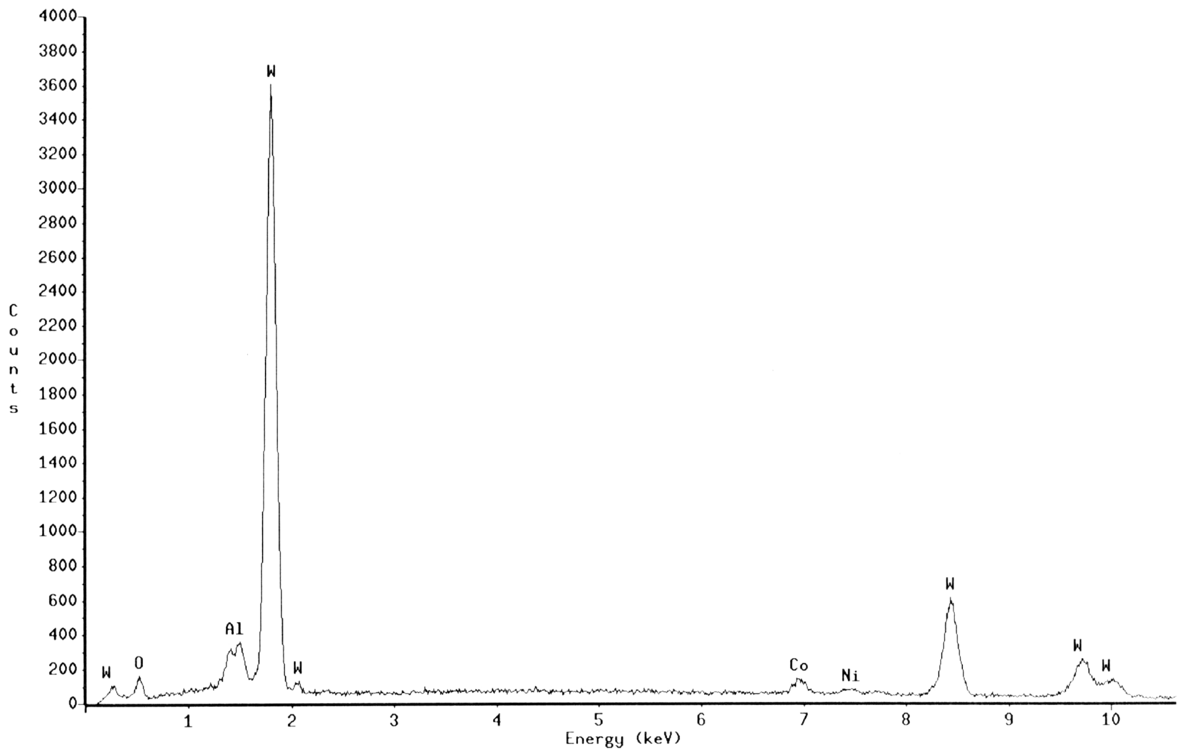

Figure 6-22. X-ray spectrum from nickel and alumina coated probe.

The data shown in Figure 6-21 shows two peaks for nickel (Ni) and several peaks for tungsten (W). Since the incident X-rays interact with 3 μm of material, the tungsten

peaks are expected in this figure. Similarly, the data shown in Figure 6-22 include peaks for aluminum (Al) and oxygen (O), the elemental components of the alumina that coats the surface of this probe. Nickel and tungsten also appear in this spectrum, but this does not in itself indicate whether or not the coating is contiguous or is more scattered. Proof of the continuity of the alumina coating must wait until the probe can be tested electrically.

The next coating step to be applied to the probe is to deposit gold over nearly the entire end surface. The goal of this coating is to provide the same function as a guard ring in a traditional capacitance probe. Areas of tungsten carbide that are completely enveloped by the gold coating cannot sense capacitance between itself and the surrounding target surface. Only openings in the gold coating allow the underlying tungsten carbide to sense the target.

Although the ebeam deposition system allows up to four materials to be applied without breaking vacuum, in practice the gold must be applied in a separate step for this probe. This is due to the need for the alumina and the gold coatings to cover different areas of the probe shaft, as illustrated in Figure 6-23. The gold coating cannot cover as much surface as the alumina coating. This need stems from both the inexact nature of the coating process, particularly at the back edge, and the need to maintain electrical isolation of the gold coating and the tungsten carbide. This isolation is critical for the gold to function properly as a guard structure. The staggering of the layers is achieved by wrapping the probe in foil during the coating process, preventing coating of the covered section. The vacuum chamber had to be opened between the alumina and the gold layer to move the position of the protective covering.

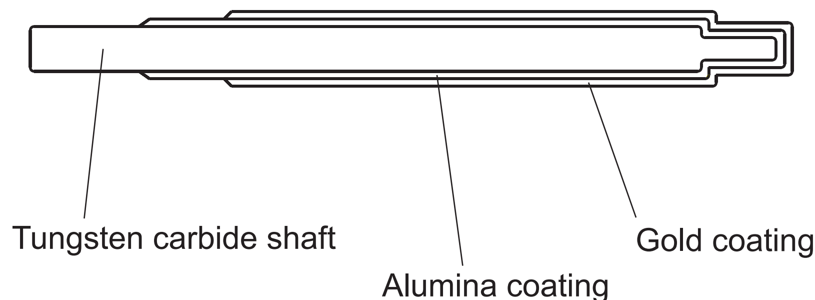

Figure 6-23. Model of coated probe, showing larger area for alumina coating than gold layer. Thicknesses of coatings are exaggerated for illustrative purposes.

As with the previous coating, the gold must remain firmly attached to the underlying material. The underlying material in this instance is the alumina, and a search of the literature reveals that chromium is commonly applied prior to a layer of gold [114, 115]. With these materials, the total number of coatings grows to four, as outlined in Table 6-5. Fortunately the chromium and the gold can be placed in the ebeam evaporation chamber at the same time, and the system pumped. Once a vacuum level of approximately 10^{-6} Torr is reached, the voltage was set to 700 V and the chromium is heated. At a rate of approximately 1 Å/s (0.1 nm/s) application of 2 nm takes less than a minute. Switching to the crucible containing gold, a target rate of between 3 and 6 Å/s (0.3-0.6 nm/s) results in a 1 μm coating in less than an hour.

Table 6-5. Materials applied to the tungsten carbide probe, in order of application.

Material	Thickness, nm	Voltage, V	Crucible
Nickel	30	800	Graphite
Alumina	1,000	900	Graphite
Chromium	2	700	Graphite
Gold	2,000	900	Fabmate

6.3.3 Probe surface metrology

One measure by which probe manufacture can be deemed "successful" is by assessing how closely the actual machined surface matches the theoretical model. Rough surfaces at some scales can cause nontrivial changes in the electric field that affect the ability of the capacitance probe to accurately measure the target surface. It is necessary, then, to quantitatively measure the probe surface, both before and after the coatings have been applied.

Although the scanning electron microscope is capable of providing excellent images of a variety of different materials over a wide range of magnifications, it is not capable of measuring surface topography. The scales shown on SEM images such as Figure 6-20 assume a flat surface projected with no distortion onto the display, an assumption perhaps suitable for a wafer process but not for a cylindrical probe. To accurately perform measurements on the probe surfaces, a 3D surface profilometer is needed.

The Zygo NewView 5000 Profilometer is available through the University of Kentucky Bearings and Seals Lab. This device offers sub-nanometer resolution, ideal for surface roughness measurements. The feature size is small for all of the coated surfaces, so the maximum magnification objective of 50x was selected. This magnification, in combination with other optics and the size of the imaging CCD array, resulted in an area of 0.11 by 0.15 mm being analyzed. The optical filter MEAS is selected as optimal for surfaces, with an R_a of less than 3.0 µm. The bandwidth of this filter as determined by the manufacturer is 125 nm with a coherence length of 2.9 µm [116].

The Windows-based MetroPro software includes several predefined applications for data collection and analysis. The program 'micro.app' is the standard microscopy application utilized, and pictured in Figure 6-24. The display includes a color-coded topographical image, a three-dimensional display of the same image area, a cross-sectional graph of a selected line of image data, and several numerical results. The results of primary interest to this project are 'PV,' 'rms,' and 'Ra'. These terms are defined in detail in the discussion below.

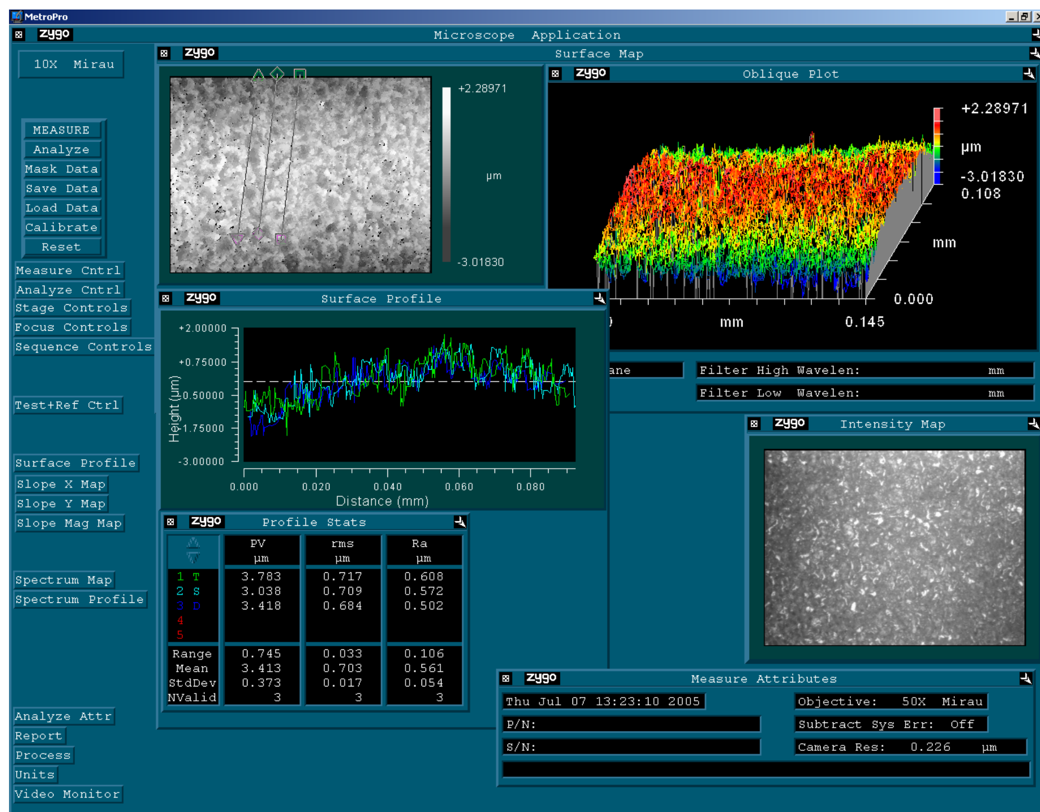

Figure 6-24. The 'micro.app' profilometry application.

Interferometric profilometers such as the NewView use coherent light to illuminate a target surface. The reflected light is then passed through optics to cause constructive or destructive interference of the illumination, depending on the distance the object is from the optics. This pattern of interference results in an image with “fringes,” or rings over part of the surface. These fringes, much the same as a topographical map, represent parts of a surface that are the same distance from the optics of the microscope. Four patterns are shown in Figure 6-25. The fringes are present in the regions that show higher contrast and are in sharper focus.

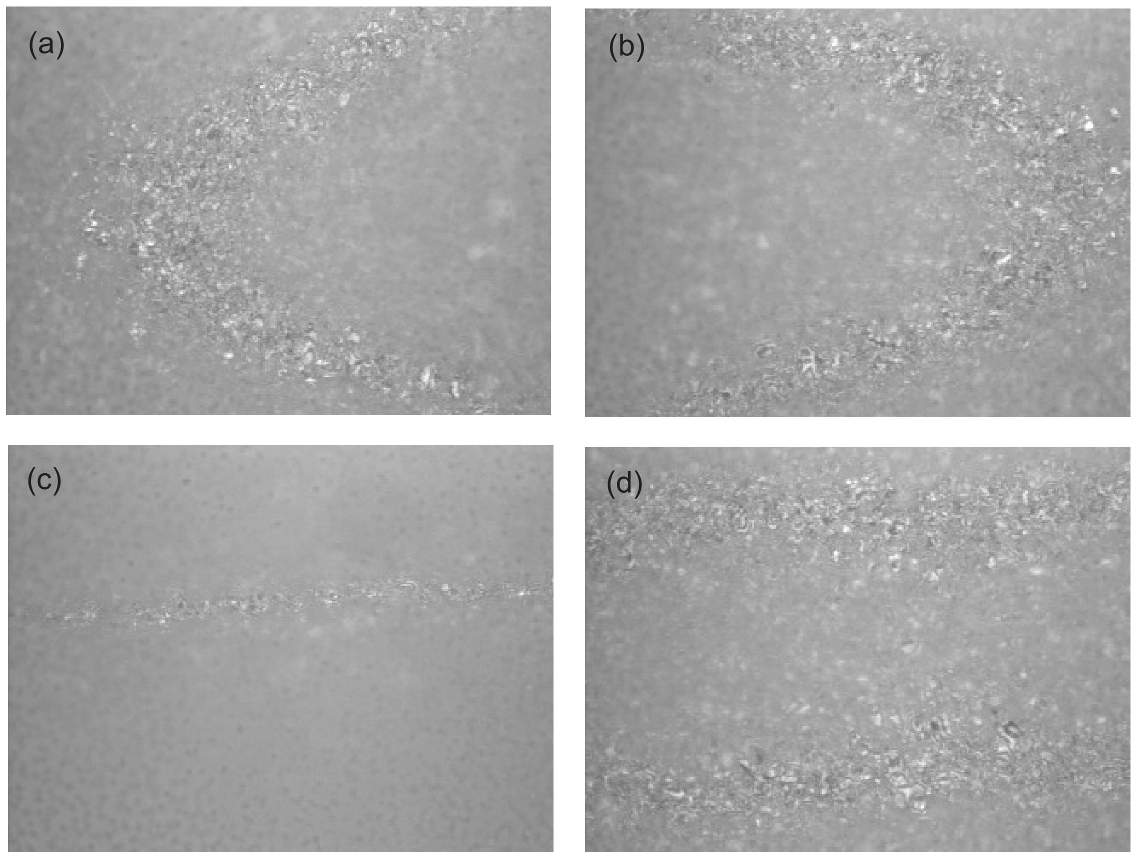

Figure 6-25. Interference patterns or “fringes” from the Zygo NewView.

These images illustrate that alignment is necessary for optimal measurements with the NewView. In images (a) and (b), the cylindrical side of a probe is tilted such that the right side (a) or left side (b) of the sample is closer to the optics. Ideally the sample is aligned so that the imaging area lies as much as possible in the plane of the optics. Fortunately, the NewView allows the entire stage to be tilted to rectify alignment errors. Image (c) of Figure 6-25 shows a single, narrow fringe. This indicates that the entire

surface is sloped, in other words the sample is not properly positioned in *x* and y. To maximize the depth that can be measured by the NewView, the sample is positioned so the surface is as close to flat as possible. Also, the starting position of the sample has the fringes placed closer to the middle depth to be measured. Image (d) shows the correct position for the placement of fringes. Since the fringes are parallel, this also indicates that the tilt has been corrected.

The NewView profilometer has inherent limitations on its vertical travel, termed its "scan length." Without special modifications, this travel is 40 μm. Although the roughness of the probe should be an order of magnitude less than this value, recall that this scan depth includes not only the surface roughness but, since this is a cylindrical probe, the curvature or form as well. Points in the image that do not fall within this range will not have data recorded. These "dropouts" can affect the statistics of the analysis, so they are minimized. Dropouts can also occur if the slope of the surface is too close to vertical. In those cases the scanning software cannot accurately count the number of fringes from the top to the bottom of such a feature, and so once again the data are left blank.

With the alignment of the sample set and the *z*-position optimized, the light level must be adjusted. This adjustment is important because the frame grabber collecting images has only a limited dynamic range. Too much light and the A/D becomes saturated, so subtle differences between fringes (and thus differences in height) cannot be determined. Too little light and some areas will fall below the minimum intensity, causing additional dropouts in the data. The light intensity is adjusted by varying the magnification of the sample and the illumination. The locations of the fringes on the sample are the point of maximum intensity, so a check of the light intensity includes the step of passing the sample back and forth through this fringing region. Intensity levels peaking above 90% of the range of the A/D are considered optimal.

With all of these settings in place, data collection began by clicking on the 'Measure' button. The 640 × 480 pixel camera has a frame rate of 20 Hz, so a complete set of data was collected and analyzed in less than a minute. The results are shown in a dialog window similar to Figure 6-24. With the probe surface the best-fit surface is a

cylinder, so the Micro.app application is set to automatically calculate this cylinder and remove it from the displayed data and the subsequent analysis.

Three values from this analysis indicate quantitatively the type of surface in question. 'PV' is the difference in height between the highest point and the lowest point of an image (not including dropouts). 'rms' is the root-mean-square deviation of the data from the best-fit cylinder. 'Ra' is the average deviation of all points from the cylinder surface. When comparing surfaces before and after coatings, it is important to note whether the coating average deviation is more or less than the original surface. If less, then the coating has tended to "fill in" the low spots and generate a smoother surface than the original. If the average deviation is greater, then the coating has adhered to the high spots, possibly leaving gaps in coverage. Finally, other filters can be applied to the surface to remove different frequency bands or to give more detailed information on the nature of the surface. If these functions are still insufficient for analysis, the raw data can be exported from the NewView software for analysis in another package.

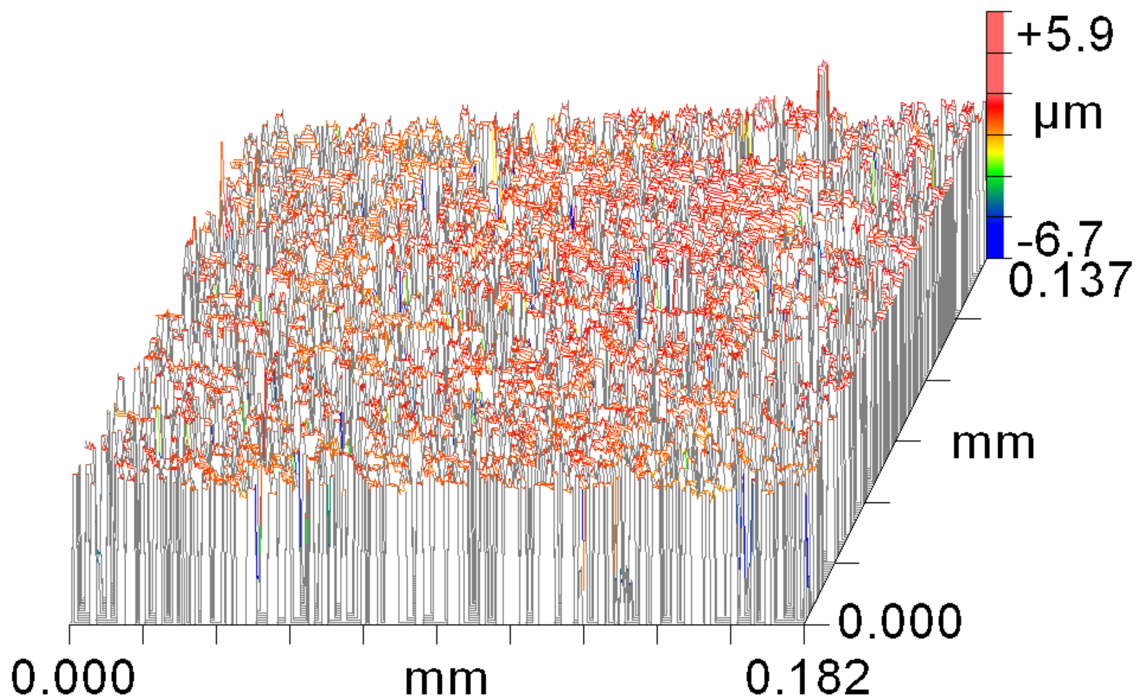

Figure 6-26. Oblique plot of incomplete alumina coating.

A particular example helps illustrate conclusions about the coating process. The data in Table 6-6 are from an early probe coating of nickel and alumina. Four different

areas of the larger diameter of the probe were measured before and after these two coatings were applied. The values in the table show how much variation there is from one area to the next over the surface, as well as the changes to these values that occurred during this coating step. For example, the rms deviation more than quadruples in the coating process, from 0.342 μm to 1.659 μm. The R_a values also quadruple, indicating that the coating has significantly increased the roughness of this surface. The standard deviations shown in the table help determine the accuracy of these values, by showing how much they vary from area to area.

Table 6-6. Values before and after incomplete alumina coating.

	PV, μm		rms, μm		R_a, μm	
	Uncoated	**Coated**	**Uncoated**	**Coated**	**Uncoated**	**Coated**
Area 1	3.350	12.180	0.311	1.697	0.240	1.218
Area 2	3.938	11.963	0.361	1.683	0.285	1.192
Area 3	3.214	11.014	0.327	1.621	0.256	1.021
Area 4	5.362	12.622	0.368	1.636	0.270	1.072
St. Dev.	0.982	0.678	0.027	0.037	0.019	0.094
Mean	**3.966**	**11.945**	**0.342**	**1.659**	**0.263**	**1.126**

The data in Table 6-6 can be contrasted with the data in Table 6-7, which represents a complete coating of both gold and alumina. Here the rms value increases by 0.12 μm and the R_a value increases by just over 0.08 μm. Compare this with the overall thickness of both coatings of over 2 μm, and it is clear that these coatings are solid and contiguous. A plot of this coating is shown in Figure 6-27.

Table 6-7. Values before and after application of gold coating.

	PV, μm		rms, μm		R_a, μm	
	Uncoated	**Coated**	**Uncoated**	**Coated**	**Uncoated**	**Coated**
Area 1	5.388	10.102	0.335	0.469	0.266	0.340
Area 2	5.042	5.423	0.355	0.478	0.284	0.380
Area 3	4.616	5.512	0.360	0.472	0.285	0.374
Area 4	5.295	5.993	0.392	0.487	0.314	0.385
St. Dev.	0.345	2.244	0.024	0.008	0.020	0.020
Mean	**5.085**	**6.758**	**0.361**	**0.477**	**0.287**	**0.370**

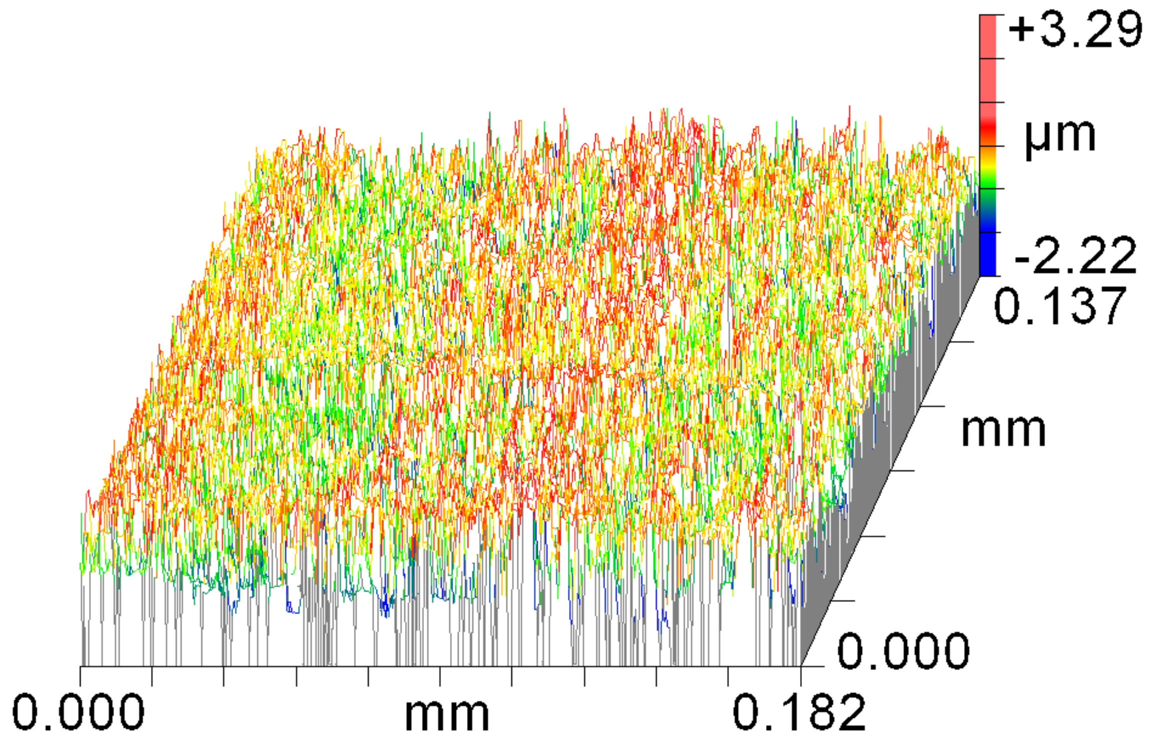

Figure 6-27. Oblique plot of complete gold coating.

6.4 Conclusions

This chapter described the manufacture operations for a prototype probe. The machining of tungsten carbide was achieved using both preprogrammed routines and custom-written code on the Panasonic MG-NC 82 µEDM machine. The operating parameters for this machine are carefully chosen to minimize the surface roughness and to optimize both precision and repeatability. Measurements of the machined tungsten carbide "blank" were recorded using a calibrated optical microscope.

Once the tungsten carbide was machined, multiple coatings were applied to the outer surface of the probe. To provide an insulating layer, alumina was first applied to the probe using ebeam deposition techniques. The thickness of the coating was measured at the time of deposition so that the correct thickness is achieved. After the alumina was applied, the probe was moved within its mount and gold is deposited. It is this outer layer of gold that became the guard structure of the new capacitance probe design.

Once both coatings were in place the surfaces were studied qualitatively using SEM imaging and quantitatively using interferometric techniques. These numerical results indicate that the coatings on the final set of probes appear to be contiguous. The

SEM images taken of the coated surfaces show no significant difference in surface roughness between the uncoated tungsten carbide probe and the probe with the completed layers. The average surface parameters also indicate that the roughness does not increase significantly when the probes are coated. The inherent limitation to having a perfectly smooth surface is due primarily to the limitations of the μEDM process.

Once the coating steps are optimized, the next step in the manufacture process is to develop techniques for etching a hole in the layers. Several possible techniques are described in Chapter 7.

Copyright © Philip T. Smith Jr. 2007

7 Probe Etching and Testing

7.1 Introduction

After depositing the insulating (Al_2O_3) and conductive (Au) coatings on the tungsten carbide probe, the next step is to selectively remove either the gold or both the gold and alumina layers from the sensing area. This "window" allows the inner tungsten carbide conductor to sense the target surface. Areas of tungsten carbide under the guard layer are prevented from sensing the target, and only sense the gold layer. The gold layer is held at the same potential as the tungsten carbide shaft, in which case the electric field between the probe and the guard surface is zero.

There are several methods to open a window through one or both coatings of the probe. Some techniques, such as focused ion beam (FIB), use a narrow beam of charged atoms (e.g., argon) focused in a pattern on the surface of a part [117]. The FIB instrument must be programmed to scan the beam in the desired pattern. This technique is useful if a large variety of patterns are to be tested. Unfortunately, the focused ion beam method is slow and expensive.

Etching is a more cost-effective method, but an optical or physical mask is required. For typical wafer applications, a mask can be generated using a photoabsorber material on a glass or quartz substrate. The latter is transparent to ultraviolet wavelengths. For the cylindrical probe, a cylindrical mask is required. The shape of the window through the layers matches the shape of the opening in the mask, taking into account any dilation that might occur due to limits in diffraction or beam collimation. The manufacture of the mask is a separate step from the removal of the probe material and therefore requires a higher initial cost. Once mechanical masks are produced, higher removal rates are possible, including parallel processing of multiple probes.

With a mechanical mask, more than one method is available for removing material. In wet etching, the probe is coated with a resist layer, just as is traditionally done with wafers. A mask in then put in position over the probe and the material is exposed to visible or UV radiation. The exposed resist is developed so that etching chemicals remove material only in the sensing area. For wet etching, the length of time to etch each material is a linear function of the thickness of the material. After etching is complete, the remaining photoresist material is removed chemically.

Dry etching is an alternative method for removing the coating layers from the surface of the probe. Two methods of dry etching are ion etching and ion milling. In both cases, a physical mask is positioned over the probe and the assembly is placed in an etching chamber. A collimated beam of high energy particles is directed toward the probe, and material is removed from all exposed surfaces, including the mask. The etch rates for these processes are determined by the intensity of the beam rather than the material being etched, so experience with a particular setup is the best guide here.

A final method for material removal is by mechanical means, where microgrinding removes the outer layers of material [121]. This technique, like FIB, requires that the grinding tool be programmed with the desired pattern. Because this is a physical, contact process, there exist certain limitations on the shape of material that can be removed from the probe. Both chemical etching and mechanical grinding were applied to coated capacitance probes. Chemical etching was capable of removing the gold and alumina, but the photoresist process proved difficult to control. Mechanical grinding successfully opened a window to the tungsten carbide, verified by SEM X-ray analysis.

7.2 Manufacture of a Physical Mask by µEDM

To create the oblong hole necessary for this capacitance probe, a physical mask must be close to the surface around the entire perimeter of the desired hole. An open-ended channel is possible, but a simpler solution is a hollow tube. Hollow tubing is readily available in stainless steel or nickel in a wide range of dimensions [118]. One commercial application of this tubing is for hypodermic syringes.

A nickel tube with an outer diameter of 1 mm and an inner diameter of 800 µm is used as the base material for a physical mask. A hole is then machined using the Panasonic µEDM MG-82 machine, but micro milling EDM is used instead of WEDG. To manufacture the mask, a tungsten electrode is first machined by WEDG, and then this electrode is used to mill a slot of the desired size in the nickel tubing with electrical discharges.

7.2.1 Creating the mask-making tool

The mask-making tool has a cylindrical shape, and it is long enough to machine through the tubing with some length to spare. Two possible patterns for the hole in the mask are a rectangle with rounded corners, where the rounds have the radius of the tool, and a slot

with semicircular ends, where the width of the slot is the diameter of the tool. The latter design maximizes the radii of curvature for the probe and therefore minimizes electric field concentration. Therefore, the simple slot is chosen as optimal. The dimensions of the slot on the probe are 400 μm by 800 μm as shown in Figure 7-1.

The QuickBasic program 'EDM72.BAS' was executed with the steps listed in Table 7-1. The surface finish on the electrode is not critical, so all of the machining steps use the maximum voltage (110 V) and largest capacitor (3300 pF) to maximize material removal rate. After machining, the probe is analyzed under the light microscope and the Image-Pro Express software is used to determine the dimensions of the tool. The diameter of the tool was 415.7±1.4 μm, and the length of the straight part of the tool was 517.0±1.0 μm.

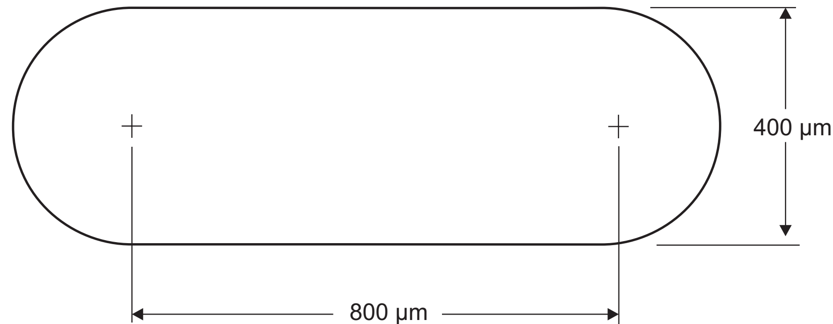

Figure 7-1. Dimensions of the slot to be machined in the nickel mask.

Table 7-1. Routine for creating the mask-making tool.

Step	1	2	3	4
X high	0	400	300	200
X low	0	400	300	200
Z length	20	500	500	500
Z offset	0	0	0	0
R	0	0	0	0
Capacitor	1	1	1	1
Voltage	110	110	110	110
Z speed min	3	3	3	3
Z speed max	50	50	50	50
Rotate	1	1	1	1

7.2.2 Machining the slot

The stock tubing used to produce the mask was mounted in the right-hand tank of the μEDM machine. A 200X (setting) microscope with ruled grid, shown in Figure 6-2 on page 150, was used to optically align holes and edges. Unfortunately the focusing *z*-stage of this scope had some parasitic motion, so an alignment procedure was performed for each machining process. This alignment procedure is as follows:

1. Mount the nickel tubing on the stage, alongside a polished piece of scrap material at the same height.
2. Focus the setting scope on the nickel tubing and lock the setting scope in place. The setting scope remains locked during the rest of the procedure.
3. Loosen the Allen screws holding the stage to align the tubing with the *x*-direction of the stage, as observed through the setting scope. Retighten the screws.
4. Center the mask tool over the polished scrap and record the *x* and *y* position of the stage.
5. Machine 5 holes in the scrap material in the pattern of a + sign with the center hole located at the x, *y* position from step 4.
6. Move the 5 holes to below the setting scope and record the *x* and *y* position of the center hole. The 4 additional holes help ensure proper alignment.
7. Use the *x* and *y* measurements to determine the difference between the machining axis of the μEDM and the crosshairs of the setting scope.
8. Locate the position on the nickel tubing where the machining is to begin. Use the difference between this *x*, *y* location and the location of the center hole of the + pattern to determine the correct *x*, *y* machining position for the tool.

The exact offset between the machining axis and the setting scope depends on the height of the sample, wear on the spindle, ambient temperature, and other factors. For this reason, this routine is applied for each change of tool or part.

The actual machining of the slot is straightforward and involves only a single command to the μEDM machine. This is the `MCV` command, which is a slot machining process with a lift command at the end of the final process. An `MCV` command has the syntax shown below, and can be passed to the μEDM machine using QuickBasic or Matlab.

```
MCV X 8000 0 2500
```

The parameters of this command are slot direction (`X`), positive feed length (`8000`), negative feed length (`0`), and depth of the slot (`2500`). The machining direction must be purely *x* or *y*. For this reason the accuracy of the alignment of the part with the *x*-axis of the machine is reflected in the final slot alignment. The slot can be machined in one or two directions, in this example the slot is only machined in the positive *x* direction. The initial alignment of the part in this case represents the center of the arc of one end of the slot, as shown in Figure 7-1. Since the diameter of the electrode is 400 μm, the end of the slot is 200 μm away from the starting point. A photograph of the machining process is shown in Figure 7-2.

The units of distance in these native commands are increments of 0.1 μm. The length of the straight sides of the finished slot was therefore programmed to be 8000, or 800 μm. Adding in the diameter of the tool, the total length of the slot was nominally 1200 μm, with a width of 400 μm. The width of the slot was determined purely by the diameter of the tool, no motion in the *y* direction can be programmed with this command. The 250 μm depth of the slot was sufficient to cut through the thickness of the nickel tube (100 μm), factoring in both the curvature of the tube and wear on the tool.

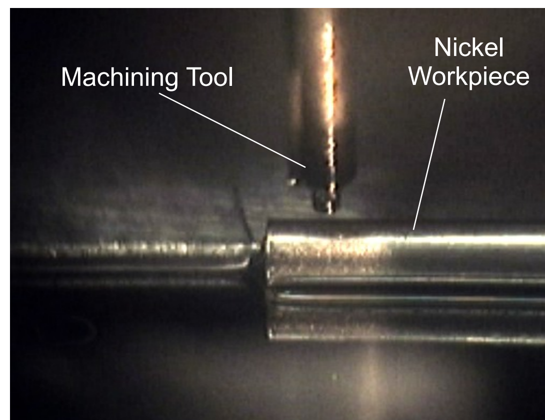

Figure 7-2. Machining the nickel mask.

Once machining is completed, the probe was ultrasonically cleaned and the slot was measured using the calibrated optical microscope. Multiple measurements of the slot were averaged to give a length of 1227.2±1.9 μm. For the height of the slot, the inner edges (i.e., the surface that will be closest to the probe itself) gave a value of 395.5±1.8 μm. The outer edges reflect a larger diameter of 470.4±5.4 μm, the discrepancy due to

wear on the probe as it machined the slot. It is the inner edges that most accurately determine the capacitance of the completed probe, so the value of 395.5 μm was used when estimating the sensing area of the finished probe. The area of the inner surface of the slot was 451,800 μm^2. Whether this area is dilated, eroded, or transferred unaltered to the probe surface is a function of the etching steps selected for the probe surface. An SEM image of the completed, machined mask is shown in Figure 7-3.

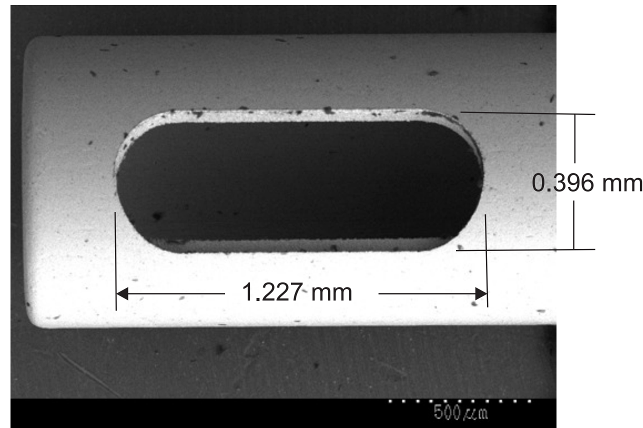

Figure 7-3. SEM image of completed nickel mask.

7.3 Etching of the Probe using the Physical Mask

Once the physical mask was completed, the next step in probe manufacture was to etch one or both coatings from the sensing area of the probe. Before etching, the probe was essentially "blind", that is the inner conductor was completely surrounded by an additional conductor and so could not sense the presence of any grounded surfaces such as the target surface of the hole. Recall that conductors are analogous to surfaces of fixed temperature, and that capacitance is only possible if, in the heat transfer analogy, there is heat flux between two surfaces. The guard structure is kept at the same voltage or "temperature" as the sensing conductor. There can be no heat transfer from the inner conductor if the geometry of the guard structure is unbroken, and models prove this to be the case.

With the etching process there are two possible approaches to removing layers. If the new probe geometry is to closely mimic a traditional capacitance probe as shown in Figure 1-1, then both the gold layer and the alumina layer must be removed so that the bare tungsten carbide is exposed. In the traditional capacitance probe the front surface is

ground flat, so that the guard ring and the sensing area are coplanar. With this new capacitance probe geometry the guard material must be removed, but it is determined that removal of the alumina is not necessary. In fact, there are several advantages to leaving the alumina in place.

7.3.1 Capacitance of probe with alumina in place

The first factor when considering whether to remove the alumina or leave it in place is to determine whether the probe will function properly with the alumina. In this case, the gap between the two capacitance plates, once again simplified as parallel plates, is filled with two different dielectric materials. To determine the capacitance of this system a parallel plate system is diagrammed in Figure 7-4, this time with two layers of dielectric material with thicknesses d_1 and d_2 and relative permittivity values of ε_{r1} and ε_{r2}.

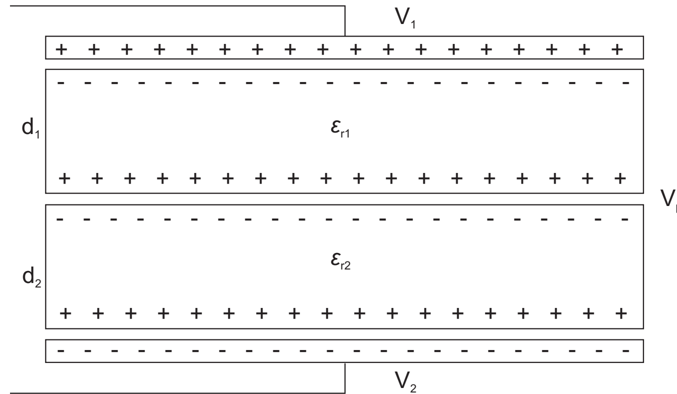

Figure 7-4. Parallel plate capacitor with two different dielectric materials.

To determine the capacitance of this system, first recall that the parallel plate capacitor equation assumes a uniform electric field between the plates, and no electric field outside the plates. The presence of a dielectric material between the plates increases the capacitance when opposing charges are induced onto the surfaces of the dielectric, as shown in Figure 7-4. With these induced charges, the electric field strength between the plates is reduced, even though the capacitance is increased.

Now consider the plane between the two dielectric materials. This plane is at some voltage potential between V_1 of the upper plate and V_2 of the lower. Most importantly, due to the symmetry of the parallel plate capacitor, this potential is constant throughout the plane. Call this voltage V_p. A third conductor can be placed at this location with the constant voltage V_p, and the capacitance of the system will not change. Negative

charges will collect on the upper surface and an equal density of positive charges will collect on the lower, so the presence of this conductor does not affect the capacitance of the system. Within this third conductor the electric field is zero (as within all conductors).

Once this third plate is in place, it is straightforward to recognize that the problem has now been reduced to two parallel plate capacitors. Rather than one single central conductor, the thin central plate of this *gedanken* experiment can be sliced in two so that the capacitors can be seen as separate entities, as shown in Figure 7-5. The functionality of the system is the same, but now the familiar rules of combining capacitors can be applied to the system.

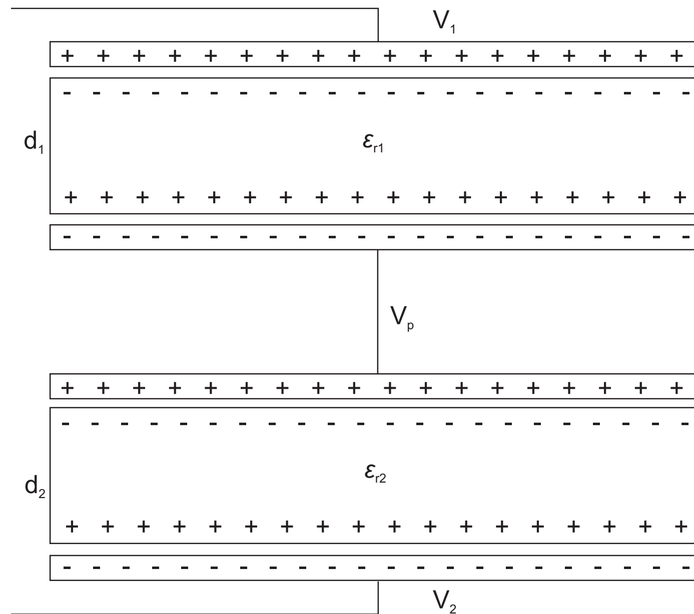

Figure 7-5. Problem reduced to parallel plate capacitors in series.

The general rule for combining two capacitors C_1 and C_2 in series was shown in Eq. (2-13). Since these capacitors have the same area A, but different gap distances d_1 and d_2, Eqs. (7-1) represent their capacitances. Substitution gives the equivalent capacitance shown in Eq. (7-2).

$$C_1 = \frac{\varepsilon_0 \varepsilon_{r1} A}{d_1}, \quad C_2 = \frac{\varepsilon_0 \varepsilon_{r2} A}{d_2} \tag{7-1}$$

$$C_{eq} = \varepsilon_0 A \frac{\varepsilon_{r1}\varepsilon_{r2}}{\varepsilon_{r1} d_2 + \varepsilon_{r2} d_1} \tag{7-2}$$

Equation (7-2) shows symmetry between the two different capacitor terms, the capacitance based on the gap to the target surface and the capacitance of the coating of alumina. For this discussion, the gap to the target surface will be d_1 and the thickness of alumina will be d_2. The term ε_{r1} then represents the relative permittivity of the gas or fluid between the probe and the target surface, and the term ε_{r2} represents the permittivity of alumina.

The last two manipulations of this equation are to isolate the variable distance d_1 from the other variables that are fixed for a given probe composition and geometry. One form of this equation is shown in Eq. (7-3).

$$C_{eq} = \frac{\varepsilon_0 \varepsilon_{r1} A}{\left(\frac{\varepsilon_{r1}}{\varepsilon_{r2}} d_2 \right) + d_1} \tag{7-3}$$

Comparing the form of Eq. (7-3) to the standard parallel plate Eq. (1-3) there is only one additional term, but it unfortunately it is added in the denominator. It is important to now consider, under what conditions would this term be negligible? Of course as the thickness d_2 of this coating goes to zero, the equation reverts back to the simplified parallel plate equation. Also, if the permittivity of the alumina is much higher than the material in the gap between probe and target surface, this term could be ignored. Finally, if the materials had similar permittivity values but the gap distance d_1 is much larger, then the second term in the denominator dominates.

Unfortunately, these last two conditions are antithetical to the primary objective, i.e., producing a sensitive capacitance probe. For maximum sensitivity it is likely that the gap between probe and target will be filled with a liquid with a high relative permittivity such as water (ε_{r2} of 80, about an order of magnitude larger than alumina). Also for maximum sensitivity for a given probe area A, the gap distance between probe and target surface must be minimized. So if the alumina is to remain covering the probe sensing area, the nonlinearity of Eq. (7-3) will be present in any output proportional to capacitance.

On the other hand, it was shown in the literature review that many circuits have been designed that do not provide output as a function of capacitance but actually provide

an output that is proportional to inverse capacitance. Inverting Eq. (7-3) gives Eq. (7-4). In this equation, the presence of the additional dielectric layer results in only an offset to the original data but does not affect linearity.

$$\frac{1}{C_{eq}} = \frac{d_1}{\varepsilon_0 \varepsilon_{r1} A} + \frac{d_2}{\varepsilon_0 \varepsilon_{r2} A} \tag{7-4}$$

It may be possible for a fluid dielectric material to be selected that matches the dielectric constant of alumina. In this circumstance, where ε_{r1} is equal to ε_{r2}, the equations simplify to just a sum of distances d_1 and d_2. For either type of output, the presence of the dielectric material does not prevent functionality, but it does affect the linearity of the output of the probe.

7.3.2 Underetching of probe layers

One reason to leave the alumina in place is to prevent underetching, where one coating is etched away from underneath another. An example of this is shown in Figure 7-6. In this electron micrograph, a hole in the gold coating allowed the alumina to be etched from underneath it. This is more likely with wet etching techniques and isotropic materials, particularly if the thickness of the material is not well known or the etching time is short. Spectral analysis confirms that tungsten carbide is exposed at the bottom surface of this opening. If, as a result of underetching, the gold outer layer comes in contact with the tungsten carbide conductor, then the effectiveness of the guard structure is negated, and the probe cannot function.

7.3.3 Redeposition of material

Other reasons to leave the alumina in place are problems of electrical shorts between the gold coating and the inner surface of tungsten carbide. In some etching techniques such as ion milling, it is possible for the material being etched to be redeposited on the surrounding surfaces. For example, as the gold is etched away, some of the gold can be deposited on surrounding surfaces (in this case, also gold). This does not affect functionality of the probe. If the user also etches away the alumina, this could also be deposited along the surrounding surfaces. Again, this makes little difference to the functioning of the probe. However, if enough of the underlying nickel or tungsten carbide

is also removed and redeposited along the side walls, it could form a conductive bridge between the outer gold layer and the inner tungsten carbide conductor. Once again, the functionality of the probe would be lost.

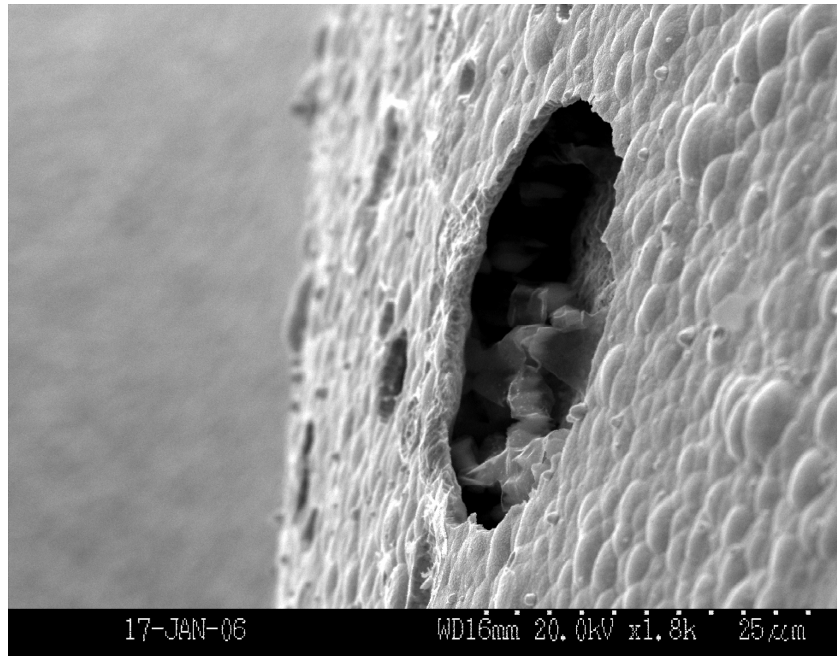

Figure 7-6. Underetching of alumina through gold coating.

Under normal wafer-processing conditions the thickness of the coatings, and therefore the etch rates, are well known. Because of the cylindrical shape of the capacitance probe, however, the thickness of the coating can vary over the surface, and therefore ensuring that one layer is etched completely while another is not etched at all is difficult. Thus, while an electrical short is not likely, it is nonetheless another argument for leaving the protective alumina in place over the entire probe. Since there are no drawbacks to leaving the alumina in place, only the gold layer was removed.

7.4 Etching Processes

Once it was decided that only the gold layer was to be removed, the next step was to decide the method of removal. Three methods are proposed, each with advantages and drawbacks for the purposes of cylindrical probe manufacture.

The first method, wet etching, is the most traditional from the standpoint of semiconductor wafer processing. In wet etching, a chemical is applied to a material to selectively dissolve that material, either isotropically or anisotropically. For the probe,

where the material is isotropic, the etch acts in all directions. The photoresist keeps the etch from attacking the gold guard layer in other places, and the selected material is not chemically capable of etching the subsequent layer.

To etch the probe, a positive photoresist material was applied in a uniform layer directly on the surface. With the physical mask placed over the probe, this photoresist was first exposed to UV radiation, and the resist was baked on. Because this is a positive photoresist, the area of photoresist that was exposed to UV radiation was easily developed away, in this case the oblong sensing area of the probe. Wet etching was then applied to the probe to remove the desired layers, with the timing corresponding to the thickness and type of material to be removed. When the wet etching was complete, the remaining photoresist was dissolved away.

In dry etching, a target material is placed in a vacuum chamber, and the target surface is bombarded with charged ions with sufficient energy to physically etch material. If the energy of the ions is sufficiently high, the impacts of these ions result in sputtering of the material from the target surface. Once again, the time necessary to complete this process depends on the thickness of the material. Relevant etch rates are shown in Table 7-2, derived in part from Williams *et al.* [119].

Table 7-2. Material removal rates for various materials and processes.

Process	Material	Etch material	Rate
Wet Etch	Gold	Aqua regia	680 nm/min
	Gold	KOH	N/A
	Chromium	Aqua regia	N/A
	Chromium	KOH	4.2 nm/min
	Alumina	KOH	> 800 nm/min
Ion Mill	Gold	Argon ions	170 nm/min
	Chromium	Argon ions	58 nm/min
	Alumina	Argon ions	10 nm/min
	Nickel	Argon ions	66 nm/min
Grinding	any	--	< 5 min total

A final method for material removal is mechanical grinding of the target area as described by Morgan *et al.* [121]. This was the only method that involved physical contact with the probe surface, so care was taken not to damage the probe. To grind away the gold layer, a hardened tool of the appropriate diameter was manufactured using the

μEDM machine, then this grinding tool was applied to the sensing area of the probe. The physical mask was not required for grinding.

7.4.1 Wet etching process

Wet etching was applied to the capacitance probe in a clean room environment under a fume hood, due to the nature of the chemicals involved. The first step in etching was to apply a layer of photoresist to the entire surface of the probe. This was done by dipping the probe into Shipley 1813 positive photoresist and spinning the probe using a Dremel tool to create an even coating. The speed of the Dremel was measured stroboscopically to be 16,724±20 rpm. The probe was then placed on a heated surface for one minute at 150˚C to soft-bake the coating, solidifying it.

The second step in the wet etching process was to expose the photoresist on the sensing area of the probe to radiation. In the case of an optical mask that comes in contact with the wafer, the resolution of the process is typically limited by the wavelength of the light that is used to expose the material. For this reason, radiation in the UV portion of the spectrum is necessary to expose the Shipley 1813 photoresist. To only expose the sensing area of the probe, the physical mask was slid over the narrow end of the probe. During this procedure care was taken not to damage the photoresist coating on this part of the probe.

Unlike the case of a flat optical mask, the clearance between this section of the probe and the inner wall of the physical mask is approximately 50 μm. The larger diameter of the probe shaft was covered with aluminum foil to prevent exposure of the photoresist on this part of the probe, as shown in Figure 7-7. Because Shipley 1813 is a *positive* photoresist, the areas exposed to UV light are areas where the photoresist was *removed*. The areas covered during the UV exposure are areas that were protected from etching. The UV exposure occured in a Karl Suss machine and lasted 11 seconds.

Once the photoresist was exposed, the mask was removed from the probe; it is not needed again during the wet chemistry process. In this process the mask was not damaged, and can be used many times. The probe was now ready for the first etching step, that of removing the gold. The end of the probe was dipped in a solution of aqua regia (3 HCl : 1 HNO_3 : 2 H_2O) for approximately 3 minutes under the fume hood. As can be seen from Table 7-2, the aqua regia does not etch chromium; once the gold is removed, the

etching reaction does not progresses further toward the center of the probe. Unfortunately, leaving the probe in the aqua regia too long caused underetching in some cases, where the gold was slowly etched from under the photoresist. If the thickness of the gold layer is well known, the etching time can be determined precisely. Unfortunately, due to the unusual shape of this probe, the thickness of the gold layer contains some uncertainty, and it was difficult to nondestructively determine this thickness for a particular probe. Over time, measurements of multiple probes will eventually allow precise prediction of the thicknesses of the coatings.

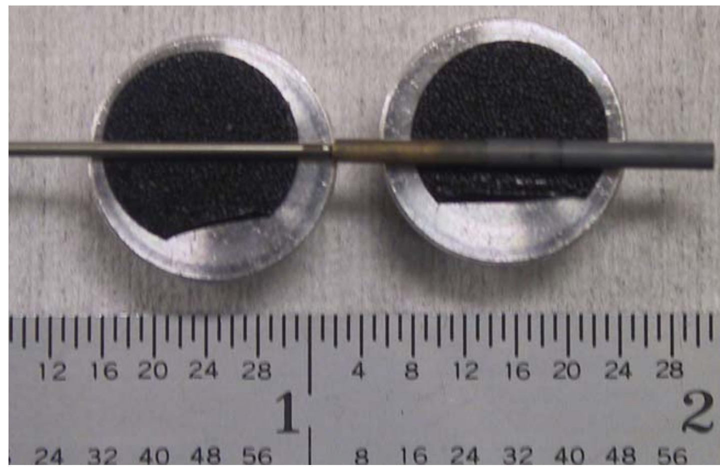

Figure 7-7. Assembly of probe and mask.

The chromium layer was wet etched in a second step with KOH (30% by weight, heated to 80˚C). KOH wet etching is common and is relatively slow. The thin layer of chromium is removed in approximately 30 seconds. Unfortunately, as can be seen from Table 7-2, the KOH also etches the underlying alumina, at a rate of almost 200 times faster. Although some removal of alumina is tolerable, there is no feedback in the wet etching process to determine whether a particular layer has been removed. The chromium must be removed for the probe to function properly, so it is best to etch too long rather than too little. The finished probe can be examined under the electron microscope after etching to determine if chromium or gold is still present in the sensing area. The final step in the wet etching process was to remove the remaining photoresist from the surface of the probe, which was easily dissolved away with acetone.

7.4.2 Dry etching process

Dry etching processes do not use wet chemistry to remove material from a surface. Instead, these techniques use energetic ions to remove material. With wet etching, different chemistry is used for each layer of material, and the only variables to the etching process are the time allowed for the chemical reaction and the temperature of the reaction. In the case of dry etching, the etch rates can vary as a function of the energy of the incident ions, the types of ions, and the number of ions incident on a given surface area. The rates in Table 7-2 cannot be taken in an absolute sense, unless the equipment used by Williams *et al.* [119] is duplicated in the lab. However, given that the same equipment is used for each of the tests that form the basis of the table, then the relative etch rates from one material to another can be considered.

Two different dry etching techniques were considered for the probe. The first, reactive ion etching (RIE), is one or two orders of magnitude faster than ion milling. This is achieved by a combination of chemistry and a high energy bombardment of the surface. Such equipment, while not available at the University of Kentucky, is present at the University of Louisville, with whom the University of Kentucky often collaborates. Unfortunately, although this lab is capable of etching silicon, it is not equipped with the chemistry to do RIE of metals.

The second method for dry etching is termed ion milling, which uses only the energy of the ions to remove material. In this technique the ions are accelerated through a potential of greater than 10 eV, so that they have sufficient energy to remove material. With lower energies material is not removed, but instead the ions are simply adsorbed by the target material [117]. Although ion milling is once again not available at the University of Kentucky, the NNIN consortium provides wafer processing services to universities so that their resources can be utilized by a wide range of users. The University of Minnesota is one member of this consortium, and they are set up to provide ion milling for three or four inch wafers.

Because this setup is designed for wafers, the simplest way of mounting the probe is to begin with a mechanical wafer sample and adhere the probe and target to the surface of this wafer. This can be achieved using a suitable material, such as wax, that can be easily removed later. The direction of the ion beam in this equipment is normal to the

wafer surface, so the mask is mounted so that the opening in the mask faces directly toward the ion beam. To allow for maximum uniformity in material removal, the wafer, probe, and physical mask are rotated during milling.

As mentioned before, the rate of material removal for ion milling is not simply a function of the material being removed (as in wet etching), but instead different from one experimental setup to the next. Material removal rates quoted by the University of Minnesota [120] are 6 nm/min for gold and 0.5 nm/min for alumina. Although these rates are slower than those listed in Table 7-2, they reflect the same order-of-magnitude difference in rate between gold and alumina.

The advantage to having a lower rate of alumina removal is to prevent the ion mill from accidentally etching all the way through the entire alumina layer. For a 1 micron thickness of gold, for example, the time to remove this is approximately 170 minutes. If, for example, the gold layer was overestimated by 40 percent, then the net result would be inadvertent removal of only 35 nm of alumina. For an alumina thickness of 1 micron, this is less than 4% of the total layer.

It is important to point out that the ion milling also damages the physical mask. The ion mill process attacks every exposed surface to some degree, and according to Table 7-2 the rate of removal of nickel is less than half the rate of gold. While the gold is being removed from within the target area, nickel is removed from that part of the mask that is exposed to the ion beam. The mask has a thickness of 100 μm, so for every micron of gold removed from a probe, less than half a micron of nickel will be removed from the mask. Each mask, then, can easily survive the processing of over 100 probes with these dimensions.

Finally, the possibility of redeposition must be addressed, since material that has been milled away can be redeposited nearby. In the case of this probe geometry, any redeposition will most likely occur at the sides of the hole being milled. If gold is redeposited along the sides during milling, it only adds a miniscule amount to the gold already present. If alumina is redeposited, only the relative permittivity of the probe will change in that very small region, once again negligible. What is to be avoided is ion milling of the underlying tungsten carbide. If this material is redeposited, an electrical

short may form between the sensing area and the guard ring structure. If this occurs, the probe becomes useless.

7.4.3 Surface grinding

A final method to remove the two unwanted layers from the probe does not require a physical mask. Instead, the µEDM machine can remove the material using a different method, micro-grinding. This technique was developed in the Precision Systems Lab at the University of Kentucky [121, 122], and is able to machine a variety of conducting and insulating materials.

In micro-grinding, a tool is first machined from a cylindrical blank. The blank and the resulting grinding tool are shown in Figure 7-8. The cylinder is made of carbide, and the tooling surface material, polycrystalline diamond (PCD Sumitomo DA220D), is deposited on the end of this cylinder. The thickness of this grinding material is 200 µm.

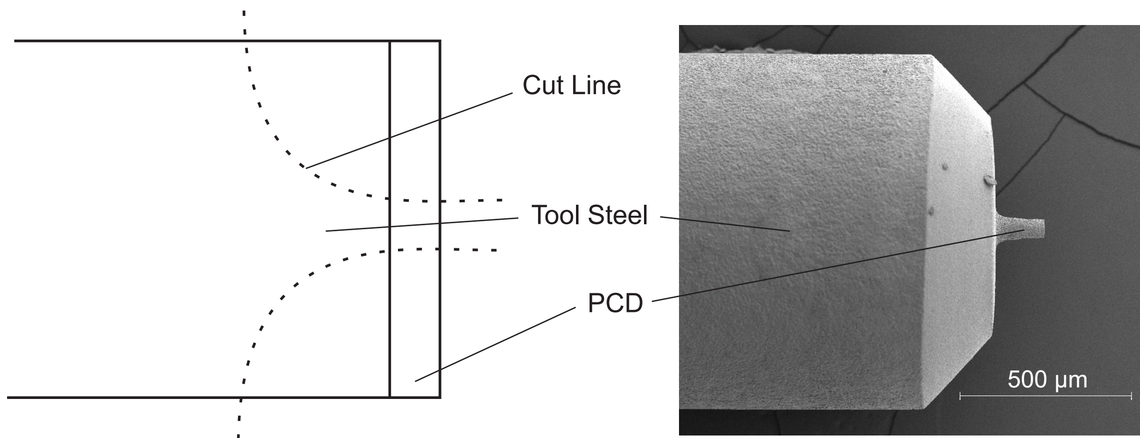

Figure 7-8. Blank and finished grinding tool. SEM image courtesy of Chris Morgan.

To retain the proper alignment of the grinding tool during both its manufacture and its use, the tool shape shown in Figure 7-8 was created using the µEDM Machine in its WEDG mode. With the largest capacitor (3300 pF) and highest voltage (110 V) selected, a tool with a diameter of 300 µm was machined in only two steps.

Once the tool was created, the setting scope was used to select the starting point of the slot. The base code for this grinding process was written by Chris Morgan, only the dimensions were changed to machine this particular tool. Like all Matlab µEDM scripts, it used the `query` command to pass ASCII text through the serial bus, and began with code to open the serial port. The first commands to move the probe are the `aps`

commands used to touch off the surface, making electrical contact to locate position. The vertical (z) value is then reset to zero.

```
query(EDM,'abs x -1000')
query(EDM,'aps z +')
query(EDM,'res z')
query(EDM,'abs z -100')
query(EDM,'cua z 1000 x 0 0')
query(EDM,'cua x 0 0 0')
query(EDM,'fsf z 10')
query(EDM,'fsm z 1')
```

The following loop made 15 passes of 1 μm each back and forth on the surface (30 passes total). The tool was raised after each pass to clear the chips, and after machining the probe was ultrasonically cleaned. The total distance traveled by the tool was 900 μm. The complete code for this machining is found in Appendix D.

```
for i=1:15
    query(EDM,['abs z ',num2str((i*20)-10)])
    query(EDM,['abs x 9000'])
    query(EDM,['abs z -100'])
    query(EDM,['abs z ',num2str(i*20)])
    query(EDM,['abs x 0'])
    query(EDM,['abs z -100'])
end
```

The target area was examined under the electron microscope, to determine the mechanical capabilities of the process and to determine the atomic makeup of the exposed surfaces. Unlike the etching process, the grinding process left debris on some parts of the machined surface, in spite of the ultrasonic cleaning. A spectral analysis of the debris, shown in Figure 7-9, revealed that the base material of the probe, tungsten carbide, was left by the final grinding process. An area analysis of the ground surface also clearly shows only tungsten carbide, as shown in Figure 7-10. The final ground surface of the probe is shown in Figure 7-11. This image shows that the machining tip, while not perfectly aligned, removed material only from the programmed area.

The micro-grinding process proved to be the most controllable technique for material removal. Unlike the etch process, which depended on known thicknesses of the gold and alumina layers, micro-grinding opened a precise window onto the tungsten carbide.

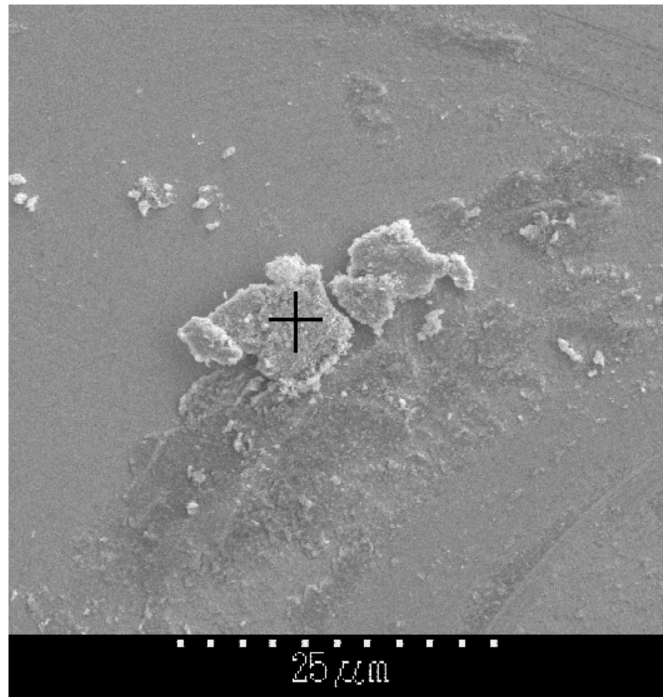

Figure 7-9. Debris left behind by grinding process.

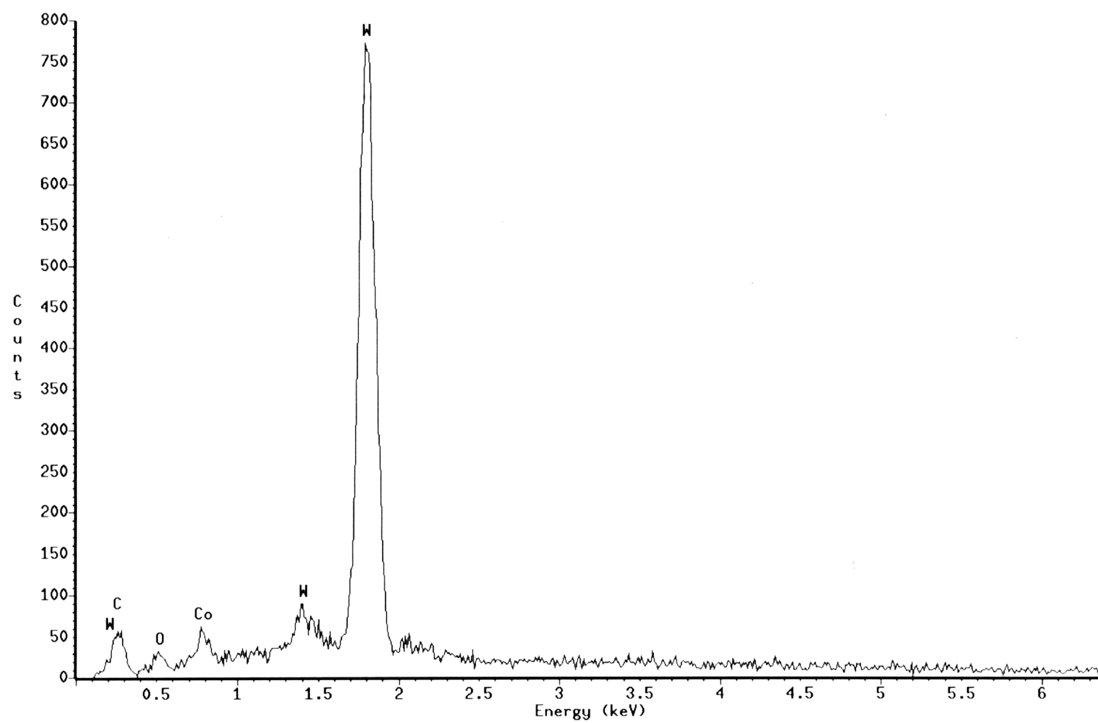

Figure 7-10. Atomic spectrum of ground surface.

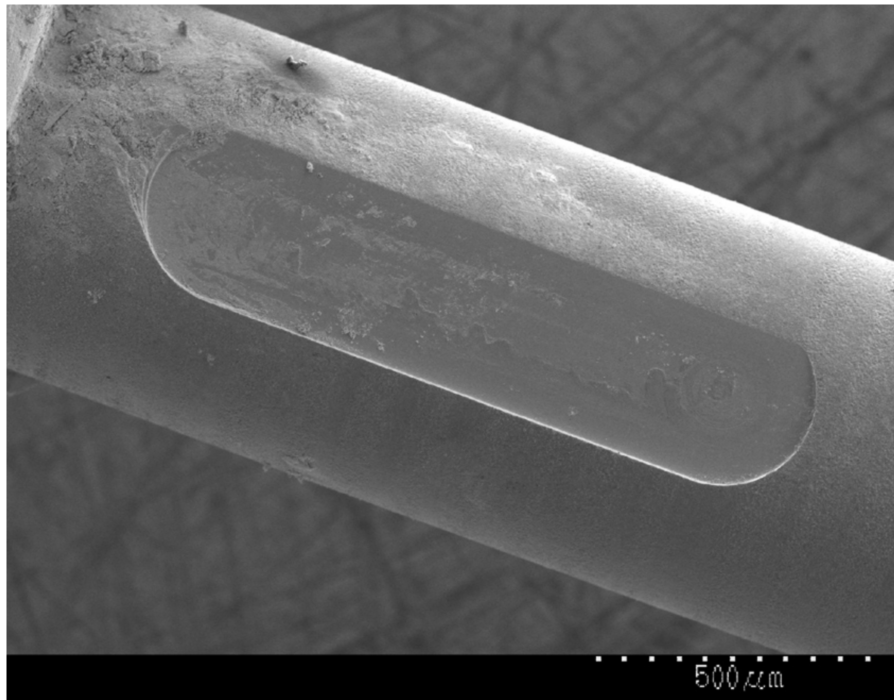

Figure 7-11. Ground surface of the probe.

7.5 Conclusions

Once layers have been added to the probe, a window must be created through those layers back to the original tungsten carbide surface. This was tested using photolithography and mechanical grinding. In the case of photolithography, a ob-round slot was machined in a physical mask of nickel. The µEDM machine was applied in a different configuration to open a slot in the hollow tube. A photoresist was applied to the surface of the probe, and then exposed to UV radiation. Chemical etching was applied to remove the conductors. The results were less than satisfactory, due to difficulty in achieving uniform material thicknesses of material and photoresist.

The second technique explored was to mechanically grind away the layers to open a window to the tungsten carbide. The tool in this case was created on the µEDM machine using a carbide probe with a PCD coating. The µEDM machine was also used to grind the slot. While the wide grinding tool has the undesirable effect of flattening the probe surface, the desired layers were successfully removed in the process.

Copyright © Philip T. Smith Jr. 2007

8 Conclusions and Future Work

Although capacitance gages have been modeled and studied for over a hundred years, their application in precision tools reflects their ability to make accurate displacement measurements. Multiple capacitance probes use the "parallel plate" model, with different geometries employed to trade off precision for sensing range, or sensitivity for gap distance. The guard ring structure has long been shown to minimize the fringing of the electric field, and thereby maximize linearity and reduce outside influences.

Several closed-form approximations are available to refine the simple parallel plate approximation. These make various assumptions on the geometry of the sensing element or the guard ring, and deviate from experimental results if the geometry changes significantly. With the advent of the desktop computer, computational methods of analysis became available, borrowing from fields such as heat transfer where the equations were similar. This is the case for the finite element method, which models the full geometry of the non-conductive medium and applies boundary conditions to the conductors present in the system. Systems with multiple conductors were easily solved by applying sets of boundary conditions and recording the energy stored in the electric field in each case. This dissertation demonstrated that these results closely matched experimental results for commercial probe geometries, and multiple studies applied finite element analysis with good success.

8.1 Calibration and Spherical Targets

Commercial capacitance probes with a ground, flat target area are frequently used to target flat surfaces for displacement or gap measurements. A narrow gap is used for the highest sensitivity; and the raw signal, based on capacitance of the system, is conditioned using electronics to provide a linear output. These probes have advantages over other probe technologies such as contact probes, where a small sphere is used to make point measurements of a surface. Such contact measurement not only risks damaging the surface with the probe, but the deflection of many kinds of surfaces even under small pressures is not inconsequential. The need for small target probes increases the pressure applied at the contact point, exacerbating this problem. Also, this type of contact technique can only be used for a small number of data points, which does not always give an accurate picture of the entire target surface.

Unfortunately, capacitance probes are difficult to apply to some rotating surfaces. Cylindrical and spherical surfaces can benefit from this level of precision measurement, and techniques have been developed for spindle measurement that depend on the linearity of these commercial probes. Unfortunately this target does not match the calibration target, and as a result the linearity and accuracy of the system is compromised. Even without full knowledge of the electronic calibration of the system, corrections were made so the capacitances of varying geometries could be compared. Of the two geometries mentioned above, the sphere was the simplest case to model, due to the axial symmetry of the system. One particular probe geometry targeting spherical surfaces was studied previously by Vallance *et al.* [94].

In this dissertation, a more complete investigation of several commercial capacitance probe-target geometries was undertaken. This first study showed how the capacitance varied in response to changes in spherical target geometry, capacitance probe geometry, and dielectric material selection. This analysis showed which probe geometries work better when the target surface is known and a choice of commercial probes is available. Also, a parametric study of the results was undertaken to analyze which geometric parameters are critical in the design of a capacitance probe and which are of secondary or tertiary importance. This is necessary to advance to new probe geometries, where each dimension must be considered from a functional standpoint.

Prior studies showed that some geometric parameters, such as the diameter of the outer housing of the probe or the outer diameter of the guard ring, had no effect on the capacitance of the system [82]. This is due to the guard ring structure restricting the electric field. The parameters that were included in this study were the diameter of the sensing element, the distance to the target surface, the width of the gap between the sensing element and the guard ring, the radius of the target surface, and the dielectric constant of the material separating the guard ring from the sensing element.

The large number of parameters involved required automation of the analyses and storage of large tables of results. The finite element analysis was optimized by determining which steps needed to be redone for each change to the model, and which steps could be retained. Changing a dielectric constant, for example, only required rerunning the results, while moving the target surface meant remeshing the model. To

maximize the range of values such as gap distances, nonlinear sets of values were applied in cases where resulting capacitances would be evenly spread.

The contribution of this work is twofold. Previously, the outcome of the analysis was only applicable to a particular target surface and a particular capacitance probe. Because the effect of variations in geometry was unknown, the results cannot be applied in any general way. With this parametric study, these effects have been quantified to a much greater extent. By applying a wide range of geometries, and by showing how scaling can be applied to these results, measurements from a larger range of capacitance probes and spherical targets can be corrected. In cases where the geometry is known, this means that significant errors can be removed from displacement measurements. In cases where an experiment has not progressed beyond the planning stages, it is possible that the geometry can be selected so the calibration errors are negligible. This set of data is a tool to help in the selection process.

The second contribution of this work is to indicate which parameters in the design of a capacitance probe are critical to linearity and sensitivity of the resulting data. Differences in curvature of the target surface were reduced using varying powers of the sensing radius, depending on the range of gap distances involved. The guard ring spacing was shown to have a negligible effect on the capacitance when the gap distance was small, but as this distance opened up, so did the differences between the gap values. Similarly, the dielectric constant of the material between the sensing element and the guard ring had a significant effect when the gap distance was large, but less of an effect when the gap distance was small. Changes in this material had the most significant effect on the capacitance between the sensing conductor and the guard ring, a topic only briefly touched upon here.

8.2 Solutions for Cylindrical Targets

For many parts of rotating machinery there are no flat surfaces to use as targets. The choices with the most symmetry in these cases are spherical or cylindrical targets. The subject of spherical targets was summarized above, so the next geometry to be analyzed is the cylinder.

It was shown in Chapter 3 that, even though both the probe and the target surface have cylindrical symmetry, the analysis of this problem necessitates a three dimensional

model. More specifically, two planes of symmetry are available, so the final solution required one-quarter of the full model to be solved. Three-dimensional models of capacitance use surfaces as boundary conditions and the energy stored in volumes to determine the capacitance. Meshing of three-dimensional spaces can be accomplished in an almost infinite variety of ways, with the number of nodes easily approaching 10,000 or more. The geometry and the solutions in this case were again generated using ANSYS scripts and a number of target diameters. The effects found for spherical targets, including the greatest deviation from linear for the smallest diameter, were again in evidence here, but to a lesser extent. The largest deviation in sensitivity values were also shown to correspond to the smallest diameters and the smallest working distance.

As the final step, the theoretical corrections were used to generate corrections to displacement measurements. Nonlinear results from one of the modeled target surfaces can then be corrected or linearized, with the absolute distance measurements restored. Such a set of experimental results was available to verify the theoretical calculations. These experiments were performed using a cylindrical target opposite a flat target. A capacitance probe in close proximity to the flat target provided a calibrated result, while the output from a second capacitance probe supplied the raw data for analysis. These nonlinear results were recalibrated based on the finite element simulations, and the results were compared to the reference surface. Once again, the vast majority of the calibration problems were removed using the results of this finite element analysis.

Although the analysis of cylindrical targets varied fewer parameters than the spherical study, the more complicated geometry adds to the knowledge base. For some applications, the nonlinearity of capacitance probes translates directly into measurement errors. This is the case with spindle metrology measurements, where two measurements are made of a cylindrical target. Spindle error and surface error are only separable if the capacitance probes are linear, and so the limits in calibration translate to limits in the measurement. By providing a way to recalibrate, the method can be applied to a wider range of target surfaces with acceptable results.

The interaction of flat surfaces and cylindrical targets must also be understood for some designs of hole probe, and a cylindrical surface is of course always the target. In other cases the center of the capacitance probe and the center of the hole are not perfectly

matched, resulting in non-parallel surfaces. Finally, the ability to generate three-dimensional models is necessary for many probe and surface interactions.

8.3 Probe Design

A capacitor consisting of two concentric cylinders has a simple approximate solution, which can be converted to the parallel plate equation if additional assumptions are made. These assumptions include a small gap distance compared to the radius, and relatively long cylinder compared to the radius. While the simplest form of the parallel plate equation gives a starting point for capacitance calculations, better solutions are available only through computer-aided techniques. The techniques applied to this solid model use Pro/Engineer for modeling and finite element meshing, ANSYS for finite element capacitance solutions, and Matlab for analysis and plotting. It was determined that Pro/Engineer was better able to mesh the complex, three-dimensional models without the need for hand coding.

With a method in place of generating and testing finite element models, the next step in the design process was to determine the optimal probe geometry. Initially it would seem that a capacitance probe can only resolve features comparable to the size of its sensing area. Two preliminary deconvolution studies showed that there was some influence of the target surface beyond the area directly parallel the sensing area. This influence was shown to be reduced when a guard structure was provided, and the gap distance minimized.

8.4 Method for Deconvolving Capacitance Measurements

Instead of assuming that the probe area defines the smallest detectable feature, how the probe interacts with the target surface as it passes linearly over it was studied using a new method. In this integral model, the probe capacitance is assumed to be linear as a function of overlapping areas. Two different two-dimensional approaches were considered, to determine which geometry minimizes the measurable feature size, angular rotation vs. longitudinal scanning. These approaches also represented two different probe geometries.

For the rotational model, the overlapping area was linear with the angle of overlap, so the capacitance was linear with angle of intersection. The capacitance of this system was written as the sum of finite areas. These sums were a function of the relationship between the sensing area, the gap distance, and the minimum measurable capacitance.

Once these values were known, the series of sums that represent the capacitance values could be rewritten in a matrix form, and the matrix solved for capacitances.

In the second probe geometry the sensing area extended the length of the probe, which had primary motion along the longitudinal axis. As before, the capacitance was modeled as the sum of a series of smaller capacitances. A matrix solution in a different form deconvolved the surface from the capacitance measurements. A further refinement to this method added small coefficients to the matrices, to include secondary target areas of influence. With this final refinement in place, a more complicated target surface was defined, one with a sinusoidal variation over its length. This data was able to be deconvolved even though the probe surface was wider than the features it is trying to resolve. Finally, this methodology was extended to three dimensions.

8.5 Manufacturing Method for Prototype Probes

Once the design of a capacitance probe was determined, methods of manufacture were developed. The probe was machined from a tungsten carbide cylinder using a Micro Electro-Discharge machine. Both standard and custom routines were needed to produce the optimal shape. During the development of the process, improvements were made to both the machining algorithms and the μEDM machine itself.

After a probe was machined, insulating and conducting layers were added to the surface using ebeam deposition. Alumina served as the insulator, and gold as the outer guard structure. Elemental analysis using an SEM verified the presence of the coatings, and was capable of checking for holes or other faults. Another check of the surface was achieved using a scanning profilometer, which performed a statistical analysis of the surface.

Two methods were applied to the coated probe to open a window through the outermost layer. Wet etching used a physical mask to expose a coating of photoresist. The area where the photoresist was exposed became the area where etching of the gold occurred. The second method was mechanical grinding of the surface coating of the probe. This method was successful in removing material from the desired area.

8.6 Future Work

Although many conclusions can be made based on the work contained in this document, the design and manufacture of these capacitance probes requires further refinement. The

mechanical adhesion of the coatings was made more robust by the addition of more layers, but the thickness of those layers proved difficult to measure. The mounting system in the ebeam chamber required a static placement, so a vertical orientation above the crucible was chosen. Although it was shown that the sides were coated to some degree, the thickness of this coating could not be measured. It is likely that the downward-facing surfaces received a greater thickness of each layer. Of particular concern is the thickness of the alumina layer, as this layer provides separation between the two conductors.

A more optimum arrangement is a horizontal spindle within the ebeam chamber that can be rotated and translated externally. The sides of the probe would receive a face-on treatment, and uniformity of coating could be ensured by automating the rotation and translation process. The sensor designed to measure such a face-on coating could also be relied upon to provide an accurate readout with only a simple correction factor. Such a mechanical feedthrough is not available on the current ebeam system.

With the gold layer and the probe itself representing the two conductors of the capacitance sensor, a connection must be made to external electronics. Fortunately the connection does not need to be made along the narrow tip, where the curvature is large and the area available to attach a wire is limited. This is in fact the location where the wires should *not* be attached, since this area is needed to maximize the depth of hole that can be measured. Instead the wires must be bump-bonded further back on the probe, where the diameter is large, and as large an area of probe as needed can be used. If additional mechanical support is needed to keep the bonding from pulling the gold coating from the surface, the entire base of the probe can be coated with a suitable epoxy. By surrounding the probe any tension on the wires is countered by the epoxy and the bond between the wire and the coating is unaffected.

8.7 Reducing the Scale

Once it has been shown that a probe of a diameter on the order of 750 microns can be successfully manufactured, the steps necessary to reduce that scale by a factor of 10 must be examined. The first question, then, is whether a blank probe can be manufactured to these tolerances. It was shown in Figure 1-8 on page 26 that a probe of 50 micron diameter and over a millimeter in length can be machined using the μEDM device. Since this machining is achieved using non-contact means, there is no mechanical strain on the

system that would prove to be the limiting factor. The support of the spindle has been shown to be repeatable as well. Currently the most limiting aspect of this machining is in measuring the diameter of the probe. The light microscope, although calibrated, has difficulty pinpointing the edges of the probe, and as a result there are errors to the measurement. A goal of 25 microns in diameter is therefore possible, but improvements are necessary to the precision of the diameter measurement.

Once the blank probe is machined, the next steps are the cleaning and coating process. The cleaning process involves wet chemistry, and so can be applied to any diameter with minimal difficulty. The coating process involves clamping the probe at its base, with the probe tip suspended in the vacuum. While a smaller radius of curvature can make it more difficult for a coating to stick to the surface, several test probes had similar radii and were able to hold their coatings. If the orientation of the probe is changed to make the coating a face-on process, this will also improve the likelihood of achieving a uniform layer.

Shrinking the physical mask is probably the most difficult aspect of the process described in this document. Not only is it difficult to find a blank material of a suitable size from which to machine a mask, but the connection between this mask and the probe is prone to snapping the probe in two. A solution to this problem is to make a more sophisticated mask, such as that shown in Figure 8-1. In this mask, a central region of the probe has an intermediate diameter, machined at the same time as the tip to ensure concentricity. The mask has a similar step, with the tolerance of the intermediate zone being much tighter than the tolerance of the tip zone. In this way the mask and the probe are held together by the mechanical strength of the central region and the tip is not at risk. Assembly of this arrangement will certainly require fixturing, but this approach minimizes the risk of damage. Finally, it should be pointed out that the mask shown in Figure 8-1 can be machined using the μEDM machine. Although deep holes often require multiple tools on the μEDM machine to produce a cylindrical hole, the same mask can be applied to multiple holes.

The other process by which material can be removed from the probe tip, grinding, presents more difficulty when scaled. This process *is* mechanical and *does* produce mechanical stresses in the material. Too much pressure from the grinding surface and the

probe tip will certainly fracture. Not enough pressure from the grinding surface and material will not be removed.

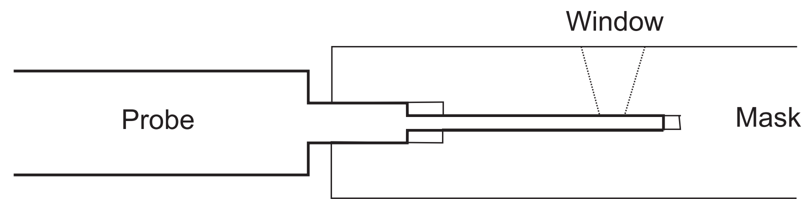

Figure 8-1. Mask with mechanical step to avoid probe fracture.

Fortunately it is possible in this system to vary the geometry of the grinding tool, and in this way the correct grinding force can be achieved. For the previous test a tool was used that ground the surface in a single pass. This resulted in a sensing area of the expected shape, but with a flat area that did not match the curvature of the target surface. A smaller tool, however, has the advantage that multiple passes are needed. The resulting slot will have some flatness at the edges, depending on the number of passes involved. More importantly, however, the grinding force can be minimized to a point well below the force necessary to fracture the tungsten carbide.

Copyright © Philip T. Smith Jr. 2007

Appendix A: List of Variables

Q	Charge on a conductor
C	Capacitance between two conductors
V	Voltage applied to a conductor
W	Energy stored in a capacitor
ε_0	Electric field permeability of vacuum
ε_R	Dimensionless, relative permeability of a medium; always greater than 1
A	Area of a conductor
d	Distance between two parallel conductors
G	Electronic gain multiplier, in farad-volts
S	Electronic gain term, in volts/meter
Δd	Displacement from a nominal distance value d_{nom}
d_{nom}	Distance that produces zero volts on electronic output of capacitance gage
I_1 and I_2	Forward and reverse measurements of rotating part
$R(\theta)$	Spindle radial error motion
$B(\theta)$	Surface profile of rotating part
k	Thermal conductivities in a heat transfer problem
q^B	Heat generation term in heat transfer, or charge density in an efield analysis
ϕ	Field potential solution to the electric field problem, in volts
C_{tot}	Total combined capacitance of gage and associated cabling
C_{probe}	Capacitance of gage only, approximated by ANSYS model
C_{cable}	Capacitance of cabling of gage, not modeled in ANSYS
r	Radius of a circular sensing conductor
g	Gap between central conductor and guard ring
R	Radius of target sphere or target cylinder
γ	Nondimensional gain multiplier correction term

Appendix B: Data Transfer from Pro/Engineer To ANSYS

As discussed in Chapter 4, there are two methods of transferring data from the solid modeling software, in this case Pro/Engineer, to the finite element analysis software, ANSYS. To determine the best method for the repeated changes in capacitance geometry, a comparison of the data structures is needed. This requires a probe geometry offered as a "test case." Such a three-dimensional test case is shown in Figure B-1. As with many of the 3D capacitance models, this image does not represent a solid object, but rather the gap between solid objects. The objects themselves, as conductors, are the boundary conditions of the model, and only the gap is ultimately meshed and solved.

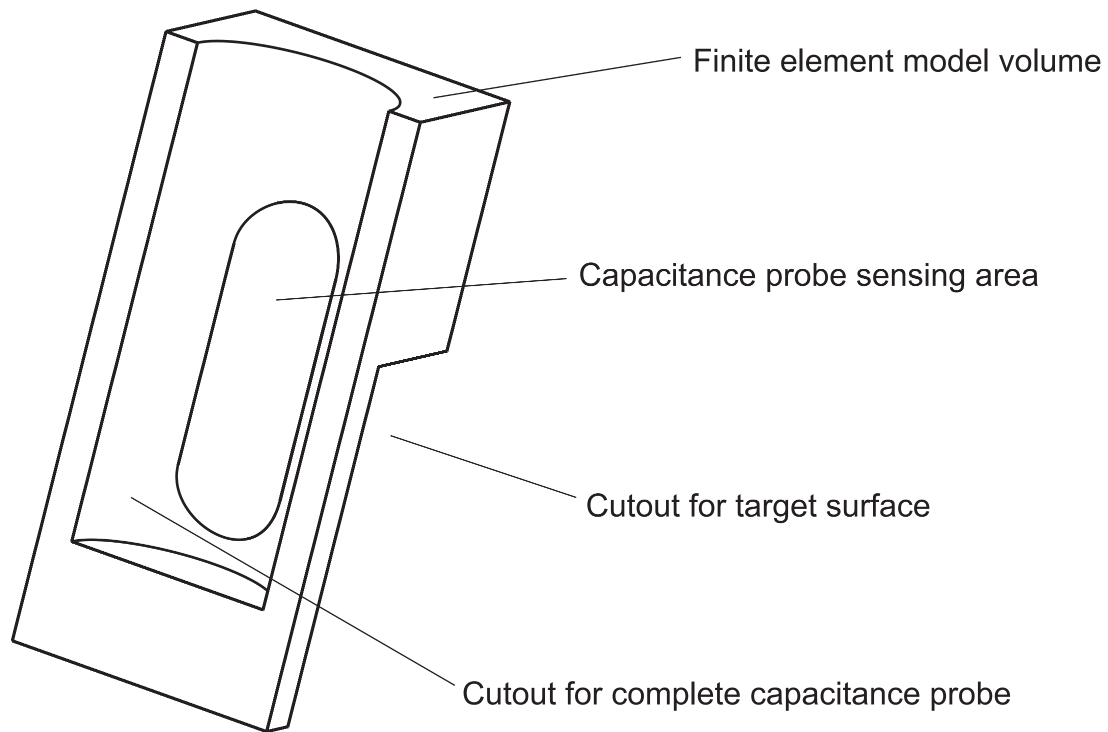

Figure B-1. Model of Probe Gap Geometry, to be Studied using FEA.

B.1 Exporting Geometry Using IGES

The first method of transferring data uses a format called "Initial Graphics Exchange Specification" or IGES. This data file format is designed to transfer geometric entities from one program to another. Once the solid model is generated in Pro/Engineer, the IGES file is used to build that precise geometry in the recipient software; in this case, ANSYS.

Consider again the geometry shown in Figure B-1. This air gap consists of several surfaces, which are in turn constructed of lines, which are in turn built from connected points. When this geometry is exported to an IGES file format and brought into ANSYS, the resulting geometry is limited to points, lines, and surfaces. Two small pieces of this code are shown below.

```
110       72        1        1        0        0        0        001010000D      27
110        0       -1        1        0                        LINE       10D      28
124       73        1        1        0        0        0        001000000D      29
124        0        0        2        0                        XFORM       1D      30
100       75        1        1        0        0       29        001010000D      31
100        0       -1        1        0                         ARC        1D      32
…
1.510742723184D3,-3.065224298481D2,-1.982833658965D2,           21P      22
1.532268715144D3,-3.076528960834D2,-1.902461252964D2,           21P      23
1.564802530088D3,-3.127544957453D2,-1.760373720303D2,           21P      24
1.597213863229D3,-3.210892157464D2,-1.552498598594D2,           21P      25
```

The relationship between the original surfaces bounding the modeled air gap has been lost. There is therefore no easy method to determine which points, lines, and areas represent the sensing area, which ones represent the guard structure, or which ones represent other boundary conditions required by the finite element model. When the IGES file is imported into ANSYS, these geometric elements are assigned numbers by ANSYS strictly based on the order they are imported.

This import can be accomplished manually, but to maintain consistency it is helpful to write an ANSYS script to automate the various import features. Several data flags must be set, including whether to smooth curved lines and surfaces, merge overlapping data points, and whether to generate solid elements from a surface import. This last feature affects the numbering of the volumes that will later be created manually by the subsequent ANSYS code, so this feature [ioptn,solid] is set to no. Other features also affect the numbering of points, lines, and areas, so these are set in a consistent manner. Below are the commands that set these options and import the IGES data file MCP-FEA.IGS. Note that a comma separates the filename from its extension in the last line of code. Certain portions of ANSYS still require DOS 8+3 filenaming conventions, so filenames are kept short.

```
/aux15
ioptn,iges,smooth
ioptn,merg,yes
ioptn,solid,no
ioptn,small,yes
ioptn,gtoler,defa
igesin,O:\Users\psmith\CurrentWork\PhD\SpindleModel\mcp-fea,igs
```

Once the geometry is imported, there are several steps necessary to generate a good quality mesh from within ANSYS. First, a mapped mesh element allows the user to wield the most control over the meshing process. The difficulty with this approach is that the geometry of each volume to be meshed with a solid, “brick” element must have the same topology as those elements. This is not the case with the imported geometry of the air gap, so additional points, lines, areas, and volumes must be created manually. This code is all contained within an ANSYS script that contains both the loading commands for the IGES file (above) as well as commands for modifying the model.

To generate some of this geometry advantage is taken of the fact that the probe geometry is centered along the default coordinate system imported through the IGES file. Unfortunately, the model of Figure B-1 is set up with its cylindrical symmetry centered on the *y*-axis, while ANSYS defaults to cylindrical symmetry about the *z*-axis. Adding a user-defined coordinate system corrects this difficulty, and lines can be generated with the same curvature as probe surface.

```
local,11,1,0,0,0,0,90,0   ! New coordinate system with new Z along old -Y
csys,11                   ! change to new coordinate system
l,31,32                   ! line 16, segmenting off the rectangular area
l,42,44                   ! line 49
```

The semicircular sections in the probe sensing area must also be segmented to allow for mapped meshing. Because the locations of these points are not included in the ANSYS script, this information must be queried by the script, based on manual identification of the keypoints. For example, one semicircular section contains the keypoints 3, 5, 7, 8, 12, 13, 18, and 20. Their coordinates in the default Cartesian system are collected using the `get` command. Keypoints are created based on these coordinates, and lines and areas are generated.

```
*get,k3x,kp,3,loc,x       ! Get X location of keypoint 3
*get,k3y,kp,3,loc,y       ! Get Y location of keypoint 3
*get,k3z,kp,3,loc,z       ! Get Z location of keypoint 3
*get,k5x,kp,5,loc,x       ! Get X location of keypoint 5
...
yoff=100
k,201,k3x,k3y+yoff,k3z
k,202,k5x,k5y+yoff,k5z
...
l,22,201                  ! line 64, bottom layer, 4 lines
l,201,3                   ! line 65
l,23,202                  ! line 66
l,202,5                   ! line 67
...
al,81,79,83,77            ! area 1, two long narrow areas in rect. region
al,80,78,82,76            ! area 2
```

```
al,27,82,50,51             ! area 3, three areas on far end
```

A total of 65 areas and 11 volumes are manually added based on the geometry automatically generated during IGES import.

Once these critical areas are properly segmented, they must be meshed. A brick electrostatic element that is well suited for a three-dimensional, mapped analysis is element 122. The complete, nondegenerate form of this element is shown in Figure B-2 (a). This 20-node element can better fit the curved shapes found throughout the critical volume of the probe model, even with relatively few elements. The degree of freedom at each node is the scalar potential or VOLT in the ANSYS nomenclature. This element can model orthotropic electrostatic permeability properties, although only a single permeability, ε_r, is used here.

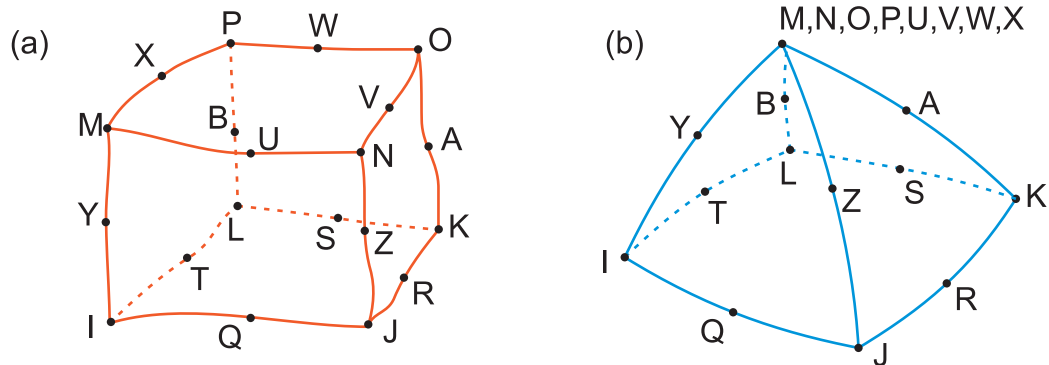

Figure B-2. Elements used to mesh the IGES-imported data within ANSYS.

Once a mapped mesh is applied to the thin, central section of the model, the meshing method is changed to a free mesh for the outer elements. Because the brick elements cannot be used in these volumes, a degenerate tetrahedral form of element 122 is applied, as shown in Figure B-2 (b). With ANSYS the exact ordering of the meshing steps is critical to achieving the desired elements, for example, the free mesh must be applied *after* the central volume is filled with mapped elements. The software can then include transitional elements to connect the two volumes.

As with previous calculations, the capacitance of the system is determined using the CMATRIX macro within ANSYS. This macro requires that all nodes for a conductor (in other words, each boundary condition) be grouped together and assigned a common component name using the CM command. Since the nodes numbers that generated by the

mesh often change, these nodes are best selected by their association with an area of the model.

With some conductors in this model represented by multiple areas, these areas must be selected together for their nodes to be included in the conductor. It is a quirk of ANSYS that sometimes area selection can include associated keypoints, lines, nodes, and elements, and sometimes area selection cannot. In particular, the command to select a new set of areas, ASEL,S, allows a flag to be set so that the underlying geometry is included. The command to extend the current set, ASEL,A, will ignore this flag. In the past, a workaround was applied that involved consecutively numbering areas associated with a particular conductor so that a single command could select all areas. This workaround proved impossible with imported data from Pro/Engineer, since some of the area numbering occurs automatically.

The new workaround is to create multiple subsets of nodes by selecting existing areas, then grouping the subsets together to form a single group that will carry the name of the conductor. For the IGES imported code the target surface consists of 4 areas that must be grouped together and given the name COND3 for the CMATRIX command to function properly. Since these areas are not numbered consecutively two subgroups, trgA and trgB are first created.

```
asel,s,,,34,34,,1          ! select area 34 and nodes
cm,trgA,node
asel,s,,,36,38,,1          ! select areas 36, 37, 38 and nodes
cm,trgB,node
cmsel,s,trgA
cmsel,a,trgB
cm,cond3,node              ! complete conductor 3
```

This grouping also facilitates graphical solutions to the electric field. Once the group of nodes associated with a particular conductor is selected, the voltage can be applied with a single command.

The application of the CMATRIX command also requires only a single line of code. The number of conductors, in this case three, must be passed to the routine, as well as the common root of the three conductors, `cond`.

```
/solution
allsel,all
cmatrix,1,'cond',3,1,'cmat'
Finish
```

If the ANSYS script is executed during a normal ANSYS session then the CMATRIX solution is presented in a separate dialog window at the conclusion of its routine. If the ANSYS script is run during a batch mode then the text of the CMATRIX solution is included in the output file. The lumped capacitance output from this text file is shown below.

```
*** Lumped Capacitance Matrix ***
Self Capacitance of conductor  1. =     0.81268E-13
Self Capacitance of conductor  2. =    -0.11058E-12
Self Capacitance of conductor  3. =     0.12434E-13
Mutual Capacitance between conductors  1. and  2. =     0.88272E+01
Mutual Capacitance between conductors  1. and  3. =     0.16401E+01
Mutual Capacitance between conductors  2. and  3. =     0.37106E+01
Lumped capacitance matrix is stored in 3d array parameter cmat    ( 3.,
       3.,2)
Capacitance matrices are stored in file cmat    .txt
```

The complete ANSYS script described in this section is found in Appendix C.

B.2 Exporting Elements Using Pro/Engineering Mechanica

A very different method of transferring a model from Pro/Engineer to ANSYS is to perform the step of meshing the model within Pro/Engineer, exporting an entirely different type of data from Pro/Engineer to ANSYS. This type of transfer ultimately proves to be the most robust as the geometry of the model changes.

The original Pro/Engineer model as shown in Figure B-1 is unchanged with this method. Once the geometry is set, the user must activate a linked application called Mechanica that is part of the Pro/Engineer suite of products. If Mechanica has not been previously applied to this model, the first question asked by the software package is to determine the desired type of finite element model, structure or thermal.

As discussed in Chapter 1, electric field analysis is very similar in its formulation, degrees of freedom, and solution set to a thermal conduction or heat transfer problem. Each node in a heat transfer problem has a single, scalar degree of freedom, temperature. Boundary conditions applicable to a heat transfer problem are either a fixed temperature or a constant heat flux. These analogs must be considered when applying this method of data transfer. The method selected within Mechanica is therefore ‘Thermal.’

Within Mechanica, the user must next apply the appropriate boundary conditions to the probe model. The correct analog to a fixed voltage in an electrostatic problem is a fixed temperature in a thermal conduction problem. This dialog can be opened by selecting ‘Prescribed Temperature’ from the ‘Insert’ menu. To keep track of different sets

of boundary conditions, each application of a particular boundary condition to a surface or set of surfaces is given a ‘name’. The collected boundary conditions that define the entire finite element problem are considered a ‘set’. The arrow button allows for graphical selection of the boundary conditions. Finally, the ‘Temperature’ section allows a set value to be applied to the selected surfaces.

The application of temperatures to geometric elements when in fact the goal is to determine the capacitance between areas seems a bit circuitous. The reason that these “pseudo-” boundary conditions need to be applied is because they serve as placeholders, a way to flag particular parts of the model for later grouping. As described below, the temperature boundary condition are changed to voltage potential in a single step.

Unlike the prior method, here Mechanica does the work of meshing the model. All of the meshing parameters must now be considered in Mechanica, by selecting ‘control’ under the ‘mesh’ menu. As with the boundary sets, the mesh control parameters are assigned a name that will be referenced later. The control parameters can be applied to a specific edge (line), surface (area) or component (volume) of the model. To generate a uniform mesh throughout the entire volume, component is selected, and the arrow button is used to graphically pick the entire model. Several parameter settings can be changed via the type pulldown menu, including ‘Maximum Element Size’, ‘Minimum Element Size’, ‘Edge Distribution’, and ‘Mesh Numbering’. For this model, a maximum element size of 100 μm and a minimum element size of 50 μm are added to the definition of ‘MeshControl1’.

The next step in Mechanica is to name and define the analysis itself, to determine which boundary set will be applied to a model. From the ‘Analysis’ menu, selecting ‘FEM Analysis’ brings up a second menu that allows the user to create a new analysis or to edit an existing analysis. The necessary step here is to add the previously defined boundary condition set to the analysis. This will enable these boundary conditions to be exported along with the data defining the mesh. Once the analysis conditions are defined in this way, selecting ‘Mesh’, ‘Create’ begins the meshing routine within Mechanica. As with ANSYS, the completed mesh can be analyzed for quality and shape of elements and improved as needed.

Once the elements are generated, the final step within Pro/Engineer Mechanica is to output an ANSYS-ready file by selecting 'Analysis', 'Run FEM Analysis'. To export the mesh, the solver 'ANSYS' is selected, along with the other features shown in the figure. It is necessary to output this data to a file rather than allow it to run online, since changes must to be made to the '.ans' file generated by Mechanica. Once this dialog is closed a warning message appears, indicating that the material properties have not been set. These will also be added later, so the user can click 'Continue' to complete the export process.

The information contained in the data file exported from Mechanica is quite different than the IGES data file exported by Pro/Engineer. The IGES data was at the level of lines, areas, and volumes, while the ANSYS data contains information about nodes, elements, and boundary conditions. Selections from these three major sections appear as shown below.

```
N,1,-500.000000,165.627907,-700.000000
N,2,-361.438649,0.000000,-700.000000
N,3,-340.944047,169.756947,-700.000000
N,4,-500.000000,0.000000,-700.000000
...
EN,1,1838,1819,1793,1837,18466,18317,18322,18539
EMORE,18465,18321
EN,2,417,416,415,418,9517,9509,9510,9521
EMORE,9518,9511
...
D,54,TEMP,5
D,55,TEMP,5
D,62,TEMP,5
D,63,TEMP,5
```

With one line for each node, two lines for each element, and one additional line for each node along a boundary, these automatically-generated scripts can run to thousands of individual lines of code. For this reason a complete example of the code is not provided in the Appendix.

To generate an electric field instead of a heat transfer solution, several changes must first be made to this script. Since these changes are independent of the specific geometry of the probe, they can be automated using any number of programs. Because Microsoft Word is adept at opening and saving large text files, a script was created in Word to automate the process described below.

The header of an example '.ans' file contains material properties applicable to heat transfer problems, several coordinate systems, and the element type. Below is an example of the header from one of these files.

```
/TITLE Model: MCP-FEA
/COM Finite Element Mesh - PTC - ANSYS 6.1 - MCP-FEA
/PREP7
/NOPR
MP,EX,1,0.000000e+00
MP,ALPX,1,0.000000e+00
MP,NUXY,1,0.000000e+00
MP,DENS,1,0.000000e+00
MP,KXX,1,0.000000e+00
MP,C,1,0.000000e+00
LOCAL,11,0,0.000000,0.000000,0.000000,0.000000,0.000000,0.000000
...
CSYS,11
ET,1,87
```

The last line in this header is the command to define the element type for the model. Element 87 is a ten-node tetrahedron with a single degree of freedom, temperature, at each node.

The material properties defined in the lines beginning with `MP` are necessary for solving a heat transfer problem. Because the material properties were not defined in Mechanica, these parameters default to the zero values shown. To convert this file into an electrostatic model, all of the `MP` lines as well as the element line beginning with `ET` must be replaced with the code shown below.

```
EMUNIT,EPZRO,8.854E-6
MAT,1
MP,PERX,1,80
ET,1,123
```

As shown above, the electrostatic constant ε_0 is set using the `EMUNIT` command. The relative permittivity, ε_r, is set using the `MP` command to a value of 80 (for water). It should be noted that, with the exception of the electrostatic constant ε_0, this ANSYS file does not contain any information on the dimensional units of the problem. Since material properties are not brought over from Mechanica, the system of units applied in that program is irrelevant. Only the coordinates from Pro/Engineer, in whatever unit system is currently applied, are imported. Defining ε_0, then, sets the units for analysis of the geometry and ultimately for the capacitance of the system.

The final step in the changes to the header is to define a new element for the ET command. Although the original heat transfer element, SOLID87, is tetrahedral, it differs

from the degenerate element 122 of Figure B-2 (b) used in the prior heat transfer model in that only ten nodes are assigned to the model. Element 122 cannot be applied to this ANSYS file without generating errors within ANSYS due to "Improperly connected degenerate brick element." The complete list of elements that were considered as a direct replacement for element 87 are listed in Table B-1. Of the element types listed, only SOLID123 is suitable as a direct, automatic replacement for element 87 in an electrostatic model.

Table B-1. Element types considered for the ANSYS electrostatic problem.

Name	DOF	Notes
SOLID5	Many	Magnetic, structural, thermal, electric, many different possible analyses with corresponding degrees of freedom
SOLID62	UX, UY, UZ, AX, AY, AZ, VOLT	Used for modeling 3-D coupled magnetic and structural problems
SOLID69	TEMP, VOLT	Used for resistive heating analysis
SOLID97	Many	For electromagnetic field studies with time dependence
SOLID123	VOLT	10 node tetrahedral element for electrostatic analysis
SOLID127	VOLT	10 node p-type element for electrostatic analysis

Once the modifications to the header are made, the next step is to modify the body of the ANSYS code. This code consists of nodes (`N` commands), elements (`EN` and `EMORE`), and degree of freedom constraints (`D` commands). The only change required is to the degree of freedom commands, as these must be modified to reflect the degree of freedom of element type 123. Specifically, a line such as `D,202,TEMP,5` becomes `D,202,VOLT,5`. The different temperature values (now voltage values) serve as placeholders for the CMATRIX process and do not need to be changed. The Microsoft Word macro automatically replaces all instances of `TEMP` with `VOLT`, and changes to the body of the ANSYS file are complete.

The last changes to the ANSYS file are modifications to the solver routine at the end of the file. The original file ends with the following commands.

```
LSWRITE,2
/GOPR
FINISH
```

The electrostatic model must not simply be solved for the given conditions, but the system of three conductors must be solved using CMATRIX. The code that replaces the above three lines at the end of the ANSYS file is as follows.

```
nsel,s,d,VOLT,10,10
cm,cond1,node
nsel,s,d,VOLT,15,15
cm,cond2,node
nsel,s,d,VOLT,5,5
cm,cond3,node
allsel,all
save
finish
!
/solution
allsel,all
cmatrix,1,'cond',3,1,'cmat'
finish
```

The first line above performs the function of selecting the nodes that were part of the sensing area in the Pro/Engineer file. These nodes were all assigned the arbitrary temperature (now voltage) value of 10. The second line gives this collected set of nodes the name `cond1`. Two more sets of commands define the guard structure (which is set to 15 volts) and the target surface (set to 5 volts). As with previous ANSYS code, the last command invokes the CMATRIX function, which solves the 3-by-3 matrix of mutual capacitances.

Appendix C: ANSYS Code for FEA

C.1 Capacitance Probe and Spherical Target

The code below models a capacitance probe and a spherical target in two dimensions, applying an axisymmetric element so that the solution will be a full three-dimensional one. Note that this particular file is for a sensing element with a diameter of 0.0625 inches (1.588 mm) and a test sphere diameter of 0.250 inches (6.35 mm). Similar files varied these two parameters but kept the remaining values unchanged.

Because the resulting data set is too large to be included in this document, it is included as a separate electronic file in ASCII text format, with the name pts_data.txt and linked in the electronic version of this dissertation.

```
finish
/clear                  ! used to erase and start over analysis
!
/title, Axisymmetric Capacitance Gauge, Actual Geometry
!
! test7 includes all three loop values, final parameter writing routine
!
! Changing geometry to add back material (for C12 accuracy)
!
! This code produces a capacitance that is the sum of all energy in the gaps.
! Use this as a starting point to do the more sophisticated and automated
      process.
!
/prep7
!
emunit,epzro,8.854e-3   !epsilon in pF per mm
!
! Define Dimensions of the capacitance gauge
!
innerb=0.0675        ! Inner brass capacitance diameter, inches
flatdia=0.200        ! Diameter of flat area
outerb=0.300          ! Outer brass diameter, inches
outerp=0.330         ! Outer epoxy diameter, inches
ss=0.375             ! Stainless steel outer diameter inches
V0=-5.0              ! voltage of base plate
V1=5.0               ! voltage of upper plate
depin=0.045          ! Depth of cap gauge in inches
addhgtin=0.275       ! additional height to model
slp=20               ! Upwards slope of gauge in degrees
TestDia=0.250        ! Diameter of test sphere, inches ******************
Agap=0.2             ! Air gap around cap gauge, mm
Cflg=1.0             ! Set to zero for flat surface, otherwise round
Nr=1.0               ! Use to refine the mesh, 2 quadruples elements, etc
!
! Set the number of loops for each part of the calculation
!
E=4                  ! Number of permittivity values to use***************
G=12                  ! number of different d gaps to use******************
S=4                  ! Number of g gaps (to guard) to use*****************

*dim,Er,array,E
Er(1)=1.0            ! Electric permittivity of epoxy, multiple values
Er(2)=1.9
Er(3)=3.8
Er(4)=5.7
!
*dim,Gapvals,array,G     ! make sure correct number of gaps given
Gapvals(1)=0.0004*0.0254
Gapvals(2)=0.0008*0.0254
```

```
Gapvals(3)=0.0016*0.0254
Gapvals(4)=0.0064*0.0254
Gapvals(5)=0.0250*0.0254
Gapvals(6)=0.1000*0.0254
Gapvals(7)=0.5000*0.0254
Gapvals(8)=2.0000*0.0254
Gapvals(9)=4.0000*0.0254
Gapvals(10)=8.000*0.0254
Gapvals(11)=16.00*0.0254
Gapvals(12)=32.00*0.0254
!
! Eventually make this an array not a single value
*dim,Ggap,array,S
Ggap(1)=0.007175
Ggap(2)=0.014350
Ggap(3)=0.028700
Ggap(4)=0.043050
!
! New dimensions first column is d, subsequent columns are with varying g
!
*dim,C12,table,G,S+1,E      ! dimension the capacitance C12 (to guard)
*dim,C13,table,G,S+1,E      ! dimension the capacitance C13 (to target)
!
! Convert measurements to metric and radii
!
innerbr=innerb*25.4/2
outerbr=outerb*25.4/2
outerpr=outerp*25.4/2
ssr=ss*25.4/2
dep=depin*25.4
addhgt=addhgtin*25.4
TestR=TestDia*25.4/2
flatrad=flatdia*25.4/2
!
!
! *******************************************************
! Begin different g gaps here
*do,L,1,S
/prep7
!
innerpr=innerbr+Ggap(L)*25.4
!
! Keypoint y values
!
k26y=(outerbr-flatrad)*tan(slp*3.1415926/180)
k27y=(outerpr-flatrad)*tan(slp*3.1415926/180)
k42y=TestR-(TestR**2-Cflg*innerbr**2)**0.5
k44y=TestR-(TestR**2-Cflg*innerpr**2)**0.5
k45y=TestR-(TestR**2-Cflg*flatrad**2)**0.5
! Next line modified for smallest diameter only
k46y=TestR
!
! Center of sphere keypoint
!
k,100,0,-TestR
!
csys,0
!
! ********************************************************
! Begin d gap loop Here
*do,I,1,G
/prep7
gap=Gapvals(I)
tp=gap+dep
!
! Erase all elements to start over geometry
asel,all
aclear,all
adele,all,,,1
!
! Define keypoints of cap gauge and ref surface
!
```

```
k,1,0,tp
k,2,innerbr,tp
k,4,innerpr,tp
!
k,21,0,gap
k,22,innerbr,gap
k,24,innerpr,gap
k,25,flatrad,gap
k,26,outerbr,gap+k26y
!
k,41,0,0
k,42,innerbr,-k42y
k,44,innerpr,-k44y
k,45,flatrad,-k45y
k,46,outerbr,-k46y
!
k,51,0,tp+addhgt
k,52,innerbr,tp+addhgt
k,53,innerpr,tp+addhgt
!
! Create All Lines, Horizontals first
! Also breaking into segments for elements as needed
!
l,2,4,72*Nr,4      ! line 1
l,22,24,72*Nr,4    ! line 2
!
! The following lines are curved for sphere, flat equivalent
! info was removed due to possible conflict
!
larc,41,42,100,TestR       ! line 3
lesize,3,,,100*Nr,0.25
larc,42,44,100,TestR       ! line 4
lesize,4,,,72*Nr,4
larc,44,45,100,TestR       ! line 5
lesize,5,,,64*Nr,1
! Changed to line for smallest diameter sphere
l,45,46,48*Nr,1            ! line 6
!
l,21,41,12*Nr,3            ! line 7
l,22,42,12*Nr,3            ! line 8
l,24,44,12*Nr,3            ! line 9
l,25,45,12*Nr,3            ! line 10
l,26,46,12*Nr,3            ! line 11
!
! Lines for conductors
!
l,21,22,100*Nr,0.25        ! line 12
l,22,2,64*Nr,4             ! line 13
l,1,2,32*Nr,0.25           ! line 14
!
l,53,4,64*Nr,0.25          ! line 15
l,24,4,64*Nr,4             ! line 16
l,24,25,64*Nr,1            ! line 17
l,25,26,48*Nr,1            ! line 18
!
! More nonconductors
!
l,51,52,32*Nr,0.25         ! line 19
l,52,53,72*Nr,4            ! line 20
l,51,1,64*Nr,0.25          ! line 21
l,52,2,64*Nr,0.25          ! line 22
!
! Define areas
!
al,1,2,13,16               ! area 1
al,3,12,7,8                ! area 2
al,8,2,4,9                 ! area 3
al,9,10,5,17               ! area 4
al,10,11,6,18              ! area 5
!
al,21,19,22,14             ! area 6
al,22,20,15,1              ! area 7
```

```
!
! Element type and meshing
!
et,1,plane121,,,1,,,,        ! area elements for efield
mp,perx,1,1                  ! efield relative permeability
mat,1                        ! using material number 1 (air)
mat,2                        ! defining type 2
mp,perx,2,Er1                ! setting permeability material 2 (epoxy)
mshkey,2
!
! Select all nonconductive areas and mesh
!
asel,s,area,,1,1               ! S for new selection, epoxy area
amesh,all                      ! mesh with type 2 material
asel,s,area,,6,7               ! Additional areas of epoxy
amesh,all                      ! meshed with epoxy
!
mat,1                          ! back to material type 1 (air)
asel,s,area,,2,5               ! Air gap on side of gage
amesh,all                      ! mesh all selected areas
!
! Defining conductors for Cmatrix analysis
!
lsel,s,,,12,14,,1           ! selecting center conductor
cm,cond1,node               ! Define 1st conductor for cmatrix analysis

lsel,s,,,15,18,,1           ! select ground ring
cm,cond2,node

lsel,s,,,3,6,,1             ! select lower sphere or plate
cm,cond3,node               ! Changed this to conductor 3
!
!
allsel,all
save
finish
!
! Permittivity loop for multiple permittivity values
*do,J,1,E
/prep7
mp,perx,2,Er(J)
save
finish
/solution                      ! running solver
cmatrix,1,'cond',3,1,'cmat'  ! solves for all cap values
finish
/post1
C12(I,1,J)=gap                 ! first value is current gap d
C13(I,1,J)=gap
C12(I,L+1,J)=cmat(1,2,2)       ! Capacitance to guard ring
C13(I,L+1,J)=cmat(1,3,2)       ! Capacitance to target surface
finish
*enddo
!
! End of  permittivity values Loop
! ***************************************************************
!
*enddo
!
! End of  gap values Loop
! ***************************************************************
!
! Output resulting table data to a file
!
/post1
!
! Output resulting table data to a file
!
*cfopen,r0250d0675,txt,,APPEND
!
! Loop to add all calculated values to table
!
```

```
*do,K,1,E
*vwrite,innerb
('Inner conductor diameter ',F8.6,' inches')
Ggapnow=Ggap(L)
*vwrite,Ggapnow
('Gaps between inner conductor and epoxy ',F8.6,' inches')
Ercurr=Er(K)
*vwrite,Ercurr
('electric permittivity of ',F6.4)
*vwrite,C12(1,1,K),C12(1,L+1,K)
('gap d:',F8.6,'   C12:',E14.7)
*vwrite,TestDia
('Target sphere diameter ',F6.4,' inches')
*vwrite,C13(1,1,K),C13(1,L+1,K)
('gap d:',F8.6,'   C13:',E14.7)
*enddo
! end of writing loop
*cfclosfinish
save
finish
!
*enddo
! End of outermost loop used for varying the gap g using L
```

C.2 Capacitance Probe and Cylindrical Target

The code below is an ANSYS routine that generates one-quarter of a three-dimensional model of a capacitance gage and target cylinder. Some of the issues related to building a three-dimensional model include the use of quadrilateral elements in a free mesh, the generation of two-dimensional “placeholder” elements to create well-spaced nodes over key surfaces, and the filling in of smooth surfaces over nonflat areas.

```
finish
/clear         ! used to erase and start over analysis
!
/title, Capacitance Gage Over Cylinder, Fourfold Symmetry
!
! Version i, refining mesh
!
! Version h, removing symmetry sides, produces a voltage solution
!
! Version g, creating default mesh in volumes with appropriate elements
! calculating first cmatrix numbers
!
! Version e and f, simplifying the number of areas on the cylinder
! And getting the final air volume functional
!
! Version d, adding geometry of target cylinder to the model. Works for
! larger diameters but will need modification for smallest diameters.
!
! Version c, modifying back side of capacitance gage to make square,
! better for meshing with rectangular cross section of cap gage cylinder.
!
! Version b, took out all code not being used,
! only working on geometry now completed cap gage geometry
!
! Version a, attempting to build the geometry correctly
!
/prep7
!
! Defining the geometry of
! the actual capacitance gauge sensor
! Set units to mm, microfarads
```

```
!
emunit,epzro,8.854e-3  !epsilon in pF per mm
!
! Define Dimensions of the capacitance gauge
!
innerb=0.0675  ! Inner brass capacitance diameter, inches
innerp=0.1249  ! Inner plastic diameter, inches
flatdia=0.200  ! Diameter of flat area
outerb=0.300  ! Outer brass diameter, inches
outerp=0.330  ! Outer plastic diameter, inches
ss=0.375    ! Stainless steel outer diameter inches
gapinitmi=0.20 ! Initial gap setting in minch ********************
gapincmi=0.04  ! Increment of the gap distance in minch
depin=0.045   ! Depth of cap gauge in inches
slp=20     ! Upwards slope of gauge in degrees
TestDia=0.250  ! Diameter of test sphere, inches *****************
Agap=0.2    ! Air gap around cap gauge, mm
Cflg=1.0    ! Set to zero for flat surface, otherwise round
Nr=1.0     ! Use to refine the mesh, 2 quadruples elements, etc
!
! Convert measurements to metric and diameters to radii
!
innerbr=innerb*25.4/2
innerpr=innerp*25.4/2
flatrad=flatdia*25.4/2
outerbr=outerb*25.4/2
outerpr=outerp*25.4/2
ssr=ss*25.4/2
dep=depin*25.4
gapinc=gapincmi*0.0254
gapinit=gapinitmi*0.0254
halfpt=(innerbr+innerpr)/2  ! Halfway across plastic spacer
TestR=TestDia*25.4/2
SimEdg=1.1*ssr        ! Edge of simulation, fix later
CylEdg=TestR         ! For large diams, for smaller set to TestR******
!
! Keypoint y values
!
k26y=(outerbr-flatrad)*tan(slp*3.1415926/180)
k27y=(outerpr-flatrad)*tan(slp*3.1415926/180)
k28y=(ssr-flatrad)*tan(slp*3.14159/180)
k48y=TestR-(TestR**2-Cflg*CylEdg**2)**0.5
k50y=TestR-(TestR**2-Cflg*SimEdg**2)**0.5
!
! Use same coordinate system for everything
!
csys,0
!
! Set the number of loops for the calculation
G=14        ! number of different gaps to use*************
*dim,C,table,G,2,1 ! dimension the capacitance array
!
! ************************************************************
! Begin Loop Here
*do,I,1,G
/prep7
gap=gapinit+gapinc*(I-1)
tp=gap+dep
!
! Next 3 lines erase all elements to start over geometry
!
vsel,all
vclear,all
asel,all
aclear,all
vdele,all,,,1
ksel,all
kdel,all
!
! Center of sphere keypoint
!
k,100,0,-TestR,0
```

```
k,101,0,gap+k26y,0
k,102,0,gap+k27y,0
k,103,0,gap+k28y,0
k,104,0,-TestR,SimEdg
!
! Define keypoints of cap gauge and ref surface
! Took out halfway point in first insulator gap for 3D model
!
k,1,0,tp,0
k,2,innerbr,tp,0
k,4,innerpr,tp,0
k,5,flatrad,tp,0
k,6,outerbr,tp,0
k,7,outerpr,tp,0
k,8,ssr,tp,0
k,9,ssr+Agap,tp,0
k,10,SimEdg,tp,0
!
k,21,0,gap,0
k,22,innerbr,gap,0
k,24,innerpr,gap,0
k,25,flatrad,gap,0
k,26,outerbr,gap+k26y,0
k,27,outerpr,gap+k27y,0
k,28,ssr,gap+k28y,0
k,29,ssr+Agap,gap+k28y,0
k,30,SimEdg,gap+k28y,0
!
k,41,0,0,0
k,48,CylEdg,-k48y,0
k,50,SimEdg,-k48y,0 ! Changed z measurement for small diameter *********
!
! These new keypoints below are needed to define the 3D problem
! Must build a model of 1/4 of cap gage and cylinder
!
k,52,0,tp,innerbr
k,54,0,tp,innerpr
k,55,0,tp,flatrad
k,56,0,tp,outerbr
k,57,0,tp,outerpr
k,58,0,tp,ssr
k,59,0,tp,ssr+Agap
k,60,0,tp,SimEdg
!
k,62,0,gap,innerbr
k,64,0,gap,innerpr
k,65,0,gap,flatrad
k,66,0,gap+k26y,outerbr
k,67,0,gap+k27y,outerpr
k,68,0,gap+k28y,ssr
k,69,0,gap+k28y,ssr+Agap
k,70,0,gap+k28y,SimEdg
!
! Keypoints for back side of cylinder surface
k,71,0,0,SimEdg
k,78,CylEdg,-k48y,SimEdg
k,80,SimEdg,-k48y,SimEdg ! Changed z measurement for small diameter
      *********
!
! Two new keypoints to make back of model square not round
k,91,SimEdg,tp,SimEdg
k,92,SimEdg,gap+k28y,SimEdg
!
!
! Create All Lines Connecting keypoints, Cap Gauge First
!
! Horizontal Lines, top of cap gage, front face
l,1,2       ! line 1
l,2,4,4      ! line 2
l,4,5       ! line 3
l,5,6       ! line 4
l,6,7,2      ! line 5
```

```
l,7,8       ! line 6
l,8,9,2      ! line 7
l,9,10,1,1     ! line 8 infinite element
!
! Horizontal lines at bottom of cap gage, front face
l,21,22,12     ! line 9
l,22,24,8     ! line 10
l,24,25,6     ! line 11
l,25,26      ! line 12
l,26,27      ! line 13
l,27,28      ! line 14
l,28,29      ! line 15
l,29,30,1,1    ! line 16 infinite element
!
! Vertical lines within cap gage, front face
l,21,1       ! line 17
l,22,2,5,2.0    ! line 18
l,24,4,5,2.0    ! line 19
l,25,5       ! line 20
l,26,6       ! line 21
l,27,7       ! line 22
l,28,8       ! line 23
l,29,9       ! line 24
l,30,10      ! line 25
!
! Horizontal lines, top of cap gage, left face
l,1,52       ! line 26
l,52,54,4     ! line 27
l,54,55      ! line 28
l,55,56      ! line 29
l,56,57,2     ! line 30
l,57,58      ! line 31
l,58,59,2     ! line 32
l,59,60,1,1    ! line 33 infinite element
!
! Horizontal lines at bottom of cap gage, left face
l,21,62,12     ! line 34
l,62,64,8     ! line 35
l,64,65,9     ! line 36
l,65,66      ! line 37
l,66,67      ! line 38
l,67,68      ! line 39
l,68,69      ! line 40
l,69,70,1,1    ! line 41 infinite element
!
! Vertical lines within cap gage, left face
l,52,62,5,0.5    ! line 42
l,54,64,5,0.5    ! line 43
l,55,65       ! line 44
l,56,66       ! line 45
l,57,67       ! line 46
l,58,68       ! line 47
l,59,69       ! line 48
l,60,70       ! line 49
!
! Create arcs for top of cap gage
! plus one back line (to keep numbering same)
larc,2,52,1,innerbr    ! line 50
lesize,50,,,6       ! 6 divisions for line 50
larc,4,54,1,innerpr    ! line 51
lesize,51,,,8
larc,5,55,1,flatrad    ! line 52
larc,6,56,1,outerbr    ! line 53
larc,7,57,1,outerpr    ! line 54
larc,8,58,1,ssr      ! line 55
larc,9,59,1,ssr+Agap   ! line 56
l,10,91          ! line 57 (straight)
!
! Create arcs for bottom of cap gage
larc,22,62,21,innerbr   ! line 58
lesize,58,,,12
larc,24,64,21,innerpr   ! line 59
```

```
lesize,51,,,18
larc,25,65,21,flatrad   ! line 60
lesize,51,,,12
larc,26,66,101,outerbr  ! line 61
larc,27,67,102,outerpr  ! line 62
larc,28,68,103,ssr    ! line 63
larc,29,69,103,ssr+Agap  ! line 64
l,30,92          ! line 65 (straight)
!
! Three additional straight lines
l,91,60          ! line 66
l,92,70          ! line 67
l,91,92          ! line 68
!
! Target surface
!
! Straight lines across surface
l,41,71,25,8       ! line 69
l,48,78,15        ! line 70
l,50,80          ! line 71
!
larc,41,48,100,TestR   ! line 72
lesize,72,,,25,8
l,48,50          ! line 73 now straight for small dia*******
!
larc,71,78,104,TestR   ! line 74
lesize,74,,,15
l,78,80          ! line 75 now straight for small dia*******
!
!
l,70,71          ! line 76
l,92,80          ! line 77
l,30,50          ! line 78
l,21,41,2         ! line 79
!
! Create Areas from Lines
!
! Front face first
al,1,18,9,17       ! area 1
al,2,19,10,18       ! area 2
al,3,20,11,19       ! area 3
al,4,21,12,20       ! area 4
al,5,22,13,21       ! area 5
al,6,23,14,22       ! area 6
al,7,24,15,23       ! area 7
al,8,25,16,24       ! area 8
!
! Side face second
al,26,17,34,42      ! area 9
al,27,42,35,43      ! area 10
al,28,43,36,44      ! area 11
al,29,44,37,45      ! area 12
al,30,45,38,46      ! area 13
al,31,46,39,47      ! area 14
al,32,47,40,48      ! area 15
al,33,48,41,49      ! area 16
!
! Top face next
al,1,50,26        ! area 17
al,2,51,27,50       ! area 18
al,3,52,28,51       ! area 19
al,4,53,29,52       ! area 20
al,5,54,30,53       ! area 21
al,6,55,31,54       ! area 22
al,7,56,32,55       ! area 23
al,8,57,33,56,66     ! area 24 (5 lines)
!
! Bottom face
al,9,58,34        ! area 25
al,10,59,35,58      ! area 26
al,11,60,36,59      ! area 27
al,12,61,37,60      ! area 28
```

```
al,13,62,38,61      ! area 29
al,14,63,39,62      ! area 30
al,15,64,40,63      ! area 31
al,16,65,41,64,67     ! area 32 (5 lines)
!
! Interior areas of model plus back side (two rect)
al,18,58,42,50      ! area 33
al,19,59,43,51      ! area 34
al,20,60,44,52      ! area 35
al,21,61,45,53      ! area 36
al,22,62,46,54      ! area 37
al,23,63,47,55      ! area 38
al,24,64,48,56      ! area 39
!
al,68,66,49,67      ! area 40 (flat side)
al,25,65,68,57      ! area 41 (flat side)
!
! Target surface areas
al,69,70,72,74      ! area 42
al,70,71,73,75      ! area 43
!
! Areas connecting air gap volume
al,74,67,76,75,77     ! area 44
al,77,65,78,71      ! area 45
lsel,s,line,,34,41
lsel,a,line,,76
lsel,a,line,,69
lsel,a,line,,79
al,all          ! area 46
lsel,s,line,,9,16
lsel,a,line,,72,73
lsel,a,line,,78,79
al,all          ! area 47
!
! Generating Volumes from Areas
!
! Cap gage volumes
va,1,17,9,25,33      ! volume 1 (conductor)
va,2,18,10,26,33,34    ! volume 2 (insulator)
va,3,19,11,27,34,35    ! volume 3 (conductor)
va,4,20,12,28,35,36    ! volume 4 (conductor)
va,5,21,13,29,36,37    ! volume 5 (insulator)
va,6,22,14,30,37,38    ! volume 6 (conductor)
va,7,23,15,31,38,39    ! volume 7 (air)
va,8,24,16,32,39,40,41  ! volume 8 (air-infinite)
!
! Air gap volume
asel,s,area,,25,32
asel,a,area,,42,47
va,all          ! volume 9 (air)
!
!
! Elements types and meshing
!
! First mesh areas and group nodes together, then mesh volumes based on this
!
et,1,mesh200,5      ! 2D meshing element only, 6 node triangle
!
vsel,s,,,1,1,,1      ! select volume 1 and areas, etc.
asel,u,,,1,1       ! removing symmetry sides
asel,u,,,9,9
asel,u,,,17,17
amesh,all         ! mesh with placeholders (triangles)
cm,cond1,node       ! Define conductor number 1 for cmatrix
!
vsel,s,,,3,4,,1      ! select guard ring
asel,u,,,35,35      ! remove common area from selection
asel,u,,,11,12
asel,u,,,3,4
asel,u,,,19,20
amesh,all         ! mesh with triangle placeholders
cm,cond2,node       ! Define conductor number 2
```

```
!
vsel,s,,,6,6,,1      ! select outer shield
asel,u,,,14,14
asel,u,,,6,6
asel,u,,,22,22
amesh,all         ! mesh with placeholders
cm,cond3,node       ! Define conductor number 3
!
asel,s,,,42,43,,1     ! select lower cylinder using areas
amesh,all         ! mesh with 2D placeholders
cm,cond4,node       ! Define conductor number 4
!
!
! Solid volumes element types and mesh
!
et,2,solid123       ! electrostatic tetrahedral volume element
mp,perx,1,1        ! efield relative permeability
mat,1           ! using material number 1 (air)
mat,2           ! defining type 2
mp,perx,2,3.8       ! setting permeability material 2 (plastic)
!
vsel,s,volu,,2      ! S for new selection, plastic volume
vsel,a,volu,,5      ! Add plastic volume 5
vmesh,all         ! mesh with type 2 material
!
mat,1           ! back to material type 1 (air)
vsel,s,volu,,7,8     ! Air gap on side of gage
vsel,a,volu,,9      ! Last of the air gaps
vmesh,all         ! mesh all selected volumes
!
! If needed, apply voltages to generate a graphical solution
!
!cmsel,s,cond1       ! select conductor 1 nodes
!d,all,volt,5       ! set voltage to 5 V
!cmsel,s,cond2       ! select conductor 2 nodes
!d,all,volt,5       ! set voltage to 5 V
!cmsel,s,cond3       ! select conductor 3 nodes
!d,all,volt,0       ! set voltage to 0 V
!cmsel,s,cond4       ! select conductor 4 nodes
!d,all,volt,0       ! set voltage to 0 V
!
allsel,all
save
finish
!
! cmatrix solver to determine capacitance values
!
/solution
cmatrix,1,'cond',4,1,'cmat' !*********************************************
!solve
finish
!
/post1
C(I,1)=gap          ! first value is current gap
C(I,2)=4*cmat(1,4,2)     ! pulling value from table, 4x for symmetry
finish
!
*enddo
!
! End of Loop
! **********************************************************************
!
! Output resulting table data to a file (need to multiply by 4 I think)
!
/post1
/output,res0250h,txt !****************************************************
*mwrite,C(1,1)
(F10.6, E18.7)
/output
finish
```

C.3 Importing IGES Format Code

The following code was developed to import a specific IGES data file from Pro/Engineer and add many geometric elements to the model. Once the critical volume is mapped meshed, the remaining volumes are free meshed and a capacitance solution is developed.

```
/title, Capacitance hole probe, geometry from ProE
!
! Version F, generate a capacitance solution using applied
! voltages or CMATRIX command
!
! Version E, meshing remaining large air volume, attempting
! to do brick elements as free mesh, should work per
! Dr. Rouch.
!
! Version C, trying to use mapped brick elements instead
! of the problematic tetrahedral elements in the thin
! sections. Import commands included in this file.
!
! Version B, try to remove super thin areas from
! meshing process, see if mesh is possible.
! import IGES file without volumes for this version.
!
! Version A, generate an electric field solution
! Attempting to generate a mesh of area "placeholders"
! before creating the volume mesh.
!
! Import IGES file commands, no spaces in path name
!
/aux15
ioptn,iges,smooth
ioptn,merg,yes
ioptn,solid,no
ioptn,small,yes
ioptn,gtoler,defa
igesin,O:\Users\psmith\CurrentWork\PhD\SpindleModel\mcp-fea,igs
!
/prep7
!
! Set units to um, picofarads, define epsilon0
!
emunit,epzro,8.854e-6     ! epsilon in pF per um
!
! Use same coordinate system for everything
!
csys,0
!
! Elements types and meshing
!
et,1,mesh200,7            ! 2D meshing element only, 8 node quadrilateral
!
local,11,1,0,0,0,0,90,0   ! New coordinate system with new Z along old -Y
csys,11                   ! change to new coordinate system
l,31,32                   ! line 16, segmenting off the rectangular area
l,42,44                   ! line 49
l,34,35                   ! line 50
l,48,47                   ! line 51
csys,0                    ! change to original (default) coordinate system
!
! Break lines into segments, connect segments
!
ldiv,16,,,3,0
ldiv,49,,,3,0
ldiv,50,,,3,0
ldiv,51,,,3,0
!
ldiv,15,,,3,0
```

```
ldiv,21,,,3,0
!
! Get keypoint location of created keypoints, use this information
! to generate additional points within the semicircular volume.
!
*get,k3x,kp,3,loc,x       ! Get X location of keypoint 3
*get,k3y,kp,3,loc,y       ! Get Y location of keypoint 3
*get,k3z,kp,3,loc,z       ! Get Z location of keypoint 3
*get,k5x,kp,5,loc,x       ! Get X location of keypoint 5
*get,k5y,kp,5,loc,y       ! Get Y location of keypoint 5
*get,k5z,kp,5,loc,z       ! Get Z location of keypoint 5
*get,k7x,kp,7,loc,x       ! Get X location of keypoint 7
*get,k7y,kp,7,loc,y       ! Get Y location of keypoint 7
*get,k7z,kp,7,loc,z       ! Get Z location of keypoint 7
*get,k8x,kp,8,loc,x       ! Get X location of keypoint 8
*get,k8y,kp,8,loc,y       ! Get Y location of keypoint 8
*get,k8z,kp,8,loc,z       ! Get Z location of keypoint 8
!
*get,k12x,kp,12,loc,x     ! Get X location of keypoint 12
*get,k12y,kp,12,loc,y     ! Get Y location of keypoint 12
*get,k12z,kp,12,loc,z     ! Get Z location of keypoint 12
*get,k13x,kp,13,loc,x     ! Get X location of keypoint 13
*get,k13y,kp,13,loc,y     ! Get Y location of keypoint 13
*get,k13z,kp,13,loc,z     ! Get Z location of keypoint 13
*get,k18x,kp,18,loc,x     ! Get X location of keypoint 18
*get,k18y,kp,18,loc,y     ! Get Y location of keypoint 18
*get,k18z,kp,18,loc,z     ! Get Z location of keypoint 18
*get,k20x,kp,20,loc,x     ! Get X location of keypoint 20
*get,k20y,kp,20,loc,y     ! Get Y location of keypoint 20
*get,k20z,kp,20,loc,z     ! Get Z location of keypoint 20
!
yoff=100
k,201,k3x,k3y+yoff,k3z
k,202,k5x,k5y+yoff,k5z
k,203,k7x,k7y+yoff,k7z
k,204,k8x,k8y+yoff,k8z
!
k,205,k12x,k12y-yoff,k12z
k,206,k13x,k13y-yoff,k13z
k,207,k18x,k18y-yoff,k18z
k,208,k20x,k20y-yoff,k20z
!
l,22,201                  ! line 64, bottom layer, 4 lines
l,201,3                   ! line 65
l,23,202                  ! line 66
l,202,5                   ! line 67
l,201,202                 ! line 68
l,201,203                 ! line 69, 2 short lines connecting layers
l,202,204                 ! line 70
l,25,203                  ! line 71, Top layer, 4 lines
l,203,7                   ! line 72
l,24,204                  ! line 73
l,204,8                   ! line 74
l,203,204                 ! line 75
!
l,3,12                    ! line 76, long lines across middle span
l,5,13                    ! line 77
l,7,18                    ! line 78
l,8,20                    ! line 79
l,3,7                     ! line 80, short lines to complete middle span
l,5,8                     ! line 81
l,12,18                   ! line 82
l,13,20                   ! line 83
l,23,24                   ! line 84
l,22,25                   ! line 85
!
al,81,79,83,77            ! area 1, two long narrow areas in rect. region
al,80,78,82,76            ! area 2
al,27,82,50,51            ! area 3, three areas on far end
al,82,83,56,58            ! area 4
al,83,26,59,57            ! area 5
al,20,80,16,49            ! area 6, three areas on near end
```

```
al,80,81,52,54             ! area 7
al,81,25,53,55             ! area 8
al,22,59,79,55             ! area 9, boundary side surface x 3
al,79,58,78,54             ! area 10
al,78,51,24,49             ! area 11
al,18,57,77,53             ! area 12, air side surface x 3
al,77,56,76,52             ! area 13
al,76,50,107,16            ! area 14
!
al,25,21,61,84             ! area 15
al,70,73,66,84             ! area 16
al,81,74,70,67             ! area 17
al,84,60,62,85             ! area 18
al,70,68,75,69             ! area 19
al,69,64,71,85             ! area 39
al,80,65,72,69             ! area 40
al,20,15,63,85             ! area 41
al,55,74,73,21             ! area 42
al,53,67,66,61             ! area 43
al,74,54,72,75             ! area 44
al,52,65,68,67             ! area 45
al,72,49,63,71             ! area 46
al,65,16,15,64             ! area 47
al,75,71,62,73             ! area 48
al,68,64,60,66             ! area 49
!
va,5,28,8,1,9,12           ! volume 1
va,1,4,2,7,10,13           ! volume 2
va,2,3,30,6,11,14          ! volume 3
va,15,16,17,8,42,43        ! volume 4
va,17,7,40,19,44,45        ! volume 5
va,40,6,41,39,46,47        ! volume 6
va,19,39,18,16,48,49       ! volume 7
!
! Create lines on bottom half of thin section
!
ldiv,17,,,3,0
ldiv,23,,,3,0
l,205,206                  ! line 90
l,206,13                   ! line 91
l,206,26                   ! line 92
l,18,207                   ! line 93
l,207,29                   ! line 94
l,207,208                  ! line 95
l,208,33                   ! line 96
l,208,20                   ! line 97
l,205,207                  ! line 98
l,206,208                  ! line 99
l,28,29                    ! line 100
l,26,33                    ! line 101
l,12,205                   ! line 102
l,205,28                   ! line 103
!
al,87,23,27,100            ! area 50
al,100,94,98,103           ! area 51
al,98,93,82,102            ! area 52
al,86,88,100,101           ! area 53
al,90,95,98,99             ! area 54
al,92,96,99,101            ! area 55
al,91,97,99,83             ! area 56
al,89,17,101,26            ! area 57
!
al,87,103,102,50           ! area 58
al,94,93,51,23             ! area 59
al,86,92,90,103            ! area 60
al,88,96,95,94             ! area 61
al,90,102,56,91            ! area 62
al,95,93,58,97             ! area 63
al,92,91,57,17             ! area 64
al,96,97,59,89             ! area 65
!
va,3,50,51,52,58,59
```

```
va,51,53,54,55,60,61
va,4,52,54,56,62,63
va,5,55,56,57,64,65
!
! Break lines to generate a better mesh
!
lesize,20,,,1              ! define these 4 short lines as single elements
lesize,25,,,1
lesize,26,,,1
lesize,27,,,1
!
lesize,16,,,8              ! line size thin volumes
lesize,52,,,8
lesize,65,,,6
lesize,91,,,6
lesize,76,,,12             ! along length of long section
!
mp,perx,1,80               ! efield relative permeability
mat,1                      ! using material number 1
et,1,solid122              ! solid brick elements
vsel,all
mshkey,1                   ! specify mapped meshing
vmesh,all                  ! mesh thin sections only
!
asel,s,,,12,14
asel,a,,,20,25
asel,a,,,31,38
asel,a,,,43,49,2
asel,a,,,58,64,2
va,all                     ! volume 12
!
mshkey,0                   ! switch to free meshing
mshape,1,3d                ! set elements to 3d tetrahedral
vmesh,12                   ! mesh volume 12
!
!
! Begin grouping boundary nodes for analysis
!
asel,s,,,9,11,,1           ! select areas 9-11 and nodes
cm,senA,node               ! give this group a name
asel,s,,,42,48,2,1         ! select areas 42,44,46,48 and nodes
cm,senB,node
asel,s,,,59,65,2,1         ! select areas 59,61,63,65 and nodes
cm,senC,node
cmsel,s,senA
cmsel,a,senB
cmsel,a,senC
cm,cond1,node              ! Complete conductor 1
!
asel,s,,,22,22,,1          ! select area 22 and nodes
cm,grdA,node
asel,s,,,25,25,,1
cm,grdB,node
cmsel,s,grdA
cmsel,a,grdB
cm,cond2,node              ! complete conductor 2
!
asel,s,,,34,34,,1          ! select area 34 and nodes
cm,trgA,node
asel,s,,,36,38,,1
cm,trgB,node
cmsel,s,trgA
cmsel,a,trgB
cm,cond3,node              ! complete conductor 3
!
! If needed, apply voltages to generate a graphical solution
!
!cmsel,s,cond1              ! select conductor 1 nodes (sensing area)
!d,all,volt,5               ! set voltage to 5 V
!cmsel,s,cond2              ! select conductor 2 nodes (guard structure)
!d,all,volt,5               ! set voltage to 5 V
!cmsel,s,cond3              ! select conductor 3 nodes (target surface)
```

```
!d,all,volt,0              ! set voltage to 0 V
!
allsel,all
save
finish
!
! cmatrix solver to determine capacitance values, or use 'solve' to
! generate a graphical solution
!
/solution
allsel,all
!cmatrix,1,'cond',3,1,'cmat'
!solve
finish
!
```

Appendix D: Matlab Code for Machining and Analysis

D.1 Machining Routines

Matlab code was also used when the machining routines on the μEDM machine were sufficiently complex that they could not be performed with existing subroutines.

D.1.1 Machining a hemisphere

The code below creates a hemisphere on the end of a tungsten carbide probe. The `query` commands are passed to the μEDM machine through the serial port.

```
% code written by Phil to manually round the edge of a probe
% at the juncture between a larger diameter and a small
% diameter.

clear all;
clc;

% Put in current home position in uEDM units
HomeX=469928;
HomeY=-50872;
%
% Radii of probe, arc in uEDM units
Rlarge=5750;
Redge=1000;
Rwire=500;
Rfudge=50;
Rsafe=Rlarge-Redge+Rwire+Rfudge;
%
% Array of values to use for motion commands
%
xmove=[33; 67; 100; 133; 167; 200; 233; 267; 300; 333; 367;
    400; 433; 467; 500; 533; 567; 600; 633; 667; 700; 733;
    767; 800; 824; 846; 866; 884; 901; 917; 930; 943; 954;
    964; 972; 980; 986; 991; 995; 998; 999; 1000];
zmove=[1; 2; 5; 9; 14; 20; 28; 36; 46; 57; 70; 83; 99; 116;
    134; 154; 176; 200; 226; 255; 286; 320; 358; 400; 433;
    467; 500; 533; 567; 600; 633; 667; 700; 733; 767; 800;
    833; 867; 900; 933; 967; 1000];
%
% These commands are general configuration commands
% to start the machine, etc.
%
EDM = serial('COM1','BaudRate',9600,'timeout',1000);
fopen(EDM);
query(EDM,['buz 2'])
query(EDM,['back x 1'])
query(EDM,['back y 1'])
query(EDM,['fsf x 100'])
query(EDM,['fsm x 10'])
query(EDM,['fsf y 100'])
query(EDM,['fsm y 10'])
query(EDM,['fsf z 50'])
query(EDM,['fsm z 10'])
query(EDM,['spn 0'])
% Next two lines capacitor and voltage
query(EDM,['con 3'])
query(EDM,['vol 2 -80'])
% Turn on voltage and wire winding
query(EDM,['vol 0'])
query(EDM,['wire 1'])
%
% Next commands are unique to this process
% they find the edge and reset the z value to zero
%
```

```
query(EDM,['abs x ',num2str(HomeX+Rsafe)])
query(EDM,['abs y ',num2str(HomeY)])
query(EDM,['map 10'])
query(EDM,['cui z 10 x 0 0 250'])
query(EDM,['res z'])
%
% Shaping a probe tip of 300 microns diameter
%
for N=1:42
    query(EDM,['abs x ',num2str(HomeX+Rsafe+xmove(N))])
    query(EDM,['cua z ',num2str(zmove(N)),' x 0 0'])
end
%
% These commands lift the probe and shut off the process
%
query(EDM,['fsf z 10000'])
query(EDM,['abs z -100000'])
query(EDM,['spn 1'])
query(EDM,['vol 1'])
query(EDM,['wire 2'])
query(EDM,['buz 2'])
Complete='Machining Finished!'

Cleanup_Device(EDM);
```

D.1.2 Grinding process for slot creation

The code below, written by Chris Morgan and only slightly modified for this application, is a grinding process rather than a traditional μEDM process. After each pass the tool is raised to clear chips from the work area.

```
clear all;
clc;

EDM = serial('COM1','BaudRate',9600,'timeout',100000);
fopen(EDM);
query(EDM,['buz 2'])
query(EDM,['back x 1'])
query(EDM,['back y 1'])
query(EDM,['res x'])
query(EDM,['res y'])
query(EDM,['res z'])
query(EDM,['fsf x 10'])
query(EDM,['fsm x 1'])
query(EDM,['fsf y 100'])
query(EDM,['fsm y 10'])
query(EDM,['fsf z 500'])
query(EDM,['fsm z 10'])
query(EDM,['spn 0'])
query(EDM,['con 1'])
query(EDM,['vol 2 -110'])
query(EDM,'vol 0')
query(EDM,'wire 1')
%query(EDM,'aps y +')
%query(EDM,'res y')
query(EDM,'abs y -100')
%query(EDM,'abs x 2000')
%query(EDM,'abs y 0')
%query(EDM,'res y')
%query(EDM,'aps x -')
%query(EDM,'res x')
%query(EDM,'abs x 100')
%query(EDM,'abs z -10000')
query(EDM,'abs x -1000')
%query(EDM,'res x')
query(EDM,'aps z +')
query(EDM,'res z')
query(EDM,'abs z -100')
query(EDM,'cua z 1000 x 0 0')
```

```
query(EDM,'cua x 0 0 0')
query(EDM,'fsf z 10')
query(EDM,'fsm z 1')
for i=1:15
    query(EDM,['abs z ',num2str((i*20)-10)])
    query(EDM,['abs x 9000'])
    query(EDM,['abs z -100'])
    query(EDM,['abs z ',num2str(i*20)])
    query(EDM,['abs x 0'])
    query(EDM,['abs z -100'])
end

query(EDM,['fsf z 10000'])
query(EDM,['abs z -5000'])
query(EDM,['buz 2'])
query(EDM,['spn 1'])
query(EDM,['vol 1'])
query(EDM,'wire 2')
Complete='Machining Finished!'

Cleanup_Device(EDM);
```

D.2 Code for Analysis

The file below, decon1.m, deconvolves capacitance data from an unshielded capacitance probe and a half-hole target. This method, based on Markiewicz and Goh [62], is a geometric deconvolution. The resulting probe shape varies as the gap distance to the target surface.

```
% This program will apply the deconvolution algorithm as proposed
% by Markiewicz and Goh to the unshielded data from "b", "d",
% and "f" series.
%
clear all;
close all;
e0=8.854e-3;
eR=80;
A=0.0712606;
angl=[5; 10; 15; 20; 25; 30; 35; 40; 45; 50;
    55; 60; 65; 70; 75; 80; 85; 90; 95; 100;
    105; 110; 115; 120; 125; 130; 135; 140;
    145; 150; 155; 160];
C1=[0.058832; 0.061498; 0.064711; 0.068192; 0.073086;
    0.077372; 0.086640; 0.10104; 0.12355; 0.15678;
    0.21014; 0.26450; 0.32541; 0.38034; 0.43677;
    0.48683; 0.53269; 0.55614; 0.56815; 0.56953;
    0.56979; 0.57148; 0.57156; 0.57113; 0.57167;
    0.57172; 0.57119; 0.56870; 0.56849; 0.56757;
    0.56651; 0.56723];
C2=[0.053849; 0.055905; 0.058319; 0.061078; 0.065063;
    0.070642; 0.078966; 0.095224; 0.12692; 0.20469;
    0.42867; 0.73900; 1.0494; 1.3575; 1.6688;
    1.9763; 2.2690; 2.5151; 2.5785; 2.5537;
    2.5870; 2.5846; 2.5899; 2.5885; 2.6053;
    2.5987];
C3=[0.061929; 0.064785; 0.068034; 0.071880; 0.076871;
    0.082745; 0.091595; 0.10280; 0.11683; 0.13522;
    0.16017; 0.18232; 0.20959; 0.23468; 0.25697;
    0.27675; 0.29286; 0.30307; 0.30822; 0.31010;
    0.31078; 0.31072; 0.31058; 0.31197; 0.30950;
    0.30691];
C2fix=[C2(1:24,:); C2(24); C2(24); C2(24); C2(25);
    C2(25); C2(25); C2(26); C2(26)];
C3fix=[C3(1:24,:); C3(24); C3(24); C3(24); C3(25);
    C3(25); C3(25); C3(26); C3(26)];
C1long=[C1(1:31); flipud(C1)];
```

```
C2long=[C2fix(1:31); flipud(C2fix)];
C3long=[C3fix(1:31); flipud(C3fix)];
FullAng=[25:5:335]';
%
% Convert capacitance to distance
%
d1=-e0*eR*A./C1long;
d1pos=d1+1.00;
d2=-e0*eR*A./C2long;
d2pos=d2+1.00;
d3=-e0*eR*A./C3long;
d3pos=d3+1.00;
%
mind1pos=min(d1pos); maxd1pos=max(d1pos);
Hole1=[(maxd1pos-mind1pos)*ones(13,1); 0*ones(37,1);
    (maxd1pos-mind1pos)*ones(13,1)];

mind2pos=min(d2pos); maxd2pos=max(d2pos);
Hole2=[(maxd2pos-mind2pos)*ones(13,1); 0*ones(37,1);
    (maxd2pos-mind2pos)*ones(13,1)];

mind3pos=min(d3pos); maxd3pos=max(d3pos);
Hole3=[(maxd3pos-mind3pos)*ones(13,1); 0*ones(37,1);
    (maxd3pos-mind3pos)*ones(13,1)];

%
% Set default values high
Tip1=5*ones(63,1);
Tip2=5*ones(63,1);
Tip3=5*ones(63,1);

for n=1:length(d1)
   m=max([n-31 1]); % start point on tip1
   p=min([n+31 63]); % end point on tip1
   r=max([33-n 1]); % start point for Hole1
   s=min([95-n 63]); % end point for Hole1
   for q=m:p % range in terms of tip1
       Hole1temp=Hole1+d1pos(n);
       Hole2temp=Hole2+d2pos(n);
       Hole3temp=Hole3+d3pos(n);
       Tip1(q)=min([Tip1(q) Hole1temp(r)]);
       Tip2(q)=min([Tip2(q) Hole2temp(r)]);
       Tip3(q)=min([Tip3(q) Hole3temp(r)]);
       r=r+1;
   end
end



%
% Plot the results
%
figure(1);
set(1,'PaperPositionMode','Manual')
set(1,'Position',[0 0 6.5*72 4.25*72])
set(1,'PaperPosition',[0 0 6.5 4.25])

plot(FullAng-180,Tip3-min(Tip3),'b');
grid on;
hold on;
plot(FullAng-180,Tip1-min(Tip1),'g');
plot(FullAng-180,Tip2-min(Tip2),'r');
xlabel('Angle width, degrees');
ylabel('Tip height, mm');
legend('radius 0.8 mm','radius 0.9 mm','radius 0.98 mm');
%title('No guard data from flatfile4x.m')
print -depsc Fig5-9tmp.eps    % export figure to color EPS format
hold off
```

References

[1] Rosa, E. B. and N. E. Dorsey. *Bull. Bur. Stds*. V. 3. p. 433-604.

[2] Lee, J. H., Y. Liu, S. H. Kweon, S. H. Yang, and Y. S. Kim. “A Measurement System Based on Capacitance Sensors for Geometric Errors of a Miniaturized Machine Tool.” *Proceedings of the 2005 IEEE/ASME International Conference on Advanced Intelligent Mechatronics.* Monterey, California. 24-28 July 2005.

[3] Morgan, V. T. and D. E. Brown. “A Differential-Capacitance Transducer for Measuring Small Displacements”. *Journal of Physics E: Scientific Instruments*. V. 2. 1969. p. 793-795.

[4] Jones, R. V. and J. C. S. Richards. “The Design and Some Applications of Sensitive Capacitance Micrometers”. *Journal of Physics E: Scientific Instruments*. V. 6. 1973. p. 589-600

[5] Stacey, F. D. , J. M. W. Rynn, E. C. Little, and C. Croskell. “Displacement and Tilt Transducers of 140 dB Range”. *Journal of Physics E: Scientific Instruments*. V. 2. 1969. p. 945-949.

[6] Schofield, J. W. “A Linear Capacitance Micrometer”. *Journal of Physics E: Scientific Instruments*. V. 5. 1972. p. 822-825.

[7] Richards, J. C. S. “Linear Capacitance Proximity Gauges with High Resolution”. *Journal of Physics E: Scientific Instruments*. V. 9. 1976. p. 639-646.

[8] Foldvari, T. L. and K. S. Lion, “Capacitive Transducers”, *Instruments and Control Systems,* Nov., 1964. V. 37. p. 77-85.

[9] Sydenham, P. H. “Microdisplacement Transducers”. *Journal of Physics E: Scientific Instruments*. V. 5. p. 721-733.

[10] Rigden, J. D. “A Capacitive Bore Gauge”. *Journal of Physics E: Scientific Instruments*. V. 10. 1977. p. 1276-1278.

[11] Maxwell, J. C. *A Treatise on Electricity and Magnetism*. V. 1. Oxford. 1873.

[12] Wolfendale, P. C. F. “Capacitive Displacement Transducers with High Accuracy and Resolution”. *Journal of Physics E: Scientific Instruments*. V. 1, Ser. 2. 1968. p. 817-818.

[13] de Jong, G. W. and G. C. M. Meijer. “An Efficient Retrieving Algorithm for Accurate Capacitive Position Sensors”. *Sensors and Actuators A*. V. 58. 1997. p. 75-84.

[14] Kolb, P. W. , R. S. Decca, and H. D. Drew. “Capacitive Sensor for Micropositioning in Two Dimensions”. *Review of Scientific Instruments*. V. 69. No. 1. 1988. p. 310-312.

[15] Hicks, T. R. , N. K. Reay, and P. D. Atherton. “The Application of Capacitance Micrometry to the Control of Fabry-Perot Etalons”. *Journal of Physics E: Scientific Instruments*. V. 17. 1984. p. 49-55.

[16] Jongeling, J. M. and W. C. Heerens, “The Comparison of Two Absolute Layer Thickness Gauges” *J. Phys. E: Sci. Instrum.* V. 17. 1984. p. 664-668.

[17] Kandala, C. V., C. L. Butts, and S. O. Nelson. “Capacitance Sensor for Nondestructive Measurement of Moisture Content in Nuts and Grain.”

Instrumentation and Measurement Technology Conference Ottawa, Canada 17-19 May 2005. p. 622-626.

[18] Hague, B., and T. R. Foord. *Alternating Current Bridge Methods*. Pittman & Sons. London. 1971.

[19] Hugill, A. L. “Displacement Transducers Based on Reactive Sensors in Transformer Ratio Bridges”. *Journal of Physics E: Scientific Instrum*ents. V. 15. 1982. p. 597-606.

[20] Dratler, J. “Inexpensive Linear Displacement Transducer Using a Low Power Lock-In Amplifier”. *Review of Scientific Instruments*. V. 48, No. 3. 1977. p. 327-335.

[21] Huang, S. M. , A. L. Stott, R. G. Green, and M. S. Beck. “Electronic Transducers for Industrial Measurement of Low Value Capacitances”. *Journal of Physics E: Scientific Instruments*. V. 21. 1988. p. 242-250.

[22] Ashrafi, A. and H. Golnabi. “A High Precision Method for Measuring Very Small Capacitance Changes”. *Review of Scientific Instruments*. V. 70. N. 8. 1999. p. 3483-3487.

[23] Lányi, S. and M. Hruškovic. “Linearization of Inverse-Capacitance-Based Displacement Transducers”. *Measurement Science and Technology*. V. 12. 2001. p. 77-81.

[24] Fritsch, K. “Linear Capacitive Displacement Sensor with Frequency Readout”. *Review of Scientific Instruments*. V. 58. No. 5. 1987. p. 861-863.

[25] Heerens, W. C. and F. C. Vermeulen. “Capacitance of Kelvin Guard-Ring Capacitors with Modified Edge Geometry”. *Journal of Applied Physics*. V. 46. 1975. p. 2486-2490.

[26] Heerens, W. C. “The Solution of Laplace’s Equation in Cylindrical and Toroidal Configurations with Rectangular Sectional Shapes and Rotation-Symmetrical Boundary Conditions”. *Journal of Applied Physics*. V. 47. No. 8. 1976. p. 3740-3744.

[27] Heerens, W. C. “Application of Capacitance Techniques in Sensor Design”. *Journal of Physics E: Scientific Instruments*. V. 19. 1986. p. 897-906.

[28] Lazzarini, A. “Sources of Error in Dynamic Applications of Electronic Displacement Sensors”. *Review of Scientific Instruments*. V. 57. No. 12. 1986. p. 3099-3106.

[29] Hicks, T., and P. D. Atherton. *Nanopositioning Book*. Queensgate Instruments.

[30] Khan, A. R., I. J. Brown, and M. A. Brown. “The Behavior of Capacitance Displacement Transducers Using Epoxy Resin as an Electrode-Guard Ring Spacer”. *Journal of Physics E: Scientific Instruments*. V. 13. 1980. p. 1280-1281.

[31] Brown, M. A. and C. E. Bulleid. “The Effect of Tilt and Surface Damage on Practical Capacitance Displacement Transducers”. *Journal of Physics E: Scientific Instruments*. V. 11. 1978. p. 429-432.

[32] Puers, R. and D. Lapadatu. “Electrostatic Forces and Their Effects on Capacitive Mechanical Sensors”. *Sensors and Actuators A*. V. 56. 1996. p. 203-210.

[33] Genossar, J. and M. Steinitz. “A Tilted-Plate Capacitance Displacement Sensor”. *Review of Scientific Instruments*. V. 61, No. 9. 1990. p. 2469-2471.

[34] Harb, S. M. , D. G. Chetwynd, and S. T. Smith. "Tilt Errors in Parallel Plate Capacitive Micrometry". *International Progress in Precision Engineering.* 8th International Precision Engineering Seminar. Elsevier. Compiegne, France. May 1995. p. 147-150.

[35] Zhao, X., "High Linearity Measurement of Large Tip-Tilt Angles with Capacitance Sensors", EUSPEN Proceedings, May, 1999, 326-332.

[36] Gladwin, M. T. and J. Wolfe. "Linearity of Capacitance Displacement Transducers". *Review of Scientific Instruments.* V. 46, No. 8. 1975. p. 1099-1100.

[37] Bonse, M. H. W., C. Mul, and J. W. Spronck. "Finite-Element Modelling as a Tool for Designing Capacitive Position Sensor". *Sensors and Actuators A*. V. 46-47. 1995. p. 266-269.

[38] Ansel, Y., B. Romanowicz, P. Renaud, and G. Schröfer. "Global Model Generation for a Capacitive Silicon Accelerometer by Finite Element Analysis". *Sensors and Actuators A*. V. 67. 1998. p. 153-158.

[39] Khan, S. H. and K. T. V. Grattan, L. Finkelstein. "Investigation of Leakage Flux in a Capacitive Angular Displacement Sensor Used in Torque Motors by 3D Finite Element Field Modeling". *Sensors and Actuators A*. V. 76. 1999. p. 253-259.

[40] Kuijpers, A. A. , G. J. M. Krijnen, R. J. Wiegerink, T. S. J. Lammerink, and M. Elwenspoek. "2D-Finite-Element Simulations for Long-Range Capacitive Position Sensor". *Journal of Micromechanics and Microengineering*. V. 13. 2003. p. S183-S189.

[41] Lányi, Š. "Analysis of Linearity Errors of Inverse Capacitance Position Sensors. " *Measurement Science and Technology* V. 9 1998. p. 1762.

[42] Yu, Q. and T. W. Holmes. "A Study on Stray Capacitance Modeling of Inductors by Using the Finite Element Method." *IEEE Transactions on Electromagnetic Compatibility* V. 43. No. 1. Feb 2001. p. 88-93.

[43] Liang, C. H., L. Li, and H. Q. Zhai. "Asymptotic closed form for the capacitance of an arbitrarily shaped conducting plate." *IEE Proceedings - Microwave Antennas Propagation.* V. 151. No. 3. June 2004. p. 217-220.

[44] Du, Y. and Q. B. Zhou. "Capacitance Matrix of Screened/Insulated Single-Core Cables of Finite Length." *IEE Proceedings – Sci. Measurement Techonology.* V. 152. No. 5. September, 2005. p. 233-239.

[45] Harrington, R. F. *Field Computation by Moment Methods.* Macmillan, New York, 1968.

[46] Shkel, Y. M. and N. J. Ferrier. "Electrostriction Enhancement of Solid-State Capacitance Sensing." *IEEE/ASME Transactions on Mechatronics.* V. 8. No. 3. September 2003. p. 318-325.

[47] Bord, I., P. Tardy, and F. Menil. "Influence of the Electrodes Configuration on a Differential Capacitive Rain Sensor Performances." *Sensors and Actuators B.* V. 114. 2006. p. 640-645.

[48] Evans, I. and T. York. "Microelectronic Capacitance Transducer for Particle Detection." *IEEE Sensors Journal.* V. 4. No. 3. June 2004. p. 364-372.

[49] He, R., C. G. Xie, R. C. Waterfall, M. S. Beck, and C. M. Beck. “Engine Flame Imaging Using Electrical Capacitance Tomography.” *Electronics Letters.* V. 30, No. 7. 31 March 1994. p. 559-560.

[50] Holler, G., T. Thurner, H. Zangl, and G. Brasseur. “A Novel Capacitance Sensor Principle Applicable for Spatially Resolving Downhole Measurements.” *IEEE Instrumentation and Measurement Technology Conference.* Anchorage, AK, 21-23 May 2002. p. 1157-1160.

[51] Al-Mously, S. I. and A. Y. Ahmed. “The Use of a Coaxial Capacitor as a Capacitance Sensor for Phase Percentage Determination in Multiphase Pipelines.” *Tenth Mediterranean Electrotechnical Conference, MEleCon 2000.* V. 2. p. 742-745.

[52] Schüller, R. B., T. Gundersen, M. Halleraker, and B. Engebretsen. “Measurement of Water Concentration in Oil/Water Dispersions with a Circular Single-Electrode Capacitance Probe.” *IEEE Transactions on Instrumentation and Measurement.* V. 53. No. 5. October 2004. p. 1378-1383.

[53] Donaldson, R. R., “A Simple Method for Separating Spindle Error from Test Ball Roundness Error.” *CIRP Annals* V. 21, No. 1. 1972. p. 125-126.

[54] “Measurement of Out-Of-Roundness.” *ANSI Standard B89.3.1-1972*. New York. American Society of Mechanical Engineers. 1972. p. 22.

[55] ANSI/ASME B89. 3. 4M. *Axes of Rotation – Methods for Specifying and Testing*. American Society of Mechanical Engineers. New York. 1985.

[56] C. J. Evans, R. J. Hocken, and W. T. Estler. “Self-Calibration: Reversal, Redundancy, Error Separation, and ‘Absolute Testing’,” *CIRP Annals* V. 45. 1996. p. 617-634.

[57] Reiss, G., J. Vancea, H. Wittman, J. Zweck, and H. Hoffman. “Scanning tunneling microscopy on rough surfaces: Tip-shape-limited resolution.” *Journal of Applied Physics* V. 67. No. 3. 1 February 1990. p. 1156-1159.

[58] Aumond, B. D. and K. Youcef-Toumi. “Experimental high precision profilometry of high aspect ratio samples.” *IEEE* 1998. p. 4435-4440.

[59] Kiely, J. D. and D. A. Bonnell. “Quantification of topographic structure by scanning probe microscopy.” *Journal of Vacuum Science and Technology B.* V. 15. No. 4 July/August 1997. p. 1483-1493.

[60] Bykov, V., A. Gologanov, and V. Shevyakov. “Test structure for SPM tip shape deconvolution.” *Applied Physics A*. V. 66. 1998. p. 499-502.

[61] Markiewicz, P., and M. C. Goh. “Atomic force microscope tip deconvolution using calibration arrays.” *Review of Scientific Instrumentation.* V. 66. No. 5. May 1995. p. 3186-3190.

[62] Markiewicz, P., and M. C. Goh. “Atomic force microscopy probe tip visualization and improvement of images using a simple deconvolution procedure.” Langmuir 1994. V. 10. p. 5-7.

[63] S. Dongmo, M. Troyon, P. Vautrot, E. Delain, N. Bonnet. “Blind restoration method of scanning tunneling and atomic force microscopy images.” *Journal of Vacuum Science Technology B.* V. 14. No. 2. March/April 1996. p. 1552-1556.

[64] Williams, P. M., K. M. Shakesheff, M. C. Davies, et al. “Toward True Surface Recovery: Studying Distortions in Scanning Probe Microscopy Image Data.” Langmuir 1996. V. 12. p. 3468-3471.

[65] Gomez-Monivas, S., J. J. Saenz, R. Carminati, and J. J. Greffet. “Theory of electrostatic probe microscopy: A simple pertubative approach.” *Applied Physics Letters*. V. 76. No. 20. 15 May 2000. p. 2955-2957.

[66] Williams, P. M., M. C. Davies, C. J. Roberts, and S. J. B. Tendler. “Noise-compliant tip-shape derivation.” *Applied Physics A* V. 66. 1998. p. S911-S914.

[67] Whitehouse, D. J. *Handbook of Surface Metrology*. CRC Press. 1994. p. 181.

[68] Voelcker, H. B., “The current state of affairs in dimensional tolerancing: 1997”. *Integrated Manufacturing Systems* V. 9 No. 4. 1998. p. 205-217.

[69] Masuzawa, T., Y. Hamasaki, M. Fujino. “Vibroscanning Method for Nondestructive Measurement of Small Holes.” *Annals of the CIRP*, V. 42. No. 1. 1993. p. 589-592.

[70] Kim, B., T. Masuzawa, and T. Bourouina. “The vibroscanning method for the measurement of micro-hole profiles.” *Measurement Science Technology.* V. 10. 1999. p. 697-705.

[71] Zhang, G. X. and S. M. Yang. “A 3D Probe for Measuring Small Blind Holes.” *Annals of the CIRP.* V. 44. No. 1. 1995. p. 461-464.

[72] Lebrasseur, E., J.-B. Pourciel, T. Bourouina, T. Masuzawa, and H. Fujita. “A new characterization tool for vertical profile measurement of high-aspect-ratio microstructures.” *J. Micromech. Microeng.* V. 12. 2002. p. 280-285.

[73] Kim, B. J., T. Masuzawa, H. Fujita, and A. Tominaga. “Dimensional Measurement of Microholes with Silicon-Based Micro Twin Probes.” *Proceedings of the Eleventh Annual International Workshop on Micro Electro Mechanical Systems.* 25-29 Jan 1998. Heidelberg, Germany. p. 334-339.

[74] Muralikrishnan, B., J. A. Stone, and J. R. Stoup. “Fiber deflection probe for small hole metrology.” *Precision Engineering* V. 30. 2006. p. 154-164.

[75] Muralikrishnan, B., J. A. Stone, and J. R. Stoup. “Enhanced Capabilities of the NIST Fiber Probe for Microfeature Metrology.” *Proceedings of the 21st Annual Meeting of the American Society of Precision Engineering*, Monterey, CA. 15-20 Oct 2006. Electronic version, p. 1-4.

[76] Wissmann, M., H. Schwenke, U. Neuschaefer-Rube. “Speckle Correlation Method for 3D-Deflection Measurement of the Tactile-Optical Microprobe.” *Proceedings of the 21st Annual Meeting of the American Society of Precision Engineering*, Monterey, CA. 15-20 Oct 2006. p. 79-82.

[77] Bauza, M. B., R. J. Hocken, S. T. Smith, and S. C. Woody. “Development of a Virtual Probe Tip with an Application to High Aspect Ratio Microscale Features.” *Review of Scientific Instruments* V. 76. 2005. p. 95-112.

[78] Bathe, K.-J., *Finite Element Procedures*. Upper Saddle River, N. J. Prentice Hall. 1996. p. 643.

[79] Binns, K. J. and P. J. Lawrenson, *Analysis and Computation of Electric and Magnetic Field Problems*. New York. Pergamon. 1973. p. 59-61.

[80] Moaveni, S., *Finite Element Analysis: Theory and Application with ANSYS.* Prentice Hall. Upper Saddle River, NJ. 1999. p. 452.

[81] *ANSYS 8.0 Online Help Files*. Element Reference, Part I. Element Library, type SOLID123.

[82] Smith, P. T. *Analysis and Application of Capacitive Displacement Sensors to Curved Surfaces*. Master's Thesis. University of Kentucky. 2003.

[83] Smith, P. T., R. R. Vallance, E. R. Marsh. "Correcting Capacitive Displacement Measurements in Metrology Applications with Cylindrical Artifacts." *Precision Engineering*. V. 29. No. 3. July 2005. p. 324-335.

[84] C. Moon and C.M. Sparks, *Journal of Research of the National Bureau of Standards* V. 22. 1948.

[85] http://hyperphysics.phy-astr.gsu.edu/hbase/electric/capcyl.html

[86] Erickson, F. M. "The Capacitance Between Two Spheres." Unpublished paper, November 3, 1999.

[87] Logan, D. L. *A First Course in the Finite Element Method*. Brooks/Cole. Pacific Grove. CA. 2000. p. 466.

[88] ASME/ANSI B89.3.1. *Measurement of Out-of-roundness*. American Society of Mechanical Engineers. New York. 1972.

[89] Horikawa, O. , N. Maruyama, and M. Shimada. "A Low Cost, High Accuracy Roundness Measuring System" *Precision Engineering*, V. 25. 2001. p. 200-205.

[90] ANSI/ASME B89. 3. 4M. *Axes of Rotation – Methods for Specifying and Testing*. American Society of Mechanical Engineers. New York. 1985.

[91] Grejda, R., E. Marsh, and R. Vallance. "Techniques for Calibrating Spindles with Nanometer Error Motion". *Precision Engineering*. V. 29. No. 1. January 2005. p. 113-123.

[92] ANSI/ASME B5. 54. *Methods for Performance Evaluation of Computer Numerically Controlled Machining Centers*. American Society of Mechanical Engineers. New York. 1992.

[93] ANSI/ASME B5. 57. *Methods for Performance Evaluation of Computer Numerically Controlled Lathes and Turning Centers*. American Society of Mechanical Engineers. New York. 2000.

[94] Vallance, R. R. , E. R. Marsh, and P. T. Smith. "Effects of Spherical Targets on Capacitive Displacement Measurements". *ASME Journal of Manufacturing Science and Engineering*. Vol. 126. 2004. p. 822-829.

[95] Donaldson RR. A Simple Method for Separating Spindle Error from Test Ball Roundness Error. *Annals of the CIRP*. 1972. V. 21. No. 1. p. 125-126.

[96] Slocum, A. H. *Precision Machine Design.* Society of Manufacturing Engineers, Dearborn, MI, 1992. p. 60-61.

[97] Whitehouse, D.J. "Some Theoretical Aspects of Error Separation Techniques in Surface Metrology." *J. of Phys. E: Sci. Inst.* 1976. V. 9. p. 531-536.

[98] Marsh E., and R. Grejda. "Experiences with the Master Axis Method for Measuring Spindle Error Motion." *Precision Engineering* 2000. V. 24. No. 1. p. 50-57.

[99] Feynman, R. P., R. B. Leighton, and M. Sands. *The Feynman Lectures on Physics.* Addison-Wesley, Reading, MA. 1964. Vol. II. p. 2-8.

[100] Lion, K. S. *Instrumentation in Scientific Research.* 1959. p. 69-70.

[101] Taylor, J. R. *An Introduction to Error Analysis.* University Science. 1982. p. 73.

[102] Schwenke, H., F. Waldele, C. Weiskirch, and H. Kunzmann. "Opto-Tactile Sensor for 2D and 3D Measurement of Small Structures on Coordinate Measuring Machines." *Annals of the CIRP*. V. 50. No. 1. 2001. p. 361-364.

[103] Masuzawa, T., M. Fujino, K. Kobayashi, and T. Suzuki. "Wire ElectroDischarge Grinding for Micro- Machining". *Annals of the CIRP. International Institution for Production Engineering Research.* V. 34. No. 1. 1985. p. 431-434.

[104] Iida, D. *High Performance Capacitive Sensors.* Master's Thesis. University of North Carolina. 2003.

[105] Vallance, R. R., E. R. Marsh, and P. T. Smith. "Effects of Spherical Targets on Capacitive Displacement Measurements." *ASME Journal of Manufacturing Science.* Vol. 126, No. 4, pp. 822-829.

[106] Smith, P. T., R. R. Vallance, and E. R. Marsh. "Correcting Capacitive Displacement Measurements in Metrology Applications with Cylindrical Artifacts" *Precision Engineering*. V.29, No. 3. 2005. p. 307-314.

[107] Morgan, V. T. and D. E. Brown. "A Differential-Capacitance Transducer for Measuring Small Displacements". *Journal of Physics E: Scientific Instruments*. V. 2. 1969. p. 793-795.

[108] Jones, R. V. and J. C. S. Richards. "The Design and Some Applications of Sensitive Capacitance Micrometers". *Journal of Physics E: Scientific Instruments*. V. 6. 1973. p. 589-600.

[109] Kurafuji, H. and T. Masuzawa. "Micro-EDM of cemented carbide alloys". *Japan Society of Electrical-Machining Engineers* V. 2. No. 3. 1968. p. 1-16.

[110] Vallance, R. R., C. J. Morgan, and E. R. Marsh. "Micro-tool Characterization Using Scanning White Light Interferometry". *Journal of Micromechanics and Microengineering*. V. 14. No. 8. August 2004. p. 1234-1243.

[111] *Handbook of Semiconductor Wafer Cleaning Technology: Science, Technology and Applications.* Werner Kern, ed. William Andrew Inc. 1993. p. 120-123.

[112] Garg, D., P. N. Dyer, D. B. Dimos, S. Sunder. "Low-Temperature Chemical Vapor Deposition Tungsten Carbide Coatings for Wear/Erosion Resistance." *J. Am. Ceram. Soc.* V. 75 No. 4. p. 1008-1011. 1992.

[113] Przybylowicz, J., J. Kusinski. "Structure of laser cladded tungsten carbide composite coatings." *Journal of Materials Processing Technology* V. 109. 2001. p. 154-160.

[114] Narasimhan, D., et al. United States Patent no. 6,811,894. "Ceramic Turbine Blade Attachment having High Temperature, High Stress Compliant Layers and Method of Fabrication Thereof." Nov. 2, 2004.

[115] Mahapatro, A. K., S. Ghosh, and D. B. Janes. "Pairs of Gold Electrodes with Nanometer Separation Performed over SiO2 Substrates with a Molecular Adhesion

Monolayer." *Condensed Matter.* Preprint "cond-mat/0503656" at http://arXiv.org. 2005.

[116] *Zygo NewView 5000 Operating Manual OMP-0423G*. Zygo Corporation, Middlefield, CT. 2002. p. 6-4.

[117] Madou, M. J. *Fundamentals of Microfabrication: The Science of Miniaturization*. 2nd ed. CRC Press, Washington D.C. 2002. p. 90.

[118] Eagle Stainless Tube and Fabrication, Franklin, MA. Online Catalog.

[119] Williams, K. R., K. Gupta, and M. Wasilik. "Etch Rates for Micromachining Processing – Part II". *Journal of Microelectromechanical Systems.* V. 12, No. 6. December 2003. p. 761-778.

[120] Unpublished email communication from Greg Cibuzar, March 21, 2006.

[121] Morgan, C. J., R. R. Vallance, and E. R. Marsh. "Micro machining glass with polycrystalline diamond tools shaped by micro electro-discharge machining." *Journal of Micromechanics and Microengineering.* V. 14. 2004. 1687-1692.

[122] Morgan, C. J. *Microgrinding with Polycrystalline Diamond Microtools to Improve the Precision of Microscale Features.* Unpublished Dissertation.

Vita

Education

Massachusetts Institute of Technology

Received a B.S. in Physics with a Minor in Music in 1991. Senior thesis documented reliability of high-speed data acquisition hardware for future use in a telescope to be built underground in Italy. Coursework included statistical physics, combinatorics and probabilities, quantum mechanics, calculus, machine design, analog circuits, and solid-state chemistry. GPA of 4.4/5.0.

University of Kentucky

Received an M.S. in Mechanical Engineering in 2003. Area of research is simulation and analysis of capacitive gage transducers. Courses taken include strength of materials, vibrations, finite element analysis, methods of theoretical physics, feedback control design, foundations of solid mechanics, advanced dynamics, radiation heat transfer, boundary element methods, optics, mechanics of composite materials, nonlinear oscillations, digital controls, and acoustics. GPA of 4.0/4.0.

Professional Positions Held

General Electric, Evendale, Ohio. Held position of Lead engineer for jet engine prognostic health management control from 2006 to present.

Texas Instruments, Versailles, Kentucky. Held position of Marketing Product Manager for ceramic capacitive pressure transducers from 1999 to 2000.

Princeton Instruments, Trenton, New Jersey. Held position of Marketing Product Manager for catadioptric UV lens and image-intensified video CCD products from 1994 to 1999. Held position of Technical Writer for all CCD camera products from 1992 to 1994.

Scholastic Honors

Recipient of Gaann Fellowship from 2000-2006.

Professional Publications

“Correcting Capacitive Displacement Measurements in Metrology Applications with Cylindrical Artifacts” *Precision Engineering*. V.29, No. 3. 2005.

“Effects of Spherical Targets on Capacitive Displacement Measurements”. *ASME Journal of Manufacturing Science and Engineering*. Vol. 126. 2004.

Analysis and Application of Capacitive Displacement Sensors to Curved Surfaces. Master’s Thesis. University of Kentucky. 2003.

“Polishing Compacted Titanium Nitride to Optimize Growth of Nanotubes.” *Proceedings of the 2001 American Society for Precision Engineering Annual Meeting*.

“Thermal Finite Difference Analysis of Threshold Heating for Nanoscale Machining.” *Proceedings of International Mechanical Engineering Conference & Exposition*.

“Thermoforming of Precision Thin-Film Mirrors.” *Proceedings of the 2002 American Society for Precision Engineering Annual Meeting*.

“Nanoscale Machining with Carbon Nanotubes” Intellectual Property Update